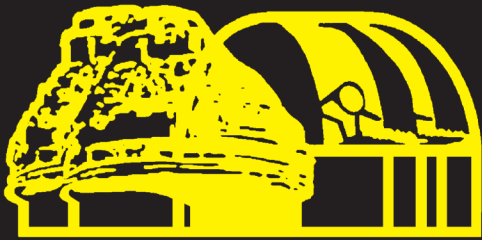


ISSN en trámite

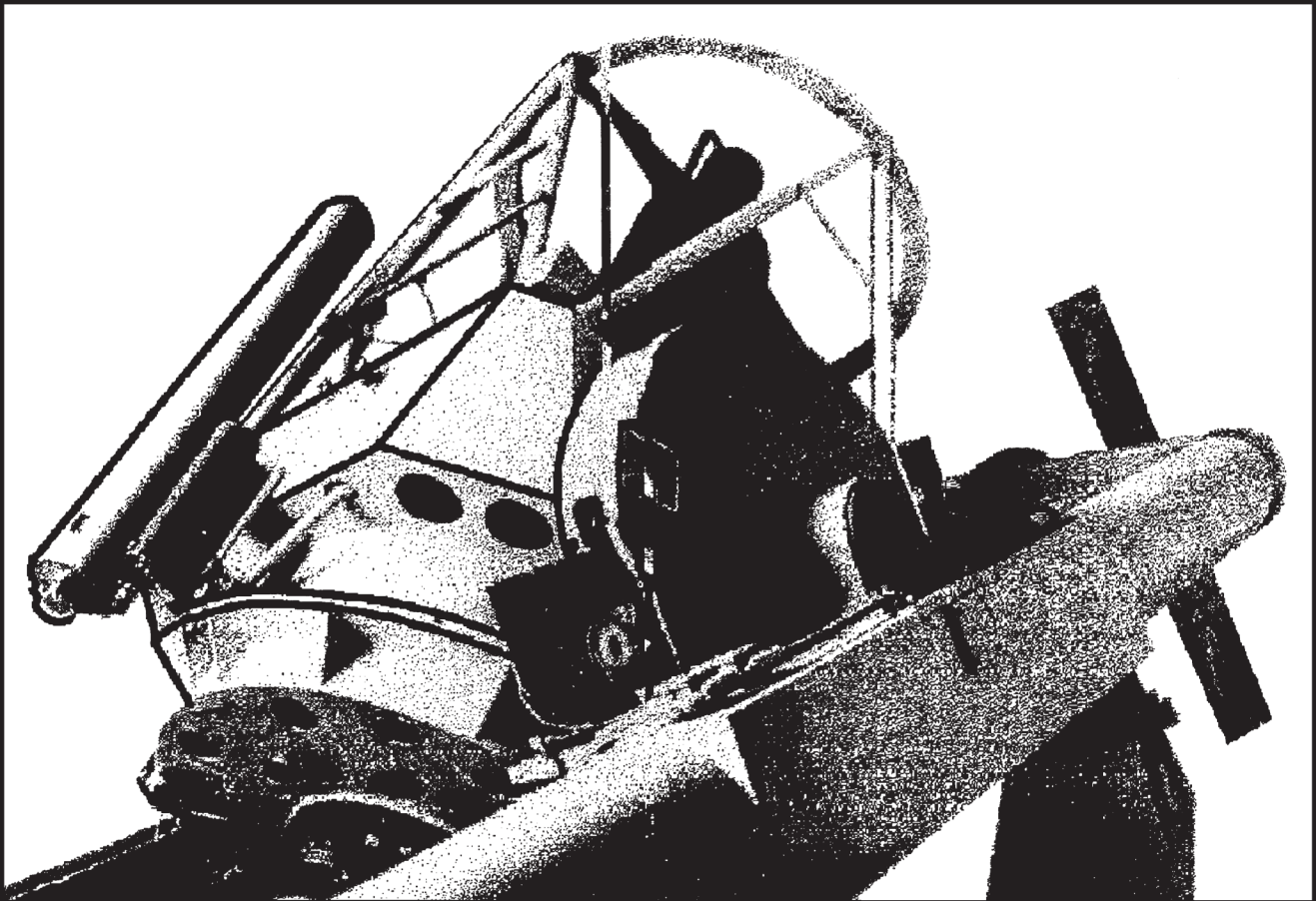
volumen 56, número 1, abril 2020



instituto de astronomía

unam

revista mexicana de astronomía y astrofísica



revista mexicana de astronomía y astrofísica

volumen 56
número 1
octubre 2020

Instituto de Astronomía
Universidad Nacional Autónoma de México

revista mexicana de astronomía y astrofísica

Editores fundadores

Eugenio E. Mendoza V., Paris Pişmiş y Silvia Torres-Peimbert

Revista Mexicana de Astronomía y Astrofísica

Editora: Christine Allen

Revista Mexicana de Astronomía y Astrofísica. Serie de Conferencias

Editora: Silvia Torres-Peimbert

Editores asociados

William Henney

Comité editorial

Horacio A. Dottori (Universidade Federal Rio Grande do Sul, Brasil)

Guido Garay (Universidad de Chile, Santiago, Chile)

Gloria Koenigsberger (Universidad Nacional Autónoma de México)

Hugo Levato (Complejo Astronómico El Leoncito, Argentina)

Luis F. Rodríguez (Universidad Nacional Autónoma de México)

José-María Torrelles (Institut d'Estudis Espacials de Catalunya, Barcelona, España)

Alan M. Watson (Universidad Nacional Autónoma de México)

Asistentes editoriales

Héctor Miguel Cejudo Camacho

Tulio Lugo Córdova

Asesoría en cómputo

Alfredo Díaz Azuara, Carmelo Guzmán Cerón, Liliana Hernández Cervantes
y Francisco Ruíz Sala

D.R. © 2020, Universidad Nacional Autónoma de México

Av. Universidad 3000

Col. Universidad Nacional Autónoma de México, C. U.

Alcaldía Coyoacán

04510 Ciudad de México

ISSN en trámite

URL de DOI: <https://doi.org/10.22201/ia.01851101p.2020.56.01>

rmaa@astro.unam.mx

<http://www.astroscu.unam.mx/RMxAA/>

La *RMxAA* aparece indexada en Current Contents, Science Citation Index, Astronomy and Astrophysics Abstracts, Physics Briefs, Publicaciones Científicas en América Latina, Astronomy and Astrophysics Monthly Index, PERIODICA, RedALyC, Latindex y SciELO.

Revista Mexicana de Astronomía y Astrofísica, volumen 56, número 1, abril 2020, es una publicación semestral, editada y distribuida por el Instituto de Astronomía, UNAM, Circuito Exterior, Ciudad Universitaria, 04510, Alcaldía Coyoacán, Ciudad de México, Teléfono: 5556223906, Correo Electrónico: rmaa@astro.unam.mx, ISSN en trámite. Editora responsable: Christine Patricia Allen Armiño. Distribución: Bienes y Servicios del Instituto de Astronomía, UNAM. Impresa por Grupo Edición, S.A. de C.V., Xochicalco 619, Colonia Letrán Valle, 03650, Alcaldía Benito Juárez, Ciudad de México. Fecha de impresión: 27 de marzo de 2020. Número de ejemplares impresos: 500 en papel Couché de 100 gramos los interiores y en cartulina Couché de 250 gramos los forros. Precio de la publicación: gratuito.

ANALYTICAL SOLUTIONS FOR THE DYNAMICAL CLOCK A+ INDICATOR IN A TOY MODEL OF PURE DYNAMICAL FRICTION	<i>M. Pasquato</i>	3
FURTHER PROPERTIES OF THE DYNAMICAL CLOCK A+ INDICATOR IN A TOY MODEL OF PURE DYNAMICAL FRICTION	<i>M. Pasquato</i>	7
A NEW NON-ECLIPSING CV SDSSJ122405.58+184102.7 – A PROBABLE MEMBER TO THE SW SEXTANTIS TYPE STARS	<i>A. Avilés, I. Arias, C. E. Chávez, J. E. Pérez, F. J. Tamayo, E. G. Pérez-Tijerina, & H. Aceves</i>	11
REVISITING FS AURIGAE AND ITS TRIPLE CATAclySMIC VARIABLE SYSTEM HYPOTHESIS	<i>C. E. Chavez, A. Aviles, N. Georgakarakos, C. Ramos, H. Aceves, G. Tovmassian, & S. Zharikov</i>	19
THE JET/COUNTERJET SYMMETRY OF THE HH 212 OUTFLOW	<i>A. Noriega-Crespo, A. C. Raga, V. Lora, & J. C. Rodríguez-Ramírez</i>	29
STAR FORMATION RATE IN LATE-TYPE GALAXIES: I- THE H_{α} AND FUV INTEGRATED VALUES	<i>M. A. Magaña-Serrano, A. M. Hidalgo-Gómez, I. Vega-Acevedo, & H. O. Castañeda</i>	39
THE PROPERTIES AND STABILITY OF SELF-GRAVITATING, POLYTROPIC SPHERES WITH $\gamma = 1$ TO 1.4 SPECIFIC HEAT RATIOS	<i>A. C. Raga, J. A. Osorio-Caballero, R. S. Chan, A. Esquivel, A. Rodríguez-González, V. Lora, & J. C. Rodríguez Ramírez</i>	55
SPECTRAL BEHAVIOR OF THE SYMBIOTIC NOVA HM SGE IN THE ULTRAVIOLET	<i>M. R. Sanad & M. A. Abdel-Sabour</i>	63
H_{α} KINEMATICS OF THE ISOLATED INTERACTING GALAXY PAIR KPG 486 (NGC 6090)	<i>M. M. Sardaneta, M. Rosado, & M. Sánchez-Cruces</i>	71
THE ENVIRONMENTAL DEPENDENCE OF THE AGE OF ACTIVE GALAXIES AND THE DEPENDENCE OF THE CLUSTERING PROPERTIES OF ACTIVE GALAXIES ON AGE	<i>X.-F. Deng & X.-Q. Wen</i>	87
CAN UVB VARIATIONS RECONCILE SIMULATED QUASAR ABSORPTION LINES AT HIGH REDSHIFT?	<i>L. A. García & E. V. Ryan-Weber</i>	97
SEARCH FOR STABLE ORBITS AROUND THE BINARY ASTEROID SYSTEMS 1999 KW4 AND DIDYMOS	<i>T. C. Oliveira & A. F. B. A. Prado</i>	113

CONTENTS

CCD PHOTOMETRY AND EVOLUTIONARY STATUS OF THE PULSAT- ING VARIABLE CSS J051053.0+071722	<i>K. B. Alton</i>	129
ON THE EVOLUTION OF ANGULAR MOMENTUM, MAGNETIC ACTIV- ITY AND MASS LOSS RATE OF LATE TYPE MAIN SEQUENCE STARS	<i>J. Bohigas</i>	139
ERRATUM: ASYMMETRIC SHAPES OF RADIO RECOMBINATION LINES FROM IONIZED STELLAR WINDS. (RMXAA, 2019, 55, 31)	<i>R. Ignace</i>	173
OBITUARY – EUGENIO E. MENDOZA VILLAREAL	<i>Armando Arellano Ferro</i>	175

ANALYTICAL SOLUTIONS FOR THE DYNAMICAL CLOCK A+ INDICATOR IN A TOY MODEL OF PURE DYNAMICAL FRICTION

M. Pasquato^{1,2}

Received July 25 2019; accepted October 7 2019

ABSTRACT

Blue straggler stars are more massive than the average star in globular clusters, as they originate from the merger of two stars. Consequently, they experience dynamical friction, progressively sinking to the cluster center. Recently, several indicators of the degree of dynamical relaxation of a globular cluster have been proposed, based on the observed radial distribution of blue straggler stars. The most successful is the Alessandrini indicator, or A+ for short, which is the integral of the cumulative distribution of the blue straggler stars minus that of a lighter reference population. A+ correlates with the dynamical age of a cluster both in realistic simulations and in observations. Here I calculate the temporal dependence of the A+ indicator analytically in a simplified model of the evolution of the blue straggler star distribution under dynamical friction only.

RESUMEN

Las estrellas rezagadas azules tienen masas mayores que las de las estrellas típicas de los cúmulos globulares, puesto que se originan de la fusión de dos estrellas. En consecuencia, experimentan fricción dinámica, y se acercan paulatinamente al centro del cúmulo. Se han propuesto recientemente varios indicadores del grado de relajamiento dinámico de un cúmulo globular basados en la distribución radial de las rezagadas azules. El más exitoso es el indicador de Alessandrini (A+), que es la integral de la distribución acumulada de las rezagadas azules menos la de estrellas menos masivas. A+ se correlaciona con la edad dinámica del cúmulo tanto en simulaciones realistas como en las observaciones. Aquí calculo analíticamente la dependencia con el tiempo del indicador A+, usando un modelo simplificado de la evolución de la distribución de las rezagadas azules, que toma en cuenta sólo la fricción dinámica.

Key Words: blue stragglers — globular clusters: general — methods: analytical

1. INTRODUCTION

Blue straggler stars are found in all globular clusters observed to date in the Milky way (Piotto et al. 2004). They are heavier than the average star in their host clusters, as they originate from stellar mergers either through direct collision (Hills & Day 1976) or by close-binary mass transfer (McCrea 1964; Knigge et al. 2009), or both (Davies et al. 2004; Mapelli et al. 2004). Since the first observations of a bimodality in the radial distribution of blue straggler stars when normalized to a reference population were done (Ferraro et al. 1993; Zaggia et al. 1997),

attempts at understanding its origin and evolution have been made based on simulations run with different software and various levels of realism (Mapelli et al. 2004, 2006; Ferraro et al. 2012; Hypki & Giersz 2013; Miocchi et al. 2015; Hypki & Giersz 2017; Solima & Ferraro 2019).

In a previous paper Pasquato et al. (2018) showed that the physical ingredients underlying the formation and motion of the minimum of the distribution are dynamical friction and diffusion respectively. While the two are connected as they ultimately arise from the same phenomenon, i.e. scatter with lighter background stellar particles, Pasquato et al. (2018) varied the diffusion coefficient and dynamical friction independently, showing that when diffusion is too

¹INAF, Osservatorio Astronomico di Padova, vicolo dell'Osservatorio 5, I-35122 Padova, Italy.

²INFN, Sezione di Padova, Via Marzolo 8, I-35131 Padova, Italy.

strong a minimum does not reliably form, whereas if diffusion is too weak a clear-cut minimum forms but does not move outwards over time. This suggests that simulation schemes should be carefully assessed regarding their ability to correctly model the dynamical friction and diffusion phenomena in order to reproduce the observed evolution of the blue straggler star distribution minimum with increasing dynamical age.

In this context Alessandrini et al. (2016) introduced a new *dynamical clock* indicator which did not require a measurement of the position of the minimum of the normalized blue straggler star distribution, as it is based on the cumulative radial distribution of blue straggler stars compared to the cumulative distribution of some other class of reference stars. The Alessandrini et al. (2016) indicator (or A+ for short) was introduced in the context of direct N-body simulations, where it was shown that it increases with the dynamical age of simulated clusters, acting as a mass-segregation powered dynamical clock. Later, Lanzoni et al. (2016) measured a slightly modified version of the A+ indicator on a sample of 25 Galactic globular clusters, showing that it correlates with the cluster dynamical age measured in terms of a cluster's current relaxation time.

The A+ indicator is defined as the difference between the integral of the cumulative distribution of the blue straggler stars, expressed as a function of the logarithm of the cluster-centric radius, and that of a reference distribution. In the following I will obtain some of its properties analytically under simplifying assumptions.

2. CALCULATIONS

2.1. A Toy Model of Dynamical Friction

I model blue straggler stars as a population of equal mass particles in circular orbits in a spherically symmetric fixed gravitational potential. The radius r of each orbit evolves due to dynamical friction, as

$$\dot{r} = -\frac{r}{\tau(r)} = -v(r), \quad (1)$$

where r is the distance from the center and $\tau(r)$ is a positive, monotonically increasing function of r , representing the dynamical friction timescale at radius r .

Equation 1 shows that orbital radii contract with an instantaneous velocity $v(r) > 0$ that depends only on r . It can be integrated, obtaining

$$\int_{r_0}^r \frac{\tau(x)dx}{x} = -t, \quad (2)$$

where r_0 is the initial value of the radius at time $t = 0$ and r is its current value at time t . In general $r_0 > r$ because the radii contract over time. If the function $\tau(x)$ is known, the integral can be calculated and r can be obtained as a function of r_0 and t :

$$r(r_0, t) = I^{-1}(I(r_0) - t), \quad (3)$$

where the primitive

$$I(r) = \int \frac{\tau(x)dx}{x} \quad (4)$$

is a monotonically increasing function because $\tau(x)/x$ always is positive. Consequently, it is invertible. Note also that $r(r_0, t)$ is a monotonically decreasing function of t for every $t > 0$ and for every r_0 , i.e. the orbit radii keep shrinking over time. This can be shown by writing

$$I(r_0) - t < I(r_0), \quad (5)$$

which holds for every $t > 0$, and applying I^{-1} , which is also monotonic, to both sides, yields

$$r(r_0, t) = I^{-1}(I(r_0) - t) < I^{-1}(I(r_0)) = r_0. \quad (6)$$

Similarly to equation 3,

$$r_0(r, t) = I^{-1}(I(r) + t), \quad (7)$$

also holds.

I now denote with $N(r, t)$ the cumulative distribution of particles at a given time as a function of radius. This is by construction such that $N(0, t) = 0$ and $\lim_{r \rightarrow \infty} N(r, t) = 1$ for all t . If for any two particles at time $t = 0$ the condition $r_{01} < r_{02}$ held, then at any subsequent t , $r_1(t) < r_2(t)$ would also hold: particles never cross. This holds due to the uniqueness of the solution of first-order ordinary differential equations. Therefore, all particles within a distance r of the center at time t were within a distance $r_0(r, t)$ at time 0, as can be seen by placing an imaginary particle exactly at r and observing that no other particle ever crosses its path. In other words, Lagrangian radii behave exactly like particle radii. So

$$N(r, t) = N(r_0(r, t), 0), \quad (8)$$

the number of particles that had a radius less than a given r_0 at the beginning still have a radius less than $r(r_0, t)$ at time t . This can be rewritten as

$$N(r, t) = N(I^{-1}(I(r) + t), 0), \quad (9)$$

which, given knowledge of the function I is a general solution for $N(r, t)$. Thus $\tau(r)$ fully determines $N(r, t)$ given an initial $N(r, 0)$.

2.2. Recovering the A+ Indicator

In the following I will assume that the reference population of stars to which the blue stragglers are compared to build the A+ indicator initially shares the same distribution as the blue stragglers and does not evolve.

Under this assumption it is trivial to obtain the evolution of the (three-dimensional) A+ indicator from equation 9. I will write $s = \log r$, so that

$$N(r, t) = N(I^{-1}(I(e^s) + t), 0), \quad (10)$$

and the A+ indicator becomes

$$A^+(t) = \int_{-\infty}^{+\infty} N(I^{-1}(I(e^s) + t), 0) ds - \int_{-\infty}^{+\infty} N(e^s, 0) ds. \quad (11)$$

2.3. Monotonicity

Note that at time $t_2 > t_1$

$$A^+(t_2) - A^+(t_1) = \int_{-\infty}^{+\infty} [N(I^{-1}(I(e^s) + t_2), 0) - N(I^{-1}(I(e^s) + t_1), 0)] ds, \quad (12)$$

and the integrand

$$N(I^{-1}(I(e^s) + t_2), 0) - N(I^{-1}(I(e^s) + t_1), 0) \quad (13)$$

is positive for every s , because $I^{-1}(I(e^s) + t_2) > I^{-1}(I(e^s) + t_1)$ as the two terms represent, per equation 7, the initial radius of a particle that is at $r = e^s$ at t_2 and t_1 respectively: a particle that took more time ($t_2 > t_1$) to fall to r was further away at the beginning. This implies that $A^+(t)$ is a monotonically increasing function of time, i.e. a working dynamical clock.

2.4. A+ Linear Dependence in Globular Cluster Cores

While equation 7 can be solved numerically for any $\tau(r)$, some choices of $\tau(r)$ will lead to a simple analytical solution. For example, following equation 1 of Mapelli et al. (2004) I take

$$\tau(r) = \tau(0) \frac{\sigma^3(r)\rho(0)}{\sigma^3(0)\rho(r)}, \quad (14)$$

where σ is the velocity dispersion of background stars at radius r and ρ is their number density. For a Plummer model this works out as

$$\tau(r) = \tau(0) \left(1 + \frac{r^2}{a^2}\right)^{7/4}, \quad (15)$$

where a is the model scale radius and $\tau(0)$ the scale time for dynamical friction at the center. Equation 4 is solved exactly, for this dependence, by

$$I(u) = \tau(0) \left[\frac{1}{2} \log\left(\frac{u-1}{u+1}\right) + \arctan(u) + \frac{2}{7}u^7 + \frac{2}{3}u^3 \right], \quad (16)$$

where

$$u = \left(1 + \frac{r^2}{a^2}\right)^{1/4} > 1, \quad (17)$$

which unfortunately cannot be inverted in terms of simple functions. However for small radii equation 15 reduces to a constant, so equation 4 becomes trivially

$$I(r) = \tau(0) \log(r/a), \quad (18)$$

and, with reference to equation 7

$$r = r_0 e^{-t/\tau(0)}, \quad (19)$$

so

$$N(r, t) = N(a e^{\log(r/a) + t/\tau(0)}, 0) = N(r e^{t/\tau(0)}, 0). \quad (20)$$

As the central regions of a Plummer model have approximately constant density $\rho(0)$, I can take at time $t = 0$

$$N_c(r, 0) = 4\pi\rho(0)r^3, \quad (21)$$

with a radial cutoff at

$$r_{c0} = (4\pi\rho(0))^{-1/3}, \quad (22)$$

after which $N_c(r, 0)$ becomes identically 1. At time t the radius at which $N_c(r, t)$ becomes identically 1 is

$$r_c = r_{c0} e^{-t/\tau(0)}. \quad (23)$$

Therefore

$$A^+(t) = \int_{-\infty}^{\log r_c} N_c(e^{s+t/\tau(0)}, 0) ds + \int_{\log r_c}^{\log r_{c0}} 1 ds - \int_{-\infty}^{\log r_{c0}} N_c(e^s, 0) ds, \quad (24)$$

which simplifies to

$$A^+(t) = \log \frac{r_{c0}}{r_c} = \frac{t}{\tau(0)}. \quad (25)$$

This result actually generalizes to any non-constant initial density as long as equation 19 holds, because of the interplay between the logarithm in the definition of the A+ indicator and the exponential dependence of equation 19, which leads to the first and the third term in equation 24 canceling out. Thus the A+ indicator should evolve linearly with time if the dynamical friction timescale is constant with radius.

3. CONCLUSIONS

Working within a pure dynamical friction picture, under a set of simplifying assumptions, I have shown that the Alessandrini et al. (2016) A+ indicator evolves monotonically in time and I have found an analytical solution for its time dependence. I worked out the case of a dynamical friction timescale that is constant with radius, which results in the A+ indicator increasing linearly with time. Monotonicity is an interesting result, as it proves that the A+ indicator is effectively a *dynamical clock*, as previously claimed by Alessandrini et al. (2016) based on the results of a set of direct N-body simulations. As my simple model neglects diffusion, which was instead treated numerically by Pasquato et al. (2018), I showed that the A+ indicator still works as a dynamical clock even in the absence of diffusion.

This project has received funding from the European Union’s Horizon 2020 research and innovation programme under the Marie Skłodowska-Curie grant agreement No. 664931. I wish to thank Dr. Pierfrancesco di Cintio, Dr. Paolo Miocchi, Dr. Alessandro Cobbe, and Dr. Stefano Pugnetti for helpful discussion on this subject. I warmly acknowledge the Referee’s contribution in pointing out some inconsistencies in my notation and in demanding additional rigorous proof for some statements.

REFERENCES

- Alessandrini, E., Lanzoni, B., Ferraro, F. R., Miocchi, P., & Vesperini, E. 2016, ApJ, 833, 252
- Davies, M. B., Piotto, G., & de Angeli, F. 2004, MNRAS, 349, 129
- Ferraro, F. R., Lanzoni, B., Dalessandro, E., et al. 2012, Natur, 492, 393
- Ferraro, F. R., Pecci, F. F., Cacciari, C., et al. 1993, AJ, 106, 2324
- Hills, J. G. & Day, C. A. 1976, ApL, 17, 87
- Hypki, A. & Giersz, M. 2013, MNRAS, 429, 1221
- . 2017, MNRAS, 471, 2537
- Knigge, C., Leigh, N., & Sills, A. 2009, Natur, 457, 288
- Lanzoni, B., Ferraro, F. R., Alessandrini, E., et al. 2016, ApJ, 833, L29
- Mapelli, M., Sigurdsson, S., Colpi, M., et al. 2004, ApJ, 605, L29
- Mapelli, M., Sigurdsson, S., Ferraro, F. R., et al. 2006, MNRAS, 373, 361
- McCrea, W. H. 1964, MNRAS, 128, 147
- Miocchi, P., Pasquato, M., Lanzoni, B., et al. 2015, ApJ, 799, 44
- Pasquato, M., Miocchi, P., & Yoon, S.-J. 2018, ApJ, 867, 163
- Piotto, G., De Angeli, F., King, I. R., et al. 2004, ApJ, 604, L109
- Sollima, A. & Ferraro, F. R. 2019, MNRAS, 483, 1523
- Zaggia, S. R., Piotto, G., & Capaccioli, M. 1997, A&A, 327, 1004

M. Pasquato: INAF, Osservatorio Astronomico di Padova, vicolo dell’Osservatorio 5, I-35122 Padova, Italy (mario.pasquato@inaf.it).

M. Pasquato: INFN, Sezione di Padova, Via Marzolo 8, I-35131 Padova, Italy.

FURTHER PROPERTIES OF THE DYNAMICAL CLOCK A+ INDICATOR IN A TOY MODEL OF PURE DYNAMICAL FRICTION

M. Pasquato^{1,2}

Received July 29 2019; accepted October 7 2019

ABSTRACT

The Alessandrini A+ indicator is a measure of star cluster dynamical evolution based on the mass-segregation of blue straggler stars. A+ is defined as the integral of the cumulative distribution of blue stragglers over log radius, minus a term related to the reference population used. In a companion paper I introduced a model of dynamical friction and calculated the A+ indicator analytically. Here I show further properties of the time evolution of A+, focusing on the physical interpretation of its time derivative dA^+/dt . I find that dA^+/dt is the mean of the reciprocal dynamical friction timescale, weighted by the density of blue stragglers. I show that it is non-negative (as expected based on monotonicity) due to the density of blue-stragglers being non-negative and that, for a radially non-decreasing dynamical friction timescale, dA^+/dt is also non-decreasing with time, making A+ a convex function.

RESUMEN

El indicador de Alessandrini A+ es una medida de la evolución dinámica de un cúmulo estelar basada en la segregación por masa de las estrellas rezagadas azules. Se define A+ como la integral de la distribución acumulada de las rezagadas azules sobre el logaritmo del radio, menos un término relacionado con la población de referencia usada. En el artículo anterior presenté un modelo con fricción dinámica y calculé analíticamente el indicador A+. Aquí muestro otras propiedades de A+, con énfasis en la interpretación física de su derivada con respecto al tiempo, dA^+/dt . Encuentro que dA^+/dt es la media del recíproco de la escala de tiempo dinámica, ponderada por la densidad de rezagadas azules. Muestro que no es negativa, pues la densidad de las rezagadas azules no es negativa. Muestro también que si la escala de tiempo de la fricción dinámica no decrece con el radio, entonces dA^+/dt no decrece con el tiempo, lo que hace que A+ sea una función convexa.

Key Words: blue stragglers — globular clusters: general — methods: analytical

1. INTRODUCTION

Alessandrini et al. (2016) recently introduced a new parameter, intended as a quantitative measurement of the dynamical age of old star clusters. This indicator, dubbed A+ for short, is based on measuring the radial distribution of massive tracers, such as blue straggler stars (Sandage 1953), which are undergoing mass segregation by virtue of being heavier than the average stars in the host cluster. The A+ indicator, in particular, involves taking the integral of the cumulative distribution of blue straggler stars

as a function of log radius, minus the same for a reference population, such as horizontal branch stars. The A+ indicator is easier to measure compared to other attempts at building a dynamical clock out of the blue straggler star distribution (Ferraro et al. 2012; Hypki & Giersz 2013; Miocchi et al. 2015; Hypki & Giersz 2017; Pasquato et al. 2018; Sollima & Ferraro 2019) as it does not depend on finding the exact position of the minimum of said distribution. While it was originally introduced in the context of N-body simulations, the A+ indicator was quickly shown to be able to capture the dynamical evolutionary stage of observed globular clusters, displaying a strong anticorrelation with their half-mass relaxation

¹INAF, Osservatorio Astronomico di Padova, vicolo dell'Osservatorio 5, I-35122 Padova, Italy.

²INFN, Sezione di Padova, Via Marzolo 8, I-35131 Padova, Italy.

time (Lanzoni et al. 2016). Throughout their paper, Alessandrini et al. (2016) argue that the A+ indicator strictly increases with time, and indeed show that this is the case in the large set of simulations they run, spanning a wide range of initial conditions and dynamical ingredients. This holds of course except for short term fluctuations due to numerical, or possibly dynamical, noise. Monotonicity with time is a crucial property for the A+ as well as for any other indicator of star-cluster dynamical aging, which is an intrinsically irreversible process. Another property of A+ that is apparent in the simulations run by Alessandrini et al. (2016), e.g. in their Figure 5, is that the derivative of A+ also increases with time, i.e. that $A+(t)$ is a convex function. In a companion paper (Pasquato 2019, referred as P19 for short in the following), I worked out an analytical formula for the (three dimensional) A+ indicator in a simplified model of mass segregation under pure dynamical friction, and showed that it evolves monotonically as a function of time for any initial blue straggler star distribution, and any radially increasing dynamical friction timescale law. Here I build on these results to obtain a few interesting properties of the A+ indicator. In particular I show that its derivative is a non-negative function, which is non-decreasing as a function of time if the dynamical friction timescale is non-decreasing with radius, making the A+ indicator a convex function of time. I provide a simple formula for the value of the A+ indicator derivative at the beginning of dynamical evolution, which directly connects it to the dynamical friction timescale. Finally, I suggest that in the late stages of dynamical evolution the A+ indicator derivative should approach a constant, making the A+ indicator asymptotically linear.

2. CALCULATIONS

In the context of the simplified model of evolution under dynamical friction introduced in P19, the A+ indicator is calculated as

$$A^+(t) = \int_{-\infty}^{+\infty} N(I^{-1}(I(e^s) + t), 0) ds - \int_{-\infty}^{+\infty} N(e^s, 0) ds, \quad (1)$$

where $N(r, t)$ is the cumulative distribution of blue straggler stars as a function of radius and time. The function $I(\cdot)$ is defined by P19 as

$$I(r) = \int \frac{\tau(x) dx}{x}, \quad (2)$$

where $\tau(r)$ is the dynamical friction timescale as a function of radius.

2.1. Time Derivative of the A+ Indicator

The second term on the right hand side of equation 1 does not depend on time, so its derivative vanishes. Regarding the first term, I redefine for simplicity

$$N_0(r) = N(r, 0), \quad (3)$$

so

$$\begin{aligned} \frac{dA^+}{dt} &= \frac{d}{dt} \int_{-\infty}^{+\infty} N_0(I^{-1}(I(e^s) + t)) ds \\ &= \int_{-\infty}^{+\infty} \frac{d}{dt} N_0(I^{-1}(I(e^s) + t)) ds, \end{aligned} \quad (4)$$

which, by using the inverse function derivative rule, becomes

$$\frac{dA^+}{dt} = \int_{-\infty}^{+\infty} \frac{dN_0}{dr}(I^{-1}(I(e^s) + t)) \frac{ds}{I'(I^{-1}(I(e^s) + t))}, \quad (5)$$

that is

$$\frac{dA^+}{dt} = \int_{-\infty}^{+\infty} \frac{dN_0}{dr}(r_0(e^s, t)) \frac{r_0(e^s, t)}{\tau(r_0(e^s, t))} ds, \quad (6)$$

where $r_0(r, t) = I^{-1}(I(r) + t)$ is the position at time $t = 0$ of a star currently at radius r (see P19 for a proof). Substituting back $s = \log r$, I obtain

$$\frac{dA^+}{dt} = \int_0^{+\infty} \frac{dN_0}{dr}(r_0(r, t)) \frac{r_0(r, t)}{r\tau(r_0(r, t))} dr; \quad (7)$$

by further substituting, for a given t , $r_0 = r_0(r, t)$, I obtain

$$\begin{aligned} \frac{dA^+}{dt} &= \int_0^{+\infty} \frac{dN_0}{dr}(r_0) \frac{r_0}{r(r_0, t)\tau(r_0)} \frac{dr}{dr_0} dr_0 \\ &= \int_0^{+\infty} \frac{dN_0}{dr}(r_0) \frac{ds}{ds_0} \frac{dr_0}{\tau(r_0)}, \end{aligned} \quad (8)$$

where $s_0 = \log r_0$. Alternatively, I can use the inverse function derivative again to obtain

$$\frac{dA^+}{dt} = \int_0^{+\infty} \frac{dN_0}{dr}(r_0) \frac{dr_0}{\tau(r)}. \quad (9)$$

This is a general formula for the derivative of the A+ indicator at time t . It is always non-negative because the integrand is non-negative as long as the derivative of the initial cumulative distribution function is. This condition is equivalent to requesting that density is always non-negative. In other words, the monotonicity of the A+ indicator derives from the condition that the number density of blue straggler stars is everywhere non-negative. Note how in

equation 9 the time dependence is all enclosed within the $\tau(r)$ term (not $\tau(r_0)$!) at the denominator. If $\tau(r)$ is constant I recover the result of P19 where the A+ indicator is linear with time, as its derivative equals $1/\tau(0)$ and its initial value is always zero by construction.

2.2. Convexity

The evolution of a star's radius given its initial value r_0 and the elapsed time t is given by equation 3 of P19:

$$r(r_0, t) = I^{-1}(I(r_0) - t). \quad (10)$$

For any $r_0, t > 0$ it holds that $r(r_0, t) < r_0$ due to the monotonicity of $I(\cdot)$. Moreover, for any $t_2 > t_1 > 0$

$$\begin{aligned} r(r_0, t_2) &= r(r_0, t_1 + (t_2 - t_1)) \\ &= I^{-1}(I(r_0) - t_1 - (t_2 - t_1)), \end{aligned} \quad (11)$$

and, defining $r_1 = r(r_0, t_1) = I^{-1}(I(r_0) - t_1)$ we obtain

$$\begin{aligned} r(r_0, t_2) &= I^{-1}(I(r_1) - (t_2 - t_1)) \\ &= r(r_1, t_2 - t_1) < r_1 = r(r_0, t_1), \end{aligned} \quad (12)$$

so for a given r_0 , the function $r(r_0, t)$ is monotonically decreasing with t . Stars can only sink towards smaller radii over time. Now, if $\tau(r)$ is non-decreasing, $\tau(r_1) \geq \tau(r_2)$ for any $r_1 > r_2$. Then the denominator $\tau(r)$ in equation 9 cannot increase with time because r decreases as shown in equation 12, and

$$\begin{aligned} \left. \frac{dA^+}{dt} \right|_{t=t_2} &= \int_0^{+\infty} \frac{dN_0}{dr}(r_0) \frac{dr_0}{\tau(r(r_0, t_2))} \geq \\ &= \int_0^{+\infty} \frac{dN_0}{dr}(r_0) \frac{dr_0}{\tau(r(r_0, t_1))} \\ &= \left. \frac{dA^+}{dt} \right|_{t=t_1}, \end{aligned} \quad (13)$$

proving that A+ is a convex function of time. This is a quite interesting result in the light of Figure 5 of Alessandrini et al. (2016) where the (two dimensional) A+ indicators calculated for different simulations appear to evolve with increasing slope for increasing times, modulo the numeric error. The physical interpretation for this result is that the evolution becomes faster as the blue straggler stars drop to smaller radii, where the dynamical friction timescale is shorter.

Equation 7 can also be used to calculate the slope of the A+ indicator at the start of the dynamical evolution, e.g. in a simulation, by setting $t = 0$.

$$\left. \frac{dA^+}{dt} \right|_0 = \int_0^{+\infty} \frac{dN_0}{dr}(r) \frac{dr}{\tau(r)}. \quad (14)$$

To further characterize this I can write

$$\left. \frac{dA^+}{dt} \right|_0 = \int_0^1 \frac{dN_0}{\tau(r(N_0))}. \quad (15)$$

So the derivative of the A+ indicator at the beginning of the dynamical evolution (e.g. at the start of a simulation) is the mean of the reciprocal of the dynamical friction timescale considered as a function of the initial cumulative number distribution of blue stragglers.

2.3. Limiting Behaviour at Large Times

If I set $\tau_0 = \tau(0) = \tau_L(0)$ and $\tau_\infty = \lim_{r \rightarrow \infty} \tau(r) = \tau_L(1)$ I obtain

$$\frac{1}{\tau_\infty} < \left. \frac{dA^+}{dt} \right|_0 < \frac{1}{\tau_0} \quad (16)$$

by substitution into equation 9, as $\tau(r)$ is increasing with radius.

In general, since a constant $\tau(r) = \tau(0)$ holds for the approximately constant-density cores of globular clusters, I expect the final stages of the evolution, when most blue stragglers have sunk to the core, to have a value of the A+ indicator's derivative that approaches the constant value $1/\tau(0)$. As I have shown, any value attained later in evolution should be larger than previous values of the derivative. This is another point where comparison with Figure 5 of Alessandrini et al. (2016) is reassuring, as all the slopes in that figure are quite smaller than one, even though their values of the A+ indicator are referred to the half-mass relaxation timescale, which is longer than the central dynamical friction timescale. Further caveats for a comparison are that:

- at some point during the evolution of a cluster, my simplified picture of dynamical friction will no longer represent reality, as diffusion effects will start to dominate right in the central regions, so the limiting value of $dA^+/dt = 1/\tau(0)$ is not necessarily reached;
- blue stragglers on very eccentric orbits already depart from my simplified picture, even at the beginning of their evolution;
- Alessandrini et al. (2016) use a projected, two-dimensional version of the A+ indicator;
- the reference stars (horizontal branch stars) they use are also evolving over time, as they are likely heavier than the average star in the simulations they run.

In subsequent papers I will address the third point, obtaining a better basis for comparison with simulations. The fourth point is addressed in the following.

2.4. Moving Reference Stars

Until now I assumed that the reference stars for the A+ indicator are fixed, i.e. that they keep the initial cumulative distribution over time. If I relax this assumption, while still assuming that the initial cumulative distribution of blue straggler and reference stars coincides, equation 1 becomes

$$A^+(t) = \int_{-\infty}^{+\infty} N(I^{-1}(I(e^s) + t), 0) ds - \int_{-\infty}^{+\infty} N(\hat{I}^{-1}(\hat{I}(e^s) + t), 0) ds, \quad (17)$$

where

$$\hat{I}(r) = \int \frac{\hat{\tau}(x) dx}{x}, \quad (18)$$

and $\hat{\tau}(r)$ is the dynamical friction timescale as a function of radius for the reference particles. If $\hat{\tau}(r) \gg \tau(r)$ for every r then we revert back to the original situation where I can neglect the effects of dynamical friction on the reference population, while if $\hat{\tau}(r) = \tau(r)$ then the A+ indicator will be identically zero over time. In the following I will assume that

$$\hat{\tau}(r) = \frac{m_{BSS}}{m_{HB}} \tau(r), \quad (19)$$

where m_{BSS} is the mass of a blue straggler star and m_{HB} the mass of a reference star. This is in line with e.g. Mapelli et al. (2004), who assume that dynamical friction scales inversely with mass. With this in mind it is easy to see that the time derivative of A+ calculated in equation 9 becomes

$$\frac{dA^+}{dt} = \int_0^{+\infty} \frac{dN_0}{dr}(r_0) \frac{dr_0}{\tau(r)} - \int_0^{+\infty} \frac{dN_0}{dr}(r_0) \frac{dr_0}{\hat{\tau}(r)}, \quad (20)$$

which, by substituting in equation 19, leads to the final result

$$\frac{dA^+}{dt} = \left(1 - \frac{m_{HB}}{m_{BSS}}\right) \int_0^{+\infty} \frac{dN_0}{dr}(r_0) \frac{dr_0}{\tau(r)}, \quad (21)$$

which shows that the slope of the time evolution of A+ is merely rescaled by a constant factor. Since both the A+ indicator referred to a static population and the one referred to a population that also suffers dynamical friction are zero at the beginning of evolution, then A+ itself is merely rescaled by a

constant factor. Thus all the results I obtained above still hold.

3. CONCLUSIONS

Working within the same pure dynamical friction picture I introduced in the companion paper P19, I have calculated the time derivative of the Alessandrini et al. (2016) A+ indicator and found that it is not decreasing in time if the dynamical friction timescale $\tau(r)$ is non-decreasing with radius. Thus the A+ indicator is a convex function of time. P19 results show that in a constant dynamical friction timescale scenario the A+ indicator is linear with time, so convexity implies that over time the A+ indicator evolves with increasing slope becoming asymptotically linear, as the late stages of evolution take place in the uniform density cores of globular clusters, where the dynamical friction timescale becomes constant. Finally, I have shown that the choice of a reference population that is also affected by mass-segregation (as is likely the case in an observational setting) merely leads to a constant rescaling of the A+ indicator.

This project has received funding from the European Union's Horizon 2020 research and innovation programme under the Marie Skłodowska-Curie grant agreement No. 664931. I wish to thank Dr. Pierfrancesco di Cintio, Dr. Paolo Miocchi, Dr. Alessandro Cobbe, and Dr. Stefano Pugnetti for helpful discussion on this subject.

REFERENCES

- Alessandrini, E., Lanzoni, B., Ferraro, F. R., Miocchi, P., & Vesperini, E. 2016, *ApJ*, 833, 252
- Ferraro, F. R., Lanzoni, B., Dalessandro, E., et al. 2012, *Nature*, 492, 393
- Hypki, A. & Giersz, M. 2013, *MNRAS*, 429, 1221
- _____. 2017, *MNRAS*, 471, 2537
- Lanzoni, B., Ferraro, F. R., Alessandrini, E., et al. 2016, *ApJ*, 833, L29
- Mapelli, M., Sigurdsson, S., Colpi, M., et al. 2004, *ApJ*, 605, L29
- Miocchi, P., Pasquato, M., Lanzoni, B., et al. 2015, *ApJ*, 799, 44
- Pasquato, M., Miocchi, P., & Yoon, S.-J. 2018, *ApJ*, 867, 163
- Sandage, A. R. 1953, *AJ*, 58, 61
- Sollima, A. & Ferraro, F. R. 2019, *MNRAS*, 483, 1523

M. Pasquato, INAF, Osservatorio Astronomico di Padova, vicolo dell'Osservatorio 5, I-35122 Padova, Italy (mario.pasquato@inaf.it).

M. Pasquato: INFN, Sezione di Padova, Via Marzolo 8, I-35131 Padova, Italy.

A NEW NON-ECLIPSING CV SDSSJ 122405.58+184102.7 – A PROBABLE MEMBER TO THE SW SEXTANTIS TYPE STARS

A. Avilés¹, I. Arias², C. E. Chávez¹, J. E. Pérez², F. J. Tamayo², E. G. Pérez-Tijerina², and H. Aceves³

Received May 14 2019; accepted October 23 2019

ABSTRACT

We present observational evidence that helps classify the non-eclipsing binary system SDSSJ 122405.58+184102.7 as a new member of the SW Sextantis (SW Sex) class. First, from the analysis of the optical light curve, we identify the presence of two periodic signals that develop on different time scales. The first one is the orbital period of 0.167811(1) days (= 4.027464 (3) h) and the second one is the white dwarf spin period of 28.6 minutes. This second period is probably the first evidence for the presence of a magnetic white dwarf in the system. The second evidence is the presence of the HeII λ 4886 emission line in its optical spectrum. In this work we interpret the detected periodicities within the context of a magnetic accretion model for SW Sex stars.

RESUMEN

Presentamos evidencia observacional que ayuda a clasificar al sistema binario no eclipsante SDSSJ 122405.58+184102.7 como un nuevo miembro de la clase SW Sextantis (SW Sex). Primero, a partir del análisis de la curva de luz en el óptico, identificamos la presencia de dos señales periódicas que se desarrollan en diferentes escalas de tiempo. La primera es el período orbital de 0.167811(1) días (= 4.027464 (3) h) y la segunda es el período de giro de la enana blanca de 28.6 minutos. Este segundo período es probablemente la primera evidencia de la presencia de una enana blanca magnética en el sistema. La segunda evidencia es la presencia de la línea de emisión HeII λ 4886 en su espectro. En este trabajo interpretamos las periodicidades detectadas dentro del contexto de un modelo de acreción magnético para estrellas SW Sex.

Key Words: binaries: general — novae, cataclysmic variables — stars: individual: SDSSJ 122405.58+184102.7

1. INTRODUCTION

Cataclysmic variables stars (CVs) are semi-detached binary systems composed by a white dwarf (WD) as primary star and a late-type main sequence secondary star. The later fills its Roche Lobe and transfers matter through the Lagrangian point L_1 onto the WD via Roche-lobe overflow.

In non-magnetic systems, the incoming material forms an accretion disk around the WD (Warner 1995). This accretion disk periodically reaches a critical surface density value, leading to the development of thermal instabilities (Meyer & Meyer-

Hofmeister 1981), triggering an outburst that increases the system brightness by up to 8 magnitudes. The system returns to quiescence in a few days or weeks. This photometric behavior defines a CV class named Dwarf Nova (Patterson et al. 1981; Howell et al. 1995; Szkody & Mattei 1984). Besides the light curve pattern method to classify CVs, there are other parameters that help to do so, such as the orbital period, the mass transfer rate or the magnetic field strength.

The orbital period defines the separation of the binary components and establishes the evolutionary status of the secondary star. CVs with periods over 3 hours contain secondaries stars with radiative cores, and as the orbital period decreases below 3 hours the companion reaches a mass low enough to become

¹Facultad de Ingeniería Mecánica y Eléctrica, UANL, México.

²Facultad de Ciencias Físico Matemáticas, UANL, México.

³Instituto de Astronomía, Universidad Nacional Autónoma de México, México.

fully convective (Verbunt & Zwaan 1981; Rappaport, Verbunt, & Joss 1983; Paczynski & Sienkiewicz 1983; Spruit & Ritter 1983).

A high mass transfer rate defines the nova-like (NL) CV class. It helps to maintain a hot and stable accretion disk and prevents dwarf-nova-type outbursts. We refer to Warner (1995) for a general review on NLs and CVs in general, or Mizusawa et al. (2010); Balman et al. (2014) where they describe the UV and X-ray properties of several NL systems.

The strength of the magnetic field defines two types of CVs named Polars and Intermediate Polars (IP). In Polars, the magnetic field is so strong ($B \geq 20$ MG) that it forces the WD to spin around its polar axis with the orbital period (Campbell 1997). When the incoming ionized accretion stream encounters the magnetosphere around the WD, it is driven by the magnetic field lines, forming a shock region at the magnetic poles, rather than an accretion disk. If the magnetic field is weaker, as in IP CVs ($B \approx 2 - 8$ MG), a truncated accretion disk may form outside the magnetosphere. The incoming material hits the magnetosphere at all points over the inner edge of the accretion disk, and the flow becomes an accretion curtain rather than a single converging stream (Rosen, Mason & Cordova 1988; Hellier, Cropper & Mason 1991). Another effect of a weaker magnetic field is that the WD rotates as fast as ten times the orbital frequency, so synchronous rotation is no longer present.

Within the CV zoo it is possible to find the SW Sex stars, which are a subclass of high accretion rate CVs; i.e. NL members. They were first identified by Thorstensen et al. (1991) as eclipsing NL CVs with an orbital period around 3 to 4 hours. Radial velocities studies reveal that the emission lines vary periodically; the Balmer series lines lagging behind the expected phase for a WD according to photometric ephemeris. Their spectra show single or double-peaked emission lines, regardless of inclination angle. The single-peaked emission lines are thought to originate from the material encountering a magnetic accretion curtain close to the surface of the WD (Hoard et al. 2003). In contrast, the double-peaked profiles are likely a consequence of phase-dependent absorption components, as revealed by their trailed spectra.

Nowadays, SW Sex stars are thought to be the dominant population of CVs with periods within 3 and 4.5 hours (Rodríguez-Gil et al. 2007). A few cases of confirmed SW Sex stars show circular polarization, reflecting its magnetic nature (Rodríguez-Gil et al. 2001). Additionally, photometric quasi-

periodic oscillations (QPOs) are features observed recently in SW Sex stars. It is possible that this QPOs reflect the rotation of an underlying magnetic WD (Patterson et al. 2002). Finally, evidence has been mounting that the SW Sex phenomenon is an evolutionary stage in the evolutionary process of CVs (Schmidtobreick et al. 2012).

SDSS J1224 (12:24:05.58+18:41:02.7) is a relatively bright star with $g = 16.01$ mag. The presence of absorption and emission lines in its spectrum point to its being a pre-CV; a possible source for this could be the irradiation from the secondary by a hot WD (Szkody et al. 2011). Szkody et al. (2014) reported 126 min of time-resolved spectra taken in 2011, and concluded that there was no significant radial velocity variation during that time interval, so the system likely has a long orbital period or a low inclination angle.

In this work we present observational evidence that allows to classify SDSS J1224. This paper is organized as follows. In § 2 we present our observations, and in § 3 the data analysis and results. In § 4 a discussion is provided with our main conclusions stated in § 5.

2. OBSERVATIONS AND DATA REDUCTION

2.1. Photometric Observations

Differential time-resolved photometry of SDSSJ 1224 was conducted using the direct CCD imaging mode of a 0.84m telescope, located at Observatorio Astronómico Nacional at the Sierra San Pedro Mártir (OAN SPM⁴) in México. We acquired a long series of photometric data in the V broadband Johnson-Cousins filter, with exposure times ranging from 30 to 60 s. We observed the system on three nights in April 2016, four nights in March 2017 and three nights in April-May 2017 with the same instrument and configuration. Table 1 shows the log of these photometric observations.

Data reduction was performed using standard IRAF procedures (Tody 1986, 1993). The images were bias-corrected and flat-fielded before aperture photometry was carried out. We used photometric aperture radii of 2.0 times the PSF FWHM. The uncertainty in the differential photometry was estimated to be in the range 0.02 to 0.05 mag, according to the magnitude dispersion observed for the field stars. We used the star TYC 1445-830-1 in the field of view as the reference star.

⁴<http://www.astrossp.unam.mx>

TABLE 1
LOG OF TIME-RESOLVED OBSERVATIONS OF
SDSSJ 1224 IN THE V BAND

Date	HJD Start + 2457000	Exp. Time Number of Integrations	Duration h
01 April 2016	480.73269	30 s \times 387	3.2
02 April 2016	481.64345	60 s \times 387	6.5
03 April 2016	482.67408	60 s \times 240	4.0
23 March 2017	836.72960	30 s \times 200	1.7
24 March 2017	837.682042	60 s \times 370	6.2
25 March 2017	838.667957	60 s \times 240	4.0
26 March 2017	839.645395	60 s \times 210	3.5
29 April 2017	872.667346	60 s \times 281	4.7
30 April 2017	873.660104	60 s \times 270	4.5
01 May 2017	874.650873	60 s \times 210	4.0

2.2. Spectroscopic Observations

We carried out spectroscopic observations using the 2.12m telescope located at OAN SPM, with the low to intermediate resolution Boller & Chivens (B&Ch) spectrograph. We acquired spectra with a resolution of 5.5 Å using a 600 lines/mm grating to cover a 4300 – 5700 Å range. The observations were made through a 1.5'' slit, oriented in the east-west direction. CuHeNeAr lamp exposures were taken every 60 min for wavelength calibration and for flux calibration; spectrophotometric standards from Oke (1990) catalog were observed. The exposure time was 900 s per spectrum. The image processing was carried out with standard IRAF procedures (Tody 1986, 1993).

3. DATA ANALYSIS AND RESULTS

3.1. Light Curve Morphology

We observed CV SDSSJ 122405.58+184102.7 over ten nights, spread over two years, covering 42 hr of total photometry. The system was at quiescence during our observations, as we can see in the top panel of Figure 1. However, individual light curves (individual 10 frames in Figure 1) have two conspicuous brightness variations, occurring at two different time scales but with almost the same amplitude: a long photometric signal with ≈ 0.2 mag amplitude and a short one with ≈ 0.1 mag amplitude.

On HJD = 836 (frame N4 on Figure 1) the light curve exhibits a sinusoidal pattern with a mean amplitude of ≈ 0.1 mag and a period of tens of minutes. We can appreciate the later in more detail in the upper panel of Figure 2. However, this modulation nearly disappears when the observation time is

longer, like in HJD = 837 (frame N5 in Figure 1). In the bottom panel of Figure 2 the long term photometric signal is highlighted. In that case, the brightness changes mainly because of the orbital motion. Even masked inside the long photometrical signal, the 0.1 mag modulation is present on other nights (darker circles in Figure 1).

3.2. Photometric Orbital Period

In Figure 1, all observations are displayed in different frames. We applied a discrete Fourier transform (DFT) algorithm, using the software Period04 (Lenz & Breger 2005), to our complete photometric data set to search for significant periodic signals. The results obtained in this way are compatible with a Lomb-Scargle periodogram.

Panel (a) of Figure 3 shows a fraction of the total power spectrum for a ten days light curve after subtracting the spectral window. We explored the frequency range from 0 to 600 cycles day⁻¹ (the Nyquist limit). However, the power spectrum is dominated by short frequencies. The maximum frequency is located at $\Omega = 5.959119$ cycles day⁻¹ with a SNR of 7.98. According to empirical results of Breger et al. (1993), and numerical simulations from Kuschnig et al. (1997), a power spectrum with a SNR larger than 4.0 is needed to ensure that the signal is a real feature. We carried out a Monte Carlo simulation to improve the orbital frequency and to calculate its uncertainty. This kind of Monte Carlo simulation is described in Mennickent & Tappert (2001), Mennickent et al. (2002) and Aviles et al. (2018). We generated 1000 data sets with the same HJD as the original time string and the magnitudes were those obtained by the last fit plus Gaussian noise. For every new data set, a least-squares fit was computed. The frequency distribution of this simulation was used to improve the orbital frequency and the uncertainty corresponds to the standard deviation of this distribution. With this procedure, the frequency was improved to 5.959076 cycles day⁻¹ which corresponds to a period $P = 1/\Omega = 0.167811(1)$ days (= 4.027464 (3) h) adopted here as the orbital one. In panel (b) of Figure 3 we present a Monte Carlo histogram that shows the frequency improvement compared with that obtained from the FFT power spectrum (inset). Finally, in panel (c) of Figure 3 we show the folded light curve with the period $P = 4.03$ h beside a sinusoidal fit to remark the 0.2 magnitude long term modulation.

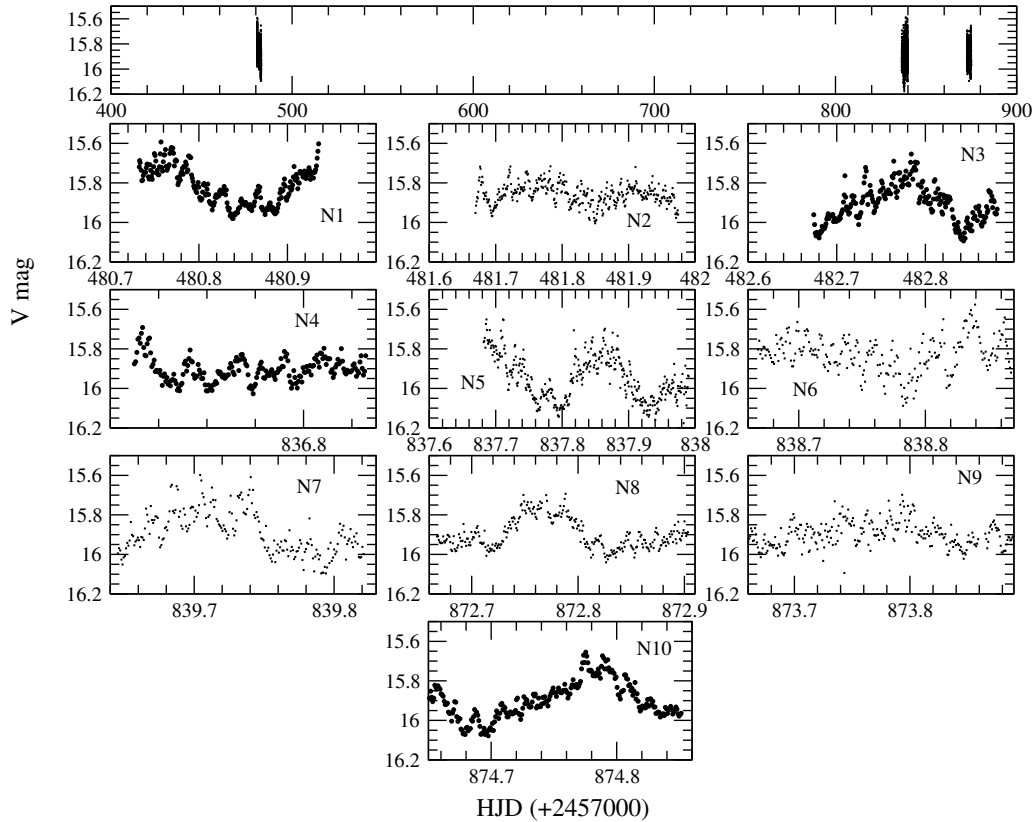


Fig. 1. The top panel shows the light curve (V magnitude as function of time) for SDSSJ1224 acquired over two years. The system was always at its quiescence state during observations (≈ 15.9 magnitudes). In the bottom panels we show individual light curves for each observation night. We identify two brightness variations occurring at different time scales. This is evident by eye inspection in the panels labeled N4 and N5.

3.3. Short Time-Scale Variability in the Light Curve

The power spectrum is the most widely used tool to detect any quasi-periodic oscillation. In such a case, the power spectrum will show a broad peak that covers many frequencies, rather than a narrow peak centered on a given frequency. In other words, these oscillations are not coherent over time. They can change in a time scale of less than a day, like in V442 Oph and RX J1643.7+3402 (Patterson et al. 2002), or can be coherent over 20 cycles like in HS 0728+6738 (Rodríguez-Gil et al. 2004).

To inquire if a short time-scale oscillation is present in other nights, and to gain insight about the HDJ = 836 light curve behavior, we used *Period 04* to analyze the data marked with darker circles in Figure 1 (Frames N1, N3, N4 and N10). We selected at least one night from each observational campaign. In some cases it was necessary to detrend the data to be able to carry out the period analysis, as in Kennedy et al. (2016), where they masked the light curve to remove the eclipses in

MASTER OTJ192328.22+612413.5. We explored a wide range of frequencies as was done for the orbital period analysis. In Panel (a) of Figure 4 we show a portion of the power spectrum, and the frequency that modulates this data with a high probability $\omega = 50.423395 \text{ day}^{-1}$, equivalent to a period of $P = 28.558 \text{ min}$. We also carried out a Monte Carlo simulation to improve this value. The histogram in Panel (b) of Figure 4 shows the most favored frequency for this variability, $\omega = 50.423990 \text{ days}^{-1}$. In Panel (c) we present the data folded with a period of 28.6 min, where a wave pattern is observed with an amplitude of ≈ 0.1 magnitudes.

We assume that this short-periodic variation may be related to the spin period of the WD. Therefore, SDSSJ1224 could be classified as an IP. Another evidence in favor of an IP nature is the detection of beat frequencies $\omega - 2\Omega$, $\omega - \Omega$, $\omega + \Omega$, $\omega + 2\Omega$, where ω and Ω are spin and orbital frequencies, respectively. The existence of the spin-orbital sidebands for IPs was pointed out by Warner (1986) and Wynn & King

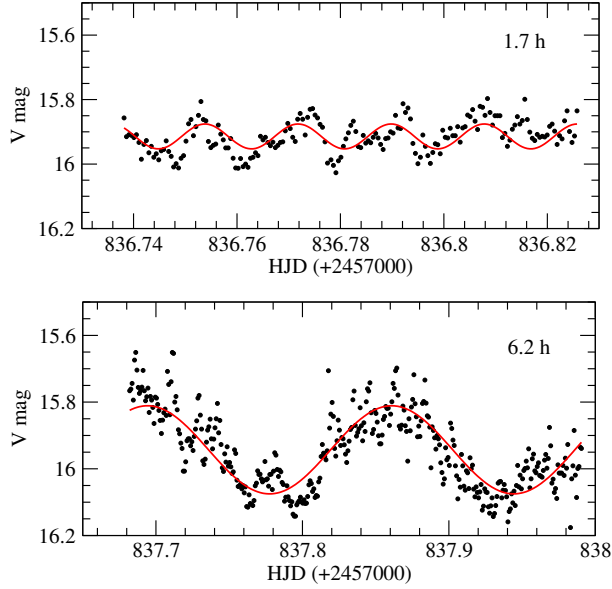
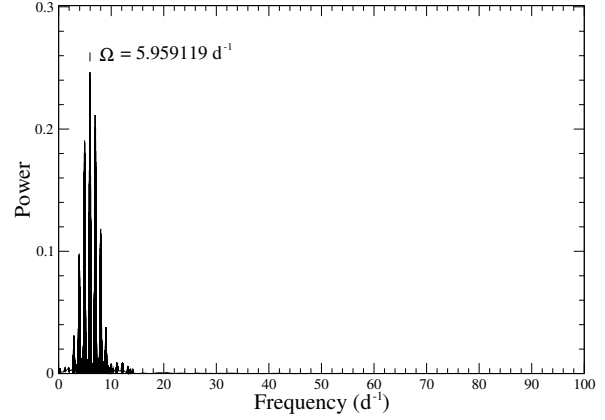


Fig. 2. Two time-scales for the two brightness variations. Upper panel, light curve for HJD = 836 showing the short photometric signal with ≈ 0.1 mag amplitude. Bottom panel, light curve for HJD = 837 showing the long photometric signal with ≈ 0.2 mag amplitude. The observation time span is indicated at each panel. The color figure can be viewed online.

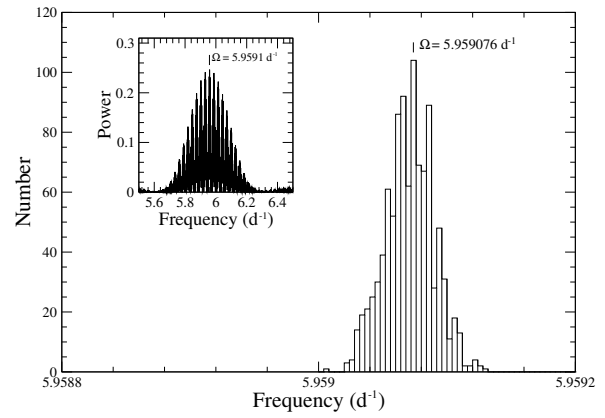
(1992). The optical beat period is thought to arise from the reprocessing of soft X-rays by parts of the system fixed on the binary frame, like the secondary star itself.

3.4. Spectroscopic Features of SDSSJ1224

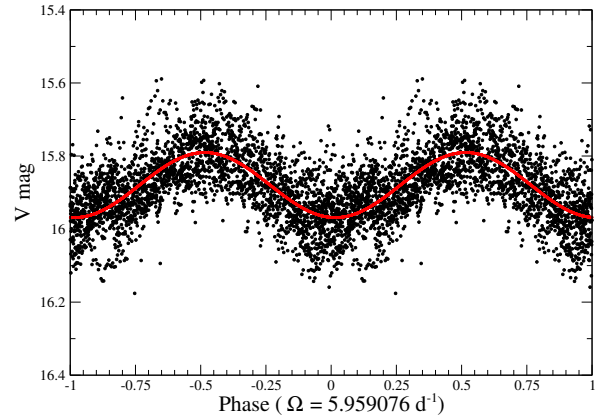
The average of 36 spectra of SDSSJ1224, acquired on March 19, 2017 (HJD ≈ 834.66), is presented in Figure 5. This spectrum shows single-peaked line profiles dominated by hydrogen (Balmer series) and HeI ($\lambda 5015$, $\lambda 4922$ and $\lambda 4388$) emission lines. High excitation lines like HeII $\lambda 4886$, the CIII / NIII $\lambda 4645$ Bowen blend and OII $\lambda 4416$ are also present. Of particular interest is the presence of the HeII $\lambda 4886$ line, because it is recognized as evidence of the presence of a source of ionizing photons, typical of magnetic CVs or NL variables (Araujo-Betancor et al. 2003; Rodríguez-Gil et al. 2004). Table 2 provides the equivalent widths (EW) and the full-width half-maximum (FWHM) of the main emission lines detected in the averaged spectrum. The FWHMs were obtained by fitting a single Gaussian to the line profiles. Taking into account the small FWHM of the lines, the inclination angle is expected to be low for SDSSJ1224.



(a) Power Spectrum

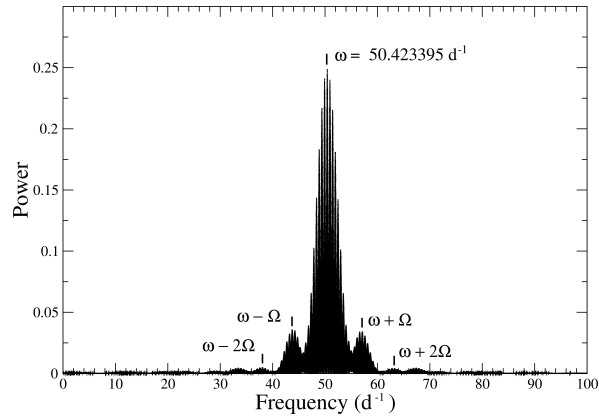


(b) Monte Carlo histogram

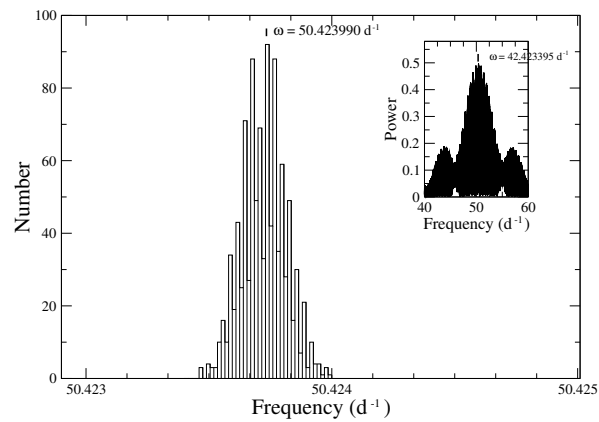


(c) Folded light curve

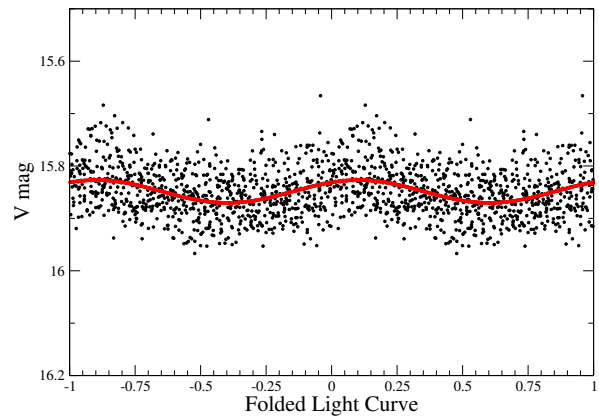
Fig. 3. (a) Power spectrum for the 10-days light curve after subtracting the spectral window, indicating the most probably frequency. (b) Histogram generated from the Monte Carlo simulation, showing an improved frequency in our data set. (c) Phase-folded light curve and least-squares fit, shown with a red solid line (see the online version); all data were fit to a period of $P = 1/\Omega$. The color figure can be viewed online.



(a) Power Spectrum



(b) Monte Carlo histogram



(c) Folded light curve

Fig. 4. (a) Power spectrum for the data marked with open circles in Figure 1, the frequency is $\omega = 50.423395 \text{ day}^{-1}$. (b) Histogram generated from the Monte Carlo simulation, showing an improved spin frequency. (c) Folded data with the frequency for the short period variability $P = 28.6 \text{ min}$. The red solid line (see the online version) is a least-squares fit to the data. The color figure can be viewed online.

TABLE 2

SDSSJ1224 EMISSION LINES: MARCH 2017

Line	FWHM [\AA]	EW [\AA]
H γ	6.425	1.312
He II λ 4886	9.512	0.506
H β	7.177	2.035
He I λ 4922	7.032	0.234
He I λ 5015	8.850	0.256

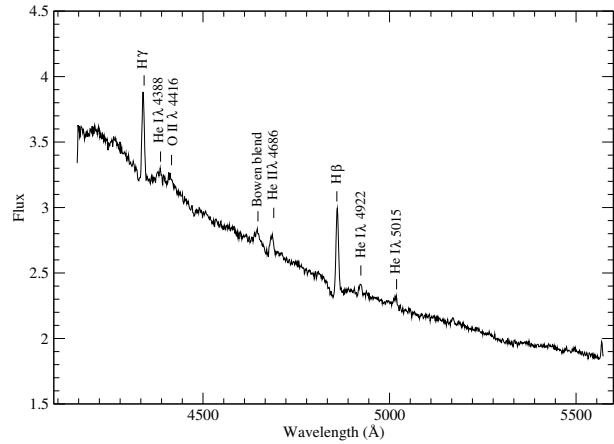


Fig. 5. Averaged flux calibrated spectrum of SDSSJ1224. The major lines are marked. Vertical axis is in units of flux density $F_{\lambda} \times 10^{-15} \text{ erg cm}^{-2} \text{ s}^{-1} \text{ \AA}^{-1}$.

SDSSJ1224 has an optical spectrum in quiescence similar to RX J1643.7+3402, HS 0728+6738 and HS 1813+6122, as reported by Patterson et al. (2002), Rodríguez-Gil et al. (2004), Rodríguez-Gil et al. (2007), respectively. In all cases, they argue the SW Sex membership according to spectroscopic properties and photometric variabilities. Rodríguez-Gil et al. (2009) detected circular polarization in RX J1643.7+3402, confirming in this way the magnetic nature of SW Sex stars.

In Figure 5 we observe strong evidence for the detection of the WD as absorption in the blue wings of both the H β and H γ lines. This is in agreement with the results reported by Szkody et al. (2011, 2014). Our photometry and FWHM measurements support the idea of a long orbital period, as well as a low inclination angle for SDSSJ1224, instead of a low accretion rate as the reason for the WD detection.

4. DISCUSSION

CV SDSSJ1224 is a non-eclipsing binary system that has certain photometric features to potentially lead to a classification as a SW Sex star. Firstly, we found

an orbital period of 4.03 h. According to Rodríguez-Gil et al. (2007), the orbital periods for such systems are from 3 to 4.5 h. Almost 50% of the CV population in this range has been classified as SW Sex stars. This sample includes eclipsing and non-eclipsing systems.

Second, we detected quasi-periodic oscillations with a period of 28.6 minutes. In terms of short period variabilities (kilo-seconds), SW Sex stars are also characterized by exhibiting quasi-periodic modulations in their light curves. In a compilation of CVs that show fast oscillations, Warner (2004) presented nine SW Sex stars that show quasi-periodic oscillations (QPOs) with a predominant time scale of $\approx 1000 - 2000$ s (16.7 – 33.3 min).

Third, another fact that supports our conjecture is that assuming an accretion disk-magnetic field interaction model, as proposed by Rodríguez-Gil et al. (2001), the spin period and the orbital one are related by

$$P_{spin} \simeq 0.31 f^{3/2} P_{orb}. \quad (1)$$

The previous equation results from considering that the shock between the gas stream and the accretion disk occurs close to the co-rotation radius. Here f represents the co-rotation radius expressed in units of R_{L1} (the distance between the WD and the inner Lagrangian point, L_1). In the case of SDSSJ1224, the value for f is 0.53, which is in good agreement with values reported for the prototype SW Sex itself (Groot 1999); LS Peg (Rodríguez-Gil 2001); V533 Her (Rodríguez-Gil & Martínez-Pais 2002). As a consequence of this model, SW Sex stars are indeed IP with the highest mass accretion rates.

Fourth, variabilities on time scales of minutes to tens of minutes have been detected in the optical light curve of several IPs (e.g., Patterson et al. 2002), and they are recognized as the spin period of the magnetic WD. We consider that, from its spectral appearance during low state (Figure 5) and the optical variability detected, SDSSJ1224 is indeed a new IP SW Sex class member. We suggest that the detected frequency of $50.423990 \text{ day}^{-1}$ is the WD spin frequency ω ($P_{spin} = 1/\omega$). The quasi-sinusoidal shape of its light curve, which is typical for the spin light curve of IPs (see e.g., the spin light curve of FO Aqr by de Martino et al. 1994), lends support to our hypothesis that this frequency is indeed the spin frequency of the WD.

Fifth, magnetic WDs in spin equilibrium should closely satisfy the ratio $P_{spin} / P_{orb} = 0.1$ (King & Lasota 1991), assuming that the accretion process is not primarily through a disk. The QPOs may reflect an underlying rotation of a magnetic WD (Patterson

et al. 2002). In the case of SDSSJ1224 this assumption seems quite valid, since if the 28.6 min signal is the spin period of the WD, then $P_{spin} = 0.12 P_{orb}$, which is very close to the value around which IPs seem to cluster on hard X-ray surveys (Scaringi et al. 2010).

5. FINAL COMMENTS AND CONCLUSIONS

We conclude that, based on the overall light curve features, the reported photometric periods and the spectroscopic properties, the system SDSSJ1224 can be classified as a new non-eclipsing SW Sex. The observed behavior matches all the conditions to be a member of this class of CVs.

It has a photometric orbital period of 4.03 h, which lies in the range of periods where the vast majority of SW Sex stars are grouped. It shows photometric features common to this type of stars and, as such, the number of non-eclipsing systems of this particular type in this range of periods is increased.

We detect a brightness variation amplitude of 0.1 mag and a period of 28.6 min, that we associate to the spin period of the WD. Also, we detect beat frequencies between the WD spin frequency, ω , and the orbital frequency, Ω , of the order of 30 minutes ($P_{orb} = 8 P_{beat}$) like in the system RX J1643.7+3402 (Rodríguez-Gil et al. 2009).

The photometric behavior fits very well with those observed on the out-of-eclipse light curve of several CVs like HS 0728+6738 (Rodríguez-Gil et al. 2004) or MASTER OTJ192328.22+612413.5 (Kennedy et al. 2016). In particular, these two objects show a QPO amplitude of 0.2 mag with a period around 20 minutes, quite similar to SDSSJ1224. This result may imply that the QPOs are not exclusive to eclipsing systems, as was pointed out by Patterson et al. (2001).

Because quasi-periodic oscillations in the range of kilo-seconds have recently been detected in confirmed SW Sex stars (Patterson 2002; Kennedy et al. 2017; Rodríguez-Gil et al. 2007), we consider that SW Sex stars are actually members of IP CVs stars.

The physical conditions present in this type of binary systems are not well understood and should be addressed both theoretically and observationally. However, such a study is beyond the scope of this work.

This work is based upon observations carried out at the Observatorio Astronómico Nacional at the Sierra San Pedro Mártir (OAN-SPM), Baja California, México. We thank the daytime and night support staff at the OAN-SPM for facilitating and help-

ing us to obtain the observations. The authors also acknowledge PAICYT-UANL grant CE642-18 for resources provided toward this research. We are also thankful to the anonymous referee for a careful reading of the manuscript and for useful comments that improved the content of this work.

REFERENCES

- Araujo-Betancor, S., Gänsicke, B. T., Hagen, H.-J., et al. 2003, *A&A*, 406, 213
- Avilés, A., Chávez, C., García, P., et al. 2018, *RMxAA*, 54, 389
- Balman, Ş., Godon, P., & Sion, E. M. 2014, *ApJ*, 794, 84
- Breger, M., Stich, J., Garrido, R., et al. 1993, *A&A*, 271, 482
- Campbell, C. G. 1997, *MNRAS*, 291, 250.
- de Martino, D., Buckley, D. A. H., Mouchet, M., et al. 1994, *A&A*, 284, 125
- Groot, P. J. 1999, Ph.D. Thesis
- Hellier, C., Cropper, M., & Mason, K. O. 1991, *MNRAS*, 248, 233
- Hoard, D. W., Szkody, P., Froning, C. S., et al. 2003, *AJ*, 126, 2473.
- Howell, S. B., Szkody, P., & Cannizzo, J. K. 1995, *ApJ*, 439, 337.
- Kennedy, M. R., Callanan, P., Garnavich, P. M., et al. 2016, *AJ*, 152, 27
- Kennedy, M. R., Callanan, P., Garnavich, P. M., et al. 2017, *MNRAS*, 466, 2202.
- King A. R., Lasota J.-P., 1991, *ApJ*, 378, 674
- Knigge, C. 2011, *ASPC*, 447, 3
- Kuschnig, R., Weiss, W. W., Gruber, R., et al. 1997, *A&A*, 328, 544
- Lenz, P. & Breger, M. 2005, *CoAst*, 146, 53.
- Mennickent, R. E. & Tappert, C. 2001, *A&A*, 372, 563
- Mennickent, R. E., Tappert, C., Gallardo, R., Duerbeck, H. W., & Augustejn, T. 2002, *A&A*, 395, 557
- Meyer, F. & Meyer-Hofmeister, E. 1981, *A&A*, 104, L10
- Mizusawa, T., Merritt, J., Ballouz, R.-L., et al. 2010, *PASP*, 122, 299
- Oke, J. B. 1990, *AJ*, 99, 1621
- Paczynski, B. & Sienkiewicz, R. 1983, *ApJ*, 268, 825
- Patterson, J., McGraw, J. T., Coleman, L., et al. 1981, *ApJ*, 248, 1067
- Patterson, J., Fenton, W. H., Thorstensen, J. R., et al. 2002, *PASP*, 114, 1364
- Rappaport S., Verbunt F., & Joss P. C. 1983, *ApJ*, 275, 713
- Rodríguez-Gil, P., Casares, J., Martínez-Pais, I. G., et al. 2001, *ApJ*, 548, L49
- Rodríguez-Gil, P., Gänsicke, B. T., Barwig, H., et al. 2004, *A&A*, 424, 647
- Rodríguez-Gil, P., Gänsicke, B. T., Hagen, H.-J., et al. 2007, *MNRAS*, 377, 1747
- Rodríguez-Gil, P., & Martínez-Pais, I. G. 2002, *MNRAS*, 337, 209
- Rodríguez-Gil, P., Martínez-Pais, I. G., & de la Cruz Rodríguez, J. 2009, *MNRAS*, 395, 973
- Rodríguez-Gil, P., Schmidtobreick, L., & Gänsicke, B. T. 2007, *MNRAS*, 374, 1359
- Rosen, S. R., Mason, K. O., & Cordova, F. A. 1988, *MNRAS*, 231, 549
- Scaringi S., Bird, A. J., Norton, A. J., et al. 2010, *MNRAS*, 401, 2207
- Schmidtobreick, L., Rodríguez-Gil, P., & Gänsicke, B. T. 2012, *MmSAI*, 83, 610
- Spruit, H. C., & Ritter, H. 1983, *A&A*, 124, 267
- Szkody, P., Anderson, S. F., Brooks, K., et al. 2011, *AJ*, 142, 181.
- Szkody, P., Everett, M. E., Howell, S. B., et al. 2014, *AJ*, 148, 63
- Szkody, P. & Mattei, J. A. 1984, *PASP*, 96, 988
- Thorstensen, J. R., Ringwald, F. A., Wade, R. A., et al. 1991, *AJ*, 102, 272
- Tody, D. 1986, *Instrumentation in Astronomy VI*, 733
- . 1993, *ASPC 52, Astronomical Data Analysis Software and Systems II*, ed. R. J. Hanisch, R. J. V. Brissenden, & J. Barnes, 173
- Verbunt, F. & Zwaan, C. 1981, *A&A*, 100, L7
- Warner, B. 1986, *MNRAS*, 219, 347
- . 1995, *Cataclysmic Variable Stars (CUP)*
- . 2004, *PASP*, 116, 115
- Wynn, G. A. & King, A. R. 1992, *MNRAS*, 255, 83

Héctor Aceves Campos: Instituto de Astronomía, Universidad Nacional Autónoma de México, Apdo. Postal 106, Ensenada, Baja California, 22860, México (aceves@astro.unam.mx).

Andrés Alberto Avilés Alvarado and Carlos Esteban Chávez Pech: Facultad de Ingeniería Mecánica y Eléctrica, Universidad Autónoma de Nuevo León, Av. Universidad s/n Ciudad Universitaria San Nicolás de los Garza, Nuevo León, México, C.P. 66451 (andres.avileslv@uanl.edu.mx, carlosepech@yahoo.com).

Itzel Arias Rodríguez, José Enrique Pérez De León, Eduardo Gerardo Pérez-Tijerina, and Francisco Javier Tamayo Amaya: Facultad de Ciencias Físico Matemáticas, Universidad Autónoma de Nuevo León, Av. Universidad s/n Ciudad Universitaria San Nicolás de los Garza, Nuevo León, México, C.P. 66451 (pgtnewoleon@hotmail.com, enrique.perezln@uanl.edu.mx, eduardo.perezjt@gmail.com, ftamayo@astrosen.unam.mx).

REVISITING FS AURIGAE AND ITS TRIPLE CATAclySMIC VARIABLE SYSTEM HYPOTHESIS

Carlos E. Chavez¹, Andres Aviles¹, Nikolaos Georgakarakos², Cesar Ramos^{3,5}, Hector Aceves⁴, Gagik Tovmassian⁴, and Sergey Zharikov⁴

Received July 17 2019; accepted November 4 2019

ABSTRACT

A very long term variability (VLPP), with period of 875 days, was observed in the long-term light curve of FS Aurigae (FS Aur) in 2011. This periodicity was calculated over 6 cycles. We re-examined the periodicity with new observations over the past 5 yrs. A total of 18 years of observations confirm the hypothesis of a third body perturbing in a secular way the cataclysmic variable (CV). Improvements to the model such as eccentric and inclined orbits for the third body and a binary post-Newtonian correction are considered. We confirm the VLPP of FS Aur and find the new period of 857 ± 78 days. The secular perturbations are most efficient when the mass of the third body is $M_3 \approx 29M_J$, much less than the $50M_J$ reported in 2011. We estimate the effect of the third body on the mass transfer rate and on the brightness of the system. We consider alternative scenarios for the VLPP. New data and analysis support the hypothesis that FS Aur is a CV in a triple system.

RESUMEN

Una variabilidad de muy larga duración (VLPP), con un período de 875 días, se observó en la curva de luz de FS Aur en 2011. El período fue calculado para 6 ciclos. Reexaminamos el período con nuevas observaciones de los pasados 5 años. Un total de 18 años de observaciones confirman la hipótesis de un tercer cuerpo perturbando de manera secular la variable cataclísmica (VC). Se consideran mejoras al modelo, como órbitas excéntricas e inclinadas para el tercer cuerpo y una corrección post-Newtoniana para la binaria. Confirmamos la VLPP de FS Aur y encontramos un nuevo período de 857 ± 78 días. Las perturbaciones seculares son más eficientes cuando la masa del tercer cuerpo es $M_3 \approx 29M_J$, menor que $M_3 \approx 50M_J$ reportada en 2011. Estimamos el efecto del tercer cuerpo en la tasa de transferencia de masa y en el brillo del sistema. Consideramos otras explicaciones para la VLPP. Estos nuevos datos y análisis apoyan la hipótesis de una VC triple para FS Aur.

Key Words: binaries (including multiple): close — novae, cataclysmic variables — stars: individual: FS Aur

1. INTRODUCTION

FS Aur is a cataclysmic variable (CV) that shows a wide range of periodic light signals. It has a short orbital period of just 85.7 min (Thorstensen et al. 1996), a long photometric period of 205.5 min (Tovmassian et al. 2003) and a long spectroscopic period of 147 min (Tovmassian et al. 2007). The latter two periods are attributed to the precession of a

fast rotating magnetic white dwarf and its beat with the orbital period, respectively (see Table 1 for details). All these frequencies were discussed in more detail in Chavez et al. (2012, hereafter CH2012). In that paper we showed the presence of a very long photometric period (VLPP) modulation observed in the long-term FS Aur light curve, with a 2-mag amplitude and a period around 900 days. We argued that the origin of such modulation could be a third substellar-body (of 25 to 65 times M_J) that perturbs the eccentricity of the inner binary star system.

This triple system hypothesis provided an explanation for the VLPP, and it also suggested a plausi-

¹FIME-UANL, México.

²New York University, Abu Dhabi, UAE.

³FCFM-UANL, México.

⁴IA-UNAM, Ensenada, México.

⁵CINVESTAV, Ciudad de México, México.

TABLE 1
SUMMARY OF PERIODICITIES DETECTED IN FS Aur

Name/Acronym	Value	Source	Reference	Comments
Spin Period of WD (SP)	$1^m68 - 1^m75$	light curve	Neustroev et al. 2005	inconclusive
Orbital Period (OP)	$85^m79736 \pm 0.00004$	RV ^a core of H lines	Thorstensen et al 1996 unpublished data	firm established
Long Spectr. Period (LSP)	147^m	RV ^b wings of H lines	Tovmassian et al. 2003	beat between OP and LPP
Long Phot. Period (LPP)	$205^m45013 \pm 0.0006$	light curve	Tovmassian et al. 2003	stable over $\approx 3\,000^d$
Previous Very Long Phot. Period (VLPP)	$875^d \pm 50^d$	light curve	Chavez et al. 2012	based on $\approx 5\,000^d$ coverage
New Very Long Phot. Period (VLPP)	$857^d \pm 78^d$	light curve	this work	based on $\approx 7\,500^d$ coverage

^aMeasured in the core of emission lines.

^bMeasured in the extreme wings of emission lines.

ble answer for other observed peculiarities of FS Aur. More importantly is the fact that it offers a new possibility for detecting planets in accretion disk environments, where other methods fail.

There are other binary systems claimed to have a third object in a close orbit. LX Ser possesses an extra component of $7.5 M_J$ that explains a sinusoidal oscillation observed in the $O - C$ diagram, with a period of 22.8 years (Li et al. 2016). Another example is V893 Scorpi where observed variations of the eclipse period of 10.2 years are interpreted as a light travel time effect caused by the presence of a giant planet with $9.5 M_J$ (Bruch 2014). Finally DP Leonis (Beuermann et al. 2011), HW Vir (Lee et al. 2009), NN Ser (Beuermann et al. 2010), NY Virginis (Qian et al. 2012a), RR Caeli (Qian et al. 2012b) and KIC 5095269 (Getley et al. 2017) are part of this small group of post-CE binaries suspected to possess planets.

The purpose of this paper is to make use of 5 additional years of observations of FS Aurigae to see whether the VLPP signal reported in CH2012 is stronger or, on the contrary, is disappearing. We also want to model the hierarchical triple hypothesis in a more realistic manner by including eccentric and inclined orbits, and also a first order post-Newtonian correction (that is, a first order general relativity correction). Then, we study the effect that these complications have on the range of possible values of mass and semi-major axis that may explain the VLPP by secular perturbations on the cataclysmic variable.

This paper is organized as follows. In §2, we review observational data of FS Aur in search of the very long photometric period (VLPP). In §3.1 we revisit the initial conditions used in our previous research and show more recent and accurate parameters for our system. In §3.2 we examine the scenario where the perturber moves in a circular and coplanar orbit, whose period is much shorter than the long period, and yet produces a binary eccentricity variation on the long period by secular perturbations. In §3.3 we extend this study to eccentric and inclined orbits. The range and properties of the allowed solutions are shown. In §3.4 we check if the VLPP could be explained as a consequence of the precession of the orbit due to first order general relativity corrections. In §3.5 we make an order of magnitude estimation for the mass transfer rate and the brightness of the system. In §4 we explore alternative scenarios for the explanation of the observed VLPP, with particular attention to the cyclic magnetic variation. In §5 we provide some final comments on the new results and their observational imprint on FS Aurigae’s features.

2. THE LONG AND PERMANENT PHOTOMETRIC BEHAVIOR OF FS AUR

Here, we use a data set 1.4 times larger than the one used earlier, covering more than 7,500 days of observations, obtained from the AAVSO public data base. From our analysis, we conclude that the long period is still present in the light curve and confirm the phenomenon reported in CH2012. The power spectrum of the data is displayed in Figure 1. The

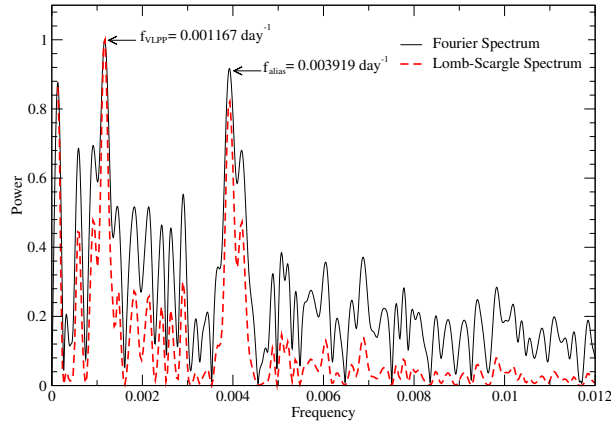


Fig. 1. Normalized power spectrum of the quiescent light curve of FS Aur. The solid black curve corresponds to our Fourier analysis and the red dashed curve to the Lomb–Scargle method. The strongest peak, $f_{VLPP} = 0.001167 \text{ day}^{-1}$ corresponds to the very long photometric period. The second highest peak frequency in the power spectrum $f_{\text{alias}} = 0.003919 \text{ day}^{-1}$ corresponds to an alias created by the yearly observational cycle $f_Y = 0.002739 \text{ day}^{-1}$ and f_{VLPP} . The color figure can be viewed online.

data set spans over 20 years and almost nine periods of ≈ 850 days, peaking in the periodogram at the $0.001167 \text{ day}^{-1}$ frequency. The other low–frequency peak of similar strength at $f = 0.003919 \text{ day}^{-1}$ is an alias related to the one year observational cycle. When taking into account a larger set of data, the estimated period is 857 ± 78 days, and coincides well with the one previously reported (875 ± 50 days) within the estimated error.

The upper panel of Figure 2 shows the long-term light curve for FS Aur in the V band. The bottom panel of Figure 2 displays the folded light curve adjusted with a VLPP period of 857 days. The amount of data for the folded light curve was reduced averaging the magnitude per phase to be able to appreciate in detail the sinusoidal behavior. We calculated the best sinusoidal fit for the bottom panel of Figure 2, shown in red in the figure. We found that the amplitude of the best fit is ≈ 0.4 magnitudes, but it is also clear that the data points are disperse. Hence, we also calculated the difference between the maximum and minimum magnitude of the observed data finding 1.1 magnitude.

3. REVISITING THE TRIPLE CATAclySMIC VARIABLE SYSTEM HYPOTHESIS

A CV is a binary system that is composed by a primary massive star (a white dwarf), and a low mass main sequence K–L type star with a predominant

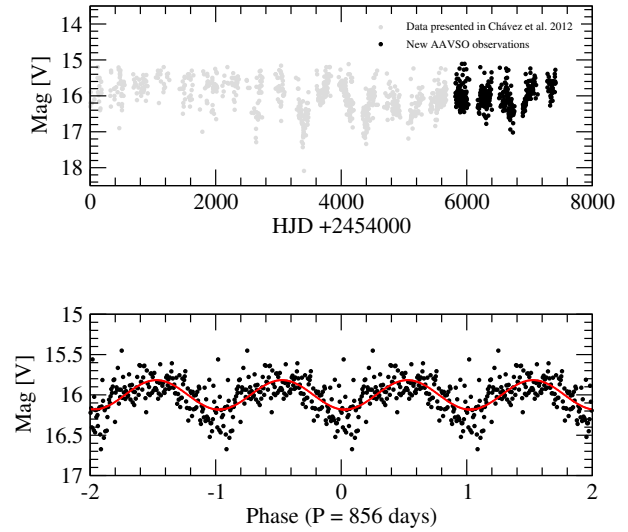


Fig. 2. Upper panel: long-term light curve of FS Aur over the past 20 years, 1.4 times larger than in CH2012 (black filled circles correspond to new observations). Lower panel: folded light curve in quiescence using the VLPP of 857 days. We also show in red the best sinusoidal fit for this curve. The color figure can be viewed online.

population of M (red dwarf) stars. They are so close to each other that the secondary star fills its Roche lobe and its surface is close to the L_1 Lagrangian point.

The material that the secondary loses cannot fall directly on the primary, but instead forms a disk of material around it (Ritter 2008, and references therein). This disk is so bright that outshines the brightness of both stars. In fact, its brightness is proportional to the mass transfer rate or to the mass accretion rate (Warner 1995). Therefore, if there is a change in the mass transfer rate, there will be also a change in the system’s brightness. Therefore, any change in the location of the Lagrangian L_1 point will change the mass transfer and therefore the brightness of the system.

We recall that there is a huge disparity between the VLPP and all other periods. This lead CH2012 to seek a cause of the variable mass transfer rate and therefore of the disk brightness not related to the binary itself, but to propose instead a third body orbiting the binary.

The presence of a third body in the system would perturb the orbit of the stellar binary over different timescales. These timescales depend on the mass, eccentricity and semi-major axis of the unseen companion. Therefore, knowing the period of the long–

TABLE 2
INITIAL PARAMETERS OF FS Aur

Parameter	Value	Reference
Orbital period	1.42996 hours	Thorstensen et al. (1996)
Orbital semi-major axis of the binary	$0.6 R_{\odot}$	Knigge et al. (2011)
Secondary star mass	$0.08 M_{\odot}$	"
Secondary star radius	$0.12 R_{\odot}$	"
Primary star mass	$0.75 M_{\odot}$	"
Primary star radius	$0.01 R_{\odot}$	"
Log secondary star mass loss rate	$-10.25 \left(\frac{M_{\odot}}{yr} \right)$	"
Secondary star temperature/spectral type	2600/M7.0	"
Mass ratio	0.1	–

term variability of the light curve of FS Aur can help us place constraints on the mass and orbital configuration of the potential companion.

For this purpose, we can make use of some previously derived analytical results. In a series of papers, Georgakarakos (2002, 2003, 2004, 2006, 2009, 2015, 2016) studied the orbital evolution of hierarchical triple systems. Some of those studies involved the secular evolution of such systems. The analytical results derived there can give us an estimate about the frequency and the period of motion of the stellar binary. Therefore, we can estimate which mass values and orbital configurations of a hypothetical third companion can yield the secular period observed in the light curve of FS Aur.

For a coplanar system with a perturber on a low eccentricity orbit we make use of the results of Georgakarakos (2009), while for coplanar systems with eccentric perturbers, those of Georgakarakos (2003). Finally, for systems with low eccentricity orbits and low mutual inclinations ($i < 39.23^{\circ}$, the limit before Kozai (1962) resonances become important) we can use the relevant material of Georgakarakos (2004).

3.1. Initial Parameters

Here we discuss briefly the origin of all parameters used in this work. In CH2012 we used the following parameters: total mass $M_T = M_1 + M_2 = 0.84 M_{\odot}$ with the primary mass $M_1 = 0.75 M_{\odot}$, and the secondary, $M_2 = 0.09 M_{\odot}$.

We decided to revisit these parameters, starting with the mass and radius of the secondary. Here we use the values that appear in Knigge et al. (2011), where they use the eclipsing CVs and theoretical constraints to obtain a semi-empirical donor sequence for CVs with orbital periods $P_{orb} \leq 6h$. They give all

key physical and photometric parameters of CV secondaries, as well as their spectral types, as a function of P_{orb} .

We use the data that appear in their Tables 6 and 8 to obtain the best physical parameters for FS Aur. We interpolate between values to find the best possible ones for our dynamical study; they are shown in Table 2. We obtain the following mass ratio between secondary and primary $q = M_2/M_1 = 0.1$ as shown in Table 2. The primary mass was obtained from Knigge et al. (2011) and is based on their previous value (Knigge et al. 2006). That value was calculated as the mean value of the WD mass among the eclipsing CV sample available at the time $\langle M_1 \rangle = 0.75 \pm 0.05 M_{\odot}$. They stated that when adding new data the mean increases but not significantly, so they decided to retain the $M_1 = 0.75 M_{\odot}$ value as a representative WD mass.

We performed simulations of the CV with a hypothetical third body. In all numerical integrations, except where otherwise stated, we used the high-order Runge–Kutta–Nyström RKN 12(10) 17M integrator of Brankin et al. (1989) for the equations of motion of the full three-body problem in the barycentre inertial reference frame. In our integrations, the total energy is monitored and it is conserved up to 10^{-5} , or better, in all experiments. At each time step, the instantaneous eccentricity of the binary is computed.

As pointed out in CH2012, tidal deformation of the stars in the close binary three-body problem can be an important effect. However, CH2012 have shown that these tidal effects are not important for this system and the two objects can be considered as point masses.

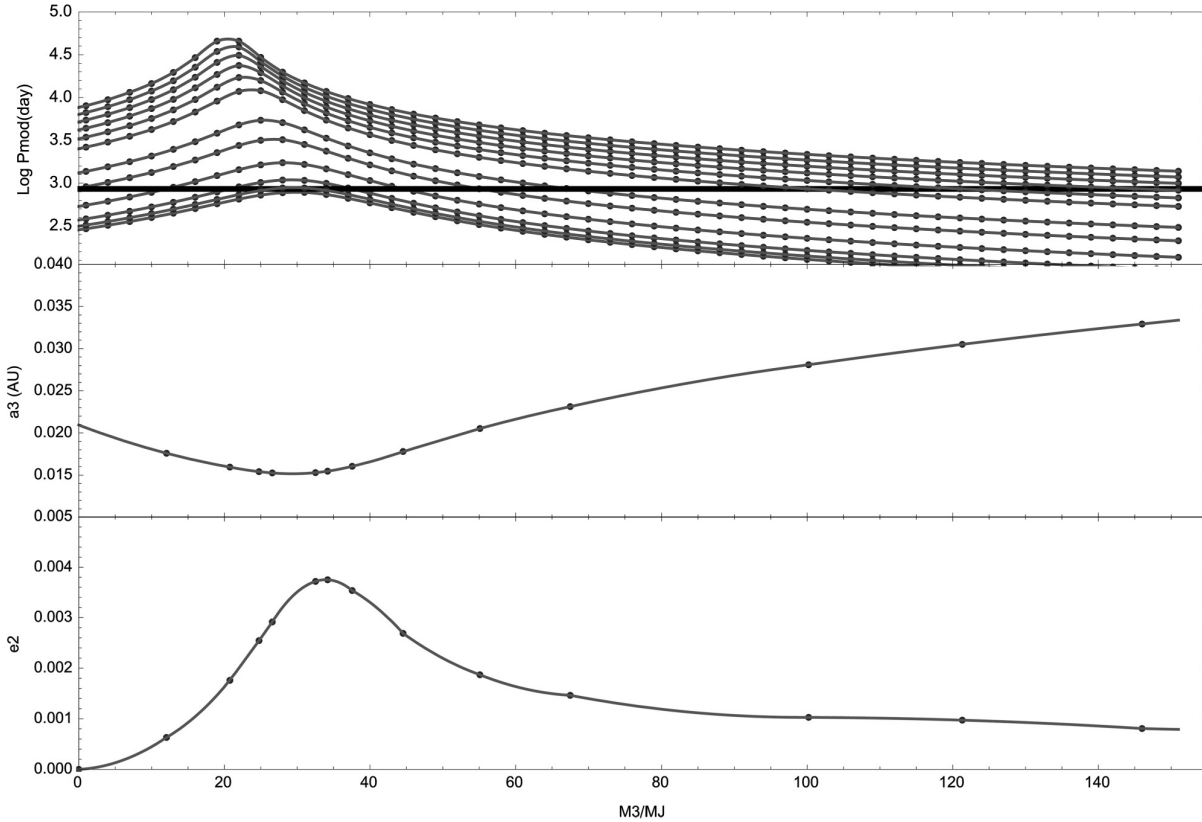


Fig. 3. The upper panel shows the logarithm of the period of the long-term modulation of the binary eccentricity as a function of the perturber mass (Jupiter masses). Each curve corresponds to different P_3/P_2 ratios taken from 12.5 to 40.8; the values are 12.5, 12.7, 12.9, 13.1, 13.4, 15.6, 19, 22, 30.6, 33.6, 37.2, 40.8, from bottom to top. The thick horizontal line shows the observed value of the VLPP (857 days). Only solutions that cross this line can explain the VLPP. The middle panel shows the perturber mass and semi-major axis combinations that result in a long-term modulation of the binary orbit equal to that of the VLPP, that is, solutions that cross the black thick line. The lower panel shows the amplitude of the binary eccentricity perturbation for those solutions. See text for discussion.

3.2. The Third Body on a Close Near-Circular and Coplanar Orbit

Hierarchical triple systems consist of two stars in a close orbit and a third body orbiting the barycentre of the close binary.

In Chavez et al. 2012 we ruled out that the VLPP could correspond directly to the period of a third body, since the object would be too far to have an important effect on the inner binary. We performed a series of numerical integrations and proved that indeed the effect is very small and could not explain the VLPP of the CV. Instead, we concluded that a third light-weight body could produce a disturbance on the central binary and that such perturbation may have a much longer period compared to the orbital period of the perturber (e.g. Mazeh & Shoham 1979, Soderhjelm 1982, Soderhjelm 1984, Georgakarakos 2002, Georgakarakos 2009). The third companion induced a long-term (secular) eccentric-

ity modulation, as shown for example in Soderhjelm (1984).

Here, just like in CH2012, we consider a binary formed by two point masses initially in a circular orbit. A third point mass (perturber) moves initially on its own circular orbit, farther away and in the same orbital plane as the other two. Its mass M_3 and orbital period P_3 are varied across an ensemble of numerical experiments.

The upper panel of Figure 3 shows the \log_{10} of the resulting periods of the long-term modulation of the binary eccentricity (vertical axis) as a function of the mass of the perturber (horizontal axis), for our ensemble of numerical experiments. Each curve corresponds to different P_3/P_2 ratios taken from a range of values between 12 to 48 (bottom and top curves, respectively). The thick horizontal line corresponds to the VLPP value. For example, the curve with $P_3/P_2 = 12$ does not cross the line and therefore it

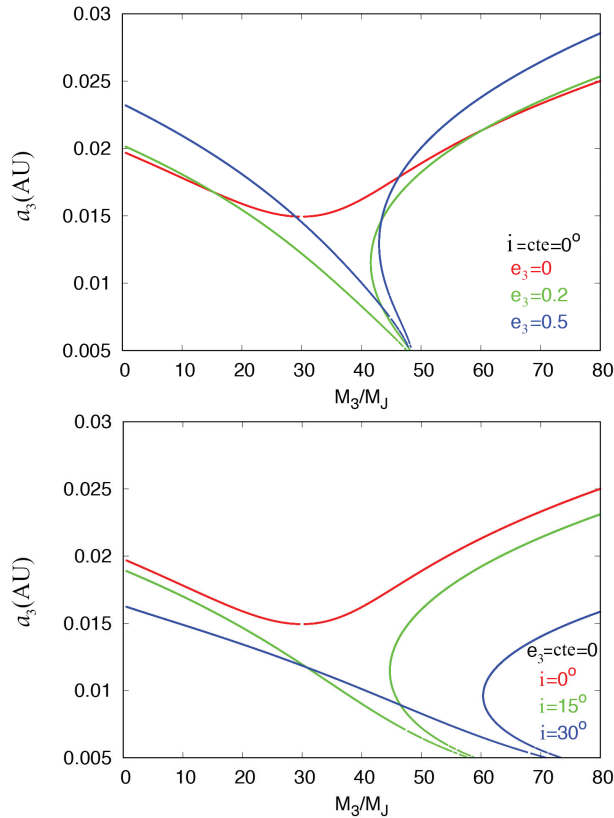


Fig. 4. Perturber mass and semi-major axis combinations that result in a long-term modulation of the binary orbit equal to the VLPP of 857 days. These results were obtained using the analytical formulas described in the text. In the top plot we explore the effect of the eccentricity of the third body; the inclination for all systems remains constant, $i = 0^\circ$. The bottom plot explores the effect of the orbital inclination; the initial eccentricities for all systems are $e_3 = 0$. See text for discussion. The color figure can be viewed online.

is a value that cannot explain the VLPP observed. For perturbers whose orbital period is smaller than 12 binary periods no solution is possible, since their respective curves do not reach the VLPP value. For perturbers with periods longer than that, but shorter than 19 binary periods, two solutions are possible: one at low mass and another at an increasingly larger mass. Finally, perturbers with periods longer than 19 produce only one solution at the large mass range.

The curve in the middle panel of Figure 3 shows the perturber's orbit semi-major axis but only for the solutions that could explain the observed VLPP value; i.e. solutions that cross the solid line on the upper panel. The lower panel shows the amplitude of the eccentricity perturbation for the solutions presented in the middle panel. The most efficient case

would be the one in which the VLPP is the predominant effect and the eccentricity pumped into the inner binary is the largest; that is, the minimum in semi-major axis and the maximum in eccentricity. According to this study, the maximum amplitude is achieved for a system that has a third body with $M_3 = 29M_J$ and $P_3/P_2 = 12.7$.

All curves in the upper panel of Figure 3 reach a maximum value for smaller values of the mass compared to Figure 8 (upper panel) of CH2012, for the same initial conditions. Therefore, in the middle panel of Figure 3, we also obtain smaller values for the masses of the possible third body compared to the middle panel of Figure 8 of CH2012 for the same initial conditions. Then, the minimum of this curve in this research is obtained when $M_3 = 29M_J$ and $P_3/P_2 = 12.7$, while the minimum in CH2012 was obtained when $M_3 = 48M_J$ and $P_3/P_2 = 13.4$.

The relative eccentricity amplitudes of these three modulations (inner binary period, third body period and secular VLPP) depend on the mass and size of the orbit of the perturber. The VLPP modulation becomes the predominant effect in the range of masses for a third body of $20M_J < M_3 < 45M_J$. The envelope of the calculated long-term modulation of the binary eccentricity for our best case is remarkably similar to the waveform of the VLPP.

3.3. The Third Body on an Eccentric and Inclined Orbit

Now we investigate the effect of the eccentricity and inclination of the third body on the outcome of the VLPP.

Figure 4 contains two plots for various dynamical scenarios. It is clear that there is a variety of combinations of masses and semi-major axes of the hypothetical companion that can produce the observed long term variation in the light curve of FS Aur. The perturber's eccentricity does not seem to affect very much, as seen when we compare the two analytical solutions for $e_3 = 0.2$ and $e_3 = 0.5$. The low e_3 solution seems to be somewhat different in the range $M_3/M_J = 30 - 50$. Similarly, there is some difference among the solutions as the mutual inclination increases.

The orbital solutions based on our analytical estimates yield a wide range of masses for our hypothetical companion, from sub-Jupiter mass bodies to big brown dwarfs. However, all solutions may not be dynamically stable. According to the empirical criterion developed by Holman and Wiegert (1999), the smallest stable semi-major axis for our unseen companion is 0.0055 AU. This value is valid for small

values of e_3 , as the criterion was based on simulations of massless particles initially on circular orbits around the binary star. For initially eccentric orbits around the stellar binary the value of the stable semi-major axis may be different. The same holds when the companion has a mass comparable to the secondary; $M_2 = 0.079M_\odot$ which is about $83M_J$, and therefore the empirical criterion of Holman and Wiegert is valid only for masses in the left part of our plots. In this case, we can get an idea about the stability limit from Table A1 of Georgakarakos (2013) which provides values for three-dimensional systems, but only for initially circular orbits. Considering the outer mass to be in the range we have in our plots, we find that for coplanar and low inclination systems ($i = 20^\circ$) the stability limit is around $a_3 = 0.01\text{AU}$.

3.4. Effect of a Post-Newtonian Correction

Here we consider the possible dynamical effects that a first order post-Newtonian correction to the binary's orbit may produce on the long-term signal we observe in the light curve of the binary. We refer to the first order general relativity correction in the precessional rate of the longitude of the pericentre.

For the binary under investigation, although its total mass is under one solar mass, the small semi-major axis of its orbit makes it interesting to consider a post-Newtonian correction. Including this effect results in the precession of the pericentre at the following rate (Georgakarakos, & Eggl 2015, Naoz et al. 2015):

$$\dot{\varpi} = \frac{3G^{\frac{3}{2}}(M_1 + M_2)^{\frac{3}{2}}}{c^2 a_1^{\frac{5}{2}}(1 - e_1^2)}, \quad (1)$$

where G is the gravitational constant and c is the speed of light in vacuum.

Based on the precession rate given by the above equation, the period of the pericentre circulation for our system is 6812 days (18.65 yrs). Since this number is much larger than the 857 day signal we observe in the light curve of the system, we conclude that general relativity (GR) by itself cannot explain the signal.

3.5. Estimation of the Effect of the Third Body on the Mass Transfer Rate and Brightness of the System

Now that we have established that a third body can explain the VLPP observed, we estimate how the modulation of the inner binary due to the secular perturbation of the third body affects the mass transfer and hence the brightness of the system.

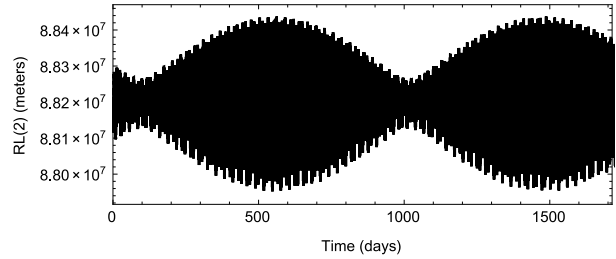


Fig. 5. Location of RL(2) as a function of time. RL(2) is the radius of the sphere with a volume equal to that of the Roche lobe of the system. See text for discussion.

From the results of our numerical integrations for the third body on a close near-circular and coplanar orbit, the most efficient solution is used for all calculations in this subsection; that is $M_3 = 29M_J$, $P_3/P_2 = 12.7$, $P_3 = 18.16$ h. In order to estimate the mass loss of the secondary we make use of the concept of RL(2). Since calculating the volume of the Roche lobe is difficult, we can define an equivalent radius of the Roche Lobe as the radius, RL(2), of a sphere with the same volume as that of the Roche lobe. This radius RL(2) has been widely studied for different mass ratios ($q = M_1/M_2$). Equation 2 by Eggleton (1983) is widely used since it is valid for a wide range of mass ratios ($0 < q < \infty$) and accurate to better than 1%. That equation assumes that the orbit is circular and that the semi-major axis is constant.

Sepinsky et al. (2007) studied the definition of RL(2) for eccentric binaries; they found the following generalization:

$$RL(2) = r_{12}(t) \frac{0.49q^{2/3}}{0.6q^{2/3} + \ln(1 + q^{1/3})}, \quad (2)$$

where r_{12} is the distance between the two stars at a given time. Since we have that distance from our integration of the most efficient case, we can plot RL(2) as a function of time, as shown in Figure 5.

We can calculate the maximum $RL(2)_{max} = 8.844 \times 10^7 \text{m}$ and $RL(2)_{min} = 8.796 \times 10^7 \text{m}$. In principle we can estimate the mass transfer rate $\dot{M}(2)$ and therefore the luminosity of the cataclysmic variable.

We proceed as follows. First we assume that the secondary is a polytrope of index $3/2$ (we assume a certain shape of the Roche Lobe). Also that the density around the L_1 point is given by equation 2.11 of Warner (1995), $\rho_{L_1} = \rho_0 e^{-(\Delta R/H')^2}$; where ρ_0 is the density of the isothermal atmosphere, and H' is a scale height given by Lubow & Shu (1975).

We can estimate the mass transfer rate using equation 2.12 of Warner (1995),

$$\dot{M}(2) = -C \frac{M(2)}{P_{12}} \left(\frac{\Delta R}{R(2)} \right)^3, \quad (3)$$

where C is a dimensional constant $\approx 10-20$ and ΔR is the amount by which the secondary overfills its Roche lobe: $\Delta R = R(2) - R_L(2)$. The $R(2)$ distance needs to be calculated carefully since the equation for $\dot{M}(2)$ is very sensitive to the amount of overflow. We decided to adjust the $R(2)$ to obtain the $\dot{M}(2)$ that we report here in Table 2, namely a logarithm of the secondary star mass loss rate of $-10.25 (\frac{M_\odot}{yr})$. Since $R_L(2)$ is a function of time, we use the mean value of $R_L(2)_{mean} = 8.821 \times 10^7$ m for the $R_L(2)$ value. Hence we obtain the value $R(2) = 8.820 \times 10^7$ m.

Therefore, we can calculate the maximum and minimum of the mass transfer rate by using the values of $RL(2)_{max}$ and $RL(2)_{min}$. We obtain $\dot{M}(2)_{max} = 7.1 \times 10^{18}$ kg/s and $\dot{M}(2)_{min} = 5.8 \times 10^{18}$ kg/s.

We now estimate the luminosity due to accretion (Warner 1995). First, we calculate the luminosity due to the so called hot spot (the place where the stream of stellar mass crosses the L_1 point and collides with the disk):

$$L(SP) \approx \frac{GM(1)\dot{M}(2)}{r_d}, \quad (4)$$

where $L(SP)$ is the luminosity due to the hot spot; the radius of the disk is typically $r_d \approx 0.40 \times a_{12}$, where a_{12} is the semi-major axis of the inner binary, both given in Table 2. Applying this equation to our extreme values on $RL(2)$ we obtain: $L(SP)_{max} \approx 4.2 \times 10^{30}$ watts and $L(SP)_{min} \approx 3.2 \times 10^{30}$ watts. The luminosity of the accretion disk, using equation 2.22a of Warner (1995), is:

$$L(d) \approx \frac{1}{2} \frac{GM(1)\dot{M}(2)}{R_1}, \quad (5)$$

With this equation for $L(d)$ we can obtain the extreme values of $L(d)_{max} \approx 4.8 \times 10^{31}$ watts and $L(d)_{min} \approx 3.6 \times 10^{31}$ watts. The total luminosity for each extreme is obtained by adding the estimated luminosity of the hot spot plus the luminosity of the disk, obtaining: $L(d)_{T_{max}} \approx 5.2 \times 10^{31}$ watts and $L(d)_{T_{min}} \approx 4.0 \times 10^{31}$ watts.

We can calculate the bolometric magnitude using $M_{bol} = -2.5 \log (\frac{L}{L_\odot})$, with $L_\odot = 3.0128 \times 10^{28}$ watts. For the extreme values we obtained $M_{B_{max}} = -8.09$ and $M_{B_{min}} = -7.79$, giving us a magnitude difference of $\Delta M_B = 0.29$.

The observed change on magnitude at quiescence is ≈ 0.4 magnitudes when using a sinusoidal best fit, as shown in Figure 2, but the data points are quite disperse; so we also calculated the difference between the maximum and minimum magnitude of the observed data, finding 1.1 magnitude. The most efficient parameters model give us an expected change of magnitude of ≈ 0.29 . We remind the reader that the latter is an order of magnitude estimate, with simplifications, assumptions and estimations.

4. ALTERNATIVE SCENARIOS FOR THE VLPP

One possible explanation to the VLPP is the cyclic magnetic variation (analogue to the Solar cycles) in the secondary star, which may lead to mass transfer variations. Long term variations have been observed in CVs, as mentioned in Richman et al. (1994) where they concluded that this explanation is plausible. But they found that the cycles did not show any strict periodicity and were decades long. In Table 3 of Mascareño et al. (2016) the magnetic cycle of medium to late M stars was found to be 7.1 years for a sample of stars of this type.

As pointed out at the end of § 3.1, in this research the secondary star on FS-Aur is expected to be a very late M star; their internal structure is not the same as that of a normal main sequence star counterpart with the same mass. Stars with $M \approx 0.4M_\odot$ become fully convective. As the mass decreases, the density increases and the internal temperature decreases, leading to a partial degeneracy of the core. Approaching the minimum hydrogen-burning mass of $0.08M_\odot$, the increased electron degeneracy induces structural changes on the secondary. This makes the star magnetic, but with very few spots.

Bianchi (1992) and Hessman et al. (2000) found evidence of a possible relation between mass accretion variations and solar cycle type phenomena. The evidence showed variations on the timescales of decades on the overall system brightness and provided theoretical support for star-spots migrating to the L_1 region (Howell 2004). This migration would help to correlate the star-spot to the changes in the position of the L_1 point due to a possible third body.

Nevertheless, the magnetic cycles in very late M stars have not been studied in detail for secondaries in CVs; we recognise this mechanism as a plausible alternative to the mechanism proposed here.

5. SUMMARY AND FINAL COMMENTS

We confirm the presence of VLPP with a refined period of 857 days based on 5 additional years (20 years total) of observations for FS Aur. This result also helps to confirm the authenticity of this signal.

We also revisit the triple CV hypothesis in which a massive planet, or a substellar object, pumps eccentricity into the inner binary orbit by secular perturbations. New parameters of mass, radius and temperature for the binary members of the CV FS Aur (Knigge et al. 2011) are calculated and used to recalculate the most efficient parameters for the third body as defined earlier. The most efficient combination that explains the 857 day period is a third body with $M_3 = 29M_J$ and $P_3/P_2 = 12.7$ ($P_3 = 18.16$ h). This new value is 1.7 times smaller than our previous estimation and is well within the limits of planetary masses. For example, the planet HD 169142b has a similar mass (Fedele et al. 2017). All numerical calculations are made for a third body in an initial circular and planar orbit, as in CH2012.

We also explore more complicated models to study the secular perturbations of systems with eccentric and inclined orbits, using previous analytical results (Georgakarakos 2002, 2003, 2004, 2006, 2009). We find that as the eccentricity increases the most efficient candidate third body has a larger mass: $M_3 = 47M_J$ for an eccentricity of 0.2, and $M_3 = 48M_J$ for an eccentricity of 0.5 of the third body.

When the mutual inclination is explored the most efficient candidate for the third body has larger mass: if the inclination is 15° the expected most efficient mass is about $M_3 = 58M_J$, but when the inclination is 30° the expected most efficient mass is now about $M_3 = 72M_J$.

We consider other dynamical effects that might produce this VLPP, such as the first order post-Newtonian correction. We find that for FS Aur the period of the pericentre circulation is 6812 days (18.65 yrs), that is, much larger than the 857 day period observed.

We calculated a first order estimation of the effect on the secular period of the third object due to the mass transfer rate, and hence on the brightness of the system; a change of magnitude of the order of only $\Delta M_{bol} = 0.29$ was obtained. Even though this change is not the 0.4-magnitude observed, it is quite close, being an order of magnitude calculation. It also gave us insight on how sensitive is the system to even small changes in the parameters used to calculate $\dot{M}(2)$; a change in the distance $R(2)$ by less than 0.01% resulted in the 0.4-magnitude observed. The $R(2)$ adjustment was based on the value of $\dot{M}(2)$ that appears in Table 2 taken from Knigge et al. (2019) and that value was calculated using statistics. The change in magnitude of FS Aur may be a mechanism to explain the VLPP observed.

We examine alternative scenarios for the VLPP. A possible explanation by a solar type magnetic cycle of the secondary cannot be ruled out, since the VLPP is only 2.346 years and most of the cyclic type magnetic periods in mid to late M stars are of the order of decades. However, there are no studies for the magnetic cycles of very late M stars in CVs to further test this hypothesis; hence, this alternative is a plausible one.

In summary, we find (a) that the new extended data confirm that there is a VLPP, but with a new value of 857 days; (b) the new data are consistent with FS Aur being a triple-system; (c) combining such data with new initial conditions yields a reduction (from $M_3 = 50M_J$ to $29M_J$) of the mass estimate for the most efficient third body candidate; (d) an order of magnitude estimation for the mass transfer rate and the brightness of the system, with the initial conditions used here, leads to a change in magnitude of 0.3. This value is 25% times smaller than the observed one, but we find that changes of less than 0.01% in the $R(2)$ parameter can increase the change in magnitude up to the observed one.

We would like to thank all the amateur observers who do a great and hard job by collecting professional grade data with persistence. We are particularly indebted to Joe Patterson, who guides the amateur community engaged in CV monitoring and who made possible the dense observational coverage of FS Aur. We acknowledge with thanks the variable star observations from the AAVSO International Database contributed by observers worldwide and used in this research. CC acknowledges UANL PAICYT grant. We appreciate the comments, suggestions and corrections by the anonymous referee, which helped us to greatly improve the quality and content of this research.

REFERENCES

- Bianchi, L. 1992, *A&A*, 253, 447
 Brankin, R., Gladwell, I., Dormand, J., Prince, P., & Seward, W. 1989, *ACM T. M. S.*, 15, 31
 Beuermann, K., Hessman, F. V., Dreizler, S., et al. 2010, *A&A*, 521, L60
 Beuermann, K., Buhlmann, J., Diese, J., et al. 2011, *A&A*, 526, A53
 Bruch, A. 2014, *A&A*, 566, A101
 Chavez, C., Tovmassian, G., Aguilar, L., Zharikov, S., & Henden, A. 2012, *A&A*, 538, A122
 Eggleton, P. P. 1983, *APJ*, 268, 368
 Fedele, D., Carney, M. R., Hogerheijde, M. R., et al. 2017, *A&A*, 600, A72
 Georgakarakos, N. 2002, *MNRAS*, 337, 559

- _____. 2003, *MNRAS*, 345, 340
- _____. 2004, *CeMDA*, 89, 63
- _____. 2006, *MNRAS*, 366, 566
- _____. 2009, *MNRAS*, 392, 1253
- _____. 2013, *NewA*, 23, 41
- Georgakarakos, N. & Eggl, S. 2015, *APJ*, 802, 94
- Georgakarakos, N., Dobbs–Dixon, I., & Way, M. J. 2016, *MNRAS*, 461, 1512
- Getley, A. K., Carter, B., King, R., & OToole, S. 2017, *MNRAS*, 468, 2932
- Hessman, F. V., Gänsicke, B. T., & Mattei, J. A. 2000, *A&A*, 361, 952
- Holman, M. & Wiegert, P. 1999, *APJ*, 117, 621
- Howell, S. B. 2004, *ASPC*, 315, 353
- Knigge, C. 2006, *MNRAS*, 373, 484
- Knigge, C., Baraffe, I., & Patterson, J. 2011, *ApJS*, 194, 48
- Kozai, Y. 1962, *AJ*, 67, 591
- Lee, J. W., Kim, S.-L., Kim, C.-H., et al. 2009, *AJ*, 137, 3181
- Li, K., Hu, S., Zhou, J., et al. 2017, *PASJ*, 69, 28
- Lubow, S. H. & Shu, F. H. 1975, *APJ*, 198, 383
- Mascareno, A., Rebolo, R., & Gonzalez Hernandez, J. I. 2016, *A&A*, 595, A12
- Mazeh, T. & Shaham, J. 1979, *A&A*, 77, 145
- Naoz, S., Kocsis, B., Loeb, A., & Yunes, N. 2013, *APJ*, 773, 187
- Neustroev, V., Zharikov, S., Tovmassian, G., & Shearer, A. 2005, *MNRAS*, 362, 1472
- Qian, S. B., Zhu, L. Y., Dai, Z. B., et al. 2012a, *APJL*, 745, L23
- Qian S. B., Liu, L., Zhu, L. Y., et al. 2012b, *MNRAS*, 422, L24
- Richman, H. R., Applegate, J. H., & Patterson, J. 1994, *PASP*, 106, 1075
- Ritter, H. 2008, *MmSAI*, 14
- Sepinsky, J. F., Willems, B., & Kalogera, V. 2007, *APJ*, 660, 1624
- Soderhjelm, S. 1982, *A&A*, 107, 54
- _____. 1984, *A&A*, 141, 232
- Thorstensen, J. R., Patterson, J. O., Shambrook, A., & Thomas, G. 1996, *PASP*, 108, 73
- Tovmassian, G., Zharikov, S., Michel, R., et al. 2003, *PASP*, 115, 725
- Tovmassian, G., Zharikov, S., & Neustroev, V. 2007, *ApJ*, 655, 466
- Warner, B. 1995, *Cataclysmic Variable Stars*, (Cambridge, UK: CUP)

H. Aceves, G. Tovmassian, and S. Zharikov: Universidad Nacional Autónoma de México, Instituto de Astronomía, Ensenada 22860, B. C., México.

A. Aviles and C. E. Chavez: Universidad Autónoma de Nuevo León, Facultad de Ingeniería Mecánica y Eléctrica, San Nicolás de los Garza, NL, México (Carlos.ChavezPch@uanl.edu.mx).

N. Georgakarakos: New York University Abu Dhabi, Saadiyat Island, P.O. Box 129188, Abu Dhabi, UAE.

C. Ramos: Centro de Investigación y de Estudios Avanzados del Instituto Politécnico Nacional, San Pedro Zacatenco, Ciudad de México, 07360, México.

C. Ramos: Universidad Autónoma de Nuevo León, Facultad de Ciencias Físico–Matemáticas, San Nicolás de los Garza, N.L. México.

THE JET/COUNTERJET SYMMETRY OF THE HH 212 OUTFLOW

A. Noriega-Crespo¹, A. C. Raga², V. Lora³, and J. C. Rodríguez-Ramírez⁴

Received February 22 2019; accepted November 21 2019

ABSTRACT

We present Spitzer (IRAC) images and a VLT 2.1 μm image of the HH 212 outflow. We find that this outflow has a strong symmetry, with jet/counterjet knot pairs with $\Delta x < 1''$ position offsets. We deduce that the jet/counterjet knots are ejected with time differences $\Delta\tau_0 \approx 6$ yr and velocity differences $\Delta v_0 \approx 2$ km s⁻¹. We also analyze the deviations of the knot positions perpendicular to the outflow axis, and interpret them in terms of a binary orbital motion of the outflow source. Through this model, we deduce a $\approx 0.7 M_\odot$ mass for the outflow source, and a separation of ≈ 80 AU between the components of the binary (assuming equal masses for the two components). Finally, using the IRAC data and the VLT 2.1 μm image we measure the proper motion velocities, obtaining values from 50 to 170 km s⁻¹.

RESUMEN

Presentamos imágenes del Spitzer (IRAC) y una imagen del VLT a 2.1 μm del flujo HH 212. Encontramos que este flujo tiene una fuerte simetría, con pares de nudos en el chorro/contrachorro con diferencias de posición $\Delta x < 1''$. Deducimos que los pares de nudos chorro/contrachorro son expulsados con diferencias de tiempo $\Delta\tau_0 \approx 6$ yr y de velocidad $\Delta v_0 \approx 2$ km s⁻¹. También analizamos las desviaciones de las posiciones de los nudos perpendiculares al eje del flujo, y las interpretamos como resultado de un movimiento binario orbital de la fuente. A través de este modelo, deducimos una masa de $\approx 0.7 M_\odot$ para la fuente, y una separación de ≈ 80 AU para la binaria (suponiendo masas iguales para sus dos componentes). Finalmente, usamos los datos de IRAC y la imagen del VLT a 2.1 μm para medir las magnitudes de los movimientos propios, obteniendo valores de 50 a 170 km s⁻¹.

Key Words: Herbig-Haro objects — ISM: individual objects: HH212 — ISM: jets and outflows — shock waves — stars: formation — stars: winds, outflows

1. INTRODUCTION

The existence of symmetric emitting knots (at similar distances from the outflow source) along some bipolar Herbig-Haro (HH) outflow systems implies highly synchronized jet/counterjet ejections, and therefore a small spatial extent for the jet production region. This was pointed out by Raga et al. (2011a) in their study of Spitzer Infrared Array Camera (IRAC) images of the HH 34 outflow. In a second paper, Raga et al. (2011b) developed a ballistic jet model which constrained the ejection asymmetries

using the observed jet/counterjet structures, and applied the model to the HH 34 and HH 111 outflows.

These analyses of jet/counterjet asymmetries have been carried out with IR Spitzer images in the 4 IRAC channels (centered at 3.6, 4.5, 5.8 and 8.0 μm). This is because at optical wavelengths, larger jet/counterjet asymmetries are found in the knots close to the outflow source, often with one of the two lobes being undetected because of a large optical extinction (this is the case, e.g., of the HH 34, HH 111 and HH 1/2 outflows). The intrinsic symmetry of the two lobes is then only visible at infrared (IR) wavelengths, as first shown in a quite dramatic way by the H₂ 2.1 μm observations of HH 111 of Gredel & Reipurth (1994).

A clear candidate for this kind of study is the HH 212 outflow, which is an impressive “IR jet”, dis-

¹Space Telescope Science Institute, USA.

²Instituto de Ciencias Nucleares, UNAM, México.

³Instituto de Radioastronomía y Astrofísica Teórica, UNAM, México.

⁴IAG, USP, Brasil.

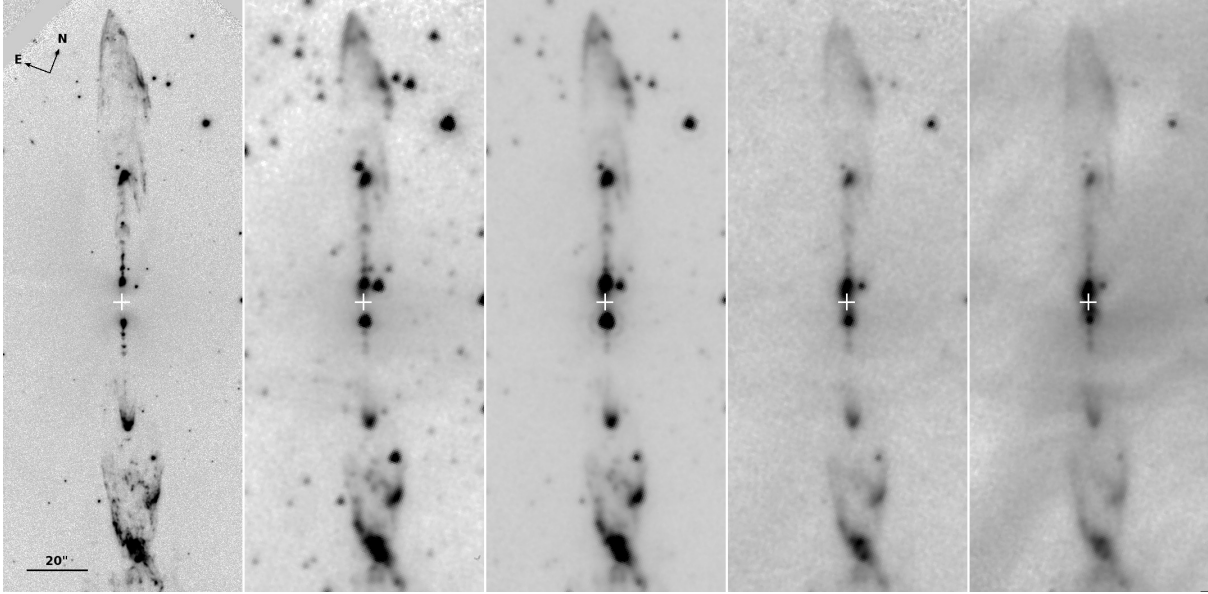


Fig. 1. The HH 212 outflow in H₂ 2.1 μm (left frame) and in the four IRAC channels I1-I4, at 3.6, 4.5, 5.8 and 8.0 μm (four frames towards the right). The orientation and the scale of the images are shown in the left frame. The white cross (in all frames) indicates the position of the outflow source.

covered at IR wavelengths by Zinnecker et al. (1998) and with only very faint optical emission (Reipurth et al. 2019). This outflow lies very close to the plane of the sky (Claussen et al. 1998) and is at a distance of approximately 400 pc (Anthony-Twarog 1982, Kounkel et al. 2017). Recent proper motion determinations (Reipurth et al. 2019) show that the jet and the counterjet have a velocity of $\approx 170 \text{ km s}^{-1}$.

H₂ 2.1 μm observations of HH 212 (Davis et al. 2000, Smith et al. 2007, Correia et al. 2009) show that this outflow has emitting structures with evident jet/counterjet symmetries. We present Spitzer images in the four IRAC channels (I1-I4, at 3.6, 4.5, 5.8 and 8.0 μm) and an archival VLT 2.1 μm image of HH 212, and determine the positions of knots along the jet and the counterjet.

We then use the knots within 40'' from the outflow source to calculate jet/counterjet knot position offsets. These offsets (as a function of distance from the outflow source) are then interpreted in terms of the ballistic outflow model of Raga et al. (2011b) in order to constrain the jet/counterjet asymmetries of the ejection process. We also study the deviations of the knot positions perpendicular to the outflow axis, and interpret them in terms of the “orbiting outflow source” model of Masciadri & Raga (2002).

The paper is organized as follows. The observations are discussed in § 2. The measurement of

knot intensities and positions (as well as the determinations of jet/counterjet knot offsets) are presented in § 3. § 4 presents interpretations of the HH 212 measurements, including an application of the jet/counterjet asymmetry model of Raga et al. (2011b), an application of the “orbiting source jet” model of Masciadri & Raga (2002), an evaluation of the difference in extinction towards the jet and the counterjet, and a discussion of the features of the outflow that do not show a clear jet/counterjet symmetry. The results are summarized in § 5.

2. THE OBSERVATIONS

The IRAC data were obtained during the Cryo-Spitzer mission, program PID 3315 (PI Noriega-Crespo) on “Emission from H₂, PAHs and Warm Dust in Protostellar Jets”. The data were collected in the four IRAC bands using a 30 sec high dynamic range (HDR) frame time and a 12 point medium scale Reuleaux dither pattern. A small 2×1 mosaic with a 260 arcsec stepsize was used to capture the outflow within the field of view (FoV) of the four IRAC (3.6, 4.5, 5.8 and 8.0 μm) channels. The resulting images have a 0.6'' pixel size.

We used the final reprocessing from the Spitzer Archive with a standard angular resolution of $\text{FWHM} \approx 2 \text{ arcsec}$. Figure 1 shows the entire outflow in the four bands. As expected, the HH 212 jet itself is brighter at 4.5 μm , given that some of

the bright pure (0-0) rotational lines fall within the IRAC Channel 2 bandpass, i.e. S(9) 4.6947, S(10) 4.4096 and S(11) 4.1810 μm (Noriega-Crespo et al 2004a, 2004b; Looney et al. 2007; Tobin et al. 2007; Ybarra & Lada 2009; Maret et al. 2009, Raga et al. 2011a; Noriega-Crespo & Raga 2012). The IRAC Channel 2 map could also be brighter because of the CO rovibrational lines that fall in its range. However these lines require high temperatures and densities that do not normally occur in protostellar jets. Nevertheless, the jet is detected in all four bands (Figure 1).

We also used a VLT H₂ 2.1 μm image obtained with the High Acuity Wide field K-Band Imager (HAWK-I), as part of its Science Verification program (PI Schneider, “How symmetric is a symmetric flow. A deep H₂ image of the Herbig Haro object 212”) observed in January 2018, and enhanced by the ground-layer adaptive optics module (GRAAL) with an image quality of the order 0.2”. The raw and reduced data are available through the ESO archive. The uncalibrated image has a 0.106” pixel size (Leibundgut et al. 2018). This image is shown in the left frames of Figures 1 and 2.

3. THE KNOT POSITIONS AND INTENSITIES

Figure 2 shows the H₂ 2.1 μm and the I1-I4 IRAC maps (with 3.6, 4.5, 5.8 and 8.0 μm central wavelengths, respectively) of the HH 212 outflow. The images have been rotated 22.5° clockwise, so that the outflow axis is parallel to the ordinate. The position of the outflow source (for which we have used the position given in § 3.1 of Galván-Madrid et al. 2004) is shown with a black circle in the central region of the I4 map. On the H₂ 2.1 μm map we show the identifications given by Lee et al. (2007) for the H₂ knots.

In order to find the positions of the jet/counterjet knots, we convolved the I1-I4 maps with a “Mexican hat” wavelet with a central peak of $\sigma = 2$ pixel radius, which has the effect of isolating well defined emission peaks from the spatially more extended emission. On these convolved maps we searched for peaks along the jet axis with an intensity larger than a cutoff value I_c (for which we have chosen values of 0.03, 0.05, 0.1 and 0.1 mJy/sterad for the I1, I2, I3 and I4 channels, respectively), and carried out paraboloidal fits in 3×3 pixel regions (around each of the peaks) to determine the knot positions. This procedure is described in detail by Raga et al. (2017).

The H₂ 2.1 μm jet/counterjet knot positions were found on a convolution of this image with a central peak of $\sigma = 5$ pixel radius. We selected peaks with

at least 10^{-2} times the peak knot intensity (which was found for one of the SB knots of Lee et al. 2007) in the convolved frame.

The resulting knot positions are shown as black crosses on the H₂ 2.1 μm and I1-I4 maps of Figure 2. It is clear that many of the knots along the NE jet (top half of the frames) have corresponding emitting structures in the SW counterjet (bottom half of the frames).

The knot located $\approx 26''$ to the N of the source (labeled NK7 by Lee et al. 2007) has no detectable counterpart in the counterjet in the IRAC I1-I4 maps. However, in the H₂ 2.1 μm image we do detect a faint counterpart along the counterjet (labeled SK7).

In Figure 3 we show the peak intensities of the jet and counterjet knots in the I1-I4 IRAC maps (measured on the convolutions with a $\sigma = 2$ pixel radius wavelet) as a function of distance x from the outflow source. This distance is measured along the ordinate of Figures 1 and 2, but (as the offsets of the knots along the abscissa are very small). Almost identical values are obtained if one takes the radial source/knot distances.

The jet and counterjet knots at similar distances from the source have intensities that differ by factors of ≈ 2 . We see that at similar distances from the source:

- in most cases the NE jet knots (in blue) are brighter than the SW counterjet knots (in red),
- the ratios between the jet and counterjet knot intensities generally become smaller for the longer wavelength IRAC channels (see Figure 2).

These trends can be interpreted as the result of a different extinction towards the two outflow lobes, as described in § 4.3.

In the top frame of Figure 4 we show the peak H₂ 2.1 μm intensities of the jet and counterjet knots (measured on the convolution with a $\sigma = 5$ pixel radius wavelet) as a function of distance x from the outflow source. The intensities are given in units of the peak intensity of the SK1 knot (see Figure 2). The jet and counterjet knots at similar distances from the source have intensities that differ by factors of ≈ 3 , except for knots NK7 and SK7 (at $\approx 26''$ from the source) which have intensities that differ by a factor of ≈ 10 .

We now use the H₂ 2.1 μm map (which has a higher angular resolution than the IRAC maps) to define jet/counterjet knot associations with pairs of knots which have values of $|x|$ (the distance to the

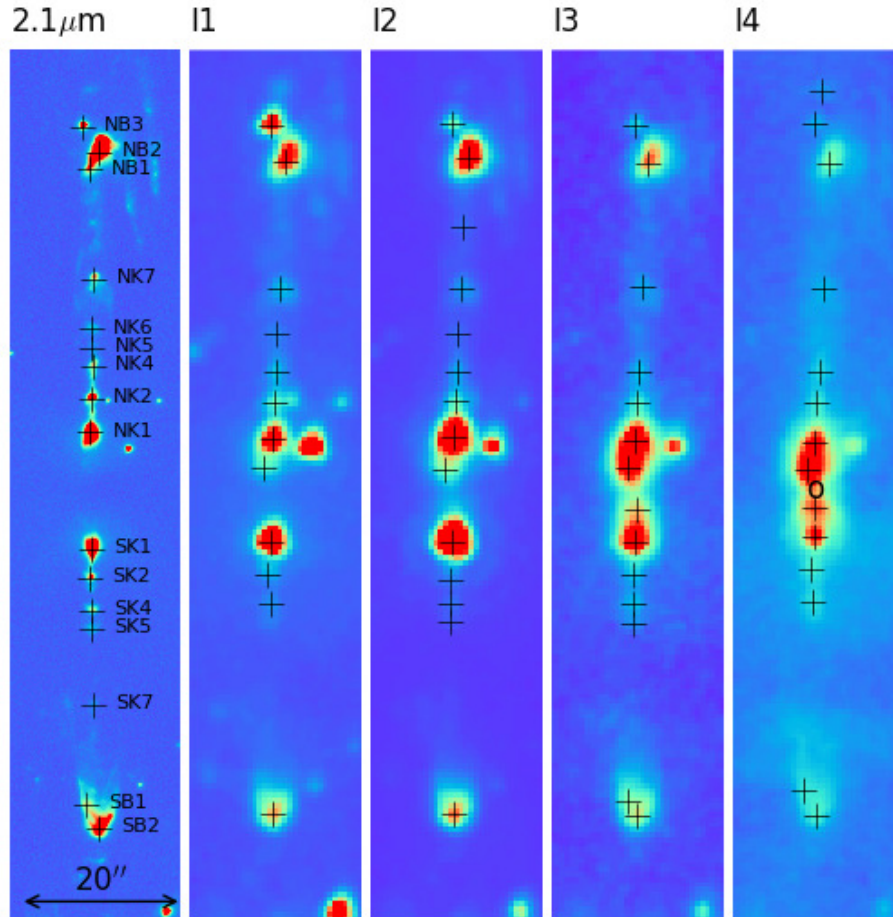


Fig. 2. The central region of the HH 212 outflow in in H_2 $2.1 \mu\text{m}$ (left frame) and in the four IRAC channels (I1-I4, with 3.6, 4.5, 5.8 and $8.0 \mu\text{m}$ central wavelengths, respectively). The ordinate points to the NNE (at 22.5° clockwise from N). The circle in the central region of the I4 map is the position of the source. The crosses indicate the positions of knots along the jet/counterjet (see the text). The knot identifications of Lee et al. (2007) are given on the H_2 $2.1 \mu\text{m}$ map. The images are displayed with a linear color scale. The color figure can be viewed online.

outflow source) differing by less than $2''$. For these pairs of knots, we calculate the jet-counterjet knot position offsets $\Delta x = x_j - x_{cj}$ as a function of $x = x_j$. In the bottom frame of Figure 4 we show the resulting Δx (crosses) and $(\Delta x)^2$ (squares) as a function of x . This plot shows a trend of marginally increasing jet-counterjet knot position offsets with distance from the outflow source.

In Figure 5 we show the (x, y) knot positions of the inner H_2 $2.1 \mu\text{m}$ knots, with x measured along (positive values for the N jet) and y across the outflow axis (positive values to the E) from the position of the outflow source. It appears that the knots with $|x| < 30''$ have offsets (with respect to the outflow direction) with a jet/counterjet mirror symmetric pattern. This result is discussed in more detail below.

Finally, we used the new H_2 $2.1 \mu\text{m}$ image (obtained in January 2018) together with the IRAC I1-I4 maps (obtained in February 2005) to estimate the proper motions of the HH 212 knots within $50''$ from the outflow source. This of course gives only rough estimates of the proper motions, since different knot morphologies in the different spectral bands can in principle lead to position offsets that are not due to proper motions.

We proceeded as follows. For the knots that are present in all the I1-I4 IRAC maps, we first calculate the average positions (along and across the outflow axis), and the standard deviations of these positions. We then use these I1-I4 “first epoch” average knot positions to calculate the knot proper motions together with their corresponding positions in the

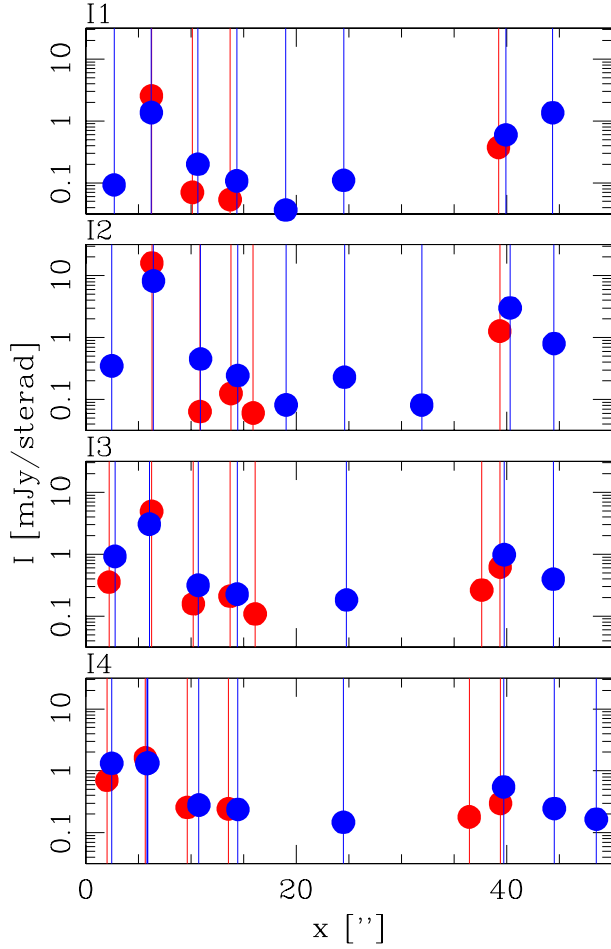


Fig. 3. Fluxes measured for the knots along the jet (blue circles with vertical lines) and counterjet (red circles) as a function of distance x along the outflow axis in the I1-I4 IRAC channel maps. The fluxes are given in mJy/sterad. The vertical lines are shown so as to highlight the occurrence of jet/counterjet knot pairs with closely matched positions. The color figure can be viewed online.

H₂ 2.1 μ m “second epoch” map. The proper motion velocities calculated from these knot offsets (assuming a distance of 400 pc to HH 212) are given in Table 1.

This table gives the knot identifications (shown in the left frame of Figure 2), the positions x along the outflow axis (measured in the H₂ 2.1 μ m map, with positive x pointing along the N jet), and the proper motion velocities along (positive values to the N) and across (positive values to the W) the outflow axis with their errors (in parentheses). Even though the errors shown are quite small for most of the knots, it is likely that there are larger systematic errors due to the fact that we compare images with different emission features.

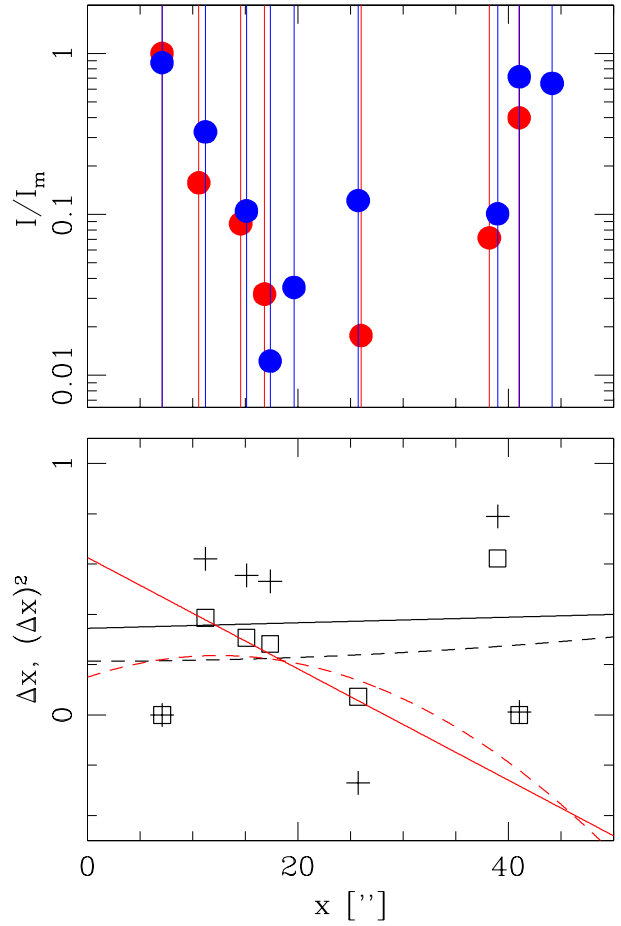


Fig. 4. Top frame: Fluxes measured for the knots along the jet (blue circles with vertical lines) and counterjet (red circles) as a function of distance x along the outflow axis in the H₂ 2.1 μ m map. The fluxes are given in units of the flux of the SK1 knot. Bottom frame: jet/counterjet knot offsets Δx (crosses) and the squares $(\Delta x)^2$ of these values (squares) as a function of distance from the source. The results of the linear (black solid lines) and quadratic fits (black dashed lines) to the Δx and $(\Delta x)^2$ vs. x dependencies are shown (see the text). The red lines are the corresponding fits to the points with $x < 30''$ only. The jet/counterjet knot offsets have measurements errors of $\approx 0.05''$ (corresponding to $\approx 1/2$ pixel). The color figure can be viewed online.

The determined proper motion velocities are well aligned with the directions of the jet and the counterjet axes, except for knot NB3. This knot has a motion directed to the NW, which could indicate that it does not belong to the HH 212 outflow or that it has a substantially different morphology in H₂ 2.1 μ m than in the other spectral bands.

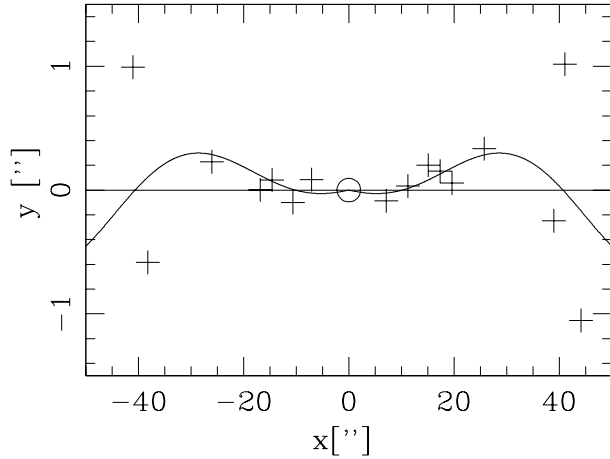


Fig. 5. Positions of the inner HH 212 knots measured on the H₂ 2.1 μ m frame. The x coordinate lies along (positive x to the N), and the y coordinate across the outflow axis (positive y to the E). The solid curve is a least squares fit to the knots with $|x| < 30''$ of the ballistic “orbiting source jet” of Masciadri & Raga (2002), as described in the text. The positions along and across the outflow axis have errors of $\approx 0.03''$.

Most of the knots have axial velocities in the range from ≈ 50 to 170 km s^{-1} , which is roughly consistent with the previously determined proper motions of the HH 212 knots: $115 \pm 50 \text{ km s}^{-1}$ by Lee et al. (2015) and somewhat higher velocities by Reipurth et al. (2019). If one compares our results (shown in Table 1) with Table 2 of Reipurth et al. (2019), one finds quite good agreements for the motions of most of the knots present in both tables (note that the knot that we have labeled NB3 does not correspond to the knot with the same denomination in Reipurth et al. 2019).

4. INTERPRETATION OF THE RESULTS

4.1. The Jet/Counterjet Knot Position Asymmetries

We use the jet/counterjet knot offsets to constrain the jet/counterjet asymmetries along the outflow axis shown in Figure 4. We do this using the model of Raga et al. (2011b). In this model, one assumes that:

- the knots travel ballistically,
- the jet/counterjet knot pairs are ejected with velocities that differ by Δv (positive values indicating a faster knot along the jet), with this velocity difference following a uniform distribution with a mean value v_0 and a half-width Δv_0 ,

TABLE 1

PROPER MOTIONS OF THE HH 212 KNOTS

Knot	x "	v_x km s^{-1}	v_y km s^{-1}
NK1	7.1	141 (30)	-3 (12)
NK2	11.2	69 (15)	-1 (12)
NK4	15.1	105 (7)	1 (10)
NK7	25.7	170 (17)	-28 (7)
NB2	41.1	165 (36)	10 (12)
NB3	44.2	-44 (10)	-29 (17)
SK1	-7.1	-145 (39)	13 (21)
SK2	-10.6	-55 (64)	48 (22)
SK4	-14.6	-128 (13)	14 (10)
SB2	-41.0	-251 (11)	32 (12)

- the knot pairs are ejected with a time-difference $\Delta\tau$ (positive values indicating an earlier jet knot ejection), with the time-difference following a uniform distribution with mean value τ_0 and a half-width $\Delta\tau_0$.

The values of v_0 , Δv_0 , τ_0 and $\Delta\tau_0$ can then be determined by carrying out a linear fit to the Δx vs. x trend and a quadratic fit to the $(\Delta x)^2$ vs. x trend observed in a particular jet/counterjet system. The mean values and half-widths of the ejection velocity and time distributions can be found from the coefficients of these fits using equations (4) and (6) of Raga et al. (2011b).

We carry out the linear and quadratic fits to the Δx vs. x and the $(\Delta x)^2$ vs. x values (respectively) obtained from the H₂ 2.1 μ m map. The results of these fits are shown with solid and dashed lines, respectively, in the bottom frame of Figure 4. With the fitting coefficients we determine the characteristics of the asymmetrical jet/counterjet ejection time and velocity distributions (see above and Raga et al. 2011b):

- $v_0 = (0.16 \pm 0.17) \text{ km s}^{-1}$, $\Delta v_0 = (1.60 \pm 0.12) \text{ km s}^{-1}$,
- $\tau_0 = (4.38 \pm 1.54) \text{ yr}$, $\Delta\tau_0 = (6.77 \pm 4.74) \text{ yr}$.

These parameters were derived assuming a distance of 400 pc and a flow velocity of $(170 \pm 30) \text{ km s}^{-1}$ for HH 212 (see Reipurth et al. 2019).

In other words, the jet/counterjet knot position asymmetries of HH 212 can be explained with:

- an ejection velocity asymmetry with a distribution centered at 0 (i.e., the value of v_0 determined from the fits is not significantly different from 0, see above) and half-width of $\approx 1.6 \text{ km s}^{-1}$,
- an ejection time asymmetry with a distribution centered at $\approx 4 \text{ yr}$, and a (barely significant) width of $\approx 7 \text{ yr}$.

These results are qualitatively similar to the ones found for the HH 34 jet/counterjet system by Raga et al. (2011b).

It is fair to say that through this analysis we are basically not detecting a significant asymmetry in the jet/counterjet ejections, and are only estimating upper boundaries (of $\approx 2 \text{ km s}^{-1}$ for the velocity and $\approx 4 \text{ yr}$ for the ejection time) for possible asymmetries in the ejections.

The large uncertainty in our estimate of the ejection asymmetries is illustrated with the following exercise. One could argue that the local intensity maxima of knots NB1, NB2, SB1 and SB2 actually correspond to local features in larger bow shocks (see Figure 2), and therefore the associations NB1-SB1 and NB2-SB2 used to calculate the offsets at $x \approx 40''$ (see the two frames of Figure 4) are not necessarily meaningful. Therefore, we repeat the linear and quadratic fits (to the Δx and $(\Delta x)^2$ vs. x dependencies) using only the knot offsets obtained for $x < 30''$.

The results of these fits are shown with the solid (linear fit to Δx vs. x) and dashed (quadratic fit to $(\Delta x)^2$ vs. x) red lines in the bottom frame of Figure 4. These fits do not yield physical estimates of the ejection variability, since the formalism of Raga et al. (2011b) gives complex values for the derived parameters for the ejection distributions when using the resulting values of the coefficients of these fits.

Given the lack of a clear correlation of the jet/counterjet knot offsets as a function of distance from the source (evidenced by the fact that the results change in a quite drastic way by removing the knots at $x \approx 40''$) it is probably fairer to just note that the knot offsets have a mean value $|\Delta x| = (0.40 \pm 0.29)''$. This corresponds to an average time-difference $\overline{\Delta\tau} = |\Delta x|/v_j = (4.5 \pm 3.3) \text{ yr}$ (for a distance of 400 pc and $v_j = 170 \text{ km s}^{-1}$, see above). This estimate is consistent with the $\Delta\tau_0 = (6.77 \pm 4.74) \text{ yr}$ width for the ejection time distribution deduced above using the formalism of Raga et al. (2011b) and the fit to all knot offsets shown in the bottom frame of Figure 4.

4.2. The Mirror Symmetric Precession Pattern

The inner jet/counterjet knot positions of HH 212 show sideways deviations from the outflow axis with an apparent “mirror symmetric pattern”. In Figure 5, we see that the jet/counterjet knots within $30''$ from the source show trends of larger values of y (i.e., towards the E) with increasing distances from the source. At $x \approx \pm 40''$ we see the NB and SB knots (respectively), which show a larger spread of y values, as a result of the larger size of the NB and SB structures.

The simplest explanation of mirror symmetric patterns in jet/counterjet systems is in terms of an orbital motion of the (binary) outflow source. A ballistic, analytic model of this situation was presented by Masciadri & Raga (2002), for the case of a circular orbit and by González & Raga (2004), for elliptical orbits.

Noriega-Crespo et al. (2011) used the “circular orbit model” of Masciadri & Raga (2002) to fit the “mirror symmetric precession pattern” of the HH 111 jet/counterjet system. From this fit, they derived estimates of the orbital parameters and stellar masses of the assumed binary source of the HH 111 system.

We follow these authors, and carry out a least squares fit of the jet/counterjet loci:

$$y = \kappa x \sin\left(\frac{2\pi}{\tau_o v_j} x - \psi\right), \quad (1)$$

$$z = \kappa x \cos\left(\frac{2\pi}{\tau_o v_j} x - \psi\right), \quad (2)$$

where x is the axial coordinate and (y, z) are the axes parallel to the orbital plane (with y being parallel to the plane of the sky). Also, ψ is the orbital phase, τ_o the orbital period, and $\kappa = v_o/v_j$ the ratio between the orbital and jet velocities. These equations (see Noriega-Crespo et al. 2011) correspond to the small orbital radius limit of the circular orbit model of Masciadri & Raga (2002). We also assume that the outflow is ejected perpendicular to the orbital plane.

We project equations (1-2) onto the plane of the sky assuming an angle of 5° between the outflow axis and this plane (see Reipurth et al. 2019), and carry out a least squares fit to the mirror symmetric pattern of the knots within $30''$ of the HH 212 source. From this fit, we obtain:

- $\kappa = 0.011 \pm 0.001$, corresponding to an orbital velocity $v_o = (1.87 \pm 0.17) \text{ km s}^{-1}$ for the $v_j = 170 \text{ km s}^{-1}$ proper motion velocity of Reipurth et al. (2019),

- $\tau_o = (638 \pm 241)$ yr, where we have also assumed a distance of 400 pc to HH 212.

With these values for the orbital velocity and the orbital period we can derive the orbital radius:

$$r_1 = \frac{v_o \tau_o}{2\pi} = (40 \pm 15) \text{ AU}, \quad (3)$$

and a mass

$$\frac{\alpha^3}{(1 + \alpha)^2} M_1 = \frac{\tau_o v_o^3}{2\pi G} = (0.168 \pm 0.068) M_\odot, \quad (4)$$

for the primary (jet source) star. In equation (4), G is the gravitational constant $\alpha = M_2/M_1$ is the mass ratio of the binary. If we have an equal mass binary (with $\alpha = 1$), we then obtain a mass $M_1 = (0.67 \pm 0.27) M_\odot$ and a binary separation of $2r_1 = (80 \pm 30)$ AU.

We should note that Lee et al. (2015) made a fit of a much tighter precession spiral (with a spatial wavelength $\approx 6''$, corresponding to a ≈ 90 yr period) to the observed CO/SiO emission of HH 212. This small scale structure of curved jet segments can also be seen in the NK1-NK4 region of the H₂ 2.1 μm jet shown in the left panel of Figure 2. Analogously, the larger scale structure (with a period of ≈ 600 yr, see above) we are describing here is also seen in the CO/SiO map (Figure 8 of Lee et al. 2015).

4.3. The Jet/Counterjet Extinction

As discussed in § 3, the jet knots (blue points) in the IRAC channel maps are generally brighter than the counterjet knots (red points, see Figure 3) at the same distances from the outflow source, especially for the shorter wavelengths channels (I1 and I2). In order to quantify this effect, we calculate the I_j/I_{cj} jet-to-counterjet knot intensity ratios for the three knots at distances $x = 5 \rightarrow 15''$ (from the outflow source), and use these ratios to calculate a mean ratio $\langle I_j/I_{cj} \rangle$ for each of the four IRAC channels. Figure 6 shows the resulting mean jet-to-counterjet $\langle I_j/I_{cj} \rangle$ ratios (shown as magnitudes) as a function of λ (where λ is the central wavelength of the four IRAC channels). In this figure we also show the jet-to-counterjet intensity ratio of the knots seen in the 2.1 μm map.

We carried out a weighted least squares fits with a linear transformation of the $R = A_v/E(B-V) = 5$ extinction curve (appropriate for star formation regions) of Fitzpatrick (1999), and we show the results in Figure 6. We show two fits:

- a fit to the jet-to-counterjet intensity ratios measured in the IRAC maps (dashed curve in Figure 6). The fit gives a visual extinction to the

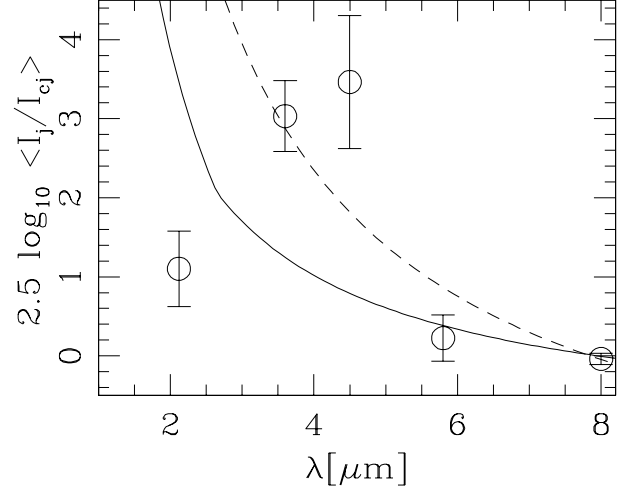


Fig. 6. Mean values of the jet/counterjet intensity ratio (calculated with the three knot pairs at $x = 5 \rightarrow 15''$, see the text) as a function of central wavelength of the IRAC channels and of the VLT H₂ map. The intensity ratios are shown as a magnitude, and as a function of the central wavelength. The solid line shows a least squares fit to the observed line ratios of a linearly transformed $R = 5$ extinction curve. The fit to the data gives a higher absorption towards the counterjet of $A_v = 16.9 \pm 2.3$. The dashed line shows a fit to the intensity ratios with $\lambda > 3\mu\text{m}$.

counterjet larger by $A_v = 16.9 \pm 2.3$ than the extinction towards the jet,

- a fit to the jet-to-counterjet intensity ratios measured in the IRAC maps and in the 2.1 μm map (solid curve in Figure 6). The fit gives a visual extinction to the counterjet larger by $A_v = 7.2 \pm 1.3$ than the extinction towards the jet.

These of course are estimates only of the difference between the jet and counterjet extinction, and not a determination of the value of the total extinction to the HH 212 outflow.

The measured I_j/I_{cj} jet-to-counterjet knot intensity ratios shown in Figure 6 have quite large deviations from the extinction curves. This indicates that the jet and counterjet knots at similar distances from the source have relatively large intrinsic intensity differences, not attributable in a direct way to a difference in the extinction.

4.4. Knot NK7

Knot NK7 is located along the NE jet at a distance $x \approx 25''$ from the outflow source (see Figures 2 and 3). Lee et al. (2007) show that this knot has a

very faint H_2 $2.1 \mu\text{m}$ southern counterpart, but they do not detect it in SiO and CO (at sub-mm wavelengths). We also see the faint SK7 counterpart to NK7 in our H_2 image (see Figure 2). This result, together with the fact that we do not see the southern counterpart of NK7 in the IRAC images, indicates that this knot is intrinsically much brighter along the NE jet than the corresponding ejection along the counterjet, and that this strong brightness asymmetry is not an extinction effect (as the extinction should be much less important at longer wavelengths).

Should we therefore conclude that even though the jet/counterjet ejection from the HH 212 source appears to have a remarkable degree of symmetry (see § 4.1), every now and then it produces highly asymmetrical ejections? This is a possible interpretation of the lack of a bright counterpart for the NK7 knot.

Another possible mechanism for producing the observed intensity asymmetry is that knot NK7 corresponds to the merger of two knots (travelling down the jet at slightly different velocities), and that the brightening is associated with the merging process (which produces a knot of boosted shock velocities). If this were the case, we might expect to see a sudden brightening of an “SK7” knot (at $x \approx 25''$ from the source) along the counterjet when the corresponding knot merger occurs in the counterjet.

5. CONCLUSIONS

We present Spitzer (IRAC) observations and an H_2 $2.1\mu\text{m}$ image of the HH 212 outflow. In these maps, the general structure of the two outflow lobes is seen (see Figure 1).

For the inner $\approx 1'$ of the outflow, we determine the positions of knots along the NE jet and SW counterjet (see Figure 2), and find that they mostly fall into “jet/counterjet knot pairs” (with distances from the source differing by at most $\approx 1.2''$). We then calculate the jet/counterjet knot offsets Δx as a function of distance x from the outflow source (see Figure 4). We carry out the analysis of knot position offsets with the $2.1 \mu\text{m}$ map, which has higher angular resolution than the IRAC maps.

We interpret the observed jet/counterjet position offsets with the quasi-symmetric ballistic ejection model of Raga et al. (2011b). Through this exercise we determine that the knot pairs are ejected with time-differences $\Delta\tau_0 \approx 6$ yr and velocity differences $\Delta v_0 \approx 2 \text{ km s}^{-1}$. These results are similar to the ones obtained for HH 34 by Raga et al. (2011b). Clearly, an appropriate ejection model should have this degree of jet/counterjet coordination.

One can in principle use the determined jet/counterjet ejection coordination to estimate a physical size for the jet production region. In the cool, magnetized ejection mechanisms appropriate for low mass young stars, the signal transmission velocity (which could be either the Alfvén or the sound speed) is expected to lie in the $v_s \approx 0.1 \rightarrow 10 \text{ km s}^{-1}$ range. We would then predict a size of $L = \Delta\tau_0 v_s \approx 0.1 \rightarrow 10 \text{ AU}$ for the jet production region. The lower limit of this size range is in agreement with the estimation of Lee et al. (2017) of a $\approx 0.1 \text{ AU}$ size for the HH 212 outflow collimation region.

We use the knot positions measured on the H_2 $2.1 \mu\text{m}$ image together with the IRAC maps (which were obtained ≈ 13 yr earlier) to determine proper motions of the knots along the jet and the counterjet. We find generally good agreement with the proper motions obtained by Reipurth et al. (2019) with two H_2 $2.1 \mu\text{m}$ epochs covering an ≈ 8 yr time-interval.

We also analyze the deviations of the knot positions perpendicular to the mean axis of the outflow. These deviations show a mirror symmetric jet/counterjet pattern, which can be interpreted in terms of a ballistic outflow from a source in an orbit around a binary companion. We fit the model of an outflow source in a circular orbit of Masciadri & Raga (2002) to the observed deviations (see Figure 5). From the model fit we deduce an $(80 \pm 30) \text{ AU}$ binary separation and a $(0.67 \pm 0.27) M_\odot$ mass for the outflow source (assuming that the binary companion has the same mass as the outflow source). This estimate for the separation between the binary components coincides with the $\approx 90 \text{ AU}$ radius of the disk around the HH 212 source observed by Codella et al. (2014). Our estimated mass is somewhat larger than the $\approx 0.15 M_\odot$ mass estimated by Lee et al. (2006, from observations of an infalling envelope) and the $\approx 0.3 M_\odot$ mass estimated by Codella et al. (2014, from the rotation of the disk) for the HH 212 outflow source.

The general structure of HH 212 has an important asymmetry in that the NK7 knot (at $\approx 25''$ along the NE jet, see Figures 2 and 3) does not have a comparably bright counterpart along the counterjet. This asymmetry is observed at all wavelengths at which the HH 212 outflow has been observed (see Lee et al. 2007), and therefore cannot be accounted for by differential extinction (see § 4.3 and § 4.4). We suggest that the asymmetric knot NK7 could be interpreted as a true ejection asymmetry, or as a recent brightening of the knot due to the merger of two “outflow events”. If this latter explanation is correct,

we might expect a future brightening of a counterjet knot at a comparable distance to the outflow source.

Finally, we use the wavelength dependence of the jet/counterjet intensity ratio (measured in the four IRAC channels) to determine the difference in the extinction to the HH 212 jet and counterjet. We conclude that the extinction towards the counterjet is larger (than the one towards the jet) by $A_v \approx 10$ magnitudes. This result is similar to the one found by Raga et al. (2019) for the HH 34 outflow. However, we find large deviations between the extinction curve and the jet/counterjet intensity ratios (as a function of wavelength). This indicates that the jet and counterjet knots at similar distance from the outflow source have relatively large intrinsic intensity differences.

AR acknowledges support from the DGAPA-UNAM grant IG100218. JCRR acknowledges the Brazilian agency FAPESP grant 2017/12188-5. We thank an anonymous referee for helpful comments, which gave rise to § 4.3.

REFERENCES

- Anthony-Twarog, B. J. 1982, *AJ*, 87, 1213
- Codella, C., Cabrit, S., Gueth, F. et al. 2014, *A&A*, 568, L5
- Correia, S., Zinnecker, H., Ridgway, S. T., & McCaughrean, M. J. 2009, *A&A*, 505, 673
- Davis, C. J. Berndsen, A., Smith, M. D., Chrysostomou, A., & Hobson, J. 2000, *MNRAS*, 314, 241
- Fitzpatrick, E. L. 1999, *PASP*, 111, 63
- Galván-Madrid, R., Ávila, R., & Rodríguez, L. F. 2004, *RMxAA*, 40, 31
- González, R. F. & Raga, A. C. 2004, *RMxAA*, 40, 61
- Gredel, R. & Reipurth, B. 1994, *A&A*, 289, L19
- Kounkel, M., Hartmann, L., Loinard, L., et al. 2017, *ApJ*, 834, A142
- Lee, C.-F., Hirano, N., Zhang, Q., et al. 2015, *ApJ*, 805, 186
- Lee, C.-F., Ho, P. T. P., Beuther, H., et al. 2006, *ApJ*, 639, 292
- Lee, C.-F., Ho, P. T. P., Hirano, N., et al. 2007, *ApJ*, 659, 499
- Lee, C.-F., Ho, P. T. P., Li, Z.-Y., et al. 2017, *NatAs*, 1, 0152
- Leibundgut, B., Hibon, P., Kuntschner, H., et al. 2018, *Msngr*, 172, 8
- Looney, L. W., Tobin, J. J., & Kwon, W. 2007, *ApJ*, 670, 131
- Masciadri, E. & Raga, A. C. 2002, *ApJ*, 568, 733
- Maret, S., Bergin, E. A., Neufeld, D. A., et al. 2009, *ApJ*, 698, 1244
- Noriega-Crespo, A., Morris, P., Marleau, F. R., et al. 2004a, *ApJS*, 154, 352
- Noriega-Crespo, A., Moro-Martin, A., Carey, S., et al. 2004b, *ApJS*, 154, 402
- Noriega-Crespo, A., Raga, V., Stapelfeldt, K. R., & Carey, S. J. 2011, *ApJ*, 732, L16
- Noriega-Crespo, A. & Raga, A. C. 2012, *ApJ*, 750, 101
- Raga, A. C., Noriega-Crespo, A., Lora, V., Stapelfeldt, K. R., & Carey, S. J. 2011a, *ApJ*, 730, L17
- Raga, A. C., Noriega-Crespo, A., Rodríguez-Ramírez, J. C., et al. 2011b, *RMxAA*, 47, 289
- _____. 2012, *ApJ*, 748, 103
- Raga, A. C., Reipurth, B., Esquivel, A., et al. 2017, *RMxAA*, 53, 485
- Raga, A. C., Reipurth, B., & Noriega-Crespo, A. 2019, *RMxAA*, in press
- Reipurth, B., Davis, C. J., Bally, J., et al. 2019, *AJ*, submitted
- Smith, M. D., O’Connell, B., & Davis, C. J. 2007, *A&A*, 466, 565
- Tobin, J. J., Looney, L. W., Mundy, L. G., Kwon, W., & Hamidouche, M. 2007, *ApJ*, 659, 1404
- Ybarra, J. E. & Lada, E. A. 2009, *ApJ*, 695, 120
- Zinnecker, H., Bastien, P., Arcoragi, J.-P., & Yorke, H. W. 1992, *A&A*, 265, 726
- Zinnecker, H., McCaughrean, M. J., & Rayner, J. T. 1998, *Natur*, 394, 862
- V. Lora: Instituto de Radioastronomía e Astrofísica Teórica, Universidad Nacional Autónoma de México, Ap.3-72, 58089 Morelia, Michacán, México.
- A. Noriega-Crespo: Space Telescope Science Institute, 3700 San Martin Drive, Baltimore, MD 21218, USA (anoriega@stsci.edu).
- A. C. Raga: Instituto de Ciencias Nucleares, Universidad Nacional Autónoma de México, Ap. 70-543, 04510 Cd. Mx., México (raga@nucleares.unam.mx).
- J. C. Rodríguez Ramírez: Instituto de Astronomia, Geofísica e Ciências Atmosféricas, Universidade de São Paulo, R. do Matão 1226, 05508-090 São Paulo, SP, Brasil.

STAR FORMATION RATE IN LATE-TYPE GALAXIES: I- THE H_α AND FUV INTEGRATED VALUES

M. A. Magaña Serrano, A. M. Hidalgo Gámez, I. Vega-Acevedo, and H. O. Castañeda

Departamento de Física, ESFM-IPN, Ciudad de México, México.

Received November 8 2018; accepted December 5 2019

ABSTRACT

The star formation rate (SFR) was determined from a sample of 36 late-type galaxies (14 dS and 22 Sm), from the SFR(H_α) and far ultraviolet (FUV) flux. We found that the SFR(FUV) is higher in most cases, larger for Sm galaxies and smaller for barred galaxies, for any morphological type, in both diagnostic methods. In addition, a study of the spatial distribution of star formation within these galaxies was made. We concluded that there is no preferential place for the star formation. Finally, we studied the role of the diffuse ionized gas in the SFR value; we found that the H_α flux contribution from this gas should not be included in the SFR determination unless it is verified that leaking photons are the only source of the neutral gas ionization.

RESUMEN

Se obtuvo la tasa de formación estelar (SFR) de una muestra de 36 galaxias tardías (14 dS y 22 Sm), a partir del flujo H_α y FUV. Se encuentra que la SFR(FUV) en la mayoría de los casos es mayor que la SFR(H_α) y que las galaxias barradas siempre presentan valores menores de la SFR que las que no tienen barra. Se obtuvo que las galaxias Sm tiene mayor SFR que las dS. Además, estudiamos la distribución espacial de la formación estelar de nuestra muestra de galaxias; concluimos que la mayoría de las galaxias son simétricas en su formación estelar, y tienen valores similares del número de regiones H II y del flujo a ambos lados del eje de simetría. Finalmente, analizamos el papel que juega el gas ionizado difuso en la SFR; encontramos que la luminosidad H_α proveniente de este gas no debería ser incluida en la determinación de la SFR a menos que se verifique que la pérdida de fotones ionizantes es la responsable de la ionización.

Key Words: galaxies: dwarf — galaxies: star formation — H II regions

1. INTRODUCTION

Although late-type galaxies are relatively simple systems and are the most abundant galaxies in the Universe (Marzke & Da Costa, 1997; Mateo, 1998; Danieli, S. et al. 2017), their formation and evolution are not yet well understood. Although there are many different parameters which might influence the evolution of galaxies, one of the most important is the star formation rate (SFR). The reasons are many. The SFR indicates how many stars are formed by the gas in a galaxy (in time). Therefore, gas mass is transformed into stars, which then process this gas transforming the primordial hydrogen into more complex atoms, like oxygen, sulfur, or iron (see, for

example, the seminal work of Tinsley on chemical evolution; Tinsley 1981). Moreover, massive stars end their lives as supernovae, which inject about 10^{51} erg of energy into the interstellar medium (ISM) of the galaxy (Pittard, 2019). Such energy can be used to collapse the gas in the vicinity and form new stars (as in Holmberg II or IC 2574, Sánchez-Salcedo, 2002), to heat the medium avoiding a new event of star formation (Jog, 2013), or even to eject gas (and metals) outside the galaxy (e.g. Dekel & Silk, 1986; D’Ercole & Brighenti, 1999; Melioli et al. 2015). In order to have a wider and more comprehensive view of such events, other parameters are needed, such as the initial mass function (IMF) which gives the

number of stars formed for each mass interval, and the star formation history (SFH), which is the number of stars formed along cosmic time in each galaxy. This set of parameters (SFR, IMF and SFH) provide information about the evolution of galaxies (López et al. 2018).

The SFR can be determined by several diagnostic methods. Two of the most important are the intensity of the recombination line H_α and the flux of the FUV (Kennicutt, 1998; Calzetti 2013; Audcent-Ross et al 2018). The H_α line has been widely used due to its many advantages, such as being easy to measure even with small aperture telescopes, because of its large flux in star-forming galaxies. Nevertheless, for galaxies with $z > 0.5$, the H_α line goes into the near infrared and it is necessary to use a detector in this wavelength range. The UV measurements also allow the determination of the SFR from the FUV continuum. Several authors have noticed differences in the SFR obtained from the H_α line and the FUV continuum and have given possible explanations for the discrepancies (e.g. Bell & Kennicutt, 2001; Lee et al. 2009): an IMF systematically deficient in the highest mass stars, a leakage of ionizing photons from a low density environment, or the fact that most methods only consider a single, solar metallicity. Most of these studies have been done on spiral and irregular galaxies of the local volume and for dwarf galaxies within 11 Mpc (Karachentsev & Kaisina, 2013; Lee et al. 2009).

It is well known that the highest star formation rates occur in Sc galaxies (Kennicutt, 1998). Late-type galaxies (Sm and dS) have a very large reservoir of neutral gas relative to their total mass (typically of the order of 6%, Huchtmeier & Richter, 1989) but a lower SFR (e.g. Hunter & Elmegreen, 2004). Therefore, the efficiency of the star formation process is very low for these galaxies. There could be several reasons for this; the lack of a clear triggering mechanism of star formation could be one of the most important ones.

There are several goals in this paper, which is focused on the integrated SFR values of a sample of late-type galaxies. Firstly, to increase the sample of late-type galaxies with SFR measurements based on H_α and FUV flux. Although there are many investigations devoted to SFR determinations (among others, James et al. 2004; Lee et al. 2009; Hunter & Elmegreen 2004; Hunter et al., 2010; Rosenberg et al. 2008; Buat et al. 2009; Boselli et al. 2015; Boselli et al. 2009; James et al. 2008; Almoznino & Brosch, 1996) there are only 50 Sm galaxies with SFR determined from the FUV continuum, so the inclusion

of another 28 galaxies increases the total sample by more than 50%. The increase is not so large for Sm galaxies with SFR based on the recombination line H_α : only about 15%.

Another goal is to check how much dS galaxies differ from Sm galaxies. Among other things, we can check the efficiency of the SFR, because dS galaxies have a larger amount of neutral gas but a less clear spiral structure, as stated above.

Another interesting study performed here is the spatial distribution of the H II regions in the galaxies. Some authors claim that most of the regions are located in the central part of the galaxies (e.g. Roye & Hunter, 2000; Hodge, 1969; Bruch et al. 1998), and that, for barred galaxies, many H II regions are located at the end of the bar (Elmegreen & Elmegreen, 1980). This is tested for the galaxies in our sample. Moreover, if there is any large asymmetry in the H II region distribution, some clues on the recent environmental history can be obtained.

Finally, we want to study how the diffuse ionized gas (hereafter, DIG) might affect the estimation of the SFR in galaxies, because not all the H_α emission outside the H II regions is due to ionizing photons emitted by massive stars, but also to mechanisms (See Hidalgo-Gómez 2004 for a review). So, the inclusion of DIG photons in the total H_α emission might give a higher, but not so accurate, SFR.

The paper is organized as follows. In § 2 we describe the galaxy sample, the data acquisition, reduction and calibration of data as well as the detection of the H II regions. The determination of the SFR values with the H_α and FUV fluxes, along with a contrast of our results with the data from the literature, and the efficiency of the star formation process are studied in § 3, while the results on the distribution of the H II regions in our sample are outlined in § 4. Finally, the importance of the DIG on the estimation of the SFR is discussed in § 5. Our conclusions are presented in § 6.

2. SAMPLE DESCRIPTION, DATA ACQUISITION AND REDUCTION

The sample used in this investigation consists of 36 late-type galaxies, that are divided into 14 dwarf spiral galaxies (dS) and 22 Sm galaxies. The galaxies in the latter subsample were selected from the RC3 and UGC catalogues, considering only Sm or types 9 or 10 galaxies. The galaxies in the former subsample were selected from Table 1 in Hidalgo-Gómez (2004). All interacting and active galaxies were disregarded. Ten of the galaxies in this sample are classified as barred, 7 of them are Sm and 3 dS. Finally, from a

visual inspection of the H_α images we divided our sample into galaxies with clear spiral structure (18 galaxies), galaxies without spiral structure (9 galaxies) and those of intermediate type (9 galaxies). The galaxies in the sample presented here were selected from the tables mentioned above and observed just because their coordinates were the right ones at the moment of the observations.

The number of Sm galaxies studied here is comparable with other samples [8 Sm galaxies in James et al. (2004), 20 Sm in Hunter & Elmegreen (2004), 25 Sm in van Zee (2001) and 7 Sm galaxies in Hunter et al. (2010)].

The characteristics of the galaxies in the sample are presented in Table 1. The name and the morphological type is given in Columns 1 and 2, while the coordinates (α and δ) are listed in Columns 3 and 4 from NED-NASA. The absolute magnitude (Column 5) was determined from the apparent magnitude and the kinematic distance (Column 7) which were obtained from the NASA Extragalactic Database (NED-NASA). The absolute magnitudes are galactic extinction-corrected (Column 8). The inclination is presented in Column 9 and was also obtained from NED-NASA. The optical size (Column 6) and the surface brightness (Column 10) were determined following equations 3 and 4 in Hidalgo-Gómez & Olofsson (1998). Finally, the HI mass and surface density were computed from equation 2 in Hidalgo-Gómez (2004).

2.1. Observations, Reduction and Calibration of the Data

The H_α images were acquired at the 1.5m telescope of the Observatorio Astronómico Nacional at San Pedro Mártir (OAN-SPM) in five different observational campaigns from 2002 to 2004. Five narrow band filters were used: three in the hydrogen H_α recombination line, centered at 6570 Å, 6607 Å and 6690 Å, and two for continuum subtraction, with central wavelengths at 6459 Å and 6450 Å. The maximum transmittance of the filter was 70% and they were between 89 Å and 127 Å wide. The integration times were in the range of 1200 and 5400 s for hydrogen H_α and 900 and 3600 s for continuum, respectively. The air mass was smaller than 1.4 for all but three of the galaxies, and the seeing was between 1.1 and 2.6, with an average value of 1.4. The convolution of the peak transmission of the filters (70%) and the high detector quantum efficiency (90%) allowed us to achieve relatively deep flux limits (7×10^{-18} erg cm $^{-2}$ s $^{-1}$).

The reduction procedure (bias, flat-fields, removal of cosmic rays and sky subtraction) as well as the flux calibration were performed using the ESO-MIDAS software. Three standard stars were observed each night with different air mass in order to perform the flux calibration.

The ultraviolet fluxes were obtained from the 6th release (GR6) of the GALEX database for a total of 30 out of the 36 galaxies of the sample. We used those data with an exposure time of 1500s. Both the FUV and NUV fluxes were determined for the 30 galaxies from the integrated flux provided by the conversion from AB magnitudes: $F_\nu[\text{erg s}^{-1} \text{cm}^{-2} \text{Hz}^{-1}] = 10^{-0.4(m_{AB} + 48.6)}$. Full details of the telescope, instruments, calibration and processing pipeline are provided by Martin et al. (2005) and Morrissey et al. (2005, 2007).

2.2. H II Regions Detection

In order to obtain the SFR, fluxes from the H_α line are needed as well as from the FUV continuum. The simplest approach is to consider the galaxy emission as a whole, e.g. the continuum-subtracted H_α emission. However, as we were interested in a further analysis of the data (such as the luminosity function and the location of the H II regions inside the galaxies) we decided not to use that technique. Instead, we selected the H II regions from the continuum-subtracted H_α images. Only those regions identified by two of us were included in the sample. A circular aperture centered on each region was used to determine the flux. Two different radii were considered for each H II region. The first one included all the emission of the region and the second one included only the emission with flux values larger than a limiting value, in order to distinguish between proper H II regions and DIG. As will be discussed in § 6, this limiting flux has been determined by spectroscopic studies and is of 10^{-17} erg s $^{-1}$ cm $^{-2}$. This procedure was performed manually; the radius aperture just depends on the galaxy distance, which defines the size of the region in the image.

The main disadvantage of this procedure is the difficulty to detect very low luminosity regions. However, as they are very faint, the contribution of their fluxes to the SFR is not significant and will only be important in the study of the luminosity function of the H II regions inside the galaxies.

In the case of galaxies with large inclinations, it is very difficult to distinguish different regions if they are in the same line-of-sight. This is the situation for 7 of the galaxies in our sample, which have inclinations larger than 70°. It can be argued that the in-

TABLE 1
GLOBAL PARAMETERS

Galaxy	Type	α 2000	δ 2000	M_B [mag]	r_{25} [kpc]	D [Mpc]	A_R [mag]	i [$^\circ$]	μ_B [mag/arcsec 2]	M(HI) [$M_\odot * 10^9$]	Σ_{HI} [$M_\odot pc^2$]	$\log(M_{HI}/L_B)$
DDO 18	Sm	02 10 44	06 45 30	-18.37	6.59	20.70	0.13	70	23.8	0.99	5.57	-1.72
UGC 560	Sm	00 54 47	13 39 29	-20.5	10.57	72.70	0.21	24	26.1	–	–	–
UGC 3086	Sm	04 32 55	00 32 12	-16.64	9.75	73.50	0.18	–	–	4.61	12.85	-1.45
UGC 3778	Sm	07 16 55	28 31 46	-17.97	9.57	65.80	0.14	–	–	4.1	11.44	-1.94
UGC 3947	Sm	07 39 02	33 54 59	-17.12	7.41	55.90	0.10	45	24.7	1.35	9.20	-1.94
UGC 3989	Sm	07 44 41	53 50 05	-17.76	11.56	79.50	0.11	0	26.3	–	9.21	–
UGC 4121	Sm	07 58 54	54 02 33	-17.55	6.44	18.90	0.08	72	24.3	1.2	6.69	-1.23
UGC 4797	Sm	09 08 11	05 55 40	-17.41	5.43	19.60	0.10	24	24.2	0.62	–	-1.5
UGC 4837	Sm	09 21 10	35 31 54	-17.50	8.78	28.90	0.06	51	24.5	1.84	14.46	-1.4
UGC 5236	Sm	09 47 00	21 43 47	-20.54	10.00	53.40	0.08	12	25.3	0.03	0.09	-4.92
UGC 6151	Sm	11 05 56	11 49 35	-17.29	6.73	24.30	0.06	45	24.3	0.88	4.74	-1.47
UGC 6205	Sm	11 09 59	46 05 44	-19.58	4.99	27.30	0.04	41	23.7	0.31	3.96	-2.94
UGC 6399	Sm	11 23 23	50 53 34	-18.02	8.13	20.30	0.04	74	23.1	0.69	7.36	-1.71
UGC 8253	Sm	13 10 44	11 42 28	-17.72	11.16	53.10	0.07	17	25.4	2.83	–	-1.82
DDO 36	SBm	05 07 47	-16 17 37	-18.74	8.49	24.90	0.17	54	23.1	–	–	–
NGC 2552	Sm	08 19 20	50 00 35	-19.37	5.14	10.20	0.12	49	23.5	0.74	8.62	-1.63
NGC 4010	SBm	11 58 38	47 15 41	-20.47	11.29	18.20	0.05	79	22.9	2.57	16.1	-2.0
UGC 4871	SBm	09 14 57	39 15 45	-17.79	9.14	37.00	0.03	69	23.7	–	6.18	–
UGC 8385	SBm	13 20 38	09 47 14	-19.70	7.29	22.40	0.05	56	23.7	–	–	–
UGC 10058	SBm	15 50 24	25 55 21	-17.99	5.49	34.4	0.14	42	25.3	–	–	–
UGCA 117	SBm	06 00 35	-28 59 31	-19.53	11.50	30.75	0.08	56	23.0	1.4	11.86	-2.37
UGC 2345	SBm	02 51 53	-01 10 20	-16.23	7.16	14.20	0.19	29	27.0	–	–	–
UGC 3775	dS	07 15 53	12 06 54	-17.34	4.68	29.40	0.24	27	25.3	0.41	5.96	-1.99
UGC 4660	dS	08 54 24	34 33 22	-15.96	5.57	32.60	0.06	21	25.5	1.5	8.52	-0.96
UGC 5296	dS	09 53 11	58 28 42	-16.06	3.02	25.20	0.03	29	24.5	0.29	10.12	-1.5
UGC 5740	dS	10 34 46	50 46 06	-16.63	2.86	11.30	0.05	46	24.6	0.41	6.31	-0.87
UGC 6304	dS	11 17 49	58 21 05	-16.40	4.72	28.90	0.03	39	25.0	–	–	–
UGC 6713	dS	11 44 25	48 50 07	-16.68	3.66	17.00	0.05	44	24.0	0.9	13.78	-0.9
UGC 9018	dS	14 05 33	54 27 40	-14.95	1.59	6.58	0.03	37	23.7	0.13	13.78	-0.23
UGC 9902	dS	15 34 33	15 08 00	-15.93	3.67	27.70	0.13	72	23.5	–	–	–
UGC 9570	dS	14 51 36	58 57 14	-17.46	–	35.50	0.03	–	–	–	–	–
UGC 11820	dS	21 49 28	14 13 52	-15.79	4.96	17.10	0.33	24	25.5	1.54	19.96	-0.32
UGC 12212	dS	22 50 30	29 08 18	-20.77	3.30	19.50	0.17	56	24.1	0.8	23.38	-2.72
UGC 891	dSB	01 21 19	12 24 43	-17.30	3.13	9.40	0.08	63	24.1	0.36	11.70	-1.04
UGC 5242	dSB	09 47 06	00 57 51	-20.57	4.86	26.30	0.34	50	24.0	0.8	10.78	-2.9
UGC 6840	dSB	11 52 07	52 06 29	-16.99	4.60	17.00	0.06	72	22.9	1.04	12.77	-0.97

Some characteristics of the galaxies in the sample are listed. The morphological type is shown in Column 2. The coordinates (2000) are given in Columns 3 and 4. The absolute magnitude and the optical size are given in Columns 5 and 6. The kinematic distance (V_{LG}/H_o) is included in Column 7. A_R extinction is listed in Column 8. The inclination is listed in Column 9. Surface brightness is given in Column 10. The mass of hydrogen gas $M(HI)$ and the mass surface density are given in Columns 11 and 12 respectively, and the mass to luminosity ratio is shown in Column 13.

clusion of such galaxies in our sample is not correct because of the difficulty of an accurate extinction correction. However, most of the classical studies of the SFR in galaxies have included high inclination objects without any further correction (e.g. James et al. 2008; Lee et al. 2009; Hunter et al. 2010; Boselli et al. 2015). In 2018, Wang et al. studied the influence of the inclination on the SFR value and they concluded that the inclination is important only for galaxies more massive than $10^{10}M_\odot$. Moreover, Buat et al. (2009) considered as high inclination galaxies only those with inclinations larger than 80° . Therefore, we included them because all the galaxies in our sample are less massive than $10^{10}M_\odot$

and have inclinations smaller than 80° ; however their SFR values should be considered as upper limits.

A similar problem might appear for those H II regions which are very close and cannot be separated due to the resolution of our observations.

With the knowledge of the positions of the H II regions from the H_α images, the GALEX images were inspected to locate the star forming regions and the fluxes from these locations were calculated.

2.3. Flux Corrections

Before the SFR could be determined, the UV and H_α fluxes need to be corrected for extinction. There are contributions to the extinction (i) from the gas

inside the galaxy (hereafter, the internal extinction), (ii) due to the intergalactic medium, (iii) due to gas inside our own Galaxy, and (iv) due to the atmosphere. The last one was corrected for the standard way. To correct for Galactic extinction we followed Cardelli et al. (1989), using values of R_V from 2.6 to 5.5 (Clayton & Cardelli, 1988) and considering the color excess values from NED.

The most difficult extinction correction is the extinction internal to the galaxy. Since there is no simple way to estimate the extinction coefficient in H_α , $A(H_\alpha)$, this correction is not generally performed. In this article, the determination of the internal extinction coefficient for H_α was computed following Calzetti et al. (2000), where they derived an extinction law $K(\lambda)$ directly from the data in the UV and optical wavelength ranges, as in Calzetti (1997b). As $K(\lambda)$ is related to the internal nebular extinction, the extinction coefficient in H_α can be obtained as:

$$A(H_\alpha) = K(\lambda) \times E(B - V).$$

On the other hand, we followed the formalism of Salim et al (2007) to estimate the extinction coefficient in FUV, A_{FUV} , as

$$A_{\text{FUV}} = \begin{cases} 3.32(m_{\text{FUV}}^0 - m_{\text{NUV}}^0) + 0.22, & \text{if } (m_{\text{FUV}}^0 - m_{\text{NUV}}^0) < 0.95, \\ 3.32, & \text{if } (m_{\text{FUV}}^0 - m_{\text{NUV}}^0) > 0.95, \end{cases}$$

where $m_{\text{FUV}}^0 - m_{\text{NUV}}^0$ is the UV color of the galaxy in the rest-frame system. The corrected fluxes obtained were of the order of 10^{-26} erg cm $^{-2}$ s $^{-1}$ with typical values of A_{FUV} between 0.1 to 2.5 mag.

The internal extinction increased the final fluxes in the galaxies of our sample 15% on average, but the increase was up to 50% for three of the galaxies (UGC 560, UGC 5242, UGC 12212).

Because of the large bandwidth of the filters used in this work (larger than 70 Å), the H_α flux is contaminated with the nitrogen line emission. From our own spectroscopy data of several of the galaxies presented here, the $[NII]/H_\alpha$ ratio is typically smaller than 0.1 (Hidalgo-Gómez et al. 2012). The flux obtained from our images was then corrected by 10% in order to eliminate this contribution.

3. INTEGRATED STAR FORMATION RATES

The star formation rates were determined from the corrected H_α and FUV fluxes using the Kennicutt

(1998) expressions. The total flux is the sum of the fluxes for all the H II regions. Recently, Hunter et al. (2010) obtained a new SFR calibration for low metallicity galaxies. There are differences of about 15% in the SFR values determined with the Hunter or Kennicutt expressions. Although the galaxies in our sample have subsolar metallicity (Hidalgo-Gómez et al., in preparation; Hidalgo-Gómez et al. 2012) we used Kennicutt's because the comparison with previous work is straightforward. The SFR values determined with Hunter et al.'s expressions are listed in Columns 7 (H_α) and 9 (UV) of Table 2 for a quick comparison with the Kennicutt values. The expressions used by Kennicutt (1998) are

$$\text{SFR}[M_\odot \text{ yr}^{-1}] = 9.93 \cdot 10^{-41} F(H_\alpha) \cdot D^2,$$

$$\text{SFR}[M_\odot \text{ yr}^{-1}] = 1.4 \cdot 10^{-28} L_{\text{FUV}}(\text{ergs}^{-1} \text{ Hz}^{-1}).$$

The distance used to determine the luminosities is the so-called kinematic distance, $D = V_{LG}/H_o$, corrected by the Virgo Cluster infall, where H_o is 73 km s $^{-1}$ Mpc $^{-1}$ (Riess et al. 2011).

The SFRs from H_α and FUV for all galaxies, separated by morphological type, as well as the total fluxes and the extinction values for both bands, are shown in Table 2. Two different fluxes were considered for H_α , with and without DIG. The latter values are shown in the last column of Table 2 (see § 6 for details). The errors were determined considering the uncertainties in the distance and the error associated with the flux determination.

3.1. Star Formation Rates of Late-Type Galaxies from H_α Luminosities

From a closer inspection of Column 6 in Table 2, it can be concluded that there are three ranges in the $\text{SFR}(H_\alpha)$ values: galaxies with values larger than $1 M_\odot \text{ yr}^{-1}$ (3 galaxies), those with $\text{SFR}(H_\alpha)$ between 0.1 and $1 M_\odot \text{ yr}^{-1}$ (9 galaxies), and galaxies with values smaller than $0.1 M_\odot \text{ yr}^{-1}$ (24 galaxies). For the galaxy UGC 9902 the SFR is taken as zero because we could not detect any H_α flux in it. The distribution of the $\text{SFR}(H_\alpha)$ values for all the galaxies in the sample is shown in Figure 1 (left). The distribution is not symmetrical, showing a clear asymmetry towards the low SFR values.

The galaxy with the largest $\text{SFR}(H_\alpha)$ value is UGC 560, one of the most distant in our sample, with a SFR similar to that of the Milky Way (MW) ($1.7 M_\odot \text{ yr}^{-1}$, Robitaille & Whitney, 2010) while the one with the smallest SFR is UGC 9018, a dS galaxy which is the nearest, one of the smallest in size, and with very few gas left.

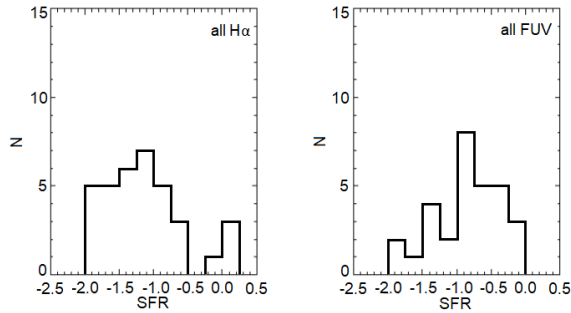


Fig. 1. Star formation rate distributions for all the galaxies in the sample from $H\alpha$ fluxes with DIG (left) and from FUV continuum (right). The range comprised for the $H\alpha$ fluxes is wider than for the FUV, with the bulk of galaxies having SFR below $0.1 M_{\odot} \text{ yr}^{-1}$ for the former and between 1 and 0.1 for the latter.

As can be seen from Figure 2 (left plots), where the distribution for Sm galaxies is shown in the top row while the one for dS galaxies in the bottom row, the former have larger SFR values than the dS galaxies: a factor of 4.7, according to the average values shown in Table 3 (second column). Actually, only one out of 14 dS galaxies has a SFR larger than $0.1 M_{\odot} \text{ yr}^{-1}$. One explanation might be the small number of dS galaxies in our sample. However, they are almost a 40% of the total sample and, therefore, such differences might be due to another reason. We will further discuss this in § 3.6.

3.2. Star Formation Rates of Late-Type Galaxies from the UV Continuum

The most interesting feature of the SFR(FUV) values, listed in Column eighth of Table 2 and shown in Figure 1 (right), is the lack of values larger than $1 M_{\odot} \text{ yr}^{-1}$. The galaxy with the largest value is UGC 5236, an almost face-on Sm galaxy, with $\text{SFR(FUV)} = 0.76 M_{\odot} \text{ yr}^{-1}$. Interestingly, the galaxy with the lowest SFR, UGC 8253, is very similar to UGC 5236 in size, inclination and distance. The SFR distribution is not symmetrical, with a deficit of galaxies with low SFRs.

Twenty one out of 30 galaxies have SFR(FUV) values between 1 and $0.1 M_{\odot} \text{ yr}^{-1}$, (14 Sm and 9 dS) and only 9 galaxies have values lower than $0.1 M_{\odot} \text{ yr}^{-1}$. There are differences of 0.11 between the SFR(FUV) of Sm and dS. Although the distribution has a similar range, as can be seen in Figure 2, Sm galaxies have a peak at $0.1 M_{\odot} \text{ yr}^{-1}$ while dS galaxies have a smooth distribution.

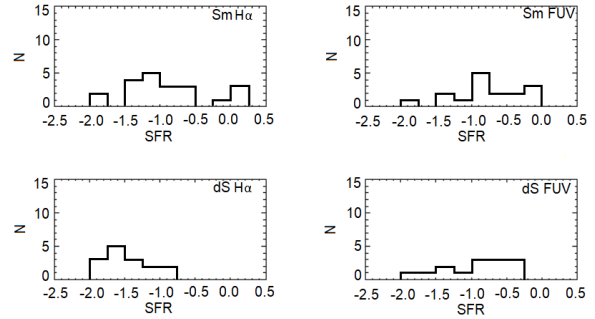


Fig. 2. Star formation rate distribution for the Sm galaxies (upper row) and dS galaxies (bottom row). The left plots show the values from the $H\alpha$ line ($\text{SFR}(H\alpha)_{\text{DIG}}$); the values from the FUV are plotted on the right.

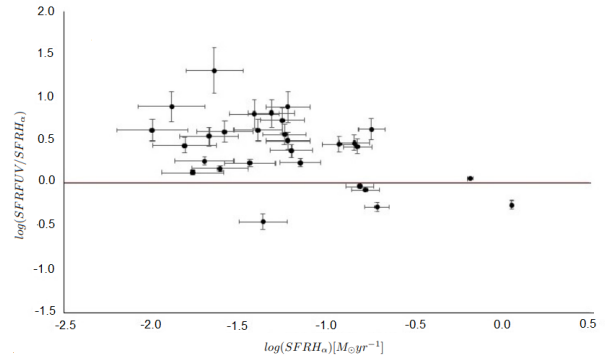


Fig. 3. Ratio of $\text{SFR(FUV)}/\text{SFR}(H\alpha)$ vs. $\text{SFR}(H\alpha)$. The solid line indicates when both values are the same. Most of the galaxies show a positive value for this ratio indicating that the SFR obtained from the UV continuum is larger than the SFR from $H\alpha$ with DIG.

3.3. Comparison Between $\text{SFR}(H\alpha)$ and SFR(UV)

It is well known that SFR(FUV) is larger than the values obtained using the $H\alpha$ luminosity (Bell & Kennicutt, 2001; Lee et al. 2009). The UV emission comes from O and B stars with masses larger than $5 M_{\odot}$, while only stars more massive than $20 M_{\odot}$ can provide the $H\alpha$ emission (Werk et al. 2010). This can be checked in Figure 3, where the $\text{SFR(FUV)}/\text{SFR}(H\alpha)$ ratio vs. the $\text{SFR}(H\alpha)$ values are plotted. Only five galaxies, all of them Sm, are in the negative part of the diagram. The lower the $\text{SFR}(H\alpha)$, the higher the differences between both values. In the earliest stages of the starburst, the emission in $H\alpha$ is higher and both fluxes are similar. At later stages of the star formation events, the differences between the fluxes in FUV and $H\alpha$ become larger as the UV continuum decreases more slowly than $H\alpha$. The main reason for this is that the UV

TABLE 2
 H_α AND FUV STAR FORMATION RATE

Galaxy	$F_{H_\alpha} 10^{-14}$ [erg s ⁻¹ cm ⁻²]	A_{H_α} [mag]	$F_{FUV} 10^{-26}$ [erg s ⁻¹ Hz ⁻¹]	A_{FUV} [mag]	$SFR(H_\alpha)_{DIG}$ [$M_\odot yr^{-1}$] 10^{-2}	$SFR(H_\alpha)_{Hunter}$ [$M_\odot yr^{-1}$] 10^{-2}	$SFR(FUV)$ [$M_\odot yr^{-1}$] 10^{-2}	$SFR(FUV)_{Hunter}$ [$M_\odot yr^{-1}$] 10^{-2}	$SFR(H_\alpha)$ [$M_\odot yr^{-1}$] 10^{-2}
DDO 18	9.12	0.28	0.95	0.78	17±2	14.8	14±2	12.70	3.7±0.5
UGC 560	11.13	0.77	0.10	2.11	113±17	97.78	63±10	57.14	56±8
UGC 3086	19.10	—	—	—	109±5	95.2	—	—	97±3
UGC 3778	6.04	—	—	—	108±16	94.28	—	—	25±3
UGC 3947	1.01	—	—	—	5.8±0.9	5.1	—	—	2.9±0.6
UGC 3989	1.23	0.19	0.43	0.52	66±2	57.6	74±13	67.12	7.3±0.4
UGC 4121	1.19	0.25	0.55	0.69	3.7±0.8	3.2	6.0±1.0	5.44	0.4±0.1
UGC 4797	1.13	0.05	2.33	0.13	4.1±0.7	3.6	17±2	15.42	0.41±0.07
UGC 4837	7.02	0.00	0.72	0.01	19±3	17	10±4	9.07	5.5±0.7
UGC 5236	6.63	0.62	0.33	1.70	18±8	16	76±14	68.93	18±4
UGC 6151	1.20	0.01	1.21	0.03	7.1±0.9	6.2	12±2	10.88	0.67±0.08
UGC 6205	5.23	0.31	0.90	0.85	4±1	3	25±4	22.68	4±1
UGC 6399	0.45	0.04	0.56	0.10	1.5±0.4	1.3	4±1	3.63	0.18±0.04
UGC 8253	1.56	0.03	0.03	0.09	4.3±0.2	3.8	1.5±0.5	1.36	4.2±0.2
DDO 36	21.94	—	—	—	69±10	60	—	—	13±2
NGC 2552	103.89	0.34	9.72	0.92	15±4	13	39±4	35.37	10±3
NGC 4010	1.50	0.42	1.30	1.16	5.8±0.6	5.1	21±6	19.05	0.47±0.07
UGC 4871	1.39	0.00	0.61	0.01	15.4±0.4	13.4	14±2	12.69	1.80±0.05
UGC 8385	8.03	0.39	2.03	1.07	6.0±0.3	5.2	45.7	41.45	3.8±0.3
UGC 10058	0.07	0.60	0.22	0.08	1.5±0.3	1.3	3.7±0.5	3.36	2.5±0.5
UGCA 117	0.54	0.01	1.91	0.04	4.9±0.7	4.3	31±5	28.12	0.49±0.06
UGC 2345	29.73	0.27	5.03	0.73	12±1	10	33±4	29.9	5.7±0.6
UGC 3775	2.88	0.16	0.69	0.45	6±1	5	15±2	13.6	2.3±0.9
UGC 4660	4.24	—	—	—	6±1	5	—	—	4.3±0.6
UGC 5296	2.56	—	—	—	2.3±0.2	2.0	—	—	1.5±0.1
UGC 5740	4.05	0.31	1.57	0.86	2.1±0.3	1.8	7±1	6.35	0.49±0.06
UGC 6304	3.74	0.01	2.06	0.04	5.6±0.1	4.9	30±4	27.21	2.95±0.07
UGC 6713	4.47	0.09	1.65	0.25	1.3±0.3	1.1	10±4	9.07	1.2±0.3
UGC 9018	7.72	0.02	5.52	0.05	1.0±0.1	0.9	4.2±0.6	3.81	0.32±0.04
UGC 9902	0.00	0.01	0.13	0.02	0.00	0.00	1.7±0.3	1.54	0.00
UGC 9570	0.19	0.15	1.52	0.40	2.3±0.1	2.0	46±6	41.72	0.23±0.01
UGC 11820	5.30	0.02	0.45	0.05	1.7±0.4	1.5	2.3	2.09	1.5±0.3
UGC 12212	20.23	0.91	0.67	2.50	14±2	12	42±6	38.1	7.3±0.9
UGC 891	8.27	0.41	2.51	1.12	2.6±0.4	2.3	10±1	9.07	0.70±0.3
UGC 5242	2.97	0.76	0.24	2.07	6.0±0.8	5.2	19±3	17.23	1.9±0.2
UGC 6840	2.79	0.01	0.74	0.02	2.01±0.02	1.75	4±2	3.63	0.76±0.02

The H_α and FUV fluxes are given in Columns 2 and 4. The internal dust extinction A_{H_α} and A_{FUV} are listed in Columns 3 and 5. The $SFR(H_\alpha)$ with DIG, and the $SFR(H_\alpha)$ obtained from the Hunter et al. calibration are shown in Columns 6 and 7. The $SFR(FUV)$ from the Kennicutt and Hunter et al. calibrations are listed in Columns 8 and 9, respectively, and the $SFR(H_\alpha)$ without DIG are shown in Column 10.

photons originate from a wider range of stars with longer lifetimes on the main sequence (e.g. Sullivan et al. 2004; Iglesias-Páramo et al. 2004).

The values of Table 3 show that the average star formation rates from H_α and FUV are very similar for the sample as a whole, as well as for the Sm galaxies, and there are only large differences for dS galaxies (a factor of 2.7). One explanation might be that the star formation event is older in the latter galaxies; therefore, all the massive stars which can ionize hydrogen have disappeared already, and the H_α flux is quite low. However, there are still a lot of less massive stars which can emit at FUV wavelengths, hence the large value of the $SFR(FUV)$.

3.4. Bars and Star Formation Rates

It has been suggested that strong barred galaxies have larger SFRs (e.g. Sérsic & Pastoriza 1967; Ho et al. 1997; Tsai et al. 2013). However, other authors proposed that bars may decrease the SFR of a galaxy (e.g. Tubbs 1982; Kim et al. 2018). Kim et al. (2017), using a large sample of galaxies from

TABLE 3
 AVERAGED STAR FORMATION RATE

	H_α	σ	Without DIG	σ	FUV	σ
All	0.19	0.2	0.08	0.3	0.23	0.3
All Sm	0.28	0.4	0.12	0.2	0.27	0.4
All dS	0.06	0.05	0.02	0.03	0.16	0.2
Barred	0.12	0.2	0.03	0.2	0.20	0.5
non-barred	0.22	0.4	0.10	0.4	0.24	0.2
Barred Sm	0.17	0.2	0.04	0.05	0.25	0.6
non-barred Sm	0.33	0.4	0.16	0.3	0.28	0.3
Barred dS	0.03	0.03	0.01	0.01	0.11	0.2
non-barred dS	0.04	0.05	0.02	0.4	0.18	0.2

Averaged star formation rate from the H_α line (left columns), the H_α emission from the HII region only, (middle columns) and from the FUV continuum (right columns). The total sample was divided into several samples: Sm and dS (upper rows), barred and non-barred galaxies (middle rows), and barred/non barred Sm and dS (bottom rows). Two things can be noted from this table: the non-barred galaxies always have larger SFR compared to the barred galaxies, and Sm galaxies have SFR larger than dwarf galaxies.

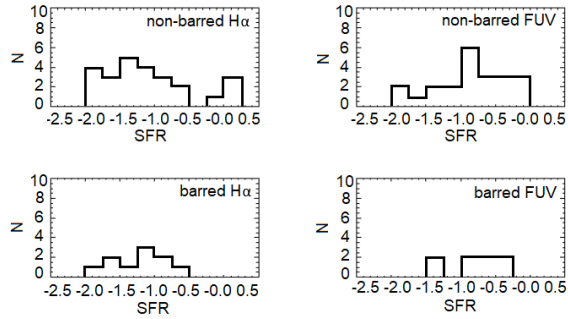


Fig. 4. Star formation rate distribution for barred (bottom row) and non-barred galaxies (top row) in the sample. The left plots show the SFR determined with the H_α luminosity while the right plots show the distribution of the SFR determined with the FUV continuum. Non-barred galaxies have, on average, larger Star Formation Rates.

SDSS, found out that barred galaxies have significantly lower star formation activity than their unbarred counterparts. Ryder & Dopita (1994) stated that the effect of the bar in the star formation rate is not important. Therefore, the problem is far from being settled yet.

We analyzed the effect of the existence of bars in the SFR of our sample. Barred galaxies represent 28% of the galaxies in our sample; therefore, the results are significant. Figure 4 shows the distribution of the SFR for barred and non-barred galaxies, with the average values presented in Table 3. Non-barred galaxies have larger SFR than barred ones from H_α values, while the SFR is similar when determined with FUV fluxes. However, the distributions are very different in both cases. Barred galaxies have a small range of SFR, with no large values (neither from H_α nor from FUV). The distribution of barred galaxies with FUV values is flat. From our sample it can be concluded that barred galaxies have a lower SFR than non-barred ones.

How can this influence the lower values of SFR for dS? Actually, the number of barred dS galaxies is small, only three out of 14; therefore, the results cannot be conclusive. However, there are no differences in $SFR(H_\alpha)$ while the differences increase for $SFR(FUV)$. So, the small SFR for dS galaxies must be due to another reason.

3.5. Comparison with Previous Results

There are several studies of SFR involving late-type galaxies that use different diagnostic methods (e.g. Hunter & Elmegreen 2004; Hunter et al. 2010;

Rosenberg et al. 2008; Lee et al. 2009; Buat et al. 2009; Boselli et al. 2015; Boselli et al. 2009; James et al. 2008; Almozni & Broch, 1996). In general, Sm galaxies have higher values than Im galaxies in all these investigations, with the values for the Im being closer to the SFR of our dS galaxies. On average, the SFR values reported for Sm galaxies are very similar to those we determined when extinction is considered. This is particularly important for the $SFR(FUV)$, because the extinction is larger than in the optical range. This might be the main reason for the differences between our $SFR(FUV)$ values and those reported by Lee et al. (2009) and Hunter & Elmegreen (2004), with the latter authors using the color excess and the extinction law of Cardelli et al. (1989) and the former ones using the Balmer decrement to determine the internal extinction. Therefore, our values are between two to five times larger than theirs.

Concerning the comparison between the $SFR(H_\alpha)$ and $SFR(FUV)$, our results are similar to other investigations, the $SFR(FUV)$ being higher than the $SFR(H_\alpha)$, except for the KISS sample by Rosenberg et al. (2008), where at least 8 out of 19 galaxies have lower $SFR(FUV)$.

Eleven of the galaxies studied here have SFR values previously determined from H_α emission (Hunter & Elmegreen, 2004; James et al. 2004; Lee et al. 2009; Van Zee, 2001), and four have previous FUV emission determinations (Hunter & Elmegreen, 2010; Lee et al. 2009). Six of the values for $SFR(H_\alpha)$ are identical to our values, while another five are similar when the uncertainties are considered. The most discordant $SFR(H_\alpha)$ values are for UGC 9018, UGC 8385, DDO 18 and James et al.'s value for UGC 11820. There are several reasons for such differences, among others: the use of different distances or differences in the internal extinction. For example, James et al. (2004) adopted a constant value of 1.1 mag for the extinction of all their galaxies, regardless of their morphological type or inclinations. This value is higher than the extinction we reported in our § 3. Also, different number of H II regions detected might change the value of the SFR, as in UGC 11820, where in a previous work up to 40 H II regions were considered, and a SFR of $2.9 \cdot 10^{-2} M_\odot \text{ yr}^{-1}$ (Reyes-Pérez, 2009) was reported.

3.6. Star Formation Efficiency

Galaxies with distinct spiral arms, like Sc type, have larger SFR due to the fact that they have a large amount of gas and a prominent density wave (Ken-

nicutt, 1998). Late-type galaxies (Sm, Im and dS) have, in general, smaller values of the SFR despite their large amount of gas. However, when the SFR surface density is considered, galaxies behave very differently. Hunter & Elmegreen (2004), using a sample of Sm, Im and blue compact dwarf galaxies (BCD), found out that the latter were the galaxies with the largest SFR surface densities (see their Figure 5). A similar result is found here, using the optical radius instead of the disk scale length in V which, according to Hunter & Elmegreen (2004), makes no difference for SFR surface densities lower than $0.05 M_{\odot} \text{ yr}^{-1} \text{ kpc}^{-2}$. The SFR surface density for dS galaxies is larger (with an average value of $1.6 \times 10^{-4} M_{\odot} \text{ yr}^{-1} \text{ kpc}^{-2}$) than that of Sm galaxies (on average $7.7 \times 10^{-5} M_{\odot} \text{ yr}^{-1} \text{ kpc}^{-2}$). So, dS are forming a larger number of stars per area than Sm, despite the fact that the latter on average have twice more gas mass than dS ($12.5 M_{\odot} \text{ yr}^{-1}$ in dS vs. $8.5 M_{\odot} \text{ yr}^{-1}$ in Sm).

In order to study this effect, the well-known Kennicutt-Schmidt law is applied to our data and is presented in Figure 5 for both H_{α} (top) and FUV (bottom). As no information is available on the amount of molecular gas in these galaxies, the gas density was determined as $1.3 \times \Sigma(HI)$, the ratio between the HI and the molecular gas being constant (Leroy et al. 2005; Saintonge et al. 2011). We plot the efficiency lines (defined as the ratio between the SFR and the gas mass) at 1, 10 and 100%, as in Kennicutt (1998). From the results of Figure 5, it cannot be concluded that dS are more efficient forming stars than Sm, or vice versa. Most of the galaxies in the sample are near the 10% efficiency line for both calibrators, although FUV values are located mostly between the 10% and 100% lines, while there are H_{α} galaxies between the 1% and 10% lines. The galaxies UGC 3086 and UGC 3778 seem to be very efficient, close to the 100% efficiency line.

If the figure were divided into three different regions according to the efficiency, the number of Sm and dS galaxies would be very similar in all regions, but at intermediate/lower efficiency the Sm type would be slightly more numerous.

The larger amount of gas in Sm with a similar HI mass might indicate that they will form stars for a longer time than dS, or that they have started to form stars more recently than dS, but we do not have yet enough information to discriminate between these options.

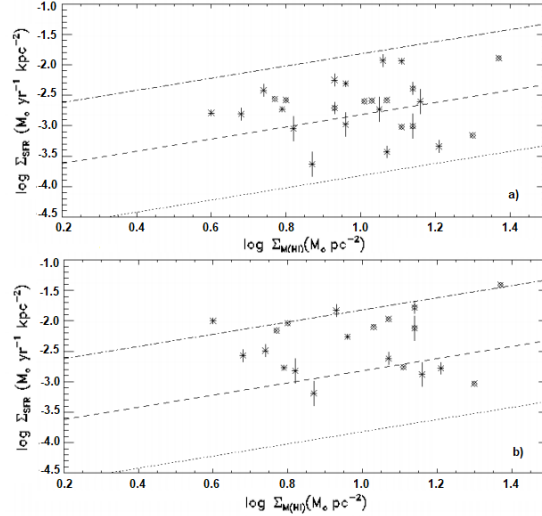


Fig. 5. Correlation between the SFR surface density and the average surface densities of H_I . The dashed lines correspond to constant global star formation efficiencies (1, 10, 100%) from Kennicutt (1998). The Sm and dS galaxies are shown with different symbols (stars and diamonds, respectively). The graph at the top shows the KS law when the star formation was determined from the H_{α} luminosity, while the one at the bottom shows the star formation determined with the FUV continuum.

4. SPATIAL DISTRIBUTION OF THE STAR FORMATION

The spatial distribution of the H II regions inside late-type galaxies was studied in previous investigations (e.g. Hodge 1969; Hunter & Gallagher 1986; Brosch et al. 1998; Sánchez & Alfaro 2008). Roye & Hunter (2000) concluded that, in irregular galaxies, the distribution of H II regions is mostly random, although the majority of the regions are concentrated in the central part of the galaxy. This is very similar to the previous results of Hodge (1969) and Brosch et al. (1998) who obtained a global asymmetry in the locations of the H II regions, with a concentration towards the center of the galaxies. On the contrary, Hunter (1982) found a random distribution of H II regions in late-type galaxies, with the exception of a few chains. Elmegreen & Elmegreen (1980) found that the largest H II regions in barred galaxies were located at the end of the bar. A study of the distribution of the H II regions within galaxies in our sample might help shed some light on the previous discussion. Moreover, the locations of the H II regions inside a galaxy might give information about possible previous interactions between galaxies.

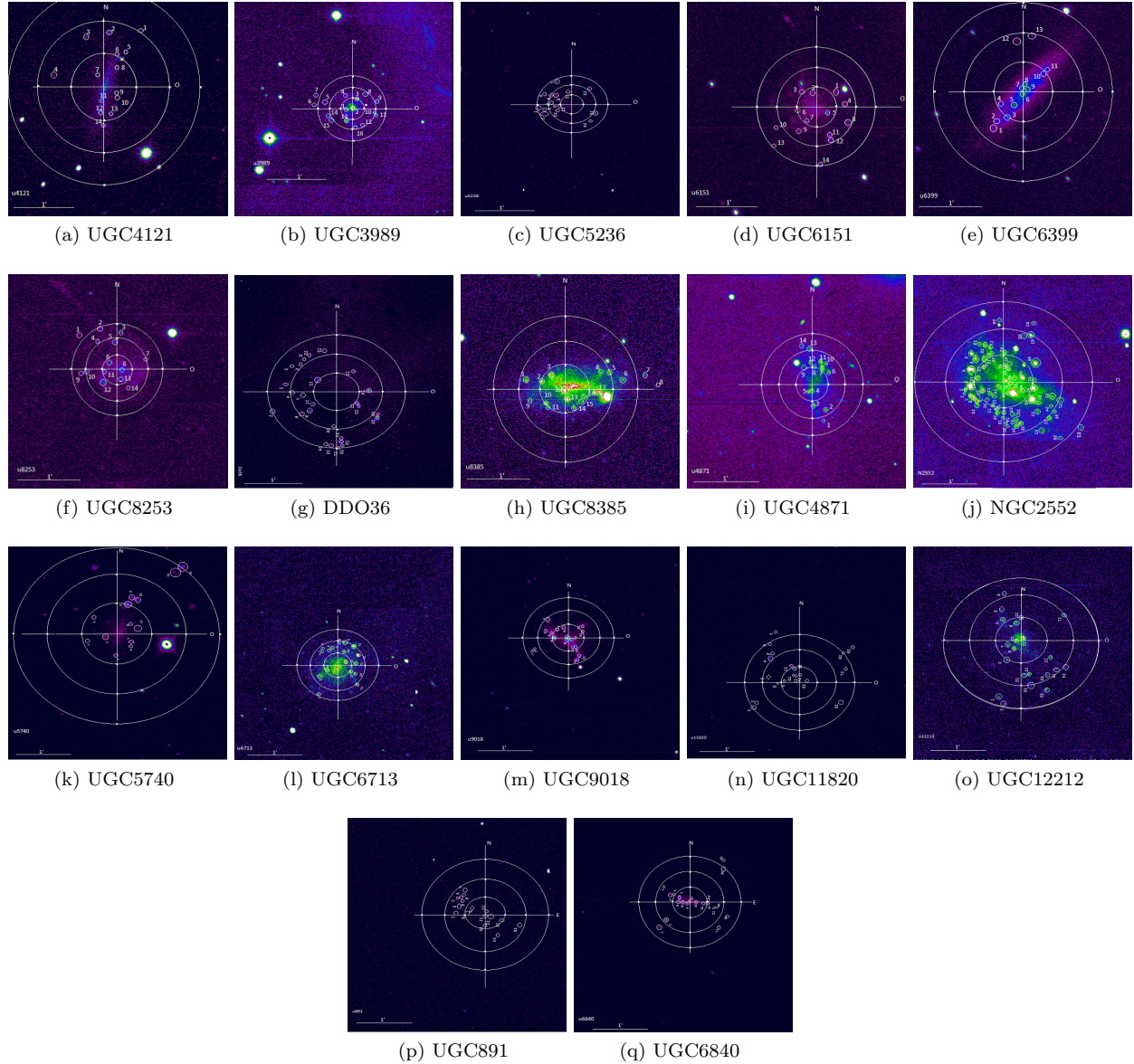


Fig. 6. H_{α} Images of those galaxies with a large number of H II regions. To study the spacial distribution of the H II regions we divided the galaxy into three concentric regions, which are marked with circles in the figures: inner, middle and outer regions, each representing 1/3 of the optical radius. The color figure can be viewed online.

In order to study if there is any particular distribution in the locations of the H II regions for the galaxies of our sample, we selected those galaxies with more than 10 H II regions (17 galaxies, 10 Sm and 7 dS) and inclinations lower than 70° to avoid problems of resolution and projection. From a quick inspection of the images (H_{α} shown in Figure 6 and broadband images not shown here) it can be concluded that only DDO 36, NGC 2552, UGC 6151 and UGC 6713 might have spiral arms, because the

H II regions are strongly aligned along the structure of the galaxy. The regions inside UGC 6399 and UGC 891 are also aligned along the major axis, but as these galaxies have large inclinations, it might be just a projection effect. For the other 11 galaxies, the H II regions are randomly distributed.

4.1. Concentration Parameter

One parameter that can give us important information about the distribution of the star formation

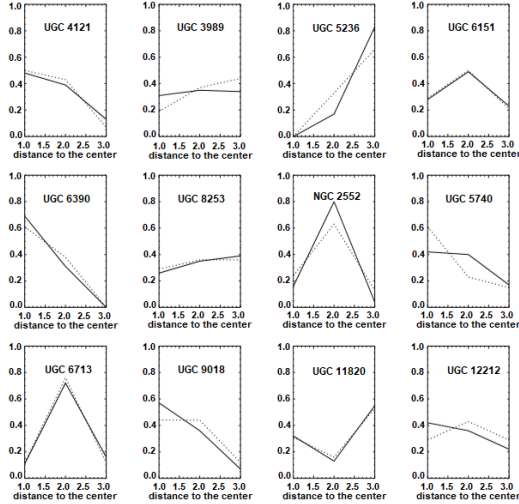


Fig. 7. Distribution of the number of H II regions (solid line) and their fluxes (dotted lines) along the distance to the center of the regions, for the non-barred galaxies. The y axis is the normalized number of H II regions (solid) or flux (dotted) of the galaxy and the x axis is the location of the galaxy in the any of the three regions we divided the galaxies into: inner, middle and outer part. Each galaxy has a different trend: some galaxies have more regions in the inner part, some others in the outer and some others in the middle. UGC 3989 has its star-forming regions quite homogeneously distributed along the radius, but the flux increases towards the edge. For most of the galaxies, the number of regions and the associated fluxes mimic each other.

within galaxies is the concentration index (hereafter CI_n), which is defined as the ratio between the number of H II regions in the inner part and outer part of the galaxy (Roye & Hunter 2000). With this definition of the CI_n , a value of 0 means that all H II regions are in the outer part of the galaxy, and the larger the CI_n the more concentrated towards the center the regions are. In the determination of the CI_n for the 17 galaxies selected before, we follow Roye & Hunter (2000); the values are listed in Column 2 of Table 4. All the galaxies have CI_n s larger than 1, and four of them have CI_n values larger than 10, indicating a large concentration of the regions towards the center. Only six of the galaxies have CI_n values smaller than 4, so their H II regions are located mostly outside the inner part. In general, it can be said that the galaxies in this subsample do not have their H II regions in their outskirts.

Another CI (hereafter, CI_f) can be defined using the flux of the H II regions (F_{in}/F_{out}) instead of the number of them. This is presented in Column 3 of Table 4. Again, large values of CI_f indicate a large amount of flux towards the center, and small values indicate a large amount of flux from the outer regions. Eight of the galaxies have CI_f smaller than 4; therefore their flux comes mostly from the outskirts. On the contrary, five galaxies have a strong luminosity from their center.

The most interesting result emerges when we compare both CI s. One might think that their values should be similar, e.g. if a galaxy has most of its H II regions in the inner part, then most of the flux of the galaxy (in H_α) should come from it as well. Thereupon, it could be said that the galaxy is “well balanced”: there is more flux because there are more H II regions. Such comparison can be done using Columns 2 and 3 of Table 4. Half of the sample has similar values of both concentration index. However, there are three galaxies (UGC 4121, UGC 6151, and UGC 6840) with much higher values of their CI_n (a factor 1.5 or larger) than the CI_f . Therefore these galaxies have a large number of regions inside their central region, but they are not very luminous. On the contrary, four of the galaxies in the sample (24 %) have a CI_f much larger than the CI_n , indicating that, despite being fewer in number, the regions in the center of the galaxy are brighter than those in the outskirts.

It can be concluded that the galaxies in this subsample have a larger number of H II regions in the inner half of the galaxy, and they are also more luminous than the regions in the outer half of the galaxy. However, this is intriguing because in a visual inspection of the galaxies (see Figure 6), the large number of the central H II regions and their dominance of the luminosity is not clear. Therefore, we divided the galaxy into three concentric regions: the inner region with a radius of 1/3 of the total optical radius, the middle region, a torus between 1/3 and 2/3 of the r_{25} , and the outer region, from there up to the optical radius. They are marked with circles in Figure 6. The number of H II regions inside each of these regions, as well as their total flux, are listed in Table 4, Columns 4 to 15. There is no clear pattern, as can be seen in Figures 7 and 8, where the profiles of the number of H II regions (solid line) and the flux (dotted line), both normalized to the total number of regions (or flux) for each galaxy, are shown. The most peculiar profile might be the one of UGC 6840, with fewer regions in the inner annulus, dropping toward the middle section and increasing dramati-

TABLE 4
DISTRIBUTION OF THE STAR FORMATION WITH RADIUS

Galaxy	CI_n CI_f		Inner				Middle				Outer			
	n	%n	n	%n	$F_{H\alpha} 10^{-14}$ [erg s ⁻¹ cm ⁻²]	%F	n	%n	$F_{H\alpha} 10^{-14}$ [erg s ⁻¹ cm ⁻²]	%F	n	%n	$F_{H\alpha} 10^{-14}$ [erg s ⁻¹ cm ⁻²]	%F
UGC4121	10.0	6.6	7	50.0	0.60	48.0	6	42.9	0.49	39.2	1	7.1	0.16	12.8
UGC3989	2.0	3.8	3	18.8	0.37	31.1	6	37.5	0.42	35.3	7	43.7	0.40	33.6
UGC5236	1.5	0.7	0	0.0	0.00	0.0	5	33.3	1.11	16.7	10	66.7	5.52	83.3
UGC6151	7.2	1.7	4	28.6	0.34	28.0	7	50.0	0.59	48.9	3	21.4	0.28	23.1
UGC6399	13.3	14.6	8	61.5	0.31	68.9	5	38.5	0.14	31.1	0	0.0	0.00	0.0
UGC8253	3.0	2.9	4	28.6	0.41	26.1	5	35.7	0.55	35.0	5	35.7	0.61	38.9
DDO36	4.0	3.0	0	0.0	0.00	0.0	11	42.3	1.05	47.9	15	57.7	1.14	52.1
NGC2552	8.8	21.4	15	23.8	15.97	15.7	40	63.5	81.43	80.2	8	12.7	4.18	4.1
UGC8385	5.1	9.0	8	47.1	5.25	62.9	5	29.4	1.53	18.3	4	23.5	1.57	18.8
UGC4871	10.0	13.0	2	14.3	0.17	12.2	9	64.3	1.02	73.4	3	21.4	0.20	14.4
UGC5740	9.0	7.7	8	61.5	1.72	42.5	3	23.1	1.63	40.2	2	15.4	0.70	17.3
UGC6713	3.6	3.0	2	11.8	0.49	11.0	13	76.4	3.24	72.5	2	11.8	0.74	16.5
UGC9018	8.8	19.2	7	43.8	3.24	56.6	7	43.8	2.06	36.1	2	12.5	0.42	7.3
UGC11820	2.9	2.9	6	31.6	1.71	32.3	3	15.8	0.67	12.6	10	52.6	2.92	55.1
UGC12212	3.0	4.5	6	28.6	8.47	41.9	9	42.8	7.21	35.6	6	28.6	4.55	22.5
UGC891	17.3	25.2	7	43.8	3.58	43.3	9	56.2	4.69	56.7	0	0.0	0.00	0.0
UGC6840	6.0	0.63	7	35.0	0.26	9.2	8	40.0	0.15	5.3	5	25.0	2.41	85.5

Galaxy name in Column 1. In Columns 2 and 3, the concentration rates are listed by number (CI_n) and by flux (CI_f), respectively. Columns 4 and 5 list the number of H II regions and their percentages. Columns 6 and 7 contain the total $H\alpha$ flux of these regions, and their percentage, within the innermost section of the galaxy. This section corresponds to a disk with a radius equal to one-third of R_{25} . Columns 8 and 9 display the number of H II regions and their percentage. Columns 10 and 11 list the total $H\alpha$ flux within the middle section of the galaxy and the corresponding percentage. This section corresponds to a ring with an outer radius equal to two-thirds to R_{25} . Columns 12 and 13 show the number of H II regions and their percentage. Columns 14 and 15 list the total $H\alpha$ flux within the outer section of the galaxy, and their percentage. This section corresponds to a torus with an outer radius equal to R_{25} .

cally at the outer part of the galaxy. Moreover, this galaxy, along with UGC 3989, has the largest differences between the number and the flux distribution. Regarding the non barred galaxies, four out of 12 have the number and the flux of their H II regions concentrated in one of the annuli of the galaxy, while for other four the distribution is very uniform along the galactocentric distance. Four of the five barred galaxies have a large number of H II regions in the middle part of the galaxy. These results do not support the idea that bars inhibit the star formation in the central part (e.g. James & Percival, 2018; Tubbs 1982; Kim et al. 2018) because only DDO 36 has fewer regions inside its central annulus. It is interesting to note that all galaxies with a clear spiral structure have all –or almost all of their star formation regions concentrated in the middle and outer sectors of the galaxy, following the spiral arms. On the other hand, the regions of star formation in galaxies without, or with a not-so-well defined spiral structure, do not show any special distribution.

From these figures and the values in Table 4 it can be concluded that the H II regions of the galaxies in our sample show a variety of distributions, more

similar to a random behavior than to a clear pattern, as observed in spiral galaxies.

4.2. Asymmetry of the H II Region Distribution

In a recent study of the dwarf, interacting spiral galaxy IC 1727, it was found that the largest and brightest of its H II regions are facing the companion galaxy, NGC 672 (Ramirez-Ballinas & Hidalgo-Gómez 2014). We aim to check if the H II regions are located in a particular zone in the galaxy, because such an accumulation of the star formation in one particular direction might indicate an interaction. There are two possible approaches: the asymmetry index AI, (Roye & Hunter, 2000), or a simpler one: to just check if there is any preferred locus of star formation inside each galaxy, dividing these into the four orientations, as was done for IC 1727. We will first consider the latter approach. To proceed, the 17 galaxies studied in the previous subsection were divided into four directions: NE, NW, SE and SW (North is up and East to the left). The values of the number of H II regions and the fluxes for each quadrant are listed in Table 5. Half of the galaxies

TABLE 5
DISTRIBUTION OF STAR FORMATION IN ORIENTATION

Galaxy	NE				NW				SE				SW				AI_n AI_f	
	n	%n	$F_{H\alpha} 10^{-14}$ [erg s ⁻¹ cm ⁻²]	%F	n	%n	$F_{H\alpha} 10^{-14}$ [erg s ⁻¹ cm ⁻²]	%F	n	%n	$F_{H\alpha} 10^{-14}$ [erg s ⁻¹ cm ⁻²]	%F	n	%n	$F_{H\alpha} 10^{-14}$ [erg s ⁻¹ cm ⁻²]	%F		
UGC4121	3	21.4	0.26	21.8	5	35.8	0.46	38.7	3	21.4	0.27	22.7	3	21.4	0.20	16.8	0.75	0.65
UGC3989	4	25.0	0.22	18.6	4	25.0	0.37	31.4	4	25.0	0.37	31.4	4	25.0	0.22	18.6	1.00	0.75
UGC5236	1	6.7	0.24	3.6	6	40.0	2.65	40.0	2	13.3	2.80	42.2	6	40.0	0.94	14.2	0.50	0.85
UGC6151	2	14.3	0.16	13.5	2	14.3	0.18	15.0	5	35.7	0.45	37.4	5	35.7	0.41	34.1	0.56	0.56
UGC6399	2	15.3	0.12	26.0	5	38.5	0.17	37.0	6	46.2	0.17	37.0	0	0.0	0.00	0.0	0.86	0.84
UGC8253	5	35.7	0.53	34.0	2	14.3	0.18	11.5	4	28.6	0.49	31.4	3	21.4	0.36	23.1	0.75	0.65
DDO36	7	26.9	0.44	20.1	2	7.7	0.34	15.5	9	34.6	0.46	21.0	8	30.8	0.95	43.4	1.00	0.90
NGC2552	12	19.0	22.40	22.2	11	17.5	16.46	16.4	17	27.0	31.15	31.0	23	36.5	30.58	30.4	0.98	0.98
UGC8385	3	17.6	0.76	9.1	5	29.5	1.89	22.6	4	23.5	1.18	14.1	5	29.4	4.52	54.2	0.89	0.46
UGC4871	4	28.6	0.26	18.7	5	35.7	0.62	44.6	2	14.3	0.17	12.2	3	21.4	0.34	24.5	0.56	0.57
UGC5740	1	7.7	0.23	5.7	7	53.8	2.75	67.9	3	23.1	0.53	13.1	2	15.4	0.54	13.3	0.86	0.87
UGC6713	4	23.6	0.41	9.2	7	41.2	2.59	57.9	3	17.6	0.41	9.2	3	17.6	1.06	23.7	0.70	0.55
UGC9018	5	31.3	1.20	20.9	2	12.4	0.45	7.9	4	25.0	1.73	30.2	5	31.3	2.35	41.0	0.78	0.57
UGC11820	5	26.3	1.58	30.2	10	52.6	2.72	52.0	1	5.3	0.21	4.0	3	15.8	0.72	13.8	0.90	0.73
UGC12212	5	23.8	4.56	22.3	2	9.5	3.36	16.5	6	28.6	6.01	29.5	8	38.1	6.46	31.7	0.91	0.88
UGC891	9	56.2	5.14	62.1	1	6.3	0.00	0.0	1	6.3	1.22	14.8	5	31.2	1.91	23.1	0.78	0.52
UGC6840	7	35.0	0.24	8.6	3	15.0	0.02	0.7	3	15.0	0.07	2.5	7	35.0	2.46	88.2	1.00	0.12

Galaxy name in Column 1. Columns 2 and 3 list the number of H II regions within the northeastern quadrant (NE) and their percentage. Column 4 shows the total $H\alpha$ flux of these regions, its percentage is listed in Column 5. In the same way, the number of H II regions (n), the corresponding percentage (%n), the total $H\alpha$ flux of these regions and its percentage (%F), are presented for the quadrants northwest (NW), southeast (SE) and southwest (SW). The asymmetry indices by number (AI_n) and by flux (AI_f) are shown in Columns 18 and 19.

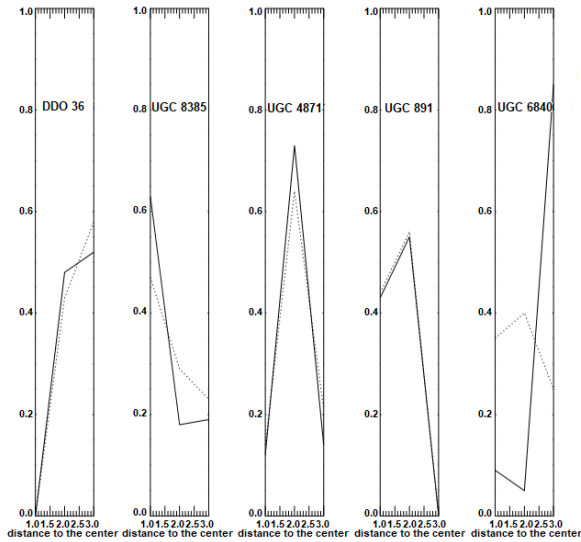


Fig. 8. Distribution of number of H II regions (solid line) and their fluxes (dotted line) along the radius for barred galaxies. Only two of them have most of their regions and flux in the middle part of the galaxy, where the bar is expected to end, and to have an important influence on the star formation. Axis as in Figure 7. From left to right the galaxies are: DDO 36, UGC 8385, UGC 4871, UGC 891 and UGC 6840.

in the sample have a quadrant (or two) with a meaningful increase in the number of H II regions (larger than 35%). This might indicate a previous interaction. Moreover, two of them, both barred galaxies, have the majority of regions in opposite quadrants, while another four galaxies have them in adjacent quadrants. A likely explanation might be that star formation is due to gas coming out along the bar, as seen in other galaxies (Sérsic & Pastoriza 1967 ; Ho et al. 1997).

The asymmetry index, based on the number of H II regions (AI_n), is defined as the ratio between the number of regions in the poorest side and the richest side. An AI by number (or by flux, see below) equal to one means that the galaxy is perfectly symmetric along that axis (major or minor axis), that is, we have the same number of H II regions on both sides. On the contrary, an AI of 0 means that all H II regions are concentrated on only one side of the galaxy. We used our images in V and R to determine the major and minor axes and counted the number of H II regions on each side of the axes. We decided to proceed as in Roye & Hunter (2000), where they a posteriori chose the axis (major or minor) with the largest symmetry. The AI_n values are shown in Column 18 of Table 5. We found that 80% of the

galaxies in the sample have an $AI_n \geq 0.75$ and three of them are perfectly symmetric ($AI_n = 1$).

As previously done with CI , an asymmetry index based on the flux can be determined as the ratio between the flux of all the regions on one side and the flux on the other side (AI_f). This index is shown in Column 19 of Table 5. Again, our galaxies appear to be very symmetric: only two of them have $AI_f < 0.5$. According to the AI , most of the galaxies in our sample are predominantly symmetric in both the distribution of the H II regions, and their luminosity.

5. IS A STARBURST ALWAYS A STARBURST?

Several authors (e.g. Kennicutt 1998; Lee et al. 2009; Gilbank et al. 2010) claimed that the H_α photons from outside the H II regions, the so-called diffuse ionized gas (hereafter DIG), can also be used in the SFR determination because this gas is ionized by photons created by OB stars and they are emerging from the H II regions, since the nebulae are density bounded instead of radiation bounded. However, this is not always the case. There are many other processes which can ionize this gas, which are not related to young stellar population, such as shock waves (Rand 1998), turbulent mixing layers (Slavin et al. 1993), hot low-mass evolved stars (Flores-Fajardo et al. 2011), and radiation from WR stars (Hidalgo-Gómez 2005).

It is not easy to know which is the most important ionizing source for a particular galaxy and how much of the H_α luminosity comes from each of the sources using only H_α images. If other processes are at work for the ionization of the DIG, the SFR might be overestimated for those galaxies with a large amount of DIG. One example might be the irregular dwarf galaxy IC 10, which is considered to be a starburst galaxy based on its color (Richer et al. 2001), the high content of WR stars (Massey & Holmes 2002) and the large number of H II regions (Hodge & Lee 1990), with a SFR of about $1 M_\odot \text{ yr}^{-1}$ (Zucker 2005). However, there is a strong emission from the DIG inside this galaxy, and up to 50% of this DIG is ionized by sources other than leaked photons (Hidalgo-Gómez 2005). Therefore, IC 10 might not be considered as a starburst galaxy (Hidalgo-Gómez & Magaña-Serrano 2017). The inclusion of the DIG within the H_α luminosity used in the SFR should overestimate the values and it can be risky, unless it is well known that leaked photons are the only source responsible for the ionization of this gas.

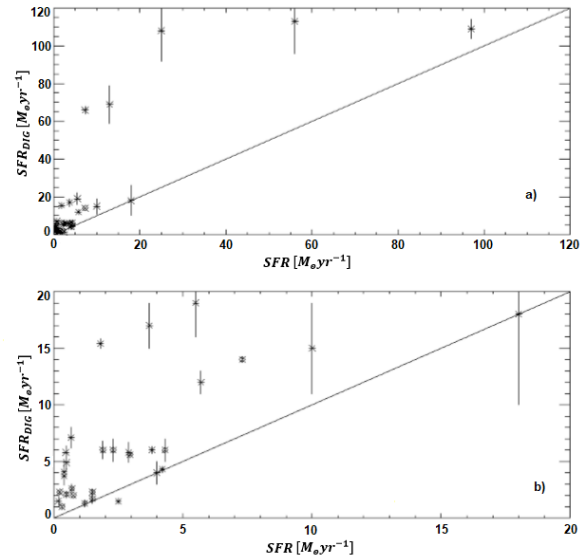


Fig. 9. Comparison of the SFR values when all the H_α photons are considered and when a limiting flux in H_α is considered. Bottom panel is a zoom to the lowest flux galaxies.

Unfortunately, the amount of DIG cannot be known in advance for a particular galaxy. Then, we decided to use previous studies on the DIG in late-type galaxies (e.g. Hidalgo-Gómez 2006; Hidalgo-Gómez, 2007; Hidalgo-Gómez 2005; Hidalgo-Gómez & Peimbert 2007) to determine the boundary flux between an H II region and the DIG. We estimate this flux to be of the order of $10^{-17} \text{ erg cm}^{-2} \text{ s}^{-1}$. Then, we extracted the part of the H_α emission with fluxes larger than this value and a new SFR was determined from the new luminosities. The results are listed in Column 10 of Table 3. A quick comparison can be done between Columns 6 and 10 and it is shown in Figure 9. The number of galaxies with differences in the SFR when DIG is not included is quite large. For a total of 21 out of 36 galaxies in the sample, the SFR without the DIG is 50% lower than with it. There is no real differences between Sm (64%) and dS (53%). For seven of these galaxies the differences in the SFR with and without DIG amount to 90%. Probably, as these are late-type galaxies with a large amount of gas, the contribution of the gas between the H II regions to the star formation rate is larger and, before including it in the calculation, a careful study on the ionization source of such gas should be done.

6. CONCLUSIONS

In this work, the star formation rates for a sample of late-type galaxies, Sm and dwarf spirals, have been determined. It is the first estimation of the star formation rate for more than half of the sample considered here. The SFR were determined using the H_α flux for 36 galaxies and the FUV flux only for 30 of them. The fluxes used, both H_α and FUV, were corrected for internal and external extinctions.

The bulk of the galaxies in our sample have SFRs lower than $0.1M_\odot \text{ yr}^{-1}$ for both diagnostic methods. These values are common for late-type galaxies. It is interesting to notice that SFR(FUV) is normally larger than the SFR determined with H_α . However, the largest SFRs were obtained from the H_α luminosities.

We also noticed a difference in the SFR between Sm and dS galaxies in the sense that the former had higher SFR values than dS with both methods.

If dS galaxies are not only smaller than Sm but a later type of galaxy intermediate between Sm and Irr galaxies, their lower SFR could be explained by an older star formation event for the dS galaxies. However, when the density of SFR (SFR/kpc^2) is considered, both types of galaxies have similar values. These are values similar to those found before (e.g. Hunter & Elmegreen 2004), although the dispersion in our sample is larger.

We studied the role played by the bars as drivers of star formation in late-type galaxies and noticed that non-barred galaxies always have larger SFR than barred ones. Also, we studied the influence of the spiral arms in the SFR and found that, for late-type galaxies, the spiral wave might be not that important, and that other mechanisms might trigger star formation, as in irregular galaxies.

Considering the star formation efficiency, both types of galaxies have a similar efficiency of star formation, despite the greater amount of gas in the Sm and the differences in their gas mass densities.

We also studied the distribution of the H II regions for those galaxies in our sample with the largest number of regions. We used two approaches: the concentration and asymmetry indexes as in Roye & Hunter (2000) and a more detailed distribution with smaller divisions. We concluded that late-type galaxies are very symmetric and have their regions quite concentrated. Moreover, although there is a gradient in the number and the fluxes of H II regions for more than half of the galaxies studied, such gradient is not unique, being positive or negative for some galaxies and even with two slopes in others.

Finally, we noticed that the inclusion of the DIG within the estimation of the H_α luminosity might increase the SFR values more than previously thought. Therefore, the H_α luminosity should not be included unless it is well known that leaking photons from the H II regions are the only source of the ionization.

The authors wish to thank an anonymous referee for comments which improved the manuscript. This investigation was supported by the Instituto Politecnico Nacional (México) under research projects SIP-20196007, SIP-20181188 and SIP-20196007. The authors wish to thank Mr. P. Garcés for his careful revision of the manuscript. Part of this work was done while one of the authors (M.A.M.S) was at ESO/Chile for a short-term visit. This work is part of M. A. Magaña-Serrano's Ph.D. thesis. This research made use of the NASA/IPAC Extragalactic Database (NED) which is operated by the Jet Propulsion Laboratory, California Institute of Technology, under contract with the National Aeronautics and Space Administration. Based upon observations carried out at the Observatorio Astronómico Nacional on the Sierra San Pedro Mártir (OAN-SPM), Baja California, México.

REFERENCES

- Almoznino, E. & Brosch, N. 1996, MNRAS, 31, 29
 Audcent-Ross, F. M., Meurer, G. R., Wong, O. I., et al. 2018, MNRAS, 480, 119
 Bell, E. F. & Kennicutt, R. C. 2001, Galaxy Disks and Disk Galaxies, 230, 305
 Boselli, A., Boissier, S., Cortese, L., et al. 2009, ApJ, 706, 1527
 Boselli, A., Fossati, M., Gavazzi, G., et al. 2015, A&A, 579, A102
 Brosch, N., Heller, A., & Almoznino, E. 1998, MNRAS, 300, 1091
 Buat, V., Takeuchi, T. T., Burgarella, D., Giovannoli, E., & Murata, K. L. 2009, A&A, 507, 693
 Calzetti, D. 1997, AIPC, 408, 403
 ———. 2013, in *Secular Evolution of Galaxies*, (Cambridge, MA: CUP) 419
 Calzetti, D., Armus, L., Bohlin, R. C., et al. 2000, ApJ, 533, 682
 Cardelli, J. A., Clayton, G. C., & Mathis, J. S. 1989, ApJ, 345, 245
 Clayton, G. C. & Cardelli, J. A. 1988, AJ, 96, 695
 Danieli, S., van Dokkum, P., Merritt, A., et al. 2017, ApJ, 837, 136
 Dekel, A. & Silk, J. 1986, ApJ, 303, 39
 D'Ercole, A. & Brighenti, F. 1999, MNRAS, 309, 941
 Elmegreen, D. M. & Elmegreen, B. G. 1980, AJ, 85, 1325
 Flores-Fajardo, N., Morisset, C., Stasińska, G., & Binette, L. 2011, MNRAS, 415, 2182

- Gilbank, D. G., Baldry, I. K., Balogh, M. L. et al. 2010, *MNRAS*, 405, 2594
- Hidalgo-Gómez, A. M. 2004, *RMxAA*, 40, 37
- _____. 2005, *A&A*, 442, 443
- _____. 2007, *AJ*, 134, 1447
- _____. 2006, *AJ*, 131, 2078
- Hidalgo-Gómez, A. M. & Magaña-Serrano, M. A. 2017, *Multi-Scale Star Formation, IRyA-UNAM*
- Hidalgo-Gómez, A. M., Moranchel-Basurto, A., & González-Fajardo, A. F. 2012, *RMxAA*, 48, 183
- Hidalgo-Gómez, A. M. & Olofsson, K. 1998, *A&A*, 334, 45
- Hidalgo-Gómez, A. M. & Peimbert, A. 2007, *AJ*, 133, 1874
- Ho, L., Filippenko, A., & Sargent, W. 1997 *ApJ*, 487, 591
- Hodge, P. W. 1969, *ApJ*, 156, 847
- Hodge, P. & Lee, M. G. 1990, *PASP*, 102, 26
- Huchtmeier, W. K. & Richter, O.-G 1989, *A&A*, 201, 1
- Hunter, D. A. 1982, *ApJ*, 260, 81
- Hunter, D. A. & Elmegreen, B. G. 2004, *AJ*, 128, 2170
- Hunter, D. A., Elmegreen, B. G., & Ludka, B. C. 2010, *AJ*, 139, 447
- Hunter, D. A. & Gallagher, J. S., III 1986, *PASP*, 98, 5
- Iglesias-Páramo, J., Boselli, A., Gavazzi, G., & Zaccardo, A. 2004, *A&A*, 421, 887
- James, P. A. & Percival, S. M. 2018, *MNRAS*, 474, 3101
- James, P. A., Prescott, M., & Baldry, I. K. 2008, *A&A*, 484, 703
- James, P. A., Shane, N. S., Beckman, J. E., et al. 2004, *A&A*, 414, 23
- Jog, C. J. 2013, *MNRAS*, 434, 56
- Karachentsev, I. D. & Kaisina, E. I. 2013, *AJ*, 146, 46
- Kennicutt, R. C., Jr. 1998, *ApJ*, 498, 541
- _____. 1998, *ARA&A*, 36, 189
- Kim, E., Hwang, H. S., Chung, H., et al. 2017, *ApJ*, 845, 93
- Kim, E., Kim, S. S., Choi, Y.-Y. et al. 2018, *MNRAS*, 479, 562
- Lee, J. C., Gil de Paz, A., Tremonti, C., et al. 2009, *ApJ*, 706, 599
- Leroy, A., Bolatto, A. D., Simon, J. D., & Blitz, L. 2005, *ApJ*, 625, 763
- López Fernández, R., González Delgado, R. M., Pérez, E., et al. 2018, *A&A*, 615, 27
- Martin, D. C. & GALEX Science Team. 2005, *BAAS*, 207, 5201
- Melioli, C., Brighenti, F., & D’Ercole, A. 2015, *MNRAS*, 446, 299
- Marzke, R. O. & da Costa, L. N. 1997, *AJ*, 113, 185
- Massey, P. & Holmes, S. 2002, *ApJ*, 580, L35
- Mateo, M. L. 1998, *ARA&A*, 36, 435
- Morrissey, P. & GALEX Science Team. 2005, *BAAS*, 37, 1454
- _____. 2007, *ApJS*, 173, 682
- Pittard J. M. 2019, *MNRAS*, 488, 3376
- Ramirez-Ballinas, I. & Hidalgo-Gómez, A. M. 2014, *MNRAS*, 442, 2282
- Rand, R. J. 1998, *ApJ*, 501, 137
- Reyes-Pérez, J. 2009, *Tasa de Formación Estelar y Funciones de Luminosidad de galaxias enanas*, Tesis de licenciatura, ESFM - IPN
- Richer, M. G., Bullejos, A., Borissova, J., et al. 2001, *A&A*, 370, 34
- Riess, A. G., Macri, L., Casertano, S., et al. 2011, *ApJ*, 730, 119
- Robitaille, T. P. & Whitney, B. A. 2010, *ApJ*, 710, L11
- Rosenberg, J. L., Wu, Y., Le Floch, E., et al. 2008, *ApJ*, 674, 814
- Roye, E. W. & Hunter, D. A. 2000, *AJ*, 119, 1145
- Saintonge, A., Kauffmann, G., Wang, J., et al. 2011, *MNRAS*, 415, 61
- Salim, S., Rich, R. M., Charlot, S., et al. 2007, *ApJS*, 173, 267
- Sánchez, N. & Alfaro, E. J. 2008, *ApJS*, 178, 1
- Sérsic, J. L. & Pastoriza, M. 1967, *PASP*, 79, 152
- Slavin, J. D., Shull, J. M., & Begelman, M. C. 1993, *ApJ*, 407, 83
- Sullivan, M., Treyer, M. A., Ellis, R. S., & Mobasher, B. 2004, *MNRAS*, 350, 21
- Ryder, S. D. & Dopita, M. A. 1994, *ApJ*, 430, 142
- Tinsley B. M. 1981, *ApJ*, 250, 758
- Tsai, C., Turner, J. L., Beck, S. C., et al. 2013, *ApJ*, 776, 70
- Tubbs, A. D. 1982, *ApJ*, 255, 458
- Van Zee, L. 2001, *AJ*, 121, 2003
- Wang, W., Kassin, S. A., Pacifici, C., et al. 2018, *ApJ*, 869, 161
- Werk, J. K., Putman, M. E., & Meurer, G. R. 2010, *ASPC*, 423, 287
- Zucker, D. 2005, *ASSL*, 329, 87

H. O. Castañeda, A. M. Hidalgo Gómez, M. A. Magaña Serrano, & I. Vega-Acevedo: Departamento de Física, Escuela Superior de Física y Matemáticas, Instituto Politécnico Nacional, U. P. Adolfo López Mateos, C. P. 07738, Ciudad de México, México (ahidalgo@esfm.ipn.mx, mmaganas1500@alumno.ipn.mx).

THE PROPERTIES AND STABILITY OF SELF-GRAVITATING, POLYTROPIC SPHERES WITH $\gamma = 1$ TO 1.4 SPECIFIC HEAT RATIOS

A. C. Raga¹, J. A. Osorio-Caballero¹, R. S. Chan¹, A. Esquivel¹, A. Rodríguez-González¹, V. Lora², and J. C. Rodríguez Ramírez³

Received November 19 2019; accepted December 6 2019

ABSTRACT

We study self-gravitating, hydrostatic spheres with a polytropic equation of state $P \propto \rho^\gamma$ (where γ is the specific heat ratio of the gas), considering structures with $\gamma \approx 1$ as a model for molecular cloud cores with small departures from isothermality. We derive the properties (i.e., mass, radius and center to edge density ratio) as a function of γ for the maximal stable sphere through an application of “Bonnor’s stability criterion”. We find that in the $\gamma = 1 \rightarrow 4/3$ range the mass of the maximal sphere (for a given central temperature) is almost constant, and that its radius and center to edge density ratio are growing functions of γ . We therefore have maximal stable, self-gravitating spheres with similar masses, but with increasing center to edge density contrasts for increasing departures from isothermality.

RESUMEN

Estudiamos esferas auto-gravitantes hidrostáticas con una ecuación de estado politrópica $P \propto \rho^\gamma$ (donde γ es el cociente de calores específicos del gas), considerando estructuras con $\gamma \approx 1$ como modelos de núcleos moleculares con pequeñas desviaciones del caso isotérmico. Derivamos las propiedades (masa, radio y cociente de densidades centro a borde) como función de γ para la esfera estable máxima, a través de una aplicación del “criterio de estabilidad de Bonnor”. Encontramos que en el intervalo $\gamma = 1 \rightarrow 4/3$ la masa de la esfera máxima (para una temperatura central dada) es casi constante, y que su radio y cociente de densidades centro a borde son funciones crecientes de γ . Por esto, tenemos esferas autogravitantes máximas con masas similares pero con contrastes de densidad centro a borde crecientes para mayores desviaciones respecto del caso isotérmico.

Key Words: ISM: clouds — ISM: kinematics and dynamics — stars: formation

1. INTRODUCTION

It is widely thought that the gravitational collapse of dense molecular cloud cores results in the formation of stars (see, e.g., Shu 1977). Detailed calculations of the thermal structure of molecular cores show that over a large radial range they have only small temperature variations (see, e.g., Falgarone & Puget 1985), so that their hydrostatic structure can be modeled as an isothermal, self-gravitating, sphere.

In this paper, we study self-gravitating spheres with a polytropic equation of state ($P \propto \rho^\gamma$, where P is the pressure, ρ the density and γ the specific heat ratio of the gas) with γ values close to 1, meant as models for cloud cores with small departures from isothermality. We first compute the density profiles of these hydrostatic structures, and then evaluate their stability to radial perturbations.

We use the method of Bonnor (1956) for determining the stability of the isothermal, self-gravitating sphere. Bonnor (1956) considers a sphere that has a fixed mass M and an outer radius R_e at which the self-gravitating structure is in contact with a much hotter environment with a pressure P_e . He then calculates the variation in the outer pressure (or density) of this fixed mass sphere as a function of a

¹Instituto de Ciencias Nucleares, UNAM, Ciudad de México, México.

²Instituto de Radioastronomía y Astrofísica Teórica, UNAM, Morelia, Michoacán, México.

³Instituto de Astronomia, Geofísica e Ciências Atmosféricas, Universidade de São Paulo, SP, Brasil.

changing outer radius R_e (assuming that the inner structure adjusts instantaneously to the steady, self-gravitating configuration). If the outer density ρ_e (or, alternatively the pressure P_e , which is a monotonically increasing function of ρ_e) satisfies the condition

$$\frac{d\rho_e}{dR_e} < 0, \quad (1)$$

the sphere will be stable. In the case of the isothermal sphere, the sphere is stable for small radii, and becomes unstable (i.e., $d\rho_e/dR_e$ becomes positive) at a radius R_S . Isothermal spheres with $R_e > R_S$ are therefore unstable to radial perturbations.

Bonnor (1958) extended his analysis to the case of self-gravitating spheres of arbitrary polytropic index $n = 1/(\gamma - 1)$. He derived (from the numerical density stratifications of Emden, 1907) the values of the maximum stable radius R_e for the cases with $n = 4, 4.5, 4.9, 5$ and 6 . Bonnor's criterion has also been applied to hydrostatic structures with thermal properties calculated using an energy equation with appropriate heat source and sink terms (see Falgarone & Puget 1985).

Bonnor (1958) finds that self-gravitating, polytropic spheres with $\gamma > 4/3$ are unconditionally stable to radial perturbations. Because of this, in the present paper we limit ourselves to polytropes with $1 \leq \gamma < 4/3$. The stability of polytropes with different γ values has been described more recently by Horedt (2013).

An interesting problem is whether or not Bonnor's stability criterion gives "correct" results, where by "correct" we mean reproducible by time-dependent, hydrodynamic collapse simulations. Until quite recently, hydrodynamic simulations of the collapse of isothermal spheres did not reproduce (at least, not in a quantitative way) the results found from Bonnor's criterion. Hunter (2001) speculated that this lack of agreement was probably the result of a lack of accuracy in the hydrodynamic simulations. More recently, Raga et al. (2013) computed more precise simulations which reproduced the stability found from Bonnor's (1956) criterion for the collapse of the isothermal sphere. Even though it has not yet been proven, in this paper we will assume that Bonnor's (1958) stability criterion for arbitrary γ also predicts successfully the stability limits found from time-dependent hydrodynamical collapse calculations.

The paper is organized as follows. In § 2 we present the Lane-Emden equation and give a summary of the analytic properties of its solutions for specific heat ratios in the $\gamma = 1 \rightarrow 4/3$ range. In

§ 3 we describe the density and mass distributions obtained from numerical integrations of the Lane-Emden equation. In § 4, we apply Bonnor's (1958) stability criterion to these solutions, and derive the properties of the maximal stable sphere as a function of γ . Finally the results are summarized in § 5.

2. THE LANE-EMDEN EQUATION

2.1. General Considerations

The hydrostatic equation for a self-gravitating, non-magnetized spherical cloud is:

$$\frac{d}{dR} \left(\frac{R^2}{\rho} \frac{dP}{dR} \right) = -4\pi G \rho, \quad (2)$$

where R is the spherical radius, P the gas pressure, ρ the density and G the gravitational constant.

We now assume that we have a polytropic law

$$P = C \rho^\gamma, \quad (3)$$

with constant C and γ . Then, equation (2) takes the form

$$\frac{d}{dR} \left(R^2 \rho^{\gamma-2} \frac{d\rho}{dR} \right) = -\frac{4\pi G}{\gamma C} R^2 \rho, \quad (4)$$

which receives the name of "Lane-Emden equation".

As we are thinking of modelling a gas cloud, possible values of γ are $5/3$ (for an atomic/ionic, non-radiative gas), $7/5$ (for diatomic molecules) and 1 (for an isothermal situation). Another interesting value is $4/3$, corresponding to a gas of ultra-relativistic fermions (relevant for degenerate stellar cores).

In a stratified cloud, there is in principle no reason for C in equation (3) to be independent of radius (individual fluid parcels will evolve satisfying equation 3, but do not necessarily share the same value of C). A unique value of C is obtained for a "well mixed" gas cloud, in which mixing due to slow turbulent motions produces a stationary stratification with a constant specific entropy. The existence of such a mixing is required for modelling gas clouds with the polytropic Lane-Emden equation (equation 4).

Finally, we should note that many times the solutions to Lane-Emden's equations are identified with the "polytropic index" $n = 1/(\gamma - 1)$ (which appears naturally under some traditional changes of variables used for this equation). However, we will use γ (and not n) throughout the present paper.

2.2. The “Small R ”, Non-Singular Solution

We assume that we have a non-singular, “flat-topped” solution, with $(d\rho/dR)_0 = 0$ in the cloud center. Proposing a second-order Taylor series for the ρ as a function of R , inserting it in equation (4) and equating terms with the same powers of R one straightforwardly obtains:

$$\frac{\rho}{\rho_0} = 1 - \left(\frac{R}{R_c}\right)^2, \tag{5}$$

where ρ_0 is the central density and

$$R_c \equiv \sqrt{\frac{3\gamma C \rho_0^{\gamma-2}}{2\pi G}} \tag{6}$$

is the “core radius” of the density stratification.

For the variables $r = R/R_c$ and $\rho' = \rho/\rho_0$ the Lane-Emden equation takes the dimensionless form:

$$\frac{d}{dr} \left[r^2 (\rho')^{\gamma-2} \frac{d\rho'}{dr} \right] = -6r^2 \rho', \tag{7}$$

with second-order solution $\rho' = 1 - r^2$.

It is possible to construct higher order solutions by proposing appropriate Taylor expansions for the density as a function of radius. However, it is a well known problem that for $\gamma \approx 1$ the resulting series solutions converge to the exact solution only for $R < R_c$ (see, e.g., Chandrasekhar 1967).

We should note that the core radius R_c used for the adimensionalization (see equations 6 and 7) has a clear dependence on γ . In order to compare solutions with different γ values, it is possible to choose solutions with the same central isothermal sound speed:

$$c_0 = \sqrt{\frac{P_0}{\rho_0}} = \sqrt{C \rho_0^{\gamma-1}}, \tag{8}$$

where the first equality is the definition of the isothermal sound speed and the second equality is obtained using equation (3). Substituting into equation (6) we then obtain

$$R_c = \sqrt{\frac{3\gamma c_0^2}{2\pi G \rho_0}} = \gamma^{1/2} R_{c,1}, \tag{9}$$

where $R_{c,1}$ is the core radius of the isothermal ($\gamma = 1$) solution with the same central sound speed c_0 .

Therefore, for comparing solutions with different γ values but with the same central temperature (corresponding to a sound speed c_0), we plot the solutions as a function of

$$\frac{R}{R_{c,1}} = \gamma^{1/2} \frac{R}{R_c} = \gamma^{1/2} r, \tag{10}$$

see equations (7) and (9).

The mass of the self-gravitating spheres as a function of the spherical radius is given by:

$$M(R) = 4\pi \int_0^R R'^2 \rho(R') dR' = 4\pi \rho_0 R_c^3 m(R/R_c), \tag{11}$$

where

$$m(r) = \int_0^r r'^2 \rho'(r') dr' \tag{12}$$

is the dimensionless mass. It is straightforward to see that $\gamma^{3/2} m(r)$ is the mass normalized to $4\pi \rho_0 R_{c,1}^2$ (where $R_{c,1}$ is the core radius of the $\gamma = 1$ solution, see above).

2.3. The Singular Solutions

In order to obtain the singular solutions, one inserts a proposed solution $\rho_{sing} = A/R^p$ into the Lane-Emden equation (4). Equating the resulting powers of R and multiplying constants one obtains:

$$p = \frac{2}{2-\gamma}, \tag{13}$$

$$A = \left[\frac{\gamma C}{2\pi G} \frac{4-3\gamma}{2(2-\gamma)^2} \right]^{1/(2-\gamma)}. \tag{14}$$

Introducing a similar power law into the dimensionless Lane-Emden equation (7) one obtains:

$$\rho'_{sing} = \left[\frac{4-3\gamma}{2(2-\gamma)^2} \right]^{1/(2-\gamma)} r^{-2/(2-\gamma)}. \tag{15}$$

Clearly, these singular solutions exist only for $\gamma < 4/3$.

From numerical solutions of the Lane-Emden equation, it is found that for $\gamma < 1.2$ the non-singular solution (with the small r solution $\rho' = 1 - r^2$ and large r regime obtained by numerically integrating equation 7) converges to the singular solution for $r \gg 1$. For $\gamma = 6/5 = 1.2$ (corresponding to a polytropic index $n = 5$), the Lane-Emden equation has the analytic, non-singular solution

$$\rho' = \left(1 + \frac{r^2}{3} \right)^{-5/2}. \tag{16}$$

This solution has a large r behaviour of the form $\rho' \propto r^{-5}$, clearly not matching the singular solution (which for $\gamma = 6/5$ has a shallower $\rho' \propto r^{-5/2}$ dependence, see equation 15). The transition between

the large r , singular solution convergence obtained for $\gamma < 6/5$ and the $\gamma = 6/5$ solution (given by equation 16) is explored in § 3.

For $\gamma > 1.2$, the numerical non-singular solution of the Lane-Emden equation has a density that goes to zero at a finite radius. Therefore, the non-singular solution has a $r \gg 1$ convergence to the singular solution only for $\gamma < 6/5$. The nature of this convergence is described in the following subsection.

2.4. The $\gamma < 6/5$, $r \gg 1$ Convergence to the Singular Solution

It is customary to write

$$\rho'(r) = \rho'_{sing}(r) [1 + q(r)] , \quad (17)$$

and use equation (7) to obtain a differential equation for the fractional deviation $q(r)$ from the singular solution. Assuming that $q(r)$, $\dot{q} = dq/dr$ and $\ddot{q} = d^2q/dr^2 \ll 1$, this differential equation can be linearized to obtain:

$$\frac{2(4-3\gamma)}{2-\gamma} (q + R\dot{q}) + R^2\ddot{q} = 0 , \quad (18)$$

which for $a > 3 - 2\sqrt{2}$ has the general solution

$$q(r) = \frac{B}{r^a} \cos(\Gamma \ln r + \phi) , \quad (19)$$

where B and ϕ are arbitrary constants,

$$a = 2 \frac{4-3\gamma}{2-\gamma} , \quad (20)$$

and

$$\Gamma = \frac{1}{2} \sqrt{6a - a^2 - 1} . \quad (21)$$

It is straightforward to see that the $a > 3 - 2\sqrt{2}$ condition (necessary for equation 19 to be valid, see above) is satisfied for the $\gamma = 1 \rightarrow 1.2$ range.

Therefore (for all values of γ in the $1 \rightarrow 1.2$ range) the large r convergence to the singular solution is oscillatory (going as $\cos \Gamma \ln r$). This oscillatory behaviour has an amplitude that decreases as r^{-a} (see equations 19-21).

The linear problem which we have presented here does not allow us to fix the values of the B and ϕ constants (see equation 19). These constants have to be determined by fitting equation (17), calculated with the linear q solution (see equation 19), to the non-singular solution calculated with a numerical integration of the Lane-Emden equation (see equation 7). This fitting can be done to a quite high level of accuracy (see, e. g., the work of Ito et al. 2018 for the $\gamma = 1$ solution).

3. NUMERICAL INTEGRATIONS

We have numerically integrated the dimensionless Lane-Emden equation (equation 7) starting from the quadratic solution $\rho' = 1 - r^2$ at small r . The results obtained for several values of γ in the $1 \rightarrow 1.2$ range are shown in log-log plots in Figure 1.

For $r < 1$, all of the logarithmic density distributions are quite flat, with $\rho' \approx 1$. For $r > 1$, the $\gamma = 1$ and 1.5 distributions start a steeper decrease, and approach the corresponding singular solutions (shown with the straight, dashed lines) with the oscillatory convergence described in § 2.3. These oscillations have larger amplitudes for solutions of increasing γ .

The bottom panel of Figure 1 shows solutions with $\gamma \approx 1.2$ values. The singular $\gamma = 1.2$ solution (not distinguishable from the $\gamma = 1.190$ and 1.199 singular solutions at the resolution of the plot) is shown with a dashed line, and the non-singular $\gamma = 1.2$ solution (obtained either from the numerical integration or from equation 16) is shown with the red line. It is clear that the $\gamma = 1.190$ and $\gamma = 1.199$ solutions follow the (analytic) $\gamma = 1.2$ solution out to $r_t \approx 10$ and 100 (respectively), and then have an oscillatory transition to the singular solution. We find that the transition radius r_t becomes progressively larger as $\gamma \rightarrow 1.2$. Solutions with $\gamma \approx 1.2$ have been previously studied by Horedt (2013).

Figure 2 shows logarithmic depictions of the $\rho'(r)$ solutions obtained for γ values in the $6/5 \rightarrow 4/3$ range. For all of the $\gamma > 1.2$ solutions we obtain densities that go to zero at a finite dimensionless radius $r_{max} = R_{max}/R_c$ (which can be straightforwardly determined from the numerical integrations).

Finally, in Figure 3 we show the inner regions of density ρ/ρ_0 and mass $\gamma^{3/2}m$ (see equation 12) stratifications with γ in the $1 \rightarrow 4/3$ range, as a function of the radius $\gamma^{1/2}r = R/R_{c,1}$, normalized to the core radius of the $\gamma = 1$ solution (see equations 9-10). The results shown illustrate the differences between self-gravitating spheres with different γ , but with the same central density ρ_0 and isothermal sound speed c_0 . We see that the lower γ solutions have lower densities and masses within the core radius, and higher densities and masses at large radii.

4. THE RADIAL STABILITY OF THE SELF-GRAVITATING SPHERES

4.1. Bonnor's Stability Criterion

For a polytropic, self-gravitating sphere of specific heat ratio γ , Bonnor's (1956, 1958) stability criterion

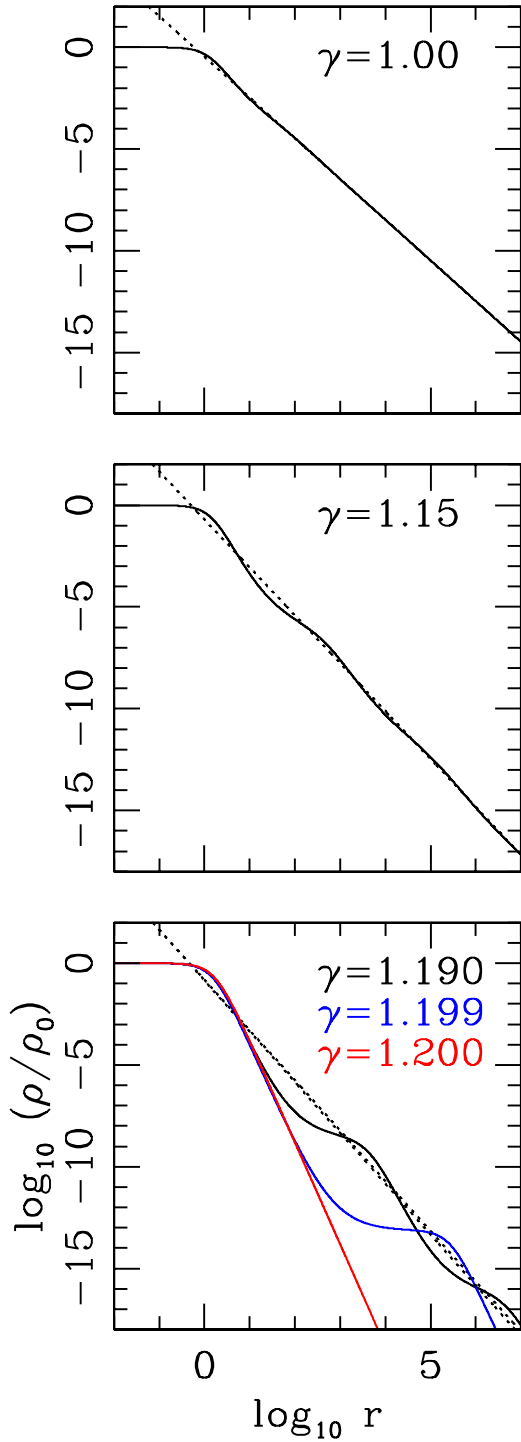


Fig. 1. The solid lines show the dimensionless nonsingular density vs. radius solutions for the isothermal, $\gamma = 1$ case (top), for $\gamma = 1.5$ center, and for $\gamma = 1.190, 1.199$ and 1.200 (bottom). The dashed curves show the $\gamma = 1, 1.15$ and 1.2 singular solutions (in the top, center and bottom frames, respectively). The color figure can be viewed online.

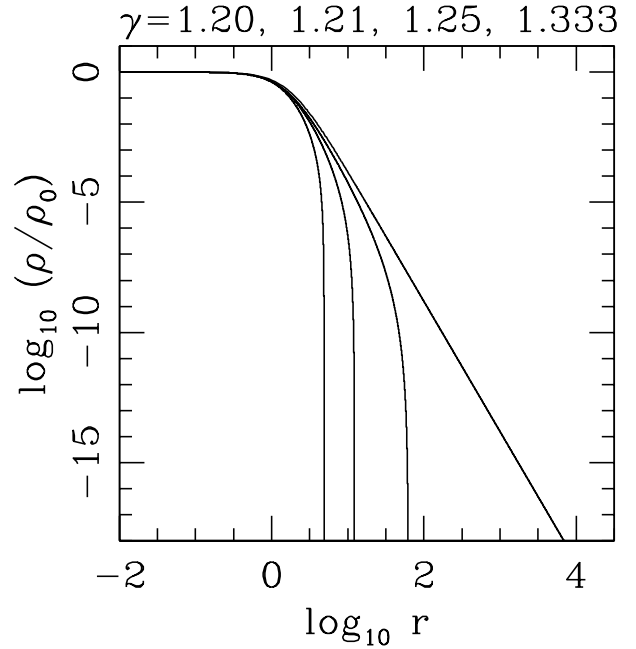


Fig. 2. Dimensionless nonsingular density (ρ/ρ_0) vs. radius ($r = R/R_c$, where R_c is the core radius defined in equation 6) solutions for $\gamma = 1.20, 1.21, 1.25$ and 1.3 . While the $\gamma = 1.20$ solution goes out to infinite r , the solutions for larger γ values reach zero densities at an outer radius r_f (which decreases for increasing γ).

can be written as:

$$\left(\frac{2\pi G}{3\gamma C}\right)^{1/(2-\gamma)} \left(\frac{d\rho_e}{dR_e}\right)_{M=const.} = \frac{r_e \dot{f}(r_e)}{1 - \left(\frac{2-\gamma}{4-3\gamma}\right) r_e^{\left(\frac{4-3\gamma}{2-\gamma}\right)} \frac{f(r_e)}{F(r_e)}} - \frac{2f(r_e)}{2-\gamma} < 0, \quad (22)$$

where $r_e = R_e/R_c$ is the dimensionless outer radius of the sphere,

$$f(r) = r^{2/(2-\gamma)} \rho'(r); \quad \dot{f}(r) = \frac{df}{dr}, \quad (23)$$

and

$$F(r) = \int_0^r (r')^{2(1-\gamma)/(2-\gamma)} f(r') dr'. \quad (24)$$

The derivation of equation (22) is completely analogous to the derivation of equation (17) of Raga et al. (2013) for the $\gamma = 1$ case.

We then take the numerically derived $\rho'(r)$ density stratifications described in § 3, calculate $f(r)$, $\dot{f}(r)$ and $F(r)$ (equations 23-24), and then evaluate the term on the left-hand-side of the inequality of equation (22) to find the smallest radius r_s at which

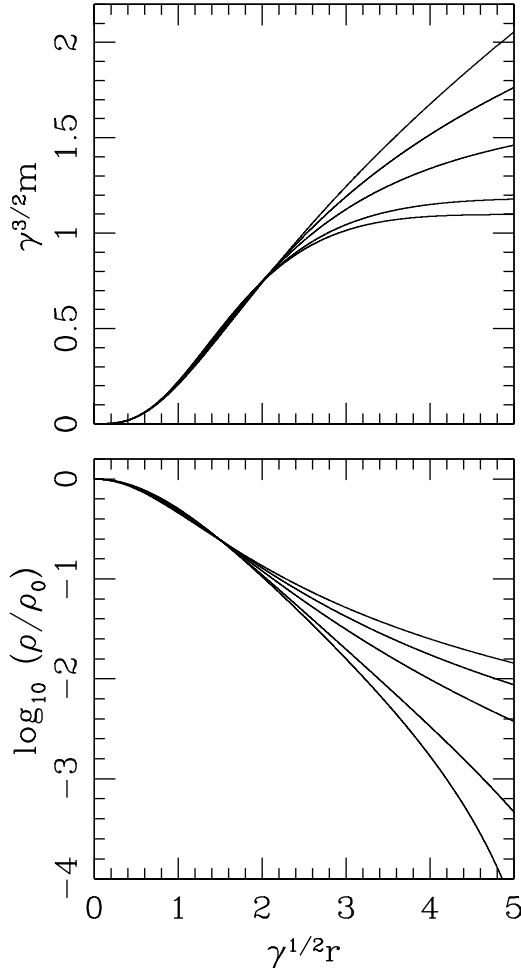


Fig. 3. Bottom frame: inner region of the nonsingular density vs. radius solutions for $\gamma = 1.0, 1.1, 1.2, 1.3$ and 1.3 . The solutions for higher γ values have steeper density decreases at larger radii. Top frame: dimensionless mass $\gamma^{3/2}m = M/(\rho_0 R_{c,1}^3)$, where ρ_0 is the central density) as a function of radius. The mass distribution has lower growths at large radii for higher γ values. Both the mass and the density profiles are shown as a function of $\gamma^{1/2}r = R/R_{c,1}$ (where $R_{c,1}$ is the core radius of the $\gamma = 1$ solution with the same central sound speed, see the text).

the inequality is violated. In this way we derive the radius $r_s = R_s/R_c$ of the maximal stable sphere for a given value of γ .

4.2. The Maximal Stable Solutions

After determining the maximum radius for stability $r_s = R_s/R_c$ from Bonnor's criterion (equations 22-24), we calculate the dimensionless mass $m_s = m(r_s)$ and center-to-edge density ratio $\rho_0/\rho_s = 1/\rho'(r_s)$ of the maximal stable solution. This exercise is re-

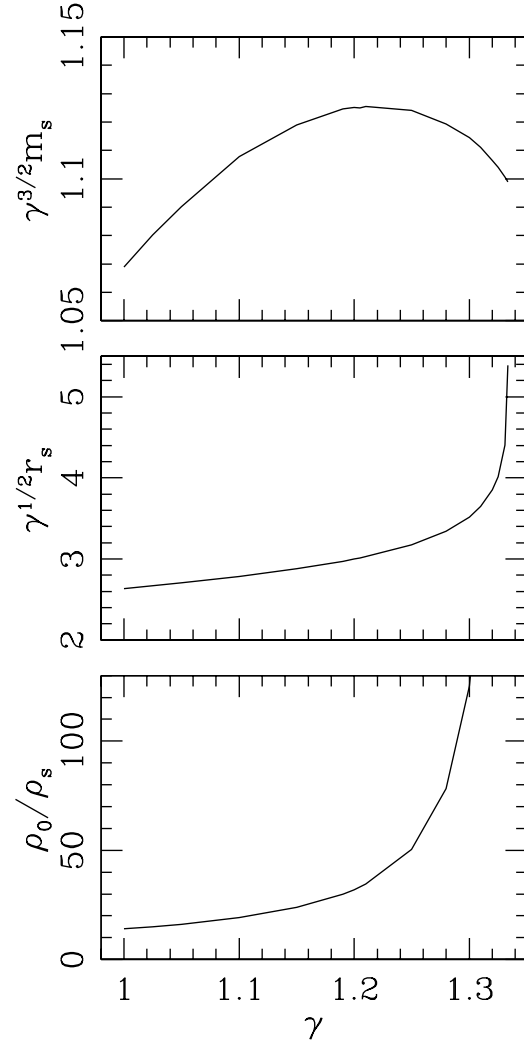


Fig. 4. Properties of the maximal stable solution as a function of γ . Bottom frame: center to edge density ratio ρ_0/ρ_s . Center: dimensionless outer radius $\gamma^{1/2}r_s = R_s/R_{c,1}$. Top: dimensionless mass $\gamma^{3/2}m_s$ (see equation 12).

peated for several values of the specific heat ratio in the $\gamma = 1 \rightarrow 4/3$ range. For $\gamma > 4/3$, Bonnor's stability criterion is satisfied for all radii of the density stratifications (see also Bonnor 1958).

In Figure 4, we show the dimensionless mass $\gamma^{3/2}m_s = 3M_s/(4\pi\rho_0 R_{c,1}^3)$ (see equations 11-12), outer radius $\gamma^{1/2}r_s = R_s/R_{c,1}$, and center to edge density ratio ρ_0/ρ_s of the maximal stable solution as a function of γ . We see that:

- ρ_0/ρ_s grows as a function of γ , and reaches high values for $\gamma \approx 1.3$, finally diverging at $\gamma = 4/3$,

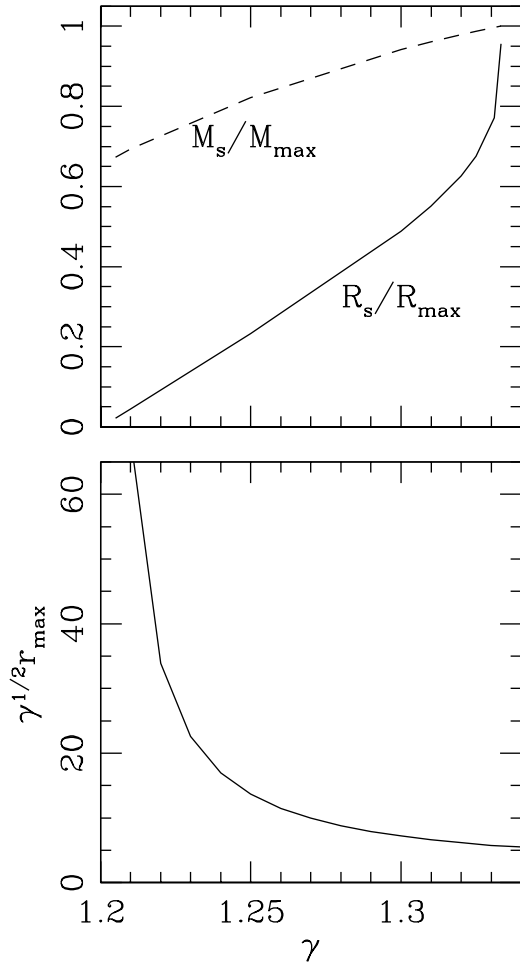


Fig. 5. Bottom frame: dimensionless maximum radius $\gamma^{1/2}r_{max} = R_{max}/R_{c,1}$ as a function of γ . Top frame: ratios M_s/M_{max} and R_s/R_{max} of the mass M_s and radius R_s of the maximal stable solution to the maximum mass M_{max} and radius R_{max} of the polytropic spheres as a function of γ . We show the results obtained for $\gamma = (6/5)^+ \rightarrow 4/3$, which have density distributions which go to zero at a maximum radius R_{max} .

- $\gamma^{1/2}r_s$ monotonically grows as a function of γ , and reaches a $\gamma^{1/2}r_s \approx 5.4$ for $\gamma = 4/3$,
- the dimensionless mass $\gamma^{3/2}m_s$ shows very small variations for γ in the $1 \rightarrow 4/3$ range.

For the $6/5 < \gamma \leq 4/3$ range (with density stratifications that end at an outer radius R_{max} , see § 2 and Figure 3), we obtain numerically the dimensionless outer radius $r_{max} = R_{max}/R_c$ and the mass $m_{max} = m(r_{max})$ (see equation 12) of the full stratification. In Figure 5, we plot the outer radius $\gamma^{1/2}r_{max} = R_{max}/R_{c,1}$ and the ratios M_s/M_{max} and R_s/R_{max} between the mass/radius of the maximal

stable solution and the corresponding values of the full stratification.

From Figure 5 we see that:

- the outer radius $\gamma^{1/2}r_{max}$ of the full stratification decreases monotonically from its infinite $\gamma = 1.2$ value to a value of ≈ 5.63 at $\gamma = 4/3$,
- the R_s/R_{max} ratio increases from 0 (for $\gamma = 1.2$) to 1 (for $\gamma = 4/3$), with a faster increase as $\gamma = 4/3$ is approached,
- the M_s/M_{max} ratio gradually increases from ≈ 0.65 (for $\gamma = 1.2$) to 1 (for $\gamma = 4/3$).

Therefore, we see that the fraction of the total radius and mass of the finite, $\gamma > 1.2$ self-gravitating spheres that is stable increases with γ . The (radial or mass) fraction that is stable tends to 1 as $\gamma = 4/3$ is approached.

5. SUMMARY

We have studied the non-singular density stratifications that are solutions to the polytropic Lane-Emden equation for self-gravitating spheres. We have first presented general analytical considerations about the proper adimensionalisation of the density and radius (using the second-order, small radius approximation to the non-singular density stratification), the derivation of the singular solutions, and the convergence at large radius of the non-singular to the singular solutions (which occurs only for $\gamma < 6/5$). The results that have been presented (see § 2) can be found in the previous literature (notably, in Chapter IV of the book of Chandrasekhar 1967 and in the book of Horedt 2004).

We have then computed numerical integrations of the Lane-Emden equation to obtain non-singular density stratifications for γ in the $1 \rightarrow 4/3$ range (see § 3). Solutions around $\gamma = 1.2$ show the curious transition between the $\gamma < 1.2$ density stratifications (which at large radii converge to the singular solutions) and the $\gamma = 1.2$ stratification (which is analytic, and differs quite dramatically from the singular solution at large radii). It is not clear whether or not this rather curious mathematical feature has any relevance for astronomical applications.

Finally, we have applied Bonnor's stability criterion (for self-gravitating solutions of arbitrary γ , see equation 22) to our numerically obtained density stratifications. We find that for spheres with $\gamma = 1 \rightarrow 4/3$ but with the same central temperature (or isothermal sound speed), the maximal stable sphere has (see Figure 4):

- a center to edge density ratio that grows quite substantially with increasing γ , diverging for $\gamma \rightarrow 4/3$,
- an outer radius that slowly grows with γ in the $1 \rightarrow 1.2$ range, and has a steeper growth for $\gamma \rightarrow 4/3$,
- an almost constant mass as a function of γ .

Also, for the finite, $\gamma > 6/5$ spheres, the maximal stable sphere has a mass and radius that grow with γ . For $\gamma > 4/3$, the whole finite sphere is stable.

Applying these results to molecular clouds cores, we see that relatively small deviations from isothermality (which could be modelled with γ values somewhat larger than 1) are not likely to lead to the formation of substantially different self-gravitating structures, in the sense that the maximal stable solutions will have almost the same mass (regardless of the value of γ in the $1 \rightarrow 4/3$ range). The outer radius of the maximal stable sphere grows for $\gamma > 1$, reaching a factor 1.5 larger value for $\gamma = 1.2$. The largest effect is found for the center to edge density ratio, which grows by a factor of ≈ 2 when γ is changed from 1 to 1.2 and by a factor of ≈ 10 when $\gamma = 1.3$.

Therefore, we conclude that small deviations from isothermality will result in the production of maximal stable spheres with approximately the same mass, with somewhat larger outer radii, and with substantially higher center to edge density ratios. Clearly, it will be interesting to see whether the hydrodynamical collapse of the $\gamma = 1 \rightarrow 4/3$ density stratifications resembles the well studied collapse of the isothermal ($\gamma = 1$) sphere.

We end by discussing the work of Kandori et al. (2005), who use near-infrared images to derive the column density distribution for a set of ≈ 10 Bok globules. They carry out fits of the non-singular solution of the isothermal Lane-Emden equation to the derived structures. From these fits, they find the center to edge density ratios and the dimensionless outer radius ξ_{max} (which, due to a different adimensionalisation is a factor of $\sqrt{6}$ larger than the $\gamma^{1/2}r_s$ outer radius shown in our Figure 4) of the observed

structures. Most interestingly, they find that while some of the globules of their sample are close to the stability limit, about half of them have center to edge density ratios and outer radii larger than the stability limit of the isothermal sphere. This result leads them to conclude that these globules above the isothermal stability limit are probably already collapsing.

Our models provide a possible alternative explanation for these results. As one can see from Figure 4, self-gravitating spheres with departures from isothermality (modeled as spheres with $\gamma > 1$) have maximal stable solutions with center to edge density ratios and dimensionless outer radii larger than the ones of the maximal isothermal ($\gamma = 1$) solution. The higher center to edge density contrast globules observed by Kandori et al. (2005) could therefore correspond to stable self-gravitating spheres with such departures from isothermality.

AR acknowledges support from the DGAPA-UNAM grant IG100218. JCRR acknowledges the Brazilian agency FAPESP grant 2017/12188-5. We thank an anonymous referee for pointing out the work of Kandori et al. (2005), which provides a most interesting connection between our models and reality.

REFERENCES

- Bonnor, W. B. 1956, MNRAS, 116, 351
 _____ . 1958, MNRAS, 118, 523
 Chandrasekhar, S. 1967, An introduction to the study of stellar structure (Dover, New York)
 Falgarone, E., Puget, J. L. 1985, A&A, 142, 157
 Horedt, G. P. 2004, Polytropes - applications in astrophysics and related fields (Kluwer: Dordrecht)
 _____ . 2013, ApJ, 773, 131
 Hunter, C. 2011, MNRAS, 328, 839
 Ito, Y., Poje, A., Lancelotti, C. 2018, NewA, 58, 15
 Kandori, R., Nakajima, Y., Tamura, M. et al. 2005, AJ, 130, 2166
 Raga, A. C., Rodríguez-Ramírez, J. C., Rodríguez-González, A., Lora, V., & Esquivel, A. 2013, MNRAS, 49, 127
 Shu, F. H. 1977, ApJ, 214, 488
- R. S. Chan, A. Esquivel, J. A. Osorio-Caballero, A. C. Raga, and A. Rodríguez-González: Instituto de Ciencias Nucleares, Universidad Nacional Autónoma de México, Ap. 70-543, 04510 Cd. Mx., México (raga@nucleares.unam.mx)
 V. Lora: Instituto de Radioastronomía y Astrofísica Teórica, Universidad Nacional Autónoma de México, Ap.3-72, 58089 Morelia, Michoacán, México.
 J. C. Rodríguez Ramírez: Instituto de Astronomia, Geofísica e Ciências Atmosféricas, Universidade de São Paulo, R. do Matão 1226, 05508-090 São Paulo, SP, Brasil.

SPECTRAL BEHAVIOR OF THE SYMBIOTIC NOVA HM SGE IN THE ULTRAVIOLET

M. R. Sanad and M. A. Abdel-Sabour

Astronomy Department, National Research Institute of Astronomy and Geophysics, Helwan, Cairo, Egypt.

Received August 25 2019; accepted December 13 2019

ABSTRACT

Ultraviolet observations of the symbiotic nova HM Sge were obtained from the International Ultraviolet Explorer (IUE) through the interval from 1980 - 1992. Three line profiles demonstrating the variations of some emission lines at different dates are presented. We determined the reddening of HM Sge from the 2200 Å absorption feature; the estimated value is $E(B - V) = 0.34 \pm 0.02$. We studied CIV at 1550 Å, He II 1640 Å, and CIII] at 1909 Å produced in the wind from the hot star. The line flux variations at different dates could be explained in terms of the variations of temperature in the emitting region as a result of mass loss variations. The IUE observations can be explained by the models of Girard & Willson (1987); Formigini et al. (1995).

RESUMEN

Se obtuvieron observaciones ultravioletas de la nova simbiótica HM Sge mediante el “International Ultraviolet Explorer” (IUE) durante el intervalo de tiempo 1980 - 1992. Se presentan tres perfiles de líneas que demuestran la variación de algunas líneas de emisión en distintos tiempos. Determinamos el enrojecimiento de HM Sge a partir de la absorción en 2200 Å, y obtuvimos un valor estimado de $E(B - V) = 0.34 \pm 0.02$. Estudiamos el CIV en 1550 Å, el He II en 1640 Å, y el C III] en 1909 Å, líneas que se producen en el viento de la estrella caliente. Las variaciones en el tiempo del flujo de las líneas podrían explicarse en términos de la variación de la temperatura de la región de emisión, como consecuencia de variaciones en la pérdida de masa. Las observaciones del IUE pueden explicarse mediante los modelos de Girard & Willson (1987) y Formigini et al. (1995).

Key Words: binaries: symbiotic — stars: individual: HM Sge — ultraviolet: stars

1. INTRODUCTION

Symbiotic systems are a group of interacting binary stars consisting of a cool giant star, a hot white dwarf or a neutron star, and in some cases a nebula (Murset et al. 1997). These systems exhibit different outburst behaviors; some authors interpret them as due to different physical processes (Mikolajewska & Kenyon 1992; Kenyon & Webbink 1984). Symbiotic binaries are divided into two classes: S type, characterized by a stellar continuum, and D type, characterized by a thick dust shell. Symbiotic novae are a subgroup of symbiotic stars displaying a major thermonuclear eruption as a result of the accretion of matter from the cool red giant onto the hot com-

ponent, with a long time - scale evolution of their decay (Tomov & Tamova 2001).

Some symbiotic systems exhibit a large variety of emission lines with different ionization states because not all systems have a nebula. The absence of emission lines may be due to the high density of the nebula. Some theoretical models attempt to interpret the spectra. Nussbaumer & Vogel (1987) employ a model consisting of a double star system with a nebula created by the mass loss of the cool component and ionized by the radiation of the hot component. As a result of their model calculations they suggest that nova-like nuclear processes were responsible for the eruption of HM Sge 1975. Slovak (1978) developed a model of a binary symbiotic system containing a late type variable.

HM Sge is a D type symbiotic nova consisting of a cool red giant Mira star with a pulsation period of 527 days (Murset & Schmid 1999; Munari & White-lock 1989). In 1975, HM Sge changed in optical magnitude from 17 to 11 (Dokuchaeva 1976). This increase in brightness was interpreted as nova eruption resulting from a thermonuclear runaway (TNR) on the surface of the hot white dwarf due to an accumulation of accreted matter.

Puetter et al. (1978) suggested that HM Sge is a binary star system containing a dust embedded cool component and an optically hot component. In their model the flux is a result of a combination of optically thin dust emission and emission from the reddened photosphere of the cool component. The presence of a cool component is inferred from the shape of the continuum.

Lee (2009) adopted a wind accretion disk model and described the emission region by a Keplerian thin disk with Raman scattering occurring in a neutral region near the cool star. By using a Monte Carlo technique, they computed the line profiles that vary by the slow spherical stellar wind from the cool component, with the ionization front approximated by a hyperboloid.

Ciatti et al. (1977), using optical photometric and spectroscopic observations, reported that HM Sge has nebular emission lines similar to V1016 Cyg. HM Sge may evolve to a compact planetary nebula like IC 4997 and Hb 12, and later on to an extended nebula such as M 2 - 9. Stover & Sivertsen (1977) using optical spectroscopic observations found a typical nebular emission spectrum. They called it a new emission line object, with R.A.=19:39, Dec.=+16:38 representing the coordinates of HM Sge.

Taranova & Yudin (1982) found that the infrared flux variations of HM Sge indicated the presence of a cool Mira star, while Corradi et al. (1999), from optical spectroscopy, reported that HM Sge has a large-scale outflow which they attributed to a fast wind from the hot white dwarf. Mueller & Nussbaumer (1985) used ultraviolet observations from IUE to calculate the temperature of the nebula and deduced that the emitting region is radiatively ionized.

Feibelman (1982) also using IUE observations, found that HM Sge has undergone large temporal variations in the ultraviolet emission line fluxes, with a trend toward higher ionization and excitation levels. Nussbaumer & Vogel (1990) proposed a model for HM Sge consisting of a binary system associated with a nebula formed by the loss of mass from the Mira star. This nebula is ionized by the radiation of

the white dwarf. They also reported that the radiation temperature increased from 4×10^4 K in 1976 to 1.7×10^5 K in 1989.

Eyres et al. (2001), using Hubble Space Telescope observations discussed the nebular conditions of HM Sge and deduced that the true value of reddening is $E(B-V) = 0.35$. They identified a number of discrete features with radio and optical emission embedded in the extended nebula, and measured directly for the first time the positions of the binary components of HM Sge. They estimated the projected angular binary separation to be 40 ± 9 mas. Temperature and density diagnostics revealed two distinct regions in the surrounding nebula.

Stauffer (1984) reported that the optical emission lines are produced in a colliding region of the wind from the hot white dwarf and the wind from the cool Mira, and interpreted the outburst of HM Sge as a result of a hydrogen flash in the envelope of the hot star.

The important observational characteristics in our study are that firstly, the ultraviolet emission line fluxes have nearly the same spectral behavior, indicating a possible common origin in the wind of the hot white dwarf; and secondly the modulations of the mass loss rate are interpreted as due to the increase and decrease in the temperature and density.

In this paper we present an analysis of the ultraviolet data obtained with the International Ultraviolet Explorer (IUE) of HM Sge. Previous studies are those of Mueller & Nussbaumer (1985); Nussbaumer & Vogel (1990). In § 2 we discuss the IUE observations and in § 3 we present the method of determining the reddening. § 4 shows the results and discussion of the spectral behavior of emission lines in the colliding wind from hot white dwarf. § 5 contains the conclusions of this paper.

2. ULTRAVIOLET OBSERVATIONS OF HM SGE WITH IUE

The International Ultraviolet Explorer (IUE) observations have been retrieved from the INES (IUE Newly Extracted Spectra) site at <http://ines.vilspa.esa.es>. The ultraviolet spectra with low resolution (6 Å) and short wavelength (1150 - 1950 Å) were used in the reduction and analysis. For more information and description of the ultraviolet spectra see Rodriguez-Pascual et al. (1999) and Gonzalez et al. (2001).

The IUE observations have been used in some previous studies, e.g. Mueller & Nussbaumer (1985). They calculated the line fluxes of some emission lines

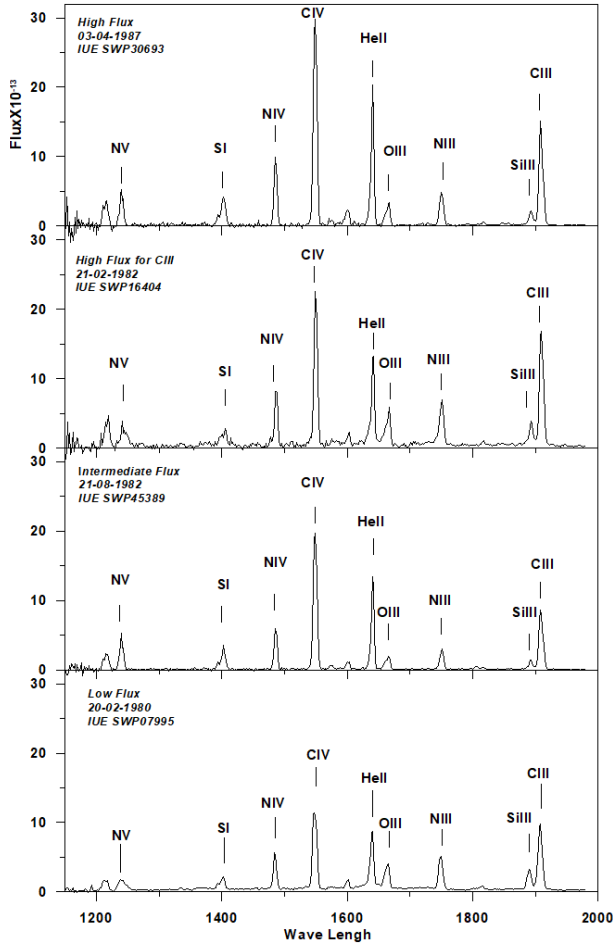


Fig. 1. IUE spectrum of HM Sge during different stages (The flux is plotted in units of $\text{erg cm}^{-2} \text{s}^{-1} \text{\AA}^{-1}$).

such as CIV 1550 Å; the variations of CIV through the period from January 1978 to April 1982 were 4.6×10^{-12} to $15.9 \times 10^{-12} \text{ erg cm}^{-2} \text{ s}^{-1}$.

Feibelman (1982) analyzed CIV 1550 Å in different epochs and found variations in the flux of the line in order of 5.02×10^{-12} to $12.93 \times 10^{-12} \text{ erg cm}^{-2} \text{ s}^{-1}$; Nussbaumer & Vogel (1990) found variations in the flux of the CIV line of order 9.4×10^{-12} to $20 \times 10^{-12} \text{ erg cm}^{-2} \text{ s}^{-1}$.

The log of the IUE observations is listed in Table 1. Figure 1 shows the variations in line fluxes with time. The MIDAS software was used for processing the spectra. For the estimations of the fluxes of emission lines we used the integrate/line command in the MIDAS software suite to estimate the continuum level and to integrate the flux of the emission line above the continuum.

TABLE 1
LIST OF IUE OBSERVATIONS

Image ID	Dispersion	Aperture	Observation Date	J.D.
SWP07995	Low	Large	1980-02-20	2444290.15734
SWP09898	Low	Large	1980-08-25	2444477.28274
SWP09943	Low	Large	1980-08-29	2444480.65055
SWP13546	Low	Large	1981-03-22	2444685.99707
SWP13548	Low	Large	1981-03-22	2444686.25105
SWP14704	Low	Large	1981-08-09	2444826.30751
SWP14756	Low	Large	1981-08-14	2444831.01329
SWP15353	Low	Large	1981-10-31	2444909.42918
SWP15355	Low	Large	1981-11-01	2444909.69151
SWP16402	Low	Large	1982-02-21	2445022.13708
SWP16404	Low	Large	1982-02-21	2445022.35865
SWP16705	Low	Large	1982-04-07	2445066.51274
SWP16706	Low	Large	1982-04-07	2445066.55572
SWP16752	Low	Large	1982-04-13	2445072.63036
SWP16753	Low	Large	1982-04-13	2445072.69293
SWP25552	Low	Large	1985-03-30	2446155.31349
SWP28896	Low	Large	1986-08-14	2446155.31349
SWP28897	Low	Large	1986-08-14	2446657.36038
SWP30693	Low	Large	1987-04-03	2446888.58032
SWP30694	Low	Large	1987-04-03	2446888.64367
SWP31033	Low	Large	1987-05-23	2446939.37905
SWP33154	Low	Large	1988-03-25	2447245.68857
SWP33155	Low	Large	1988-03-25	2447245.79245
SWP35921	Low	Large	1989-04-03	2447619.73762
SWP35922	Low	Large	1989-04-03	2447619.79851
SWP36951	Low	Large	1989-09-07	2447777.19521
SWP37572	Low	Large	1989-11-12	2447843.02143
SWP37573	Low	Large	1989-11-12	2447843.14039
SWP38638	Low	Large	1990-04-21	2448002.60074
SWP38939	Low	Large	1990-04-21	2448002.70632
SWP39837	Low	Large	1990-10-15	2448180.41296
SWP39838	Low	Large	1990-10-15	2448180.47445
SWP42154	Low	Large	1991-08-01	2448470.46081
SWP42547	Low	Large	1991-09-24	2448524.19478
SWP42548	Low	Large	1991-09-24	2448524.30658
SWP45354	Low	Large	1992-08-16	2448850.97169
SWP45355	Low	Large	1992-08-16	2448851.01356
SWP45387	Low	Large	1992-08-21	2448855.75214
SWP45389	Low	Large	1992-08-21	2448855.86235
SWP46011	Low	Large	1992-10-19	2448915.12249
SWP46012	Low	Large	1992-10-19	2448915.21653

3. METHOD OF ESTIMATING THE REDDENING

The reddening of HM Sge was determined using the 2200 Å absorption feature. We used the best data set of *Short Wavelength Prime* spectra (SWP) with low resolution (6 Å) in the range of wavelengths between 1150 - 1950 Å and *Long Wavelength Redundant* (LWR) spectra with low resolution (6 Å) in the range of wavelengths between 2000 - 3000 Å. The spectra are binned in 15 Å bins for SWP and 25 Å bins for LWR. The following observations were selected for our determination of the reddening (LWP08880 - LWP12920 - LWP19016 - LWP24119) & (SWP28896 - SWP33154 - SWP38638

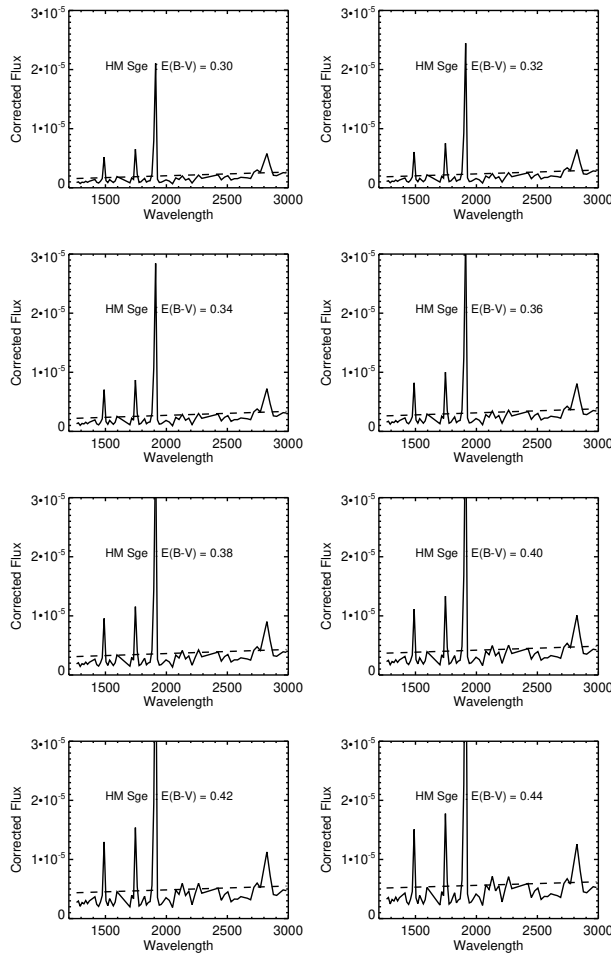


Fig. 2. Reddening determination for HM Sge.

- SWP46011) which gave the best smoothing spectrum suitable for our determination of the reddening value.

The most suitable value is determined by visual inspection of the plots for the best fit to the 2200 Å absorption feature, which represented the best agreement between observations and standard theoretical (dashed line) values. The estimated value of the reddening for HM Sge is $E(B - V) = 0.34 \pm 0.02$ as shown in Figure 2.

Eyres et al. (2001) reported the reddening for HM Sge as $E(B - V) = 0.35$; Ivison et al. (1991) found the reddening to be $E(B - V) = 0.58$; Mueller & Nussbaumer (1985) determined a reddening of $E(B - V) = 0.61$, Murset et al. (1991) found the reddening to be $E(B - V) = 0.63$. Our estimated value is very close to that determined by Eyres et al. (2001) using the extinction map method.

4. RESULTS AND DISCUSSION

4.1. Method of Calculating the Line Fluxes of Emission Lines.

We fitted the observed portions of the wings of emission lines by a Gaussian function. The “integrate/line” command in the software ESO/MIDAS was effectively used to estimate the continuum level and to integrate the flux of the CIV 1550 Å, He 1640 Å and CIII] 1909 Å emission lines above this continuum. For the measurements of emission line fluxes, we determined the integrated fluxes for the emission lines in units of $\text{erg cm}^{-2} \text{s}^{-1}$.

4.2. Time Variations of the Spectral Lines from the Wind of Hot Star

The CIV spectral line at 1550 Å is a resonance emission line, the He II spectral line at 1640 Å is a recombination line, and the CIII] emission line at 1909 Å is an intercombination line, previously discussed by Mueller & Nussbaumer (1985), Nussbaumer & Vogel (1990).

The line fluxes of CIV & He II and CIII] emission lines vary with time over short and long time scales, from hours to years. There was a steady increase in line fluxes until April 1982, and they reached a maximum flux in April 1987. The origin of the emission lines may be the wind from the hot white dwarf since their spectral behavior is similar. Table 2 contains fluxes for CIV, He II and CIII] emission lines and Figures 3, 4, 5 represent the spectral behavior of such lines. The errors for the measured line fluxes are in the range of 1σ , as determined by the methods reported in Lenz and Ayres (1992).

The transferred mass from the cool star (Mira) to the hot white dwarf increases the temperature of the hydrogen layer on top of the white dwarf (WD). The transfer of mass leads to an outburst and consequently to a rise in both luminosity and radiation pressure. The increased radiation pressure will eject some of the atmosphere of the WD as a stellar wind. At this stage HM Sge contains a wind from a cool Mira and a wind from the white dwarf. As a result of the motion of two winds toward each other, the collision between them occurs at some distance and forms what is known as the colliding wind region. As a result of this collision, two shocks are formed, one toward the white dwarf, the other toward the cool star, (Girard & Willson 1987; Formigini et al. 1995).

The radiation from the hot WD increased the temperature of this facing shock and led to a steady increase in the line fluxes of CIV, He II and CIII] until 1982, reaching a maximum in 1987. The shock

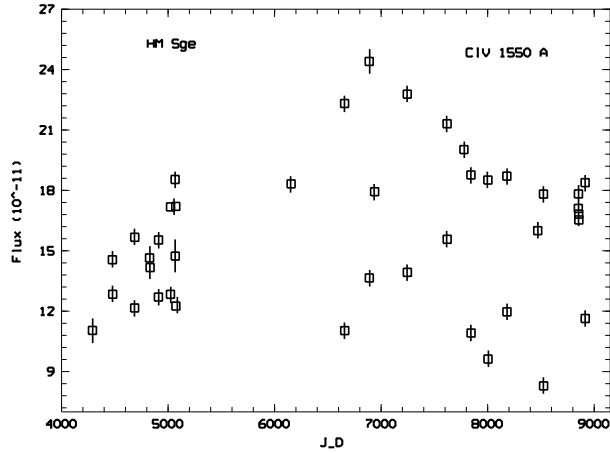


Fig. 3. Time evolution (JD - 2440000) of the CIV emission line flux. The 1σ error bars are shown on each data point (The flux is plotted in units of $\text{erg cm}^{-2} \text{s}^{-1} \text{\AA}^{-1}$).

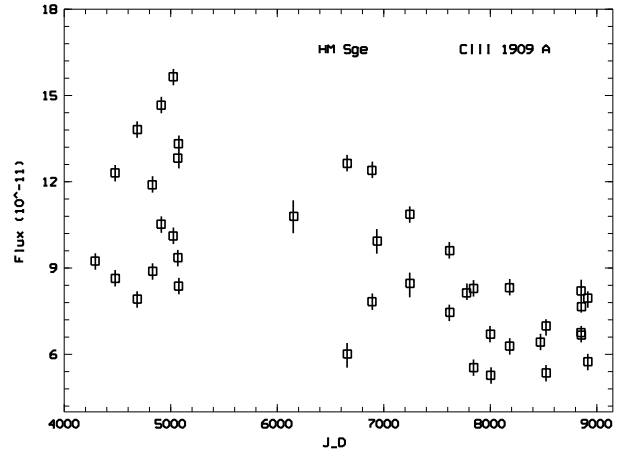


Fig. 5. Time evolution (JD - 2440000) of the CIII] emission line flux. The 1σ error bars are shown on each data point (The flux is plotted in units of $\text{erg cm}^{-2} \text{s}^{-1} \text{\AA}^{-1}$).

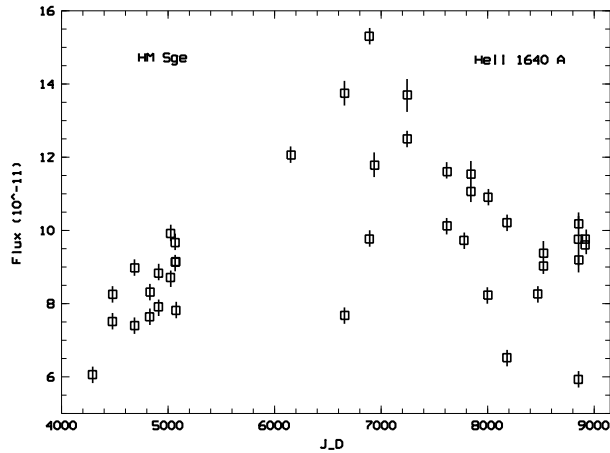


Fig. 4. Time evolution (JD - 2440000) of the He II emission line flux. The 1σ error bars are shown on each data point (The flux is plotted in units of $\text{erg cm}^{-2} \text{s}^{-1} \text{\AA}^{-1}$).

facing the WD weakened with time. The decline in this shock led to a decrease of the velocity of the hot wind, and consequently a decrease in the rate of mass loss from the hot white dwarf; so, both the density and temperature of the emitting region (wind of WD) decreased and therefore the line fluxes decreased.

The spectral behavior of the symbiotic nova HM Sge differs from the ultraviolet spectral behavior of classical novae such as GQ Mus, (Sanad & Abdel-Sabour 2016). The nature of the physical environment in the emitting regions of the two systems is different, and consequently the effect of the physical conditions on the emission lines also differs, as do

the wind of the hot white dwarf for HM Sge and the expanding shell of ejecta for GQ Mus.

Similarly, the spectral behavior of HM Sge differs from the spectral behavior of PU Vul, because of different physical environments. For PU Vul, there is a nebula around the white dwarf, which is partially eclipsed by a cool giant star, as opposed to the wind of a hot white dwarf in the case of HM Sge (Sanad 2016).

However, the spectrum of HM Sge is similar to the ultraviolet spectral behavior of both V 1016 Cyg and AG Peg, since the spectral lines are produced in the same emitting region with similar physical effects: a wind from a hot white dwarf for the three symbiotic novae (Sanad 2017 a,b).

The velocity of the emitting region can be determined from the expansion of this region. The Full Width at Half Maximum (FWHM) of emission lines increases as a result of the Doppler shift. Table 3 shows the velocities of the CIV line.

The integrated fluxes (F) of CIV 1550 Å, He II 1640 Å and CIII] 1909 Å are used to determine the average ultraviolet luminosities from the following equation. The distance of ≈ 1000 pc to the HM Sge is used, as estimated by Richards et al. (1999).

$$L_{UV} = 4\pi F d^2.$$

The ultraviolet luminosity of the emitting region is $\approx 4 \times 10^{34} \text{erg s}^{-1}$. This value is comparable to that derived by Willson et al. (1984).

The radius of the hot white dwarf is determined to be 9.3×10^8 cm by the following equation, assuming the mass of the hot white dwarf to be $0.7 M_{\odot}$,

TABLE 2

IUE LINE FLUXES OF CIV, He II AND CIII] IN
UNITS OF 10^{-11} erg cm $^{-2}$ s $^{-1}$

Image ID	CIV 1550 Å	He II 1640 Å	CIII 1909 Å	Observation Date	J.D.
SWP07995	11.04	6.06	9.24	1980-02-20	2444290.15734
SWP09898	14.55	7.51	12.30	1980-08-25	2444477.28274
SWP09943	12.84	8.25	8.64	1980-08-29	2444480.65055
SWP13546	12.16	7.40	7.92	1981-03-22	2444685.99707
SWP13548	15.67	8.97	13.81	1981-03-22	2444686.25105
SWP14704	14.64	7.64	11.89	1981-08-09	2444826.30751
SWP14756	14.16	8.31	8.88	1981-08-14	2444831.01329
SWP15353	12.70	7.91	10.52	1981-10-31	2444909.42918
SWP15355	15.53	8.83	14.66	1981-11-01	2444909.69151
SWP16402	12.83	8.71	10.11	1982-02-21	2445022.13708
SWP16404	17.17	9.91	15.64	1982-02-21	2445022.35865
SWP16705	18.54	9.66	12.82	1982-04-07	2445066.51274
SWP16706	14.73	9.13	9.36	1982-04-07	2445066.55572
SWP16752	17.20	9.14	13.32	1982-04-13	2445072.63036
SWP16753	12.25	7.81	8.37	1982-04-13	2445072.69293
SWP25552	18.32	12.05	10.79	1985-03-30	2446155.31349
SWP28896	22.31	13.74	12.63	1986-08-14	2446155.31349
SWP28897	11.03	7.67	6.01	1986-08-14	2446657.36038
SWP30693	24.40	15.30	12.39	1987-04-03	2446888.58032
SWP30694	13.65	9.76	7.83	1987-04-03	2446888.64367
SWP31033	17.93	11.78	9.93	1987-05-23	2446939.37905
SWP33154	22.78	12.50	10.86	1988-03-25	2447245.68857
SWP33155	13.92	13.70	8.46	1988-03-25	2447245.79245
SWP35921	21.31	10.12	9.60	1989-04-03	2447619.73762
SWP35922	15.57	11.60	7.45	1989-04-03	2447619.79851
SWP36951	20.02	9.72	8.13	1989-09-07	2447777.19521
SWP37572	18.76	11.06	8.29	1989-11-12	2447843.02143
SWP37573	10.91	11.53	5.53	1989-11-12	2447843.14039
SWP38638	18.51	8.23	6.69	1990-04-21	2448002.60074
SWP38939	9.62	10.90	5.27	1990-04-21	2448002.70632
SWP39837	18.71	6.52	8.31	1990-10-15	2448180.41296
SWP39838	11.96	10.21	6.28	1990-10-15	2448180.47445
SWP42154	16.01	8.26	6.42	1991-08-01	2448470.46081
SWP42547	17.81	9.02	6.98	1991-09-24	2448524.19478
SWP42548	8.29	9.37	5.35	1991-09-24	2448524.30658
SWP45354	17.10	5.93	6.75	1992-08-16	2448850.97169
SWP45355	17.82	9.75	8.20	1992-08-16	2448851.01356
SWP45387	16.82	10.18	6.66	1992-08-21	2448855.75214
SWP45389	16.53	9.19	7.65	1992-08-21	2448855.86235
SWP46011	18.38	9.60	7.95	1992-10-19	2448915.12249
SWP46012	11.63	9.76	5.74	1992-10-19	2448915.21653

TABLE 3

CIV (FWHM) IN kms $^{-1}$

Image ID	CIV (FWHM)	Observation Date	J.D.
SWP07995	1457	1980-02-20	2444290.15734
SWP09898	1263	1980-08-25	2444477.28274
SWP09943	1477	1980-08-29	2444480.65055
SWP13546	1417	1981-03-22	2444685.99707
SWP13548	1311	1981-03-22	2444686.25105
SWP14704	1323	1981-08-09	2444826.30751
SWP14756	1403	1981-08-14	2444831.01329
SWP15353	1411	1981-10-31	2444909.42918
SWP15355	1258	1981-11-01	2444909.69151
SWP16402	1423	1982-02-21	2445022.13708
SWP16404	1085	1982-02-21	2445022.35865
SWP16705	1226	1982-04-07	2445066.51274
SWP16706	1429	1982-04-07	2445066.55572
SWP16752	1199	1982-04-13	2445072.63036
SWP16753	1479	1982-04-13	2445072.69293
SWP25552	1357	1985-03-30	2446155.31349
SWP28896	1291	1986-08-14	2446155.31349
SWP28897	1702	1986-08-14	2446657.36038
SWP30693	1216	1987-04-03	2446888.58032
SWP30694	1632	1987-04-03	2446888.64367
SWP31033	1501	1987-05-23	2446939.37905
SWP33154	1185	1988-03-25	2447245.68857
SWP33155	1520	1988-03-25	2447245.79245
SWP35921	1238	1989-04-03	2447619.73762
SWP35922	1501	1989-04-03	2447619.79851
SWP36951	1212	1989-09-07	2447777.19521
SWP37572	1207	1989-11-12	2447843.02143
SWP37573	1556	1989-11-12	2447843.14039
SWP38638	1183	1990-04-21	2448002.60074
SWP38939	1665	1990-04-21	2448002.70632
SWP39837	1178	1990-10-15	2448180.41296
SWP39838	1538	1990-10-15	2448180.47445
SWP42154	1194	1991-08-01	2448470.46081
SWP42547	1243	1991-09-24	2448524.19478
SWP42548	1731	1991-09-24	2448524.30658
SWP45354	1189	1992-08-16	2448850.97169
SWP45355	1212	1992-08-16	2448851.01356
SWP45387	1202	1992-08-21	2448855.75214
SWP45389	1244	1992-08-21	2448855.86235
SWP46011	1194	1992-10-19	2448915.12249
SWP46012	1502	1992-10-19	2448915.21653

Nussbaumer & Vogel (1990).

$$R_{WD} = 0.78 \times 10^9 \left[\left(\frac{1.44 M_{\odot}}{M_{WD}} \right)^{2/3} - \left(\frac{M_{WD}}{1.44 M_{\odot}} \right)^{2/3} \right]^{1/2} \text{ cm.}$$

Our calculated value of the radius is comparable to that calculated by Murset et al. (1997).

The rate of the wind mass loss is determined from the following equation (Bode & Evans 2008):

$$M_{wind}^{\bullet} = \frac{3.3 \times 10^{-11}}{\alpha_w} \left(\frac{R_{WD}}{M_{WD}} \right)^{1/2} L_{UV} M_{\odot} \text{ yr}^{-1},$$

where α_w is an arbitrary parameter. We found an average value of the rate of wind mass loss to be

$\approx 5 \times 10^{-6} M_{\odot} \text{ yr}^{-1}$. This value is comparable to that calculated by Livio et al. (1989) and Nussbaumer & Vogel (1990)

The Steffan-Boltzmann equation is used to calculate the temperature of the emitting region,

$$L = \sigma A T^4,$$

where $\sigma \approx 5.6704 \times 10^{-5} \text{ erg cm}^{-2} \text{ s}^{-1} \text{ K}^{-4}$ is the Steffan Boltzmann constant, and $A = 4\pi r^2$ is the surface area. The average temperature is $\approx 1 \times 10^5 \text{ K}$. Our estimated value is comparable to that reported by Nussbaumer & Vogel (1990) and Muellar & Nussbaumer (1985).

5. CONCLUSIONS

In this paper we studied ultraviolet observations of the symbiotic nova HM Sge obtained by the IUE. The main purpose of this work was to constrain and diagnose the emitting region (wind of the hot star) using some specific spectral lines (CIV, He II & CIII) and to estimate some physical parameters. The calculated physical parameters agree with previous determinations. The main results are as follows:

1. The accumulation of mass from the Mira star leads to an outburst of HM Sge.
2. The emission lines are produced in the wind from the hot white dwarf. This emitting region is formed as a result of the collision between two winds from the two stars and, consequently, the collision leads to the formation of two shocks, one toward the white dwarf and the other toward the cool Mira.
3. The line flux modulations are attributed to the variations of mass loss.
4. The estimated ultraviolet luminosity, wind mass loss rate and temperature are consistent with previous calculations.
5. The ultraviolet observations with the IUE can be interpreted with the wind models of symbiotic novae.

REFERENCES

- Bode, M. F., Evans, A. 2008, *Classical Novae*, ed. M. F. Bode and A. Evans. Cambridge Astrophysics Series, No. 43, Cambridge: Cambridge University Press
- Ciatti, F., Mammano, A., & Vittone, A. 1977, *A&A*, 61, 459C
- Corradi, R. L. M., Ferrer, O. E., Schwarz, H. E., Brandi, E., & Garcia, L. 1999, *A&A*, 348, 978C
- Dokuchaeva, O. D. 1976, *IBVS*, 1189, 1D
- Eyres, S. P. S., Bode, M. F., Taylor, A. R., et al. 2001, *ApJ*, 551, 512
- Feibelman, W. A. 1982, *ApJ*, 258, 584
- Formiggini, L., Contini, M., & Leibowitz, E. M. 1995, *MNRAS*, 277, 1071
- Formiggini, L., Contini, M., & Leibowitz, E. M. 1995, *MNRAS*, 277, 1071F
- Girard, T. & Willson, L. A. 1987, *A&A*, 183, 247
- Gonzalez-Riestra, R., Cassatella, A., & Wamsteker, W. 2001, *A&A*, 373, 730G
- Iverson, R. J., Bode, M. F., Roberts, J. A., et al. 1991, *MNRAS*, 249, 374
- Kenyon, S. J. & Webbink, R. F. 1984, *ApJ*, 279, 252
- Lee, H.-W. 2009, *ASPS*, 404, 82L
- Lenz, D. D. & Ayres, T. R. 1992, *PASP*, 104, 1104
- Livio, M., Prialnik, D., & Regev, O. 1989, *ApJ*, 341, 299L
- Mikolajewska, J. & Kenyon, S. J. 1992, *MNRAS*, 256, 177M
- Mueller, B. E. A. & Nussbaumer, H. 1985, *A&A*, 145, 144
- Munari, U. & Whitelock, P. A. 1989, *MNRAS*, 237, 45
- Murset, U. & Schmid, H. M. 1999, *A&AS*, 137, 473
- Murset, U., Nussbaumer, H., Schmid, H. M., & Vogel, M. 1991, *A&A*, 248, 458M
- Murset, U., Wolff, B., & Jordan, S. 1997, *A&A*, 319, 201M
- Nussbaumer, H. & Vogel, M. 1987, *A&A*, 182, 51N
- _____. 1990, *A&A*, 236, 117
- Paczynski, B. 1971, *AcA*, 21, 417P
- Puetter, R. C., Russell, R. W., Soifer, B. T., & Willner, S. P. 1978, *ApJ*, 223L, 93P
- Richards, A. M. S., Bode, M. F., Eyres, S. P. S., et al. 1999, *MNRAS*, 305, 380R
- Rodriguez-Pascual, P. M., Gonzalez-Riestra, R., Scharrel, N., & Wamsteker, W. 1999 *A&AS*, 139, 183R
- Sanad, M. R. 2016, *Ap&SS*, 361, 386
- _____. 2017, *NewA*, 52, 14S
- _____. 2017, *NewA*, 53, 20S
- Sanad, M. R. & Abdel-Sabour, M. A. 2016, *Ap&SS*, 361, 152
- Slovak, M. H. 1978, *A&A*, 70L, 75S
- Stover, R. J. & Sivertsen, S. 1977, *ApJ*, 214L, 33S
- Taranova, O. G. & Yudin, B. F. 1982, *SvAL*, 8, 46T
- Tomov, N. & Tomova, M. 2001, *Ap&SS*, 278, 311T
- Willson, L. A., Wallerstein, G., Brugel, E. W., & Stencel, R. E. 1984, *A&A*, 133, 154W

H α KINEMATICS OF THE ISOLATED INTERACTING GALAXY PAIR KPG 486 (NGC 6090)

M. M. Sardaneta¹, M. Rosado², and M. Sánchez-Cruces¹

Received March 19 2019; accepted December 17 2019

ABSTRACT

In optical images, the barely studied isolated interacting galaxy pair KPG 486 (NGC 6090) displays similar features to the Antennae (NGC 4038/39) galaxy pair. To compare the distribution of ionized hydrogen gas, morphology and kinematic and dynamic behaviour of both galaxy pairs, we present observations in the H α emission line of NGC 6090 acquired with the scanning Fabry-Perot interferometer, PUMA. For each galaxy in NGC 6090 we obtained several kinematic parameters, its velocity field and its rotation curve. We also analysed some of the perturbations induced by their encounter. We verified the consistency of our results by comparing them with kinematic results from the literature. The comparison of our results on NGC 6090 with those obtained in a previous similar kinematic analysis of the Antennae highlighted great differences between these galaxy pairs.

RESUMEN

En imágenes del óptico, el par de galaxias aislado poco estudiado, KPG 486 (NGC 6090), muestra características similares al par de galaxias Las Antenas (NGC 4038/39). Para comparar la distribución del gas ionizado, morfología y comportamiento cinemático y dinámico entre ambos pares de galaxias, se presentan observaciones en la línea de emisión H α de NGC 6090 adquiridas con el interferómetro Fabry-Perot de barrido, PUMA. Para cada galaxia en NGC 6090 se obtuvieron varios parámetros cinemáticos, su campo de velocidades y su curva de rotación. Además, se analizaron algunas de las perturbaciones inducidas por su encuentro. Se verificó la consistencia de estos resultados comparándolos con los de la literatura. La comparación de los resultados de NGC 6090 con los de un análisis cinemático similar previo para las Antenas destacó grandes diferencias entre estos pares de galaxias.

Key Words: galaxies: individual: NGC 6090 — galaxies: interactions — galaxies: kinematics and dynamics — methods: data analysis — techniques: interferometric

1. INTRODUCTION

Instead of evolving in isolation, galaxies are found in clusters and groups, and they can interact quite strongly with their nearby companions. These interactions can have a profound impact on the properties of galaxies, resulting in intense bursts of star formation, the onset of quasar-like activity in galactic nuclei and perhaps even the complete transformation of spiral galaxies into elliptical galaxies. Studies of galaxies in the early universe show a significant fraction of interacting and merging systems, and theo-

ries of cosmological structure formation indicate that most galaxies have had some form of strong interaction during their lifetime. Rather than being rare events, galaxy interactions may be the dominant process shaping the evolution of the galaxy population in general (Mihos 2000).

The evolution and interaction of galaxies is governed by gravitational effects. Morphologically, in the interacting galaxies there are large bridges and tails, stellar bars and/or increased spiral structures and, commonly, the bodies of galaxies are distorted (Schweizer 1986). Toomre & Toomre (1972), through numerical simulations, established that the gravitational interaction with another galaxy may be

¹Aix Marseille Univ, CNRS, CNES, LAM, Marseille, France.

²Instituto de Astronomía, UNAM, Ciudad de México, México.

the source not only of spiral structures, but also of the filamentary structure, which they called ‘tidal tails’; thus, gravity is solely responsible for these large and thin tails and several other deformations seen in several surveys (e.g. Arp 1966; Karachentsev 1987; Vorontsov-Velyaminov et al. 2001).

Numerical simulations show that during a merger, tidal forces from a companion galaxy trigger the formation of a bar in the disc of a perturbed galaxy (Noguchi 1987; Salo & Laurikainen 2000a,b; Renaud et al. 2015). The bar acts to trigger starburst activity by rapidly funnelling large amounts of gas to the nuclear region (Barnes & Hernquist 1992; Dinshaw et al. 1999; Gabbasov et al. 2014; Martin & Soto 2016). When a bar is clearly observable in the stellar component, the gas dynamics shows very distinctive characteristics, corresponding to elliptical and non-circular orbits; the isoveLOCITIES contour curves are deformed symmetrically. Hence, the inclination of the central isoveLOCITY contour curve along the minor axis is one of the main features used to identify a bar (Bosma 1981; Combes et al. 2002).

The simplest case in the process of galaxy interactions is that of isolated galaxy pairs, which are systems composed of two galaxies located so close in space that the gravitational effect of their nearest neighbours can be neglected relative to the gravitational effects exerted between each other (Fuentes-Carrera et al. 2004; Rosado et al. 2011; Gabbasov et al. 2014). Systematic research on double galaxies provides us with important information about the conditions of formation and properties of the evolution of galaxies (Karachentsev 1987).

Obtaining kinematic information from interacting galaxies is useful for understanding the effect that the interaction can have on each of the members of the pair (Fuentes-Carrera et al. 2004, 2007; Repetto et al. 2010). In highly disturbed velocity fields, double nuclei, double kinematic gas components, and high amplitude discrepancies between both sides of the rotation curves imply strong galaxy-galaxy interactions or mergers. On the other hand, stellar and gaseous major axes misalignments and tidal tails suggest collisions that may not always lead to merging (Amram et al. 2003; Torres-Flores et al. 2014).

From the observational point of view, most of the kinematic work on interacting galaxies has been carried out using long-slit spectroscopy along certain positions (e.g. Günthardt et al. 2016), restricting kinematic information to only a few points on the galaxy. However, for an asymmetric perturbed system, it is important to obtain the kinematic in-

formation from large portions of the disc, using observational techniques such as integral field spectroscopy with a scanning Fabry-Perot interferometer (FP). In this way, the extended kinematic information can help us determine the interaction process which has been produced on each of the members of the interacting system, in addition to the fact that, sometimes the axial symmetry of each galaxy is lost during the interaction (Fuentes-Carrera et al. 2004, 2015; Epinat et al. 2008).

1.1. NGC 6090

The isolated interacting galaxy pair KPG 486 (NGC 6090) has been described as a double nuclei system with an asymmetric disc and two long tidal tails of ≈ 60 kpc in length (e.g. Dinshaw et al. 1999). At optical wavelengths, this galaxy system looks like the NGC 4038/39 galaxy system (The Antennae) (e.g. Toomre & Toomre 1972; Hummel et al. 1987; Martin et al. 1991; Mazzarella & Boroson 1993; Dinshaw et al. 1999; Bryant & Scoville 1999). This feature can be observed in the upper panel of Figure 1 which shows the optical image of NGC 6090 taken from the Digitized Sky Survey (DSS) in a field of view of 4 arcmin.

In radio-wavelengths NGC 6090 appears as a pair of interacting spirals separated by 0.14 arcsec, with nuclei in contact and with enormous curved wings (Martin et al. 1991). Meanwhile, molecular gas appears elongated and aligned along the direction of the nuclei as a rotating disc (Wang et al. 2004) or ring (Bryant & Scoville 1999; Sugai et al. 2000). The position angle of that disc is $\approx 60^\circ$ with a major axis length of ≈ 3.4 arcsec; the CO source appears to peak between the radio nuclei rather than on one of them (Bryant & Scoville 1999) and the molecular gas component does not appear to belong to any of the galaxies in the system based on kinematics (Wang et al. 2004).

Due to the interaction evidence that NGC 6090 shows it was defined as a merger by Chisholm et al. (2015). But NGC 6090 has also been defined as a galaxy system in an intermediate stage of merging or pre-merging because, in addition of its two nuclei and tidal tails, the galaxy system has an identifiable bridge (Miralles-Caballero et al. 2011). In the near-infrared, the galaxies that make up NGC 6090 are seen as follows: NGC 6090 NE has a distorted spiral structure and evidence of a stellar bar, and NGC 6090 SW looks like an irregular galaxy; the position of its nucleus is still under discussion (Dinshaw et al. 1999; Cortijo-Ferrero et al. 2017). In Table 1 we list the general parameters of NGC 6090 which

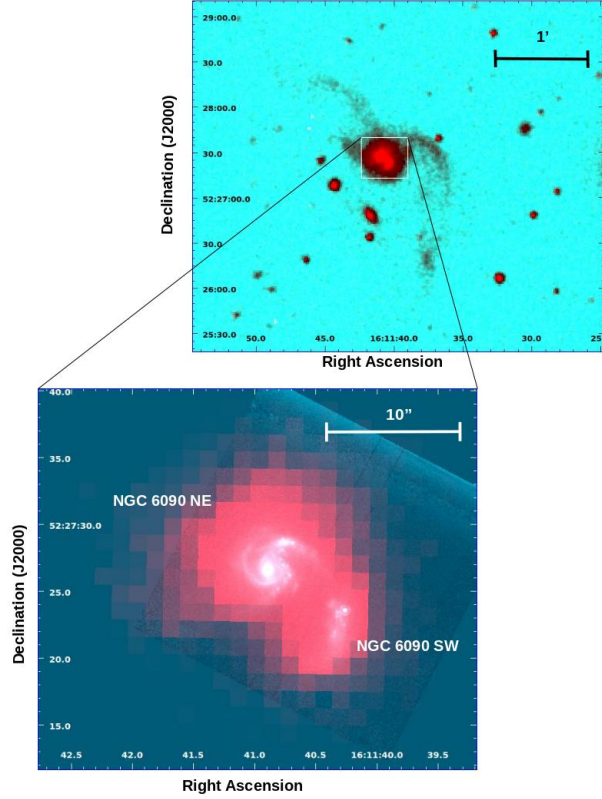


Fig. 1. Top: Image from the Digitized Sky Survey (DSS) in a 4 arcmin field of view centred on the galaxy system NGC 6090 over which, superposed in red, is shown the H α direct image, taken with a 6819 Å filter with a FWHM of 86 Å (obtained from the PUMA in its direct image mode at the 2.1 m telescope from the Observatorio Astronómico Nacional in San Pedro Mártir, OAN-SPM, Baja California, México). Bottom: 2.22 μ m image from the Near-Infrared Camera Multi-Object on the *Hubble Space Telescope* (NICMOS/HST) over which, superposed in red, is shown the H α direct image from OAN-SPM in a 28 arcsec field of view centred on NGC 6090. The color figure can be viewed online.

hitherto have been reported only for a single galactic system.

To investigate the distribution of ionized hydrogen gas, the morphology, and kinematic and dynamic behaviour of the galaxy system NGC 6090, we obtained a FP data cube spectrally centred on the H α emission line of the system. In this paper we present the analysis of the H α image, the velocity field and dispersion velocity map of the pair of galaxies NGC 6090, as well as the rotation curves obtained for each member. Lastly, we comment on our results and those found in the literature, and compare

TABLE 1

PARAMETERS OF THE GALAXY SYSTEM NGC 6090

Parameters	NGC 6090 system
Coordinates (J2000)	$\alpha = 16^{\text{h}} 11^{\text{m}} 40.7^{\text{s}}$ $\delta = +52^{\circ} 27' 24''^{\text{a}}$
Other names	KPG 486 ^{a,c} NGC 6090 ^a UGC 10267 ^a Mrk 496 ^a
Morphological type	G Pair ^a Multiple galaxy ^b Merger, double nucleus ^e Merger ^g
Mean heliocentric	8906 ^a
Radial velocity (km s ⁻¹)	8855 ^b
Distance (Mpc)	122 ^{d,*} 123.3 ^{e,*} 128 ^{g,**} 127.7 ^{h,**}
L _{IR} (L_{\odot})	3×10^{11} ^f
m_b	14.36 ^a
D _{25/2} (arcmin)	4.36 ^b
Photometric nuclear	
Separation (arcsec)	5.4 ^e

^aNASA/IPAC (2014) (NASA/IPAC Extragalactic Data Base (NED) is operated by the Jet Propulsion Laboratory, California Institute of Technology, under contract with the National Aeronautics and Space Administration. <https://ned.ipac.caltech.edu/>).

^bHyperLeda (HyperLeda: <http://leda.univ-lyon1.fr/>).

^cKarachentsev (1987).

^dCondon et al. (1990).

^eBryant & Scoville (1999).

^fAcosta-Pulido et al. (1996).

^gChisholm et al. (2015).

^hCortijo-Ferrero et al. (2017).

*Distance $D = v/H_0$ computed using $H_0 = 75 \text{ km s}^{-1} \text{ Mpc}^{-1}$.

**Distance obtained from $z = 0.02930$ with $H_0 = 70 \text{ km s}^{-1} \text{ Mpc}^{-1}$.

the kinematic characteristics of the galaxy system NGC 6090 with those of the Antennae made by Amram et al. (1992).

This paper is organized as follows: in § 2 there is an overview of the observational parameters and the reduction process; in § 3 we present the morphological features of NGC 6090 observed from its H α monochromatic and continuum maps; § 4 is devoted

TABLE 2
INSTRUMENTAL AND OBSERVATIONAL
PARAMETERS

Parameter	Value
Telescope	2.1 m (OAN, SPM)
Instrument	PUMA
Detector	Site3 CCD
Detector size	2048 × 2048 pix
Image scale (binning 4 × 4)	1.27 arcsec/pix
Scanning FP interferometer	ET-50
Finesse	≈ 10
FP interference order at H α	330
Free spectral range at H α	19.9 Å (909 km s ⁻¹)
Spectral sampling resolution at H α	0.97 Å (44.1 km s ⁻¹)
Interference filter	6819 Å (FWHM = 86 Å)
Total exposure time	72 min
Calibration line	6717 Å (Ne)
Average seeing	1.67 arcsec

to the kinematic analysis made from our FP data. We show the derived velocity fields, the associated rotation curve of each member of the galaxy system NGC 6090 and we analyse the non-circular motions of each galaxy through the velocity dispersion map of the system; § 5 is dedicated to the dynamical analysis, including the computation of the mass of each galaxy. A discussion is presented in § 6, and our conclusions are given in § 7.

In this paper, we considered $H_0 = 75 \text{ km s}^{-1} \text{ Mpc}^{-1}$ (Condon et al. 1990) and adopted a distance of 118 Mpc for NGC 6090.

2. OBSERVATIONS AND DATA REDUCTIONS

Our observations of NGC 6090 were performed in July 2015 with the $f/7.5$ Cassegrain focus at the 2.1 m telescope at the Observatorio Astronómico Nacional in San Pedro Mártir, Baja California, México (OAN-SPM) using the scanning Fabry-Perot interferometer, PUMA (Rosado et al. 1995). PUMA is a focal reducer built at the Instituto de Astronomía-UNAM and used to obtain images and Fabry-Perot interferometry of extended emission cosmical sources. The FP used is an ET-50 (Queensgate Instruments) with a servostabilization system; it has a free spectral range of 19.9 Å (909 km s⁻¹) at H α . The effective finesse of PUMA is ≈ 24 which implies a sampling spectral resolution in H α of 0.414 Å (19.0 km s⁻¹) achieved by scanning the interferometer free spectral range through 48 different equally

spaced channels (Rosado et al. 1995). However, due to the parallelism of the FP mirrors during the data acquisition for the observations, particularly of NGC 6090, the measured finesse for this data cube was ≈ 10 which leads to a sampling spectral resolution of 0.97 Å (44.1 km s⁻¹) at H α .

We used a 2048 × 2048 CCD detector with a pixel scale of 0.317 arcsec and we set a 4 × 4 binning to enhance the signal, obtaining a 512 × 512 pixel window inside of a field of view of 10 arcmin. So, we obtained a final spatial sampling per pixel of 1.27 arcsec which is slightly better than the average seeing of 1.67 arcsec. To isolate the redshifted H α emission line an interference filter centred at 6819 Å with FWHM of 86 Å was used. Thus, we obtained an H α data cube with a total exposure time of 72 minutes (90 s per channel).

In order to avoid phase wavelength dependence of the FP layers it is necessary to calibrate the data cube in wavelength. So, we used a Ne lamp whose line at 6717 Å is close to the redshifted nebular wavelength to obtain a calibration cube at the end of the observation. The parabolic phase map was computed from the calibration cube in order to obtain the reference wavelength for the line profile observed inside each pixel. The instrumental and observational parameters are listed in Table 2.

For the data reduction and analysis we used the ADHOCw³ software to make the standard corrections to the cube: removal of cosmic rays and bias subtraction, subtraction of the OH sky lines at 6828.5 Å, 6842.2 Å and 6863.9 Å (Chamberlain 1961; Krassovsky et al. 1962) and application of a spectral Gaussian smoothing with $\sigma = 57 \text{ km s}^{-1}$ in the data cube. We applied IRAF⁴ tasks such as IMEXAMINE to determine the average seeing of our data and MSCSETWCS to add the World Coordinate System (WCS) to the resulting maps of NGC 6090. To complete the data analysis we used our own Python scripts.

The FP scanning process allows us to obtain a flux value in arbitrary units at pixel level for each of the 48 scanning steps. The calibration in wavelength was fixed for each profile at each pixel using the calibration data cube. Thus, the intensity profile found throughout the scanning process contains information about the monochromatic emission (ionized gas emitting at H α), the continuum emission of the object, as well as the velocity of the ionized gas.

³<http://cesam.lam.fr/fabryperot/index/software> developed by J. Boulesteix.

⁴IRAF: “Image Reduction and Analysis Facility” <http://iraf.noao.edu/>.

The computation of the image of the continuum was made considering the average of the 3 lowest intensities of the 48 channels of the cube (e.g. Vollmer et al. 2000; Fuentes-Carrera et al. 2004; Repetto et al. 2010; Rosado et al. 2013; Cárdenas-Martínez & Fuentes-Carrera 2018). For the monochromatic image, the intensity of the H α line was obtained by integrating the maximum value of the line profile for each pixel.

ADHOCw calculates the radial velocity fields using the barycentre of the profile of the H α line for each pixel with an accuracy for the central velocities of $\pm 5 \text{ km s}^{-1}$. We masked the velocity field including only a rectangular area that contains the part of the radial velocity map corresponding to NGC 6090. Then, we superimposed the radial velocity profiles on the resulting velocity field and masked the radial velocity field based on the signal-to-noise ratio of each pixel, whose values were in the range from 24 in the centre of the galaxy system down to 4 in the most external pixels.

In addition to the data cube, we obtained a direct H α image of NGC 6090 having the FP out of the optical path and with the same filter, with an exposure time of 90 seconds.

3. MONOCHROMATIC AND CONTINUUM IMAGES

On the DSS optical image of NGC 6090 (upper panel of Figure 1) we superimposed the direct H α image obtained with PUMA. The ionized gas emitting at H α that we detected was found within the central area of the object, which has 20.32 arcsec per side, i.e. 16 pixels per side, where 1 pix = 1.27 arcsec = 0.726 kpc. The mean heliocentric radial velocity that we determined for the galactic system NGC 6090 is 8885 km s $^{-1}$. We did not detect ionized gas emitting in H α in the tidal tails (antennae), so we limited our kinematic analysis to the central area of NGC 6090 disregarding the antennae. In the bottom panel of Figure 1 we show the NICMOS/HST 2.22 μm image whose 22 arcsec field of view matches our results.

To visualize the morphology of NGC 6090 that the PUMA data show the contours of the H α continuum (Figure 2 left panel) and monochromatic (Figure 2 right panel) emissions of NGC 6090 were superposed on the NICMOS/HST image.

The coordinates of the continuum maximum of NGC 6090 NE are $\alpha_{J2000} = 16^{\text{h}}11^{\text{m}}40.8^{\text{s}}$, $\delta_{J2000} = +52^{\circ}27'27''.32$, and the maximum H α monochromatic emission occurs at $\alpha_{J2000} = 16^{\text{h}}11^{\text{m}}40.8^{\text{s}}$, $\delta_{J2000} = +52^{\circ}27'27''.0$. For NGC 6090 NE we can observe that the ionized gas

emitting in H α has a greater presence towards the west, i.e. towards its companion galaxy. But the isophotes of the continuum show that the stellar population has a greater presence towards the east. In addition, we note that the isophotes of the continuum are symmetrical with respect to the photometric position angle (PA), which is the angle of the major axis of the continuum with respect to the north in a counter-clockwise direction and whose value is $\simeq 0^{\circ}$. The pattern of the isophotes suggests the likely presence of a stellar bar.

For the galaxy NGC 6090 SW, the coordinates of the photometric maximum are $\alpha_{J2000} = 16^{\text{h}}11^{\text{m}}40.4^{\text{s}}$, $\delta_{J2000} = +52^{\circ}27'22''.21$ and the coordinates of the H α monochromatic maximum are $\alpha_{J2000} = 16^{\text{h}}11^{\text{m}}43.3^{\text{s}}$, $\delta_{J2000} = +52^{\circ}27'23''.0$. For this galaxy, we note that the continuum has a greater presence towards the south, the opposite side of its companion, and also that it is accumulated towards the opposite direction of its H α maximum emission. Moreover, we note that the H α monochromatic maximum is nearer to the the knot described in the literature as the maximum of the 2.22 μm image (e.g. Dinshaw et al. 1999) than the photometric centre of the galaxy; this has created controversy in the literature about the position of the nuclei of NGC 6090 SW.

4. KINEMATIC RESULTS

4.1. Velocity Fields

In the previous section it was shown that the ionized gas emitting at H α does not have the same morphology as the continuum emission. As a consequence of this phenomenon, due to the interaction between the galaxies, we do not expect that all the photometric and kinematic parameters will exactly match. In Figure 3, which shows the velocity field of NGC 6090 (with its isovelocity contour curves and the 2.22 μm image superposed) it is possible to notice the velocity field of two independent galaxies, i.e. NGC 6090 presents two velocity fields ordered roughly on each one of its photometric maxima. Also, each velocity field has distortions towards the outside, mainly toward the northern side of both galaxies.

For NGC 6090 NE, the values of the radial velocities within its ordered velocity field, which reaches a radius of $R = 5.6$ arcsec, lie in the range from 8783 to 8919 km s $^{-1}$. For NGC 6090 SW, the radial velocities lie in the range from 8799 to 9143 km s $^{-1}$ within its velocity field ordered up to a radius of $R = 4.5$ arcsec. Furthermore, Figure 3 for NGC 6090 NE, shows that the isovelocity contour curves of the disc of the galaxy are not symmetric with respect to the kine-

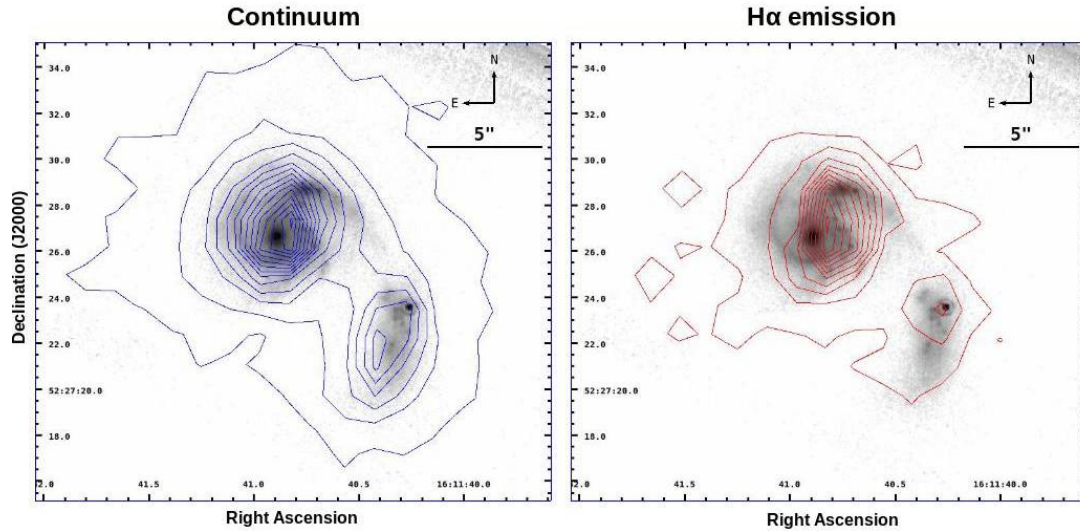


Fig. 2. Left: contours of the continuum linearly spaced from 1500 to 10000 ADU obtained from the $H\alpha$ data cube by the scanning FP interferometer, PUMA, overlaid on the NICMOS/HST $2.22 \mu\text{m}$ image in a 22 arcsec field of view centred on NGC 6090. Right: contours of the $H\alpha$ monochromatic image linearly spaced from 4000 to 240000 ADU obtained with PUMA, overlaid on the NICMOS/HST $2.22 \mu\text{m}$ image in a 22 arcsec field of view centred on NGC 6090. The color figure can be viewed online.

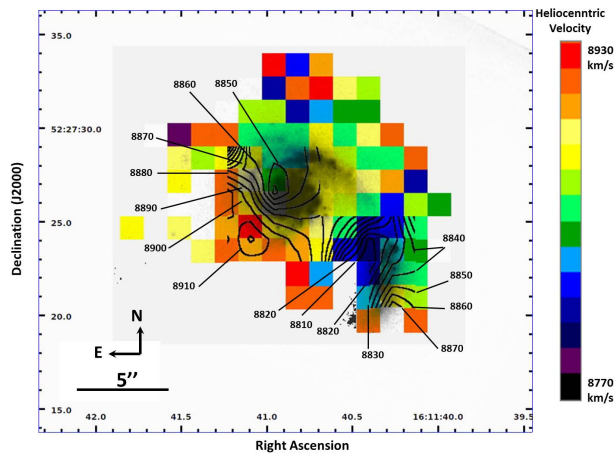


Fig. 3. Velocity field acquired with the $H\alpha$ data cube observation obtained with the scanning FP interferometer, PUMA, in a 26 arcsec field of view centred in NGC 6090. On the velocity field are overlaid, firstly, the NICMOS/HST $2.22 \mu\text{m}$ image and, secondly, the isovelocity contours of each galaxy which are linearly spaced by a factor of 10 starting from 8810 km s^{-1} . Each isovelocity is labelled in km s^{-1} units. The color figure can be viewed online.

matic minor axis. This feature, added to the morphology indicated by the continuum contours described in the previous section, suggests the pres-

ence of a stellar bar, in agreement with the criteria proposed by Bosma (1981).

4.2. Rotation Curves

From the morphological and kinematic features described in previous sections, we can argue that we have detected two independent galaxies inside the NGC 6090 galactic system. In this kind of interacting systems the radial motions, such as inflows/outflows or motions perpendicular to the galactic disc, are second order effects, otherwise the discs would be destroyed. We started studying the circular motion of each galaxy in NGC 6090, which corresponds to the most basic motion that can be assumed in a disc galaxy. In this way, the rotation curve of each galaxy was obtained from the kinematic data acquired with our FP observations using the ADHOCw software, which computes the radial velocity of the galaxies in every single pixel using the bary centre of the $H\alpha$ profile observed in each pixel.

In doing so, we use the geometric and kinematic assumptions proposed by Mihalas & Binney (1981). Supposing that each galaxy has a well-defined disc and that the system rotates about an axis that is perpendicular to the galactic plane which is inclined an angle i to the plane of the sky; we use the polar coordinate systems (R, θ) in the plane of the galaxy

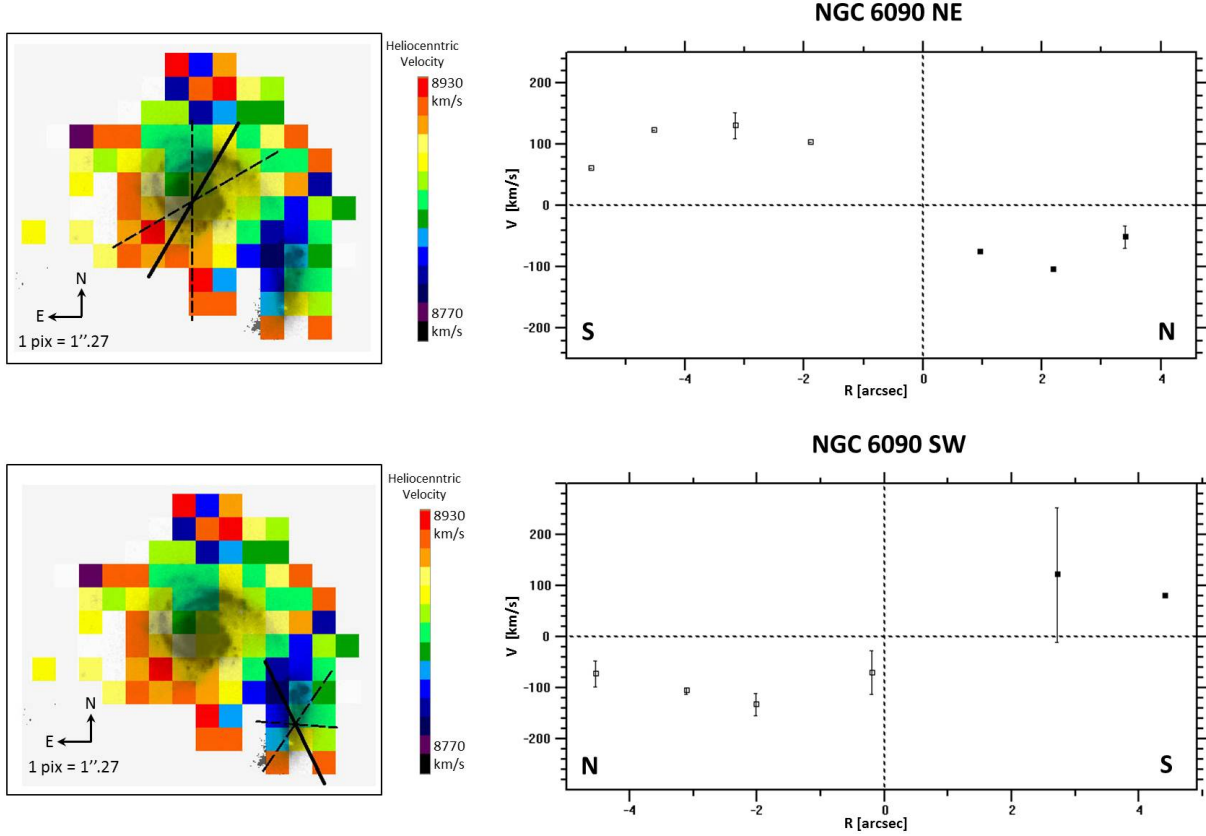


Fig. 4. Left panels show the velocity maps acquired with the H α data cube obtained with the scanning FP interferometer, PUMA, in a 22 arcsec field of view. On these maps was superposed the NICMOS/HST 2.22 μ m image as a frame of reference for the position of galaxy components in the galactic pair; then, on each map, the solid line represents the major kinematic axis which indicates the kinematic PA, and the dashed lines represent the sector angle that was considered for the computation of the rotation curve of each galaxy: NGC 6090 NE above and NGC 6090 SW below. In the right panels are shown the rotation curves of each galaxy, obtained up to where the velocity field is ordered for each galaxy; the dispersion associated with the averaged value of pixels within the same sector is indicated with bars. The color figure can be viewed online.

and (ρ, ϕ) in the plane of the sky, locating the origin at the point where the rotation axis lies in the plane of the sky; the radial velocity (V_{obs}) measured at (ρ, ϕ) is $V_{obs}(\rho, \phi) = V_{sys} + V_r(R, \theta) \sin \theta \sin i + V_{\Theta}(R, \theta) \cos \theta \sin i + V_z(R, \theta) \cos i$, where $R^2 = \rho^2(\cos^2 \phi + \sec^2 i \sin^2 \phi)$ and $\tan \phi = \sec i \tan \theta$, with V_{sys} the mean heliocentric radial velocity of the system as a whole (that is, of its centre of mass); V_r and V_{Θ} are the radial and tangential velocities in the plane, respectively, and V_z is the velocity perpendicular to the plane. Given that rotation is generally the dominant form of motion in disc galaxies, we assume V_r and V_z equal to zero. Moreover, under the assumption that there is axial symmetry about the centre of galaxy, V_{Θ} will depend only on R . Thus, the tangential velocity in the plane of the galaxy (V_{Θ}) was obtained with the radial velocity V_{obs_k} of

the k th region on the galaxy in terms of observable quantities:

$$V_{\Theta}(R_k) = \frac{V_{obs_k} - V_{sys}}{\cos \theta_k \sin i}, \quad (1)$$

where R_k and θ_k are given in terms of the coordinates ρ_k and ϕ_k of the k th galaxy region on the sky which corresponds to the k th pixel of the velocity field that was obtained with our FP observations.

The ADHOCw software averages the measured velocity of the pixels that are at the same distance from the kinematic centre along the major axis, indicating the dispersion associated to this average with bars on the points of the rotational observed curves. In order to avoid strong dispersions associated to the points of the rotation curves the pixels within an angular sector along the kinematic major axis

TABLE 3

ROTATION CURVE PARAMETERS AND MASS RANGE OF EACH GALAXY IN THE NGC 6090 PAIR

Parameter	NGC 6090 NE	NGC 6090 SW
Coordinates (J2000)	$\alpha = 16^{\text{h}}11^{\text{m}}40.84^{\text{s}}$ $\delta = +52^{\circ} 27' 26''.94$	$\alpha = 16^{\text{h}}11^{\text{m}}40.42^{\text{s}}$ $\delta = +52^{\circ} 27' 22''.21$
Distance (Mpc)	118	118
Systemic velocity (km s^{-1})	8880	8890
Max. rotation velocity (km s^{-1})	130 ± 5	132 ± 5
Kinematic PA ($^{\circ}$)	150 ± 3	26 ± 3
Inclination ($^{\circ}$)	13.9 ± 0.5	64.8 ± 0.5
Radius (arcsec)	5.6	4.5
Radius (kpc)	3.2	2.6
Mass (M_{\odot})	0.76×10^{10} to 1.26×10^{10}	0.63×10^{10} to 1.05×10^{10}

were considered (e.g. Fuentes-Carrera et al. 2004, 2007; Repetto et al. 2010) as shown in left panels of Figure 4. Then, assuming that each galaxy has a well-defined disc, due to its inclination it would look like an ellipse on the sky plane with apparent axis lengths a and b ; so, its inclination can be computed by $i = \cos^{-1}(b/a)$. We applied the ELLIPSE task of IRAF to the $2.22 \mu\text{m}$ image to estimate the inclination of the galaxies from the isophotal ellipses traced on these images. Finally, we considered that the systemic velocity of each galaxy is in agreement with the radial velocity of its own kinematic centre.

Table 3 contains the parameters used to calculate the rotation curve of each galaxy. The listed values correspond to those values with which we obtained the rotation curves from our observations; changes in these values would result in scattered points in the rotation curves instead of symmetric rotation curves.

The rotation curve of NGC 6090 NE presented in the upper right panel of Figure 4 was obtained with pixels in the velocity field within an angular sector of 30° around the kinematic major axis of the galaxy as marked in the upper left panel of Figure 4. The physical coordinates of the kinematic centre, derived as the position around the photometric centre at which the scatter in rotation curve is minimized, are $\alpha_{\text{J2000}} = 16^{\text{h}}11^{\text{m}}40.84^{\text{s}}$, $\delta_{\text{J2000}} = +52^{\circ} 27' 26''.94$. The kinematic centre used to compute the rotation curve in this galaxy matches the photometric centre within 0.4 arcsec. Using ADHOCw software, the kinematic parameters that give us the most symmetric, smooth and least scattered curve inside of the radius $R = 5.6$ arcsec are $PA = 150^{\circ} \pm 3$, $i = 13.9^{\circ} \pm 0.5$, and $V_{\text{sys}} = 8880 \text{ km s}^{-1}$. We determined that the heliocentric distance to this

galaxy is 118 Mpc through the Hubble law (Hubble 1936). The rotation curve shows that the north of the galaxy is blue-shifted, i.e. in the north side of NGC 6090 NE the gas approaches us, while in the south the gas moves away. Its maximum rotational velocity reaches $V_{\Theta \text{max}} = 130 \pm 5 \text{ km s}^{-1}$ at 3 arcsec to the south from its kinematic centre.

The rotation curve of NGC 6090 SW (bottom right panel of Figure 4) was obtained with pixels in the velocity field within an angular sector of 60° around the kinematic major axis of the galaxy. The physical coordinates of the kinematic centre are $\alpha_{\text{J2000}} = 16^{\text{h}}11^{\text{m}}40.42^{\text{s}}$, $\delta_{\text{J2000}} = +52^{\circ} 27' 22''.21$. The kinematic centre used to compute the rotation curve in this galaxy matches the photometric centre within 0.77 arcsec. The kinematic parameters that reduce significantly the asymmetry and scatter in the rotation curve inside of radius $R = 4.5$ arcsec were, in this case, $PA = 26^{\circ} \pm 3$, $i = 64.8^{\circ} \pm 0.5$, and $V_{\text{sys}} = 8890 \text{ km s}^{-1}$. Just as we calculated the heliocentric distance for NGC 6090 NE, we have obtained that the heliocentric distance of NGC 6090 SW is 118 Mpc. The rotation curve of NGC 6090 SW shows that the north side is blue-shifted as well as the northeastern galaxy. The maximum rotational velocity of NGC 6090 SW is $V_{\Theta \text{max}} = 132 \pm 5 \text{ km s}^{-1}$ at 2 arcsec to the north from its kinematic centre.

In the rotation curve of NGC 6090 SW there is a point on the receding side with a high dispersion associated to the average of the radial velocities computed using only two pixels of the velocity field; the pixel on the kinematic centre considered the framework to draw the radial velocities in the rotation curve and hence, considered the point with the lowest radial velocity value, and the pixel at the south-

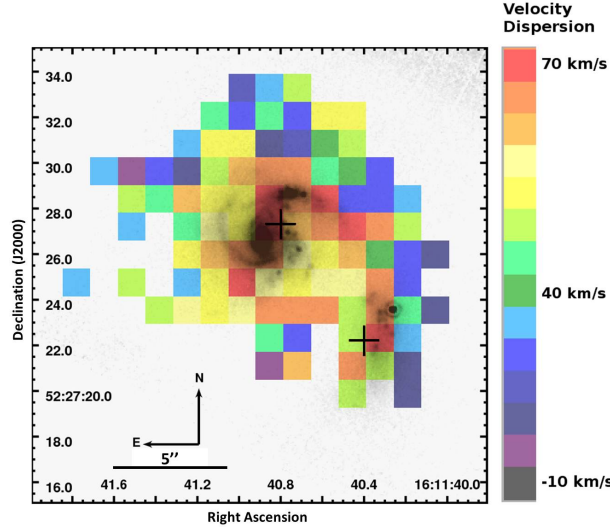


Fig. 5. Velocity dispersion map obtained using the PUMA in a 22 arcsec field of view centred on NGC 6090 superposed on the NICMOS/HST 2.22 μm image. Symbols ‘+’ represent the photometric centre of each galaxy. The color figure can be viewed online.

west of the kinematic centre with the highest radial velocity value of the velocity field of the entire system. Despite that, we decided to use this point only to get a better view of the rotation curve of this galaxy toward the south.

4.3. Velocity Dispersion Field

Through the full width at half maximum (FWHM) of Gaussian functions fitted to the velocity profile of the H α line in each pixel we obtained the velocity dispersion map of the galaxy system. Figure 5 displays the velocity dispersion map of NGC 6090 with the NICMOS/HST image overlaid. In NGC 6090 NE the velocity dispersion increases gradually from $\approx 45 - 55 \text{ km s}^{-1}$ in the eastern side of the galaxy, to $59 - 66 \text{ km s}^{-1}$ in the centre, and then up to 75 km s^{-1} in its north-western spiral arm near to what might look like a bridge between the galaxies. In NGC 6090 SW, the velocity dispersion maximum is 85 km s^{-1} next to the position of its photometric centre. Then, in its surroundings the velocity dispersion range is $\approx 40 \text{ km s}^{-1}$ increasing to the north, where it is $\approx 69 \text{ km s}^{-1}$.

In the north side of the galaxy system and between both galaxies, broader profiles were noticed through double radial velocity profiles with a low signal to noise ratio, detected with PUMA and mainly

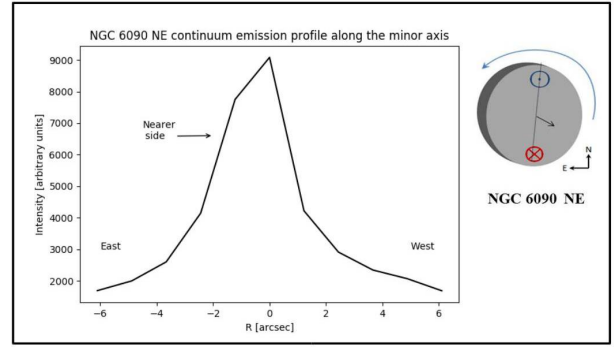


Fig. 6. Intensity profile of the continuum map of NGC 6090 NE along the minor axis centred on the galactic photometric centre. Following the gradient criterion of Pasha (1985), the far side of the galaxy would be the one that decreases more smoothly. Therefore, the nearest side to the observer of NGC 6090 is the eastern one. The top-right panel shows a schematic 3D orientation of NGC 6090 NE derived from our kinematic analysis. The color figure can be viewed online.

located in the bridge zone. Those broader profiles were already detected by Cortijo-Ferrero et al. (2017) and interpreted as a consequence of shocks in early-stage mergers. This feature of the velocity dispersion field indicates that NGC 6090 has an interaction bridge between its galaxies. Those pixels with double velocity profiles are outside of the ordered velocity field of each galaxy, so that they do not contribute at any point in the computation of the rotation curves. Moreover, given their low signal to noise ratio we do not consider them in this work.

4.4. The Rotation Sense of NGC 6090 NE

Radial-velocity measurements cannot by themselves distinguish leading and trailing spirals in thin disks. To determine whether a given galaxy leads or trails, we must determine which side of the galaxy is closer to us. Thus, to determine if the galaxies in NGC 6090 lead or trail, we followed the gradient criterion of Pasha (1985): the apparent brightness of the nuclear region falls off unequally from the centre outward along the minor axis, the far side being the one where the surface-brightness profile declines more smoothly. This means that if the inner disc is dusty, it absorbs a significant fraction of the starlight passing through it, then the surface brightness of the bulge at a given distance along its apparent minor axis will be lower on the near side (Binney & Tremaine 1987). In this way, for each galaxy in the

NGC 6090 pair the intensity profile of the continuum emission was obtained along their minor axis in order to determine the rotation sense of each one.

For NGC 6090 NE, we extracted the intensity profile of the continuum from its minor photometric axis (see Figure 2 in § 3), as shown in Figure 6. This profile indicates that the side nearest to the observer is the eastern side of the galaxy. Then, considering that the rotation curve indicates that the gas on the northern side is blue-shifted and, availing us of the dust lanes which trace the arms structure of this galaxy (see right panel of Figure 1), we can infer that this galaxy has its arms rotating in a trailing direction.

On the other hand, for NGC 6090 SW it was not possible to obtain an accurate result through which we might determine its rotation sense, due to the low number of pixels with continuum emission along its minor axis. In addition, the image of 2.22 μm does not clearly mark the structure of spiral arms.

5. MASS ESTIMATES USING DYNAMICAL ANALYSIS

A range of possible values for the mass of each galaxy in the NGC 6090 system was calculated using the approach described by Lequeux (1983), as has been done before when studying pairs of galaxies (e.g. Amram et al. 1992; Fuentes-Carrera et al. 2007; Repetto et al. 2010). This approach consists in calculating the mass $M(R)$ up to a certain radius where the rotation velocity $V(R)$ has been measured. The method considers two extreme cases to evaluate the mass of galaxies: the galaxy as a flat disc or the galaxy as a spherical system. Thus, the mass of the spiral galaxies is in the range of $M(R) = \kappa R V^2(R)/G$, where G is the gravitational constant and the coefficient κ is a constant in the range (0.6, 1.0), whose limiting values correspond to the galaxy being dominated by a flat disc or by a massive spherical halo, respectively.

Thus, from the NGC 6090 NE rotation curve, the maximum rotation velocity of this galaxy is $V_{NE} = 130 \text{ km s}^{-1}$ which is reached at a radius of $R = 2.47 \text{ arcsec}$. For this galaxy the mass range obtained is $M_{NE} = 1.26\kappa \times 10^{10} M_{\odot}$. From the NGC 6090 SW rotation curve, the maximum rotation velocity is $V_{SW} = 132 \text{ km s}^{-1}$ reached at $R = 1.97 \text{ arcsec}$. For this galaxy the mass range is $M_{SW} = 1.05\kappa \times 10^{10} M_{\odot}$. Therefore, the sum of both masses when both galaxies are dominated by a massive spherical halo is $M_{sph} = 2.31 \times 10^{10} M_{\odot}$, and when both galaxies are dominated by flat disc, the mass is $M_{flat} = 1.39 \times 10^{10} M_{\odot}$.

When two galaxies of roughly equal mass have an encounter, their extended halos may merge to form a common halo. Then, the galaxies are expected to orbit in a common halo until dynamical friction and tidal interactions remove sufficient orbital energy for the galaxies to merge (e.g. Binney & Tremaine 1987; Mo et al. 2010). Thus, due to the active state of interaction of the galaxies in NGC 6090 it is possible to infer that they are dominated by a flat disc individually, but a further study on the dynamics of this encounter would be necessary to dismiss the case in which both galaxies are dominated by a spherical halo.

A second independent way of obtaining the mass value of a pair of galaxies is the method proposed by Karachentsev (1987), which calculates the mass from the relative orbital motion of the components. This method consists of assuming that the components of the pair move in a circular orbit with a velocity V_{12} and a spatial separation r . When V_{12} and r are transformed into observable quantities, they become the difference of the velocity projected in the line of sight, $y = V_{12} \sin i \cos \Omega$, and the separation projected on the sky plane, $X = r(1 - \sin^2 i \sin^2 \Omega)^{1/2}$, where i is the angle between the plane of the orbit and the plane of the sky, and Ω the angle between the line of sight and the line connecting both galaxies of the pair. For circular motion, Karachentsev (1987) obtained the projection factor $\langle \eta \rangle = 3\pi/32$. Therefore, the total mass of the pair is:

$$M = \frac{32}{3\pi} \frac{X y^2}{G}, \quad (2)$$

where G is the gravitational constant. As y and X depend on a sinusoidal function, in order to obtain the upper limit of mass with this method without loss of generality, we assumed that the orbital plane has an inclination of $i = 90^\circ$. Then, the angle between the line of sight and the line connecting the pair is $\Omega = \sin^{-1}(L/D)$, where $L = 4.1 \text{ kpc}$ is the distance of the nuclei projected on the sky plane and $D = 133.1 \text{ kpc}$ is the size of the line connecting the galaxies, which results in $\Omega = 1.76^\circ$. Thus, the velocity projected on the line of sight and the separation projected on the sky plane is $y \approx V_{12}$ and $X \approx r$. Assuming a circular orbit, the total mass would be:

$$M_{\text{orbital}} = \frac{32}{3\pi} \frac{r V_{12}^2}{G}, \quad (3)$$

where V_{12} is the difference between the velocities of the galaxies, and r is the projected separation between the nucleus of each galaxy. For the system NGC 6090 we have, $V_{12} = 10 \text{ km s}^{-1}$

and $r = 4.1$ kpc. Therefore, the orbital mass is $M_{\text{orbital}} = 3.23 \times 10^8 M_{\odot}$, which is two orders of magnitude smaller than the sum of the individual masses obtained with the method proposed by Lequeux (1983). We think that this low value of the mass is due to the fact that the projected velocity difference V_{12} is quite small.

6. DISCUSSION

At optical wavelengths, NGC 6090 appears as a double nuclei system with two curved antennas (tidal tails), so that this galaxy system has been described as similar to NGC 4038/39 (the Antennae) (e.g. Toomre & Toomre 1972; Martin et al. 1991; Mazzarella & Boroson 1993; Dinshaw et al. 1999; Bryant & Scoville 1999). With the goal of studying kinematic similarities between both systems produced by the interaction of their own galaxies, we studied the H α kinematics of NGC 6090 using the scanning Fabry-Perot interferometer, PUMA. The H α kinematics of the galaxy pair the Antennae has been studied through observations obtained with another FP by Amram et al. (1992). In neither galaxy system, NGC 6090 and the Antennae, was emission of ionized hydrogen detected in their tidal tails, i.e. in both galaxy systems ionized gas emitting at H α was only detected in the central zone. Therefore, Amram et al. (1992) performed a kinematic analysis of the disc of the Antennae, as we have done for NGC 6090 in this paper.

Amram et al. (1992) reported that in the Antennae, ionized gas emitting at H α is deficient compared with its continuum emission, but that the emissions tend to grow toward its part farthest from its companion. Then, the Antennae nuclei matched unambiguously with observations at $2.2 \mu\text{m}$. The velocity field is not ordered throughout the system; none of its component galaxies show the behaviour of a rotating disc. Additionally, there were no detected pixels with double velocity profiles. Finally, using the Lequeux (1983) method to measure the mass of the galaxies, Amram et al. (1992) found that the individual masses of the galaxies in the Antennae are approximately $2 \times 10^{10} M_{\odot}$.

For NGC 6090, in § 3 we noted that the intensity of ionized gas emitting in H α is lower with respect to that of the continuum; but within each galaxy, the ionized hydrogen gas is situated near to its companion, while the old stellar population is lagging in the opposite direction. The positions of the nuclei reported at $2.22 \mu\text{m}$ by Dinshaw et al. (1999), the HI continuum maxima reported by Condon et al.

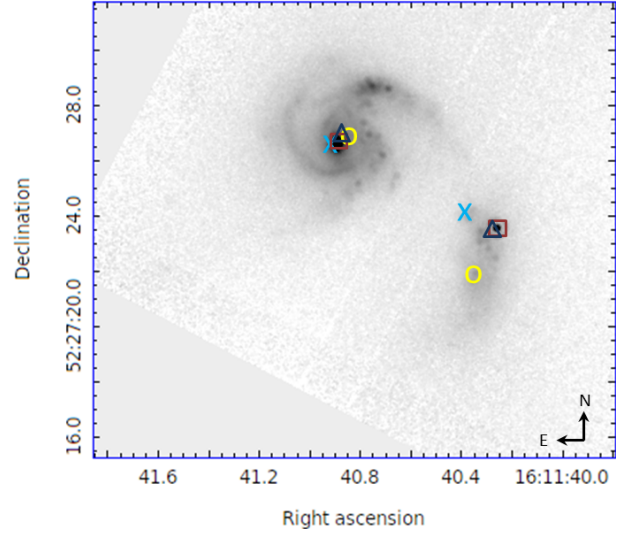


Fig. 7. NICMOS/HST image at $2.22 \mu\text{m}$ of a field of view of 16 arcsec centered at NGC 6090. In this image we have marked the positions of the maximum emissions of the continuum (O), the H α monochromatic emission (Δ), the radio continuum (X) and the infrared (\square). The color figure can be viewed online.

(1990), and the monochromatic and continuum H α maxima that we obtained in this paper are marked on the NICMOS/HST image in Figure 7.

For NGC 6090 NE, we found that the maxima of the monochromatic and continuum of the PUMA observations almost completely coincide and match the kinematic centre (within 0.4 arcsec). In Figure 7 we show that the differences between the position of the nucleus of this galaxy reported in the literature and our results are minimal.

However, for the galaxy NGC 6090 SW the maxima of the continuum and the monochromatic emissions derived from our observations of the ionized gas emitting in H α are not nearly in the same position as those in NGC 6090 NE. This galaxy presents greater emissions of ionized hydrogen towards the north than the south, so that the photometric maximum is located to the south, while the maximum monochromatic emission is in the north. Thus, for NGC 6090 SW, the position of the monochromatic emission maximum is $\alpha_{J2000_{\text{H}\alpha}} = 16^{\text{h}}11^{\text{m}}40.3^{\text{s}}$, $\delta_{J2000_{\text{H}\alpha}} = +52^{\circ}27'23''$, and the maximum of the continuum is $\alpha_{J2000_{\text{cont}}} = 16^{\text{h}}11^{\text{m}}40.4^{\text{s}}$, $\delta_{J2000_{\text{cont}}} = +52^{\circ}27'22''$, which match the kinematic centre and the velocity dispersion maximum. The maximum of the $2.22 \mu\text{m}$ emission is at $\alpha_{J2000} = 16^{\text{h}}11^{\text{m}}40.3^{\text{s}}$, $\delta_{J2000} = +52^{\circ}27'23''$ (Dinshaw et al. 1999), and

TABLE 4

MASSES OF THE GALAXY SYSTEM NGC 6090 FOUND IN THE LITERATURE AT DIFFERENT WAVELENGTHS COMPARED WITH THE ONES FOUND IN THIS WORK

Author	Phase of the IM observed	Mass [$M_{\odot} \times 10^{10}$]
Sanders et al. (1991)	H ₂	1.4
Bryant & Scoville (1999)	H ₂ (dyn)	0.46
	H ₂ (gas)	2.29
Hummel et al. (1987)	HI	3.9
Chisholm et al. (2016a)	MIR	5.02
Cortijo-Ferrero et al. (2017)	MIR	4.2
Cortijo-Ferrero et al. (2017)	3650 – 6950 Å	6.8
This work	H α _{sum flat disc}	1.39
	H α _{sum sph halo}	2.31
	H α _{orbital}	0.032

the maximum radio continuum is at $\alpha_{J2000} = 16^{\text{h}}11^{\text{m}}40.8^{\text{s}}$, $\delta_{J2000} = +52^{\circ}27'27''$ (Hummel et al. 1987; Condon et al. 1990).

Dinshaw et al. (1999) compared the position of the brightest point in the 2.22 μm image with the maximum of the radio-continuum of this galaxy; they proposed that the infrared peak could be a field star. However, the emission of a field star could not be detected as the maximum of the redshifted H α line of our observations of NGC 6090. Therefore, it may be concluded that the infrared maximum for the southwestern galaxy is a component itself. This possibility is supported by Cortijo-Ferrero et al. (2017), who argued that the main absorption lines of their observations in the range from 3700 to 7100 Å at the knot of 2.22 μm have the same redshift as the galaxy. However, Cortijo-Ferrero et al. (2017) obtained that the position of the continuum maximum is southward of the infrared peak, near where we detected the continuum maximum, the kinematic centre and the velocity dispersion maximum of NGC 6090 SW. Thus, taking the maximum of the H α continuum as the nucleus of the southwest galaxy, we determined that the separation of the nuclei of the two members of NGC 6090 is 7.11 arcsec. Assuming that the average distance of the galaxy system NGC 6090 is 118 Mpc, the distance between its nuclei is 4.1 kpc.

Regarding the velocity field of NGC 6090, we said in § 4.1 that this galaxy system has two ordered velocity fields which allowed us to compute the rotation curves of each galaxy in the NGC 6090 system. The rotation curves have maximum rotational velocity larger than the dispersion or residual velocity

fields: the northeast galaxy has a maximum rotational velocity $V_{NE} = 130 \text{ km s}^{-1}$ and its velocity dispersion is in the range $\approx 45 - 66 \text{ km s}^{-1}$ inside of its disc; meanwhile NGC 6090 SW has a maximum rotational velocity $V_{SW} = 132 \text{ km s}^{-1}$, with its velocity dispersion in the range $\approx 40 - 69 \text{ km s}^{-1}$ inside the disc. Both galaxies reach their maximum velocity dispersion outside the disc, but even these values were less than their maxima rotational velocities.

Furthermore, with the continuum map obtained from our observations, with the asymmetric isoveLOCITIES contour curves, and the non-circular motions that we detected in NGC 6090 NE, we confirmed the assumption about the presence of a bar structure in this galaxy made in the infrared by Dinshaw et al. (1999) (see figure 2 of their paper) and at optical wavelengths by Cortijo-Ferrero et al. (2017).

In their paper, Amram et al. (1992) concluded that the encounter of the galaxies that make up the Antennae is in an advanced stage of interaction. In the case of NGC 6090, the features that we have discussed about its two ordered velocity fields, continuum and monochromatic maps, and the behaviour of its velocity dispersion field that signals an interaction bridge between galaxies, allow us to conclude that NGC 6090 is a system in a less advanced stage of interaction than the Antennae, although both systems are in an interaction stage previous to a merger.

Regarding the mass values, Table 4 contains the values of the masses reported in the literature for the NGC 6090 system at different wavelengths compared to our results. The range of the sum of independent masses estimated in this paper from the rota-

tion curves of each galaxy obtained with the method of Lequeux (1983) is of the same order of magnitude as the masses estimated by other authors in the infrared (Sanders et al. 1991; Bryant & Scoville 1999; Chisholm et al. 2016a; Cortijo-Ferrero et al. 2017) and radio continuum (Martin et al. 1991), which were determined by means of the mass-to-light ratio. However, the mass of the NGC 6090 system calculated with the method proposed by Karachentsev (1987) is two orders of magnitude smaller than the former values, and an order of magnitude smaller than the dynamic mass estimated by Bryant & Scoville (1999).

The sum of the masses computed from the maximum rotation velocity is of the same order of magnitude as the masses acquired from the mass-to-light ratio at other wavelengths. They also coincide with the value determined by Sanders et al. (1991) and Bryant & Scoville (1999), both if each galaxy is dominated by a flat disc or a spherical halo. Hence, we can argue that the kinematic parameters that we obtained in this work are reliable. The difference of an order of magnitude in the orbital mass can be consequence to our geometrical assumptions of the movement of NGC 6090 SW around of its companion.

Most of the numerical simulations have assumed similar initial conditions to model different features of the Antennae (e.g. Toomre & Toomre 1972; Barnes 1988; Teyssier et al. 2010; Renaud et al. 2008, 2015), either its morphology or the formation of star clusters during the merger. They obtain always the same feature: two long tidal tails that form the antennae. Therefore, in general, the symmetry of the tidal action allows the formation of four arms if the two companions are disc galaxies; when the masses of the two interacting galaxies are equal or similar, the two internal spiral arms join up to form a bridge, while the two external arms are drawn into two *antennae* which remain for one or two billion years (Combes et al. 2002). This phenomenon is happening to the galaxies of NGC 6090, which have similar mass values. We note the two tidal tails and the bridge between them, well defined by the northwestern arm of NGC 6090 NE.

Finally, Sugai et al. (2004) observed young starbursts occurring in regions offset from the galactic nuclei to the northwestern spiral arm of NGC 6090 NE. They inferred that if NGC 6090 NE had its arms trailing, the molecular gas clouds were just finishing an interaction with the central molecular gas. In § 4.4 we showed that the spiral arms in the

north-eastern galaxy are trailing, favoring this theory. Another likely consequence of the trailing arms of NGC 6090 NE could be the outflow at the north-eastern side of NGC 6090 SW detected by Chisholm et al. (2016b) in the UV band (see Figure 1 of their paper), which coincides with a region of high H α velocity dispersion in NGC 6090 SW, which could have been formed by ram pressure during the interaction.

7. CONCLUSIONS

In this paper we present our observations of the ionized gas emitting at H α of the isolated pair of galaxies NGC 6090 (KPG 486) carried out with the scanning Fabry-Perot interferometer, PUMA. This emission was detected solely in the central area of the system. Through our observations we obtained the monochromatic emission (ionized gas emitting at H α), the continuum, the velocity field and the velocity dispersion maps. The velocity field of NGC 6090 shows two regions with ordered isovelocity contour curves from which we computed the rotation curve of each galaxy of the pair.

Using the rotation curves we obtained the maximum rotation velocity, the mass of each galaxy, and the mass of the galaxy system. The sum of the individual masses that we calculated is consistent with the masses found in the literature, obtained with the mass-to-light ratio for different wavelengths. In addition, we obtained the orbital mass of NGC 6090, which differs by two orders of magnitude from the sum of the individual masses. We conclude that this difference is due to projection effects.

In addition, enough emission was detected in the northeast galaxy to observe specific characteristics therein. In this galaxy, the isophotes of the continuum show signs of a stellar bar; the velocity field shows no symmetry with respect to the minor axis, which again suggests that this galaxy has a stellar bar. It was also possible to conclude that the arms of the NGC 6090 NE galaxy rotate in a trailing direction.

We concluded that the photometric centre of the southwest galaxy is in a location different from those reported of radio and infrared wavelengths, which were inconsistent. Furthermore, the maximum of ionized gas emitting at H α and the maximum of the 2.22 μm coincide, confirming that this knot is part of the galaxy, and therefore cannot be a field star. However, we were not able to study the morphological characteristics of the southwestern galaxy due to the size of the emission area that was detected.

As regards optical wavelength images of NGC 6090, the system is similar to the Antennae (NGC 4038/39), while also it has been defined as a merger. In this paper we have discussed the kinematic differences between these galaxy systems from observations made at the same wavelength with similar instruments. This allowed us to conclude that their differences are mainly due to the stage of interaction of the galaxies that make up these systems. Through the kinematic analysis of NGC 6090 we concluded that these galaxies are in a stage of merger earlier than that of the galaxies in the Antennae.

Our research was carried out thanks to the Program UNAM-DGAPA-PAPIIT IN109919.

The authors express their gratitude to the Mexican National Council for Science and Technology (CONACYT) for financing this paper through project CY-109919.

This paper is based on observations performed with the scanning Fabry-Perot interferometer, PUMA, at the Observatorio Astronómico Nacional on Sierra San Pedro Mártir (OAN-SPM), Baja California, México.

We thank the day - and night time support staff at OAN-SPM for facilitating and helping us to obtain our observations.

The Digitized Sky Surveys were produced at the Space Telescope Science Institute under U.S. Government Grant NAG W-2166. The images of these surveys are based on photographic data obtained using the Oschin Schmidt Telescope on Palomar Mountain and the UK Schmidt Telescope. The plates were processed into the present compressed digital form with the permission of these institutions.

REFERENCES

- Acosta-Pulido, J. A., Klaas, U., Laureijs, R. J., et al. 1996, *A&A*, 315, L121
- Amram, P., Marcelin, M., Boulesteix, J., & Le Coarer, E. 1992, *A&A*, 266, 106
- Amram, P., Plana, H., Mendes de Oliveira, C., Balkowski, C., & Boulesteix, J. 2003, *A&A*, 402, 865
- Arp, H. 1966, *ApJS*, 14, 1
- Barnes, J. E. 1988, *ApJ*, 331, 699
- Barnes, J. E. & Hernquist, L. 1992, *ARA&A*, 30, 705
- Binney, J. & Tremaine, S. 1987, *Galactic dynamics*, Princeton, N.J. : Princeton University Press
- Bosma, A. 1981, *AJ*, 86, 1825
- Bryant, P. M. & Scoville, N. Z. 1999, *AJ*, 117, 2632
- Cárdenas-Martínez, N. & Fuentes-Carrera, I. 2018, *ApJ*, 868, 141
- Chamberlain, J. W. 1961, *Physics of the aurora and airglow*, International Geophysics Series, New York: Academic Press
- Chisholm, J., Tremonti, C. A., Leitherer, C., Chen, Y., & Wofford, A. 2016a, *MNRAS*, 457, 3133
- Chisholm, J., Tremonti, C. A., Leitherer, C., Chen, Y., Wofford, A., & Lundgren, B. 2015, *ApJ*, 811, 149
- Chisholm, J., Tremonti Christy, A., Leitherer, C., & Chen, Y. 2016b, *MNRAS*, 463, 541
- Combes, F., Boisse, P., Mazure, A., Blanchard, A., & Seymour, M. 2002, *Galaxies and cosmology*, 2nd ed. by F. Combes et al. (M. Seymour, Trans.). New York: Springer
- Condon, J. J., Helou, G., Sanders, D. B., & Soifer, B. T. 1990, *ApJS*, 73, 359
- Cortijo-Ferrero, C., González Delgado, R. M., Pérez, E., et al. 2017, *MNRAS*, 467, 3898
- Dinshaw, N., Evans, A. S., Epps, H., Scoville, N. Z., & Rieke, M. 1999, *ApJ*, 525, 702
- Epinat, B., Amram, P., Marcelin, M., et al. 2008, *MNRAS*, 388, 500
- Fuentes-Carrera, I., Cárdenas-Martínez, N., Sánchez-Cruces, M., 2015, *IAUS*, 309, 314
- Fuentes-Carrera, I., Rosado, M., Amram, P., et al. 2004, *A&A*, 415, 451
- Fuentes-Carrera, I., Rosado, M., Amram, P., Salo, H., & Laurikainen, E. 2007, *A&A*, 466, 847
- Gabbasov, R. F., Rosado, M., & Klapp, J. 2014, *ApJ*, 787, 39
- Günthardt, G. I., Díaz, R. J., & Agüero, M. P. 2016, *AJ*, 152, 150
- Hubble, E. 1936, *ApJ*, 84, 517
- Hummel, E., van der Hulst, J. M., Keel, W. C., & Kenicutt, Jr., R. C. 1987, *A&AS*, 70, 517
- Karachentsev, I. 1987, *Double galaxies*
- Krassovsky, V. I., Shefov, N. N., & Yarin, V. I. 1962, *Atlas of the airglow spectrum 3000-12400 A*
- Lequeux, J. 1983, *A&A*, 125, 394
- Makarov, D., Prugniel, P., Terekhova, N., Courtois, H., & Vauglin, I. 2014, *A&A*, 570, A13
- Martin, C. L. & Soto, K. T. 2016, *ApJ*, 819, 49
- Martin, J. M., Bottinelli, L., Gouguenheim, L., & Dennefeld, M. 1991, *A&A*, 245, 393
- Mazzarella, J. M. & Boroson, T. A. 1993, *ApJS*, 85, 27
- Mihalas, D. & Binney, J. 1981, *Galactic astronomy: Structure and kinematics*, 2nd edn.
- Mihos, C. 2000, *Galaxies: Interactions and Mergers*, ed. P. Murdin, 2623
- Miralles-Caballero, D., Colina, L., Arribas, S., & Duc, P.-A. 2011, *AJ*, 142, 79
- Mo, H., van den Bosch, F. C., & White, S. 2010, *Galaxy Formation and Evolution*
- NASA/IPAC. 2014, *NASA/IPAC Extragalactic Database (NED)*, <https://ned.ipac.caltech.edu/>
- Noguchi, M. 1987, *MNRAS*, 228, 635
- Pasha, I. I. 1985, *Soviet Astronomy Letters*, 11, 1
- Renaud, F., Boily, C. M., Fleck, J.-J., Naab, T., & Theis, C. 2008, *MNRAS*, 391, L98

- Renaud, F., Bournaud, F., & Duc, P.-A. 2015, MNRAS, 446, 2038
- Repetto, P., Rosado, M., Gabbasov, R., & Fuentes-Carrera, I. 2010, AJ, 139, 1600
- Rosado, M., Gabbasov, R., & Fuentes-Carrera, I. 2011, IAUS, 277, 259
- Rosado, M., Gabbasov, R. F., Repetto, P., et al. 2013, AJ, 145, 135
- Rosado, M., Langarica, R., Bernal, A., et al. 1995, RMxAC, 3, 263
- Salo, H. & Laurikainen, E. 2000a, MNRAS, 319, 377
- _____. 2000b, MNRAS, 319, 393
- Sanders, D. B., Scoville, N. Z., & Soifer, B. T. 1991, ApJ, 370, 158
- Schweizer, F. 1986, Science, 231, 227
- Sugai, H., Davies, R. I., Ishii, M., & Ward, M. J. 2000, MNRAS, 317, 447
- Sugai, H., Hattori, T., Kawai, A., et al. 2004, ApJ, 615, L89
- Teyssier, R., Chapon, D., & Bournaud, F. 2010, ApJ, 720, L149
- Toomre, A. & Toomre, J. 1972, ApJ, 178, 623
- Torres-Flores, S., Amram, P., Mendes de Oliveira, C., et al. 2014, MNRAS, 442, 2188
- Vollmer, B., Marcelin, M., Amram, P., Balkowski, C., Cayatte, V., & Garrido, O. 2000, A&A, 364, 532
- Vorontsov-Velyaminov, B. A., Noskova, R. I., & Arkipova, V. P. 2001, A&AT, 20, 717
- Wang, J., Zhang, Q., Wang, Z., Ho, P. T. P., Fazio, G. G., & Wu, Y. 2004, ApJ, 616, L67

Minerva Muñoz Sardaneta and Mónica Sánchez-Cruces: Aix Marseille Univ, CNRS, CNES, Laboratoire d'Astrophysique de Marseille (LAM). 38 rue F. Joliot-Curie, 13388 Marseille cedex 13 France (minerva.munoz@lam.fr).

Margarita Rosado: Instituto de Astronomía, Universidad Nacional Autónoma de México (UNAM). Apdo. Postal 70-264, 04510, Ciudad de México, México (margarit@astro.unam.mx).

THE ENVIRONMENTAL DEPENDENCE OF THE AGE OF ACTIVE GALAXIES AND THE DEPENDENCE OF THE CLUSTERING PROPERTIES OF ACTIVE GALAXIES ON AGE

Xin-Fa Deng and Xiao-Qing Wen

School of Science, Nanchang University, Jiangxi, China, 330031.

Received October 5 2019; accepted December 17 2019

ABSTRACT

We explore the environmental dependence of the age and the clustering-age dependence of active galaxies in two volume-limited active galaxy samples of the SDSS. In the luminous volume-limited sample, the age of active galaxies apparently depends on environments: at low density the fraction of young galaxies with ages less than 2 Gyr is significantly higher than the one in the high density case, at high density the fraction of old galaxies is significantly higher than the one at low density. Young active galaxies have a higher prevalence than old ones at small multiplicity, corresponding to isolated galaxies, close pairs and small groups, whereas old active galaxies have a higher prevalence in the multiplicity bins corresponding to dense groups and clusters. But in the faint volume-limited sample, although the environmental dependence of the age is fairly weak, a substantial clustering-age dependence can be observed.

RESUMEN

Exploramos la dependencia ambiental de la edad y la dependencia agrupamiento-edad de las galaxias activas de dos muestras, ambas limitadas por volumen, obtenidas del SDSS. En la muestra luminosa, la edad de las galaxias activas aparentemente depende del medio ambiente: cuando la densidad es pequeña, la fracción de galaxias jóvenes (< 2 giga-años) es mucho mayor que cuando la densidad es grande. A altas densidades la fracción de galaxias viejas es mucho mayor que a bajas densidades. Las galaxias activas jóvenes prevalecen sobre las viejas para multiplicidades bajas (galaxias aisladas, pares cerrados y grupos pequeños). En cambio, las galaxias activas viejas prevalecen sobre las jóvenes en los intervalos de multiplicidad correspondientes a grupos densos y cúmulos. En la muestra débil, la dependencia entre la edad y el medio ambiente es débil, si bien se observa una considerable dependencia entre la edad y el agrupamiento.

Key Words: galaxies: fundamental parameters — large-scale structure of Universe

1. INTRODUCTION

It has been known for a long time that there is a strong correlation between galaxy age and local density: galaxies in low-density regions are generally younger than galaxies in high-density regions (e.g., Bernardi et al. 1998; Trager et al. 2000; Kuntschner et al. 2002; Terlevich & Forbes 2002; Proctor et al. 2004; Mendes de Oliveira et al. 2005; Thomas et al. 2005; Gallazzi et al. 2006; Sánchez-Blázquez et al. 2006; Silchenko 2006; Rakos et al. 2007; Reed et al. 2007; Wegner & Grogin 2008; Smith et al. 2012;

Deng 2014). For example, Kuntschner et al. (2002) reported that at a given luminosity, the E/S0 galaxies in low-density regions are ≈ 2 -3 Gyr younger than the E/S0s in clusters. Smith et al. (2012) explored the variation in stellar population ages for Coma Cluster galaxies as a function of projected cluster-centric distance, and found that the average age of dwarfs at the 2.5 Mpc limit of their sample is approximately half that of dwarfs near the cluster centre. In two volume-limited Main Galaxy (Strauss et al. 2002) samples of the Sloan Digital Sky Survey

Data Release 10 (SDSS DR10) (Ahn et al. 2014), Deng (2014) investigated the environmental dependence of galaxy age, and obtained the same conclusions in two volume-limited Main Galaxy samples: old galaxies exist preferentially in the densest regions of the universe, while young galaxies are located preferentially in low density regions. Such a conclusion is in good agreement with the current hierarchical assembly paradigm, which predicts a younger age of galaxies in lower density environments (e.g., Lanzoni et al. 2005; De Lucia et al. 2006).

Many works shed light on the dependence of the clustering properties of galaxies on various galaxy parameters (Davis & Geller 1976; Loveday et al. 1995; Brown et al. 2000; Norberg et al. 2001, 2002; Zehavi et al. 2002, 2005, 2011; Zheng et al. 2007, 2009; Loh et al. 2010; Tinker et al. 2010; Wang et al. 2011; Deng 2013). For example, Brown et al. (2000) reported a strong dependence of the clustering properties of galaxies on their colors. Norberg et al. (2001, 2002) demonstrated that the clustering amplitude of the correlation function of galaxies increases with absolute magnitude. Using cluster analysis (Einasto et al. 1984), Deng et al. (2016) explored the dependence of the clustering properties of galaxies on galaxy age, and concluded that young galaxies preferentially form isolated galaxies, close pairs and small groups at all scales, whereas old galaxies preferentially inhabit dense groups and clusters. This actually showed the environmental dependence of galaxy age by an alternative approach.

In the last several decades, many works have focused on the study of active galactic nuclei (AGNs) (Dressler et al. 1985; Miller et al. 2003; Krumpke et al. 2012; Enoki et al. 2014; Kagaya et al. 2017; Chen et al. 2018; Liu et al. 2019; Zou et al. 2019). Dressler et al. (1985) and Miller et al. (2003) explored the correlation between the presence of AGNs and the local environment of AGN host galaxies. Krumpke et al. (2012) measured the clustering amplitudes of both X-ray-selected and optically selected SDSS broad-line AGNs. Enoki et al. (2014) presented the AGN space density evolution predicted by a semi-analytic model of galaxy and AGN formation based on the hierarchical structure formation scenario. Kagaya et al. (2017) investigated the possibility of acceleration of ultra-high-energy cosmic rays (UHECRs) in nearby AGNs. Chen et al. (2018) studied how to quantify the systematic differences resulting from using different stellar population models (SPM) in optical spectroscopic identification of type II AGNs. Zou et al. (2019) confirmed the prediction of the unified model of AGNs. Liu et al. (2019) pre-

sented a new, complete sample of 14,584 broad-line AGNs at $z < 0.35$.

The primary goal of this study is to explore the environmental dependence of the galaxy age for the active galaxy samples, and to examine the dependence of the clustering properties of active galaxies on age. The outline of this paper is as follows. In § 2, we describe the active galaxy samples. We present statistical results in § 3 and § 4. We summarize our main results and conclusions in § 5.

To calculate the distance, we used a cosmological model with a matter density of $\Omega_0 = 0.3$, a cosmological constant of $\Omega_\Lambda = 0.7$, and a Hubble constant of $H_0 = 70 \text{ km s}^{-1} \text{ Mpc}^{-1}$.

2. DATA

Data Release 12 (DR12) (Alam et al. 2015) of the SDSS is the final public release of spectroscopic data from the SDSS-III BOSS. In this work, the data of the Main Galaxy sample (Strauss et al. 2002) was downloaded from the Catalog Archive Server of SDSS Data Release 12 (Alam et al. 2015) by the SDSS SQL Search (with SDSS flag: LEGACY_TARGET1 & (64 | 128 | 256) > 0). We extracted 631968 main galaxies with spectroscopic redshifts $0.02 \leq z \leq 0.2$.

Two template fittings (passive and star-forming) and two adopted initial mass functions (IMFs) (Salpeter and Kroupa) were employed by Maraston et al. (2013). In this work, we use best-fit age of galaxy [in Gyr] obtained with the star-forming template and the Kroupa IMF (Maraston et al. 2013). Thus, the data set of age measurement stems from the StellarMassStarFormingPort table (<http://www.sdss3.org/dr12/>).

The galSpecExtra table contains estimated parameters for all galaxies in the MPA-JHU spectroscopic catalogue. BPT classification in this table is based on the methodology of Brinchmann et al. (2004):

All. The set of all galaxies in the sample regardless of the S/N of their emission lines.

SF. The star-forming galaxies. These are the galaxies with $S/N > 3$ in all four BPT lines that lie below the lower line in Figure 1 of Brinchmann et al. (2004). This lower line is taken from equation (1) of Kauffmann et al. (2003).

C. The composite galaxies. They are the objects with $S/N > 3$ in all four BPT lines that are between the upper and lower lines in Figure 1 of Brinchmann et al. (2004). The upper line has been taken from equation (5) of Kewley et al. (2001).

AGN. The AGN population consists of the galaxies above the upper line in Figure 1 of Brinchmann et al. (2004). This line corresponds to the theoretical upper limit for pure starburst models.

Low S/N AGNs. They have $[\text{NII}]\lambda 6584/\text{H}\alpha > 0.6$ (and $\text{S/N} > 3$ in both lines) (e.g. Kauffmann et al. 2003), and still are classified as an AGN even though their $[\text{O III}]\lambda 5007$ and/or $\text{H}\beta$ have too low S/N. Miller et al. (2003) called such AGNs the “two-line AGNs”.

Low S/N SF. The remaining galaxies with $\text{S/N} > 2$ in $\text{H}\alpha$ are considered low S/N star formers.

Unclassifiable. Those remaining galaxies that are impossible to classify using the BPT diagram. This class is mostly made up of galaxies with no or very weak emission lines.

In the past, different authors often applied different AGN classification techniques. By requiring at least four greater than 3σ -detected emission lines for each galaxy, Ivezić et al. (2002) actually set a higher threshold for separating AGNs from star-forming galaxies than that used by Miller et al. (2003). In the BPT diagram, the four lines (the $[\text{NII}]$, $[\text{OIII}]$, $\text{H}\alpha$, and $\text{H}\beta$ emission lines) often are required to have signal-to-noise ratio $\text{S/N} > 3$. Miller et al. (2003) called such AGNs the “four-line AGNs”. Carter et al. (2001) and Miller et al. (2003) also identified galaxies with either a high $[\text{NII}]/\text{H}\alpha$ or a high $[\text{OIII}]/\text{H}\beta$ line ratio as AGNs, regardless of the other line ratio. Such AGNs are called the “two-line AGNs” as they are classified using only two lines. The “two-line AGNs” criterion of Miller et al. (2003) is slightly different from the one of Carter et al. (2001). Miller et al. (2003) used $\log([\text{NII}]/\text{H}\alpha) > -0.2$, while Carter et al. (2001) required $\log([\text{NII}]/\text{H}\alpha) > -0.25$. Deng et al. (2012) used the empirical demarcation line between star-forming galaxies and AGNs developed by Kauffmann et al. (2003). In this work, composite galaxies (C) are objects that are located between the upper and lower lines in the BPT diagram of Brinchmann et al. (2004). The lower line is taken from equation (1) of Kauffmann et al. (2003), while the upper line is equation (5) in Kewley et al. (2001). The AGN population consists of the galaxies above the upper line in the BPT diagram of Brinchmann et al. (2004). So AGN samples of Deng et al. (2012) actually contain C and AGN populations in this work. AGN samples of Deng et al. (2012) only contain the “four-line AGNs”, while in the AGN sample of Miller et al. (2003), the most frequent AGNs are the “two-line AGNs”.

In this work, we select C, AGN and Low S/N AGN populations and construct our AGN sample which contains 122923 active galaxies. When constructing volume-limited samples, we make use of the K-correction formula of Park et al. (2005): $K(z) = 2.3537(z - 0.1)^2 + 1.04423(z - 0.1) - 2.5 \log(1 + 0.1)$.

The luminous volume-limited sample is constructed by selecting 39373 active galaxies with the r -band absolute magnitudes $-22.5 \leq M_r \leq -20.5$, in the redshift range $0.05 \leq z \leq 0.102$; the faint volume-limited sample is constructed by selecting 5148 active galaxies with $-20.5 \leq M_r \leq -18.5$ and $0.02 \leq z \leq 0.0436$.

3. ENVIRONMENTAL DEPENDENCE OF AGE OF ACTIVE GALAXIES

Like Deng (2010) did, we measure the local three-dimensional galaxy density (galaxies Mpc^{-3}) which is defined as the number of galaxies ($N=5$) within the three-dimensional distance to the 5th nearest galaxy to the volume of the sphere with the radius of this distance. For each sample, we arrange galaxies in a density order from the smallest to the largest, select approximately 5% of the galaxies, construct two subsamples at both extremes of the density, and compare the distribution of age in the lowest density regime with that in the densest regime.

Figure 1 shows the age distribution at both extremes of density for the faint (left panel) and luminous (right panel) volume-limited active galaxy samples. As shown by this figure, in the luminous volume-limited sample, the age of active galaxies apparently depends on local environments: at low density the fraction of young galaxies with age less than 2 Gyr is significantly higher than the one in the high density case; at high density the fraction of old galaxies is significantly higher than the one at low density, although the prevalence of young galaxies with respect to old ones is higher in both the low- and high-density subsample. But in the faint volume-limited sample, the environmental dependence of the age of active galaxies is fairly weak. The decreasing trends as a function of age are similar regardless of density and luminosity range, even if the differences between low and high density are significant only for the high luminosity range.

We further perform the Kolmogorov-Smirnov (KS) test which can show the degree of similarity or difference between two independent distributions in a figure by calculating a probability value. A large probability implies that it is very likely that the two distributions are derived from the same parent distribution. Conversely, a lower probability value in-

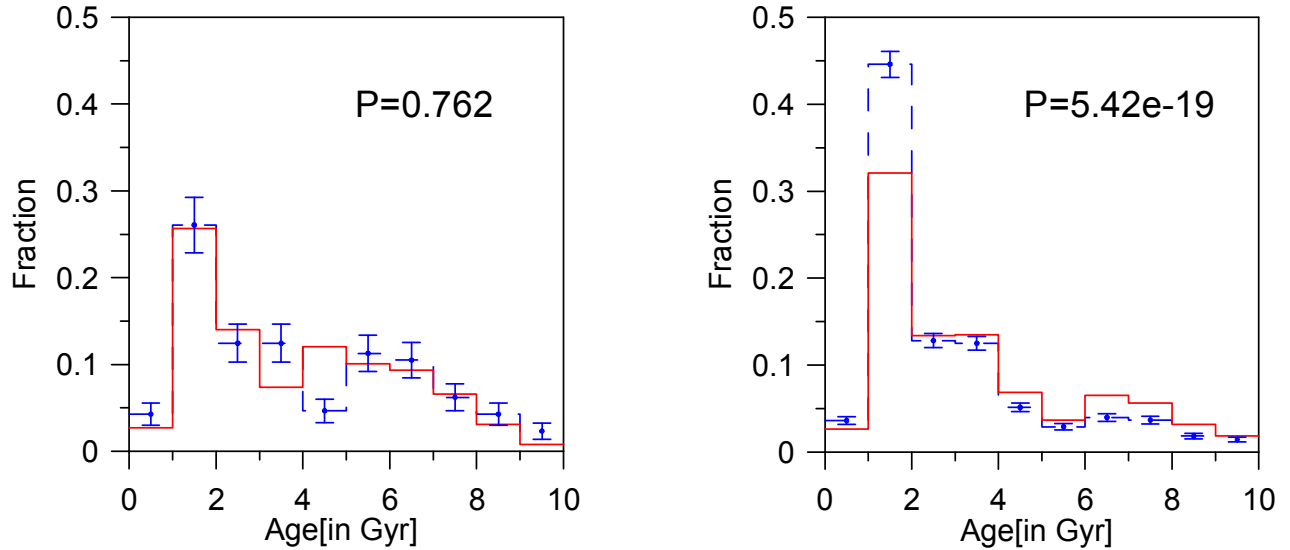


Fig. 1. Age distribution at both extremes of density for the faint (left panel) and luminous (right panel) volume-limited active galaxy samples: red solid line for the subsample at high density, blue dashed line for the subsample at low density. The error bars of the blue lines are 1σ Poissonian errors, those of the red lines are omitted for clarity. The color figure can be viewed online.

indicates that the two distributions are less likely to be similar. The probability of the two distributions coming from the same parent distribution is listed at the right upper corner of each figure. The K-S probability of the left panel in Figure 1 is much larger than 0.05 (5% is the standard in a statistical analysis), while the K-S probability of the right panel in Figure 1 is very small. This is in good agreement with the conclusion obtained by the step figures.

The luminosity and redshift ranges of the faint volume-limited active galaxy sample in this work are the same as ones of the faint volume-limited Main Galaxy sample used by Deng (2014). But Deng (2014) still observed strong environmental dependence of the age in the faint volume-limited Main Galaxy sample. Zheng et al. (2017) presented the stellar age and metallicity distributions for 1105 galaxies of the SDSS-IV MaNGA (Mapping Nearby Galaxies at APO) (Bundy et al. 2015) integral field spectra, studied the environmental dependence of age and metallicity values at the effective radii, and found that the age and metallicity values are dependent on the local density. Low-mass galaxies tend to be younger and have lower metallicity in low-density environments, while high-mass galaxies are less affected by the environment. The above-mentioned results show that the environmental dependence of the age of active galaxies is likely different from the one of general galaxies, which merits further studies.

Deng et al. (2009) demonstrated that the galaxy luminosity strongly depends on the local environments only for galaxies above the value of $M_r^* \simeq -20.5$ found for the overall Schechter fit to the galaxy luminosity function (Ball et al. 2006), but this dependence is very weak for galaxies below this value of M_r^* . In this work, we again note that M_r^* is an important characteristic parameter for the environmental dependence of the age of active galaxies: it is fairly different between galaxies above and below the value of M_r^* .

4. DEPENDENCE OF THE CLUSTERING PROPERTIES OF ACTIVE GALAXIES ON AGE

The cluster analysis (Einasto et al. 1984) is a simple and straightforward method of studying the distribution of galaxies. § 4 of Einasto et al. (1984) describes this method in detail. The key step of this method is how to select a neighbourhood radius r for identifying various systems of objects. Finally, the galaxy sample is separated into galaxy systems of different size and density contrast, such as isolated galaxies, galaxy pairs, galaxy groups or clusters, and superclusters. The cluster analysis often was used for studies of superclusters (e.g., Einasto et al. 1984, 1994, 2001; Wray et al. 2006) and for the compilation of catalogs of galaxy groups (e.g., Eke et al., 2004; Berlind et al. 2006).

TABLE 1
SOME PARAMETERS OF TWO SUBSAMPLES IN EACH VOLUME-LIMITED ACTIVE GALAXY SAMPLE

Sample	Subsamples	Galaxy number	Poisson radius R_0 (Mpc)
Luminous volume-limited	Young (age<2.5[in Gyr])	19740	8.760
active galaxy sample	old (age \geq 2.5[in Gyr])	19633	8.776
Faint volume-limited	Young (age<3.1[in Gyr])	2642	7.490
active galaxy sample	old (age \geq 3.1[in Gyr])	2506	7.623

The cluster analysis is suitable for volume-limited samples. To investigate the dependence of the clustering properties of active galaxies on age, like Deng et al. (2016) did, we divide each volume-limited active galaxy sample into two subsamples with different ages: young and old, and then compare the clustering properties of young active galaxies with those of old active galaxies. Table 1 lists some parameters of the subsamples. To decrease the statistical bias of this method, like Deng et al. (2016) did, we select the age thresholds in volume-limited samples to ensure that the number density of the two subsamples is nearly the same.

The Poisson radius is that of the sphere with unit population, and is defined as $R_0 = [3V/(4\pi N)]^{1/3}$, where N and V are the number of galaxies in the sample and the volume of the sample, respectively. Following Deng et al. (2016), the neighborhood radius is expressed in dimensionless units, $r = R/R_0$. Table 1 lists the Poisson radius (comoving distance) of each subsample. For the cluster analysis, it is difficult to define a proper neighborhood radius for the identification of galaxy systems. Here, we work with the dimensionless radii range of $r = 0.5 \rightarrow r = 1.3$, like Deng et al. (2016) did.

The multiplicity functions giving the fraction of the galaxies in systems with membership between n and $n+dn$, can describe the distribution of galaxy systems of different size and density contrast in the galaxy sample, which depend on the neighbourhood radius of the cluster analysis. This function is often plotted as a histogram. Following Deng et al. (2016), we divide the whole interval from 1 to N (the total number of galaxies in the sample) into 7 subintervals: $n=1$; $2 \leq n < 5$; $5 \leq n < 20$; $20 \leq n < 50$; $50 \leq n < 100$; $100 \leq n < 200$; $n \geq 200$, and show histograms of the multiplicity functions from dimensionless radii $r=0.5$ to $r=1.3$, to follow the multiplicity functions in detail.

Figure 2 shows histograms of the multiplicity functions for young and old galaxies in the luminous volume-limited active galaxy sample for dimensionless radii of $r=0.5$ to $r=1.3$. As can be seen from Figure 2, at all scales, young active galaxies have a higher prevalence than old ones at small multiplicity, corresponding to isolated galaxies, close pairs and small groups, whereas old active galaxies have a higher prevalence in the multiplicity bins corresponding to dense groups and clusters. This further confirms the clustering-age dependence of galaxies. When exploring this subject, previous works often focused on the cluster/field comparisons. However, the selection of the linking length for defining the cluster is often somewhat arbitrary. This work investigates the difference of clustering properties between young galaxies and old galaxies at all scales, thereby avoiding the ambiguity related to the definition of cluster.

Gao et al. (2005) explored the dependence of the clustering of haloes on halo age in Λ CDM simulations, and showed that older haloes are more strongly clustered than younger haloes. One possible explanation is that haloes of a given mass generally form earlier within denser regions (Reed et al. 2007). Thus, older haloes tend to populate denser regions, which naturally leads to stronger clustering with halo age. Reed et al. (2007) demonstrated that in mock galaxy catalogs, older mock galaxies are significantly more clustered, and suggested that the clustering-age dependence is manifest in real galaxies. Indeed, Proctor et al. (2004) and Mendes de Oliveira et al. (2005) observed that the member galaxies of compact groups are generally older than field galaxies. Such a clustering-age dependence of galaxies is also in good agreement with the above-mentioned environmental dependence of galaxy age (e.g., Bernardi et al. 1998; Trager et al. 2000; Kuntschner et al. 2002; Terlevich & Forbes 2002; Proctor et al. 2004; Mendes de Oliveira et al. 2005;

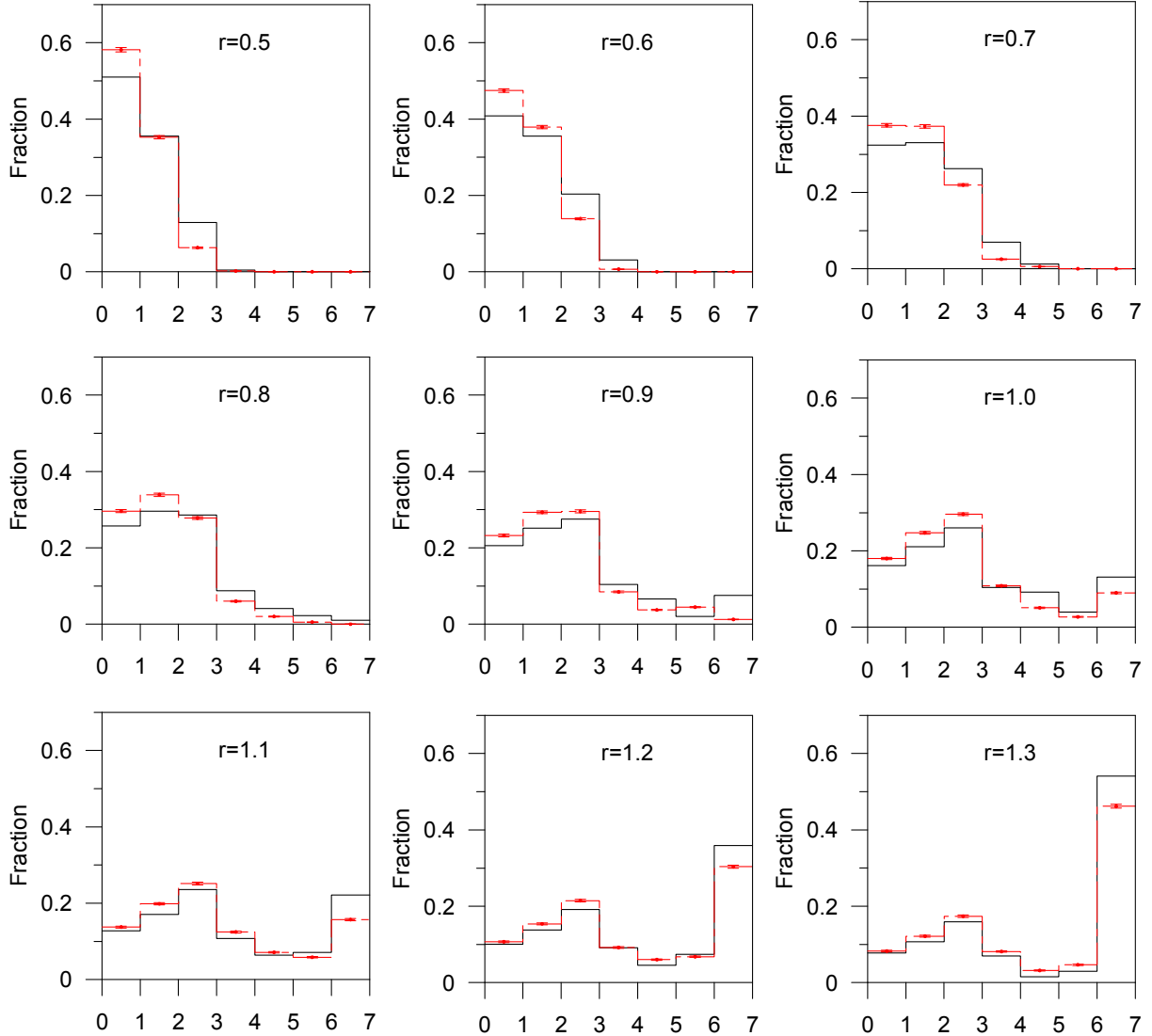


Fig. 2. Histograms of the multiplicity functions for old (black solid line) and young (red dashed line) galaxies in the luminous volume-limited active galaxy sample for dimensionless radii ranging from $r=0.5$ to $r=1.3$. The error bars in the red dashed histograms are 1σ Poissonian errors. The error bars in the black solid histograms are omitted for clarity. The color figure can be viewed online.

Thomas et al. 2005; Gallazzi et al. 2006; Sánchez-Blázquez et al. 2006; Silchenko 2006; Rakos et al. 2007; Reed et al. 2007; Wegner & Grogin 2008; Smith et al. 2012; Deng 2014).

Figure 3 shows histograms of the multiplicity functions for young and old galaxies in the faint volume-limited active galaxy sample for dimensionless radii from $r=0.5$ to $r=1.3$. A substantial dependence of the clustering properties on galaxy age is observed in the faint volume-limited active galaxy sample, while as indicated above, the environmental dependence of the age of active galaxies in the faint

volume-limited active galaxy sample is fairly weak. One possible explanation is that the galaxy number of the faint volume-limited active galaxy sample is too small to allow an ideal statistical analysis. Conclusions are affected by sampling fluctuations that are difficult to quantify.

5. SUMMARY

From the Main Galaxy data of SDSS DR12, we use the BPT classification in the galSpecExtra table, and select C, AGN and Low S/N AGN populations, which contain a total of 122923 active galax-

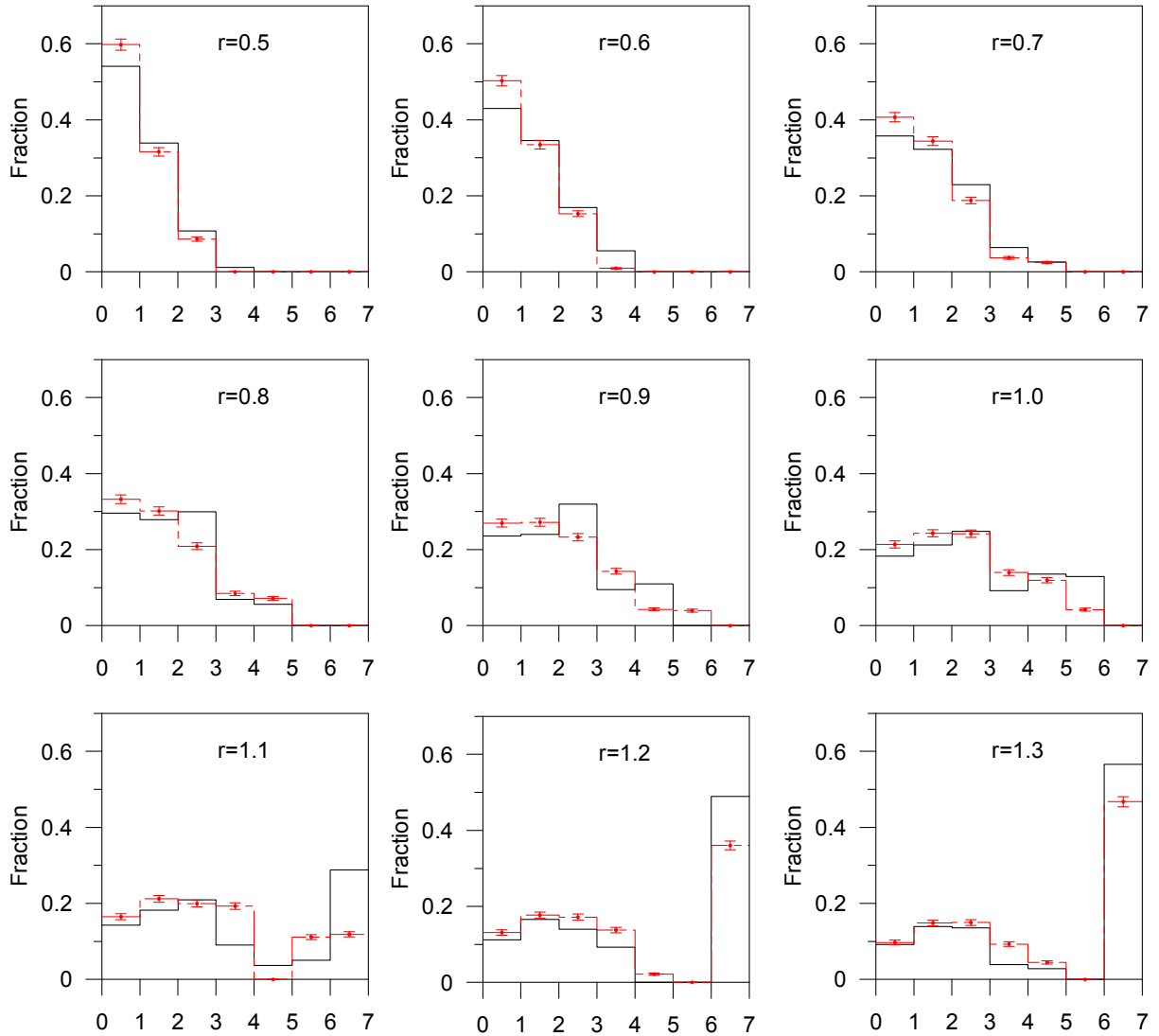


Fig. 3. Similar to Figure 2. Shown are histograms of the multiplicity functions for old (black solid line) and young (red dashed line) galaxies in the faint volume-limited active galaxy sample for dimensionless radii ranging from $r=0.5$ to $r=1.3$. The color figure can be viewed online.

ies. Considering that statistical conclusions may be quite different between galaxies above and below the value of M_r^* found for the overall Schechter fit to the galaxy luminosity function, we further construct two volume-limited samples of active galaxies with the luminosities $-20.5 \leq M_r \leq -18.5$ and $-22.5 \leq M_r \leq -20.5$ respectively, and explore the environmental dependence of galaxy age in these two volume-limited active galaxy samples. As shown by Figure 1, in the luminous volume-limited sample, the age of active galaxies apparently depends on local environments: at low density the fraction of young galaxies with age less than 2 Gyr is significantly higher than the one in the high density case, while

at high density the fraction of old galaxies is significantly higher than the one at low density. However, the prevalence of young galaxies with respect to old ones is higher in both the low- and high-density subsamples. But in the faint volume-limited sample, the environmental dependence of the age of active galaxies is fairly weak.

An alternative approach is to examine the dependence of the clustering properties of active galaxies on age by cluster analysis. We divide each volume-limited active galaxy sample into two subsamples (young and old) with nearly same number density and then perform comparisons between them. The multiplicity functions in the dimension-

less radii range from $r = 0.5$ to $r = 1.3$ are analyzed, enabling the clustering properties to be explored on all relevant scales. Figure 2 shows histograms of the multiplicity functions for young and old galaxies in the luminous volume-limited active galaxy sample for dimensionless radii of $r=0.5$ to $r=1.3$. As can be seen from Figure 2, at all scales, young active galaxies have a higher prevalence than old ones at small multiplicity, corresponding to isolated galaxies, close pairs and small groups, whereas old active galaxies have a higher prevalence in the multiplicity bins corresponding to dense groups and clusters. A substantial dependence of the clustering properties on galaxy age is also observed in the faint volume-limited active galaxy sample, which is inconsistent with the environmental dependence of the age of active galaxies in the faint volume-limited active galaxy sample. One possible explanation is that the number of galaxies in the faint volume-limited active galaxy sample is too small to allow an ideal statistical analysis. Conclusions are affected by sampling fluctuations that are difficult to quantify.

We thank the anonymous referee for many useful comments and suggestions. This study was supported by the National Natural Science Foundation of China (NSFC, Grant 11533004, 11563005).

Funding for SDSS-III has been provided by the Alfred P. Sloan Foundation, the Participating Institutions, the National Science Foundation, and the U.S. Department of Energy. The SDSS-III web site is <http://www.sdss3.org/>.

SDSS-III is managed by the Astrophysical Research Consortium for the Participating Institutions of the SDSS-III Collaboration including the University of Arizona, the Brazilian Participation Group, Brookhaven National Laboratory, University of Cambridge, University of Florida, the French Participation Group, the German Participation Group, the Instituto de Astrofísica de Canarias, the Michigan State/Notre Dame/JINA Participation Group, Johns Hopkins University, Lawrence Berkeley National Laboratory, Max Planck Institute for Astrophysics, New Mexico State University, New York University, Ohio State University, Pennsylvania State University, University of Portsmouth, Princeton University, the Spanish Participation Group, University of Tokyo, University of Utah, Vanderbilt University, University of Virginia, University of Washington, and Yale University.

REFERENCES

Ahn, C. P., Alexandroff, R., Allende Prieto, C., et al. 2014, *ApJS*, 211, 17

- Alam, S., Albareti, F. D., Allende Prieto, C., et al. 2015, *ApJS*, 219, 12
- Ball, N. M., Loveday, J., Brunner, R. J., Baldry, I. K., & Brinkmann, J. 2006, *MNRAS*, 373, 845
- Berlind, A. A., Frieman, J., Weinberg, D. H., et al. 2006, *ApJS*, 167, 1
- Bernardi, M., Renzini, A., & da Costa, L. 1998, *ApJ*, 508, L143
- Brinchmann, J., Charlot, S., White, S. D. M., et al. 2004, *MNRAS*, 351, 1151
- Brown, M. J. I., Webster, R. L., & Boyle, B. J. 2000, *MNRAS*, 317, 782
- Bundy, K., Bershady, M. A., Law, D. R., et al. 2015, *ApJ*, 798, 7
- Carter, B. J., Fabricant, D. G., Geller, M. J., et al. 2001, *ApJ*, 559, 606
- Chen, Y. P., Zaw, I., & Farrar, G. R. 2018, *ApJ*, 861, 67
- Davis, M. & Geller, M. J. 1976, *ApJ*, 208, 13
- Deng, X. F. 2010, *ApJ*, 721, 809
- . 2013, *Canadian Journal of Physics*, 91, 12
- . 2014, *BASI*, 42, 59
- Deng, X. F., He, J. Z., & Wen, X. Q. 2009, *MNRAS*, 395, L90
- Deng, X. F., Qi, X. P., Wu, P., et al. 2016, *Chinese Journal of Physics*, 54, 263
- Deng, X. F., Xin, Y., Wu, P., et al. 2012, *AN*, 333, 767
- De Lucia, G., Springel, V., White, S. D. M., et al. 2006, *MNRAS*, 366, 499
- Dressler, A., Thompson, I. B., & Shectman, S. A. 1985, *ApJ*, 288, 481
- Einasto, J., Klypin, A. A., Saar, E., et al. 1984, *MNRAS* 206, 529
- Einasto, M., Einasto, J., Tago, E., Dalton, G. B., & Anderson, H. 1994, *MNRAS*, 269, 301
- Einasto, M., Einasto, J., Tago, E., Müller, V., & Anderson, H. 2001, *AJ*, 122, 2222
- Eke, V. R., Baugh, C. M., Cole, S., et al. 2004, *MNRAS*, 348, 866
- Enoki, M., Ishiyama, T., Kobayashi, M. A. R., et al. 2014, *ApJ*, 794, 69
- Gallazzi, A., Charlot, S., Brinchmann, J., et al. 2006, *MNRAS*, 370, 1106
- Gao, L., Springel, V., & White, S. D. M. 2005, *MNRAS*, 363, 66
- Ivezić, Z., Menou, K., Knapp, G. R., et al. 2002, *AJ*, 124, 2364
- Kagaya, M., Katagiri, H., Yoshida, T., et al. 2017, *ApJ*, 850, 33
- Kauffmann, G., Heckman, T. M., Tremonti, C., et al. 2003, *MNRAS*, 346, 1055
- Kewley, L. J., Heisler, C. A., Dopita, M. A., et al. 2001, *ApJS*, 132, 37
- Krumpe, M., Miyaji, T., Coil, A. L., et al. 2012, *ApJ*, 746, 1
- Kuntschner, H., Smith, R. J., Colless, M., et al. 2002, *MNRAS*, 337, 172
- Lanzoni, B., Guiderdoni, B., Mamon, G. A., et al. 2005, *MNRAS*, 361, 369

- Liu, H. Y., Liu, W. J., Dong, X. B., et al. 2019, *ApJS*, 243, 21
- Loh, Y. S., Rich, R. M., Heinis, S., et al. 2010, *MNRAS*, 407, 55
- Loveday, J., Maddox, S. J., Efstathiou, G., & Peterson, B. A. 1995, *ApJ*, 442, 457
- Maraston, C., Pforr, J., Henriques, B. M., et al. 2013, *MNRAS*, 435, 2764
- Mendes de Oliveira, C., Coelho, P., González, J. J., et al. 2005, *ApJ*, 130, 55
- Miller, C. J., Nichol, R. C., Gómez, P. L., et al. 2003, *ApJ*, 597, 142
- Norberg, P., Baugh, C. M., Hawkins, E., et al. 2001, *MNRAS*, 328, 64
- Norberg, P., Baugh, C. M., Hawkins, E., et al. 2002, *MNRAS*, 332, 827
- Park, C., Choi, Y. Y., Vogeley, M. S., et al. 2005, *ApJ*, 633, 11
- Proctor, R., Forbes, D., Hau, G., et al. 2004, *MNRAS*, 349, 1381
- Rakos, K., Schombert, J., Odell, A. 2007, *ApJ*, 658, 929
- Reed, D. S., Governato, F., Quinn, T., et al. 2007, *MNRAS*, 378, 777
- Sánchez-Blázquez, P., Gorgas, J., Cardiel, N., et al. 2006, *A&A*, 457, 809
- Silchenko, O. K. 2006, *ApJ*, 641, 229
- Smith, R. J., Lucey, J. R., Price, J., et al. 2012, *MNRAS*, 419, 3167
- Strauss, M. A., Weinberg, D. H., Lupton, R. H., et al. 2002, *AJ*, 124, 1810
- Terlevich, A. & Forbes, D. 2002, *MNRAS*, 330, 547
- Thomas, D., Maraston, C., Bender, R., & Mendes de Oliveira, C. 2005, *ApJ*, 621, 673
- Tinker, J. L., Wechsler, R. H., & Zheng, Z. 2010, *ApJ*, 709, 67
- Trager, S. C., Faber, S. M., Worthey, G., et al. 2000, *AJ*, 120, 165
- Wang, W., Jing, Y. P., Li, C., et al. 2011, *ApJ*, 734, 88
- Wegner, G. & Grogan, N. A. 2008, *AJ*, 136, 1
- Wray, J. J., Bahcall, N., Bode, P., et al. 2006, *ApJ*, 652, 907
- Zehavi, I., Blanton, M. R., Frieman, J. A., et al. 2002, *ApJ*, 571, 172
- Zehavi, I., Zheng, Z., Weinberg, D. H., et al. 2005, *ApJ*, 630, 1
- Zehavi, I., Zheng, Z., Weinberg, D. H., et al. 2011, *ApJ*, 736, 59
- Zheng, Z., Coil, A. L., & Zehavi, I. 2007, *ApJ*, 667, 760
- Zheng, Z., Wang, H., Ge, J., et al. 2017, *MNRAS*, 465, 4572
- Zheng, Z., Zehavi, I., Eisenstein, D. J., et al. 2009, *ApJ*, 707, 554
- Zou, F., Yang, G., Brandt, W. N., et al. 2019, *ApJ*, 878, 11

CAN UVB VARIATIONS RECONCILE SIMULATED QUASAR ABSORPTION LINES AT HIGH REDSHIFT?

L. A. García^{1,2,3} and E. V. Ryan-Weber^{2,3}

Received September 16 2019; accepted December 19 2019

ABSTRACT

In this work we present new calculations of the observables associated with synthetic metal and HI absorption lines in the spectra of high redshift quasars, inspired by questions and limitations raised in work with a uniform Haardt-Madau 2012 ultraviolet background (UVB). We introduce variations at $z \approx 6$ to the UVB and HI self-shielding and explore the sensitivity of the absorption features to modifications of the hardness of the UVB. We find that observed SiIV and low ionization states (e.g. CII, SiII, OI) are well represented by a soft UV ionizing field at $z = 6$, but this same prescription, fails to reproduce the statistical properties of the observed CIV ion absorber population. We conclude that small variations in the UVB (not greater than a dex below Haardt-Madau 2012 emissivity at 1 Ryd) and HI SSh at $z \approx 6$ play a major role in improving the estimation of metal ions and HI statistics at high z .

RESUMEN

Presentamos resultados de los observables asociados a líneas de absorción sintéticas de HI y metales en el espectro de cuásares a gran corrimiento al rojo, inspirados por las limitaciones encontradas en un trabajo previo con el fondo ionizante uniforme (UVB) de Haardt-Madau 2012. Introducimos variaciones del fondo ionizante y el modelo de *self-shielding* del hidrógeno neutro y exploramos la sensibilidad de las líneas de absorción al modificar la intensidad del UVB. Encontramos que los estados de baja ionización (por ejemplo, CII, SiII, OI) y SiIV están bien representados por un UV ionizante más suave, pero este mismo modelo falla en reproducir las propiedades estadísticas de la población observada de CIV. Concluimos que pequeñas variaciones en el fondo de UV (menores que un orden de magnitud por debajo de la emisividad de Haardt-Madau 2012 a 1 Ryd) y en el apantallamiento del hidrógeno neutro en $z \approx 6$ juegan un papel determinante en el mejoramiento de la estimación de las estadísticas de metales y HI a gran corrimiento al rojo.

Key Words: cosmology: theory — dark ages, reionization, first stars — intergalactic medium — methods: numerical — quasars: absorption lines

1. INTRODUCTION

Unveiling the end of the epoch of reionization (EoR) and the sources that complete the budget of ionizing photons is currently a key topic in Astronomy. The phase transition of neutral hydrogen (HI) into its ionized state (HII) is caused by the radiation released by the first stars (POP III, Abel et al. 2002;

Bromm et al. 2002; Yoshida et al. 2003), the second generation of stars (POP II, Ciardi et al. 2005; Mellema et al. 2006) and quasars (with a black hole seed of $10^6 M_\odot$, Dijkstra et al. 2004; Hassan et al. 2018). Other candidates are proposed, such as mini-quasars, with masses around $10^{3-6} M_\odot$ (Mortlock et al. 2011; Bolton et al. 2011; Smith et al. 2017), decaying or self-annihilating dark matter particles or decaying cosmic strings. Nonetheless, the latter objects seem to be unlikely to ionize the Universe by themselves.

¹Grupo de Simulación, Análisis y Modelado, Vicerrectoría de Investigación, Universidad ECCI, Bogotá Colombia.

²Centre for Astrophysics and Supercomputing, Swinburne University of Technology, Australia.

³ARC Centre of Excellence for All-Sky Astrophysics (CAASTRO).

Understanding the EoR is intimately tied to the evolution of the ultraviolet background (UVB): the grand sum of all photons that have escaped from quasars and galaxies. Its spectral energy distribution is reasonably well determined at $z < 5$ (Bolton et al. 2005) and modelled (Haardt et al. 2001). Haardt et al. (2012) used a cosmological 1D radiative transfer model that follows the propagation of H and He Lyman continuum radiation in a clumpy ionized intergalactic medium (IGM), and uses mean free path and hydrogen photoionization rate decreasing with redshift⁴. However, as $z \geq 6$ is approached, the population of UV sources is not well determined (Haardt et al. 1999). The uncertainty in estimating the UV photon emissivity from each type of object is caused by the lack of knowledge on the star formation rate, clumping factor and UV escape fraction (Cooke et al. 2014) at the redshift of interest, which are strongly model-dependent. Measuring Lyman series absorption or UV emissivity in a spectrum blueward of Ly α at 1216 Å is rendered almost impossible by the increasing density of matter and neutral hydrogen fraction at redshifts greater than 5.5.

On the other hand, the assumption of a uniform UV radiation field breaks down close to and during the EoR, when the interaction of the ionizing sources with the IGM requires a very accurate description (Lidz et al. 2006). A real-time reionization simulation should first ionize high density regions and fill some regions before others, leading to a multiphase IGM with spatial fluctuations (Lidz et al. 2016).

Alternatively, intervening metal absorption lines detected in the spectra of high redshift quasars offer a completely different method to calibrate the UVB at high redshift. A growing number of absorption systems has been detected (Bosman et al. 2017; Codoreanu et al. 2018; Meyer et al. 2019; Becker et al. 2019) and with the advent of bigger telescopes (e.g. GMT), the expectation is that the sample of absorption lines detected will significantly increase.

An increase in the sample of absorption lines (of at least an order of magnitude compared to the current observational sample) is possible with numerical simulations. A number of works have directed their efforts to describing the evolution of metal absorption lines in the intergalactic and circumgalactic medium (CGM). These simulations take into account different feedback prescriptions, photoionization modelling and variations in the UV ionizing background in the high redshift Universe (Oppenheimer et al. 2006, 2009; Tescari et al. 2011; Cen et al. 2011; Finlator et al. 2013; Pallottini et al. 2014;

Keating et al. 2014; Finlator et al. 2015; Rahmati et al. 2016; Keating et al. 2016; García et al. 2017b; Doughty et al. 2018, 2019). The methods employed in each of these works, as well as the set-up of the hydrodynamical simulations, show advantages for the description of the IGM.

However, the result of García et al. (2017b) with a uniform UV background (Haardt et al. 2012) show that the calculated column densities of the low ionization states (CII, SiII, OI) in the simulations have difficulty matching the values observed by Becker et al. (2011). The lack of spatial resolution on the scale of the low ionization absorbers evidences that further work needs to be done to reach a better description of the environment of these absorbers. Nonetheless, the uncertainties on the assumed UVB at high z suggest that varying its normalization could alleviate the discrepancy between simulated results and the current observations. Works from Finlator et al. (2015, 2016); Doughty et al. (2018) also show that alternative models to the HM12 UVB can reduce the gap between the observables associated to metal lines calculated with their simulations and the observations. Their models account for simulated UVB with contribution from galaxies + quasars and quasar-only.

The triply ionized state of silicon (SiIV) offers a unique avenue of investigation. Although it is classified as a high ionization state, its ionization potential energy is significantly lower than CIV; it does not necessarily lie in the same environment and it exhibits the same physical conditions as CIV. Detections at high redshift of this ion have been made by Songaila et al. (2001, 2005); D’Odorico et al. (2013), Boksenberg et al. (2015) and more recently by Codoreanu et al. (2018). The latter authors identify 7 systems across a redshift path of 16.4 over the redshift range $4.92 < z < 6.13$. They are $\approx 50\%$ complete down to a column density of $\log N_{\text{sys}} \text{ (cm}^{-2}\text{)}$ of 12.50. This limiting column density allows them to study the identified SiIV population across the column density range [12.5, 14.0] over the full redshift path of their survey. In addition, Codoreanu et al. (2018) show that the fiducial configuration in García et al. (2017b) at $z = 5.6$ is compatible with the SiIV observations.

On the other hand, the self-shielding (SSh) of HI gas in very high density regions (above 10^{17} cm^{-2}) is also a component that needs to be refined in the description, specifically when HI statistics are made. Current studies implement the self-shielding prescription proposed by Rahmati et al. (2013a), but unfortunately, this is only valid up to $z = 5$. At red-

⁴We refer to Haardt et al. (2012) model as HM12.

shifts when reionization is concluding, this treatment is no longer valid. A new scheme has recently proposed by Chardin et al. (2018), using radiative transfer calculations to find the best fitting parameters from the functional form of the photoionization rate Γ_{phot} described in Rahmati et al. (2013a). Different SSh prescriptions could have a different outcome in the HI statistics. HI column densities are commonly classified in three regimes: Lyman- α forest ($12 < \log N_{\text{HI}} \text{ cm}^{-2} < 17.2$), Lyman limit systems (or LLS with $17.2 < \log N_{\text{HI}} \text{ cm}^{-2} < 20.3$) and damped Lyman- α absorbers (DLAs) with $N_{\text{HI}} > 10^{20.3} \text{ cm}^{-2}$. Works carried out by Tescari et al. (2009); Nagamine et al. (2004); Pontzen et al. (2008); Barnes et al. (2009); Bird et al. (2014); Rahmati et al. (2015); Maio et al. (2015); Crighton et al. (2015); García et al. (2017b) on DLAs showed that DLAs are the main contributors to the cosmological mass density of HI. The HI self-shielding and molecular cooling prescriptions are important factors as these absorbers reside in low temperature and high density environments.

This paper, in particular, builds on previous findings of García et al. (2017b). The aim of this work is to explore and discuss to a first approximation variations in the assumed UVB and the HI self-shielding prescriptions.

The paper is presented as follows: § 2 describes the simulations and the method used to post-process them. In § 3 we explore two variations to the uniform HM12 assumed in García et al. (2017b). Additionally, we propose an alternative method to compare the current observations with the synthetic sample of metal absorbers, in contrast with previous works that compare two or more ions at once. § 4 shows results for HI statistics when two different HI self-shielding prescriptions are implemented in post-process. Finally, § 5 summarizes the findings of this paper and explores the limitations encountered.

2. THE NUMERICAL SIMULATIONS AND POST-PROCESS

The results presented in this work are a follow-up to García et al. (2017b), and are based on the simulations and the methodology presented in that paper. The suite of numerical simulations uses a customized version of GADGET-3 (Springel 2005): P-GADGET3(XXL). The model was first tested in the context of the Angus project. In Tescari et al. (2014) and Katsianis et al. (2015); Katsianis et al. (2016, 2017), the authors showed that their simulations were compatible with observations of the cosmic star formation rate density and the galaxy stellar mass

function at $1 < z < 7$. The model takes into account the following physical processes: a multiphase star formation criterion; self-consistent stellar evolution and chemical enrichment modeling; supernova (SN) momentum- and energy-driven galactic winds; AGN feedback, metal-line cooling; low-temperature cooling by molecules and metals (Maio et al. 2007, 2015). Moreover, the model is supported by: a parallel Friends-of-Friends FoF) algorithm to identify collapsed structures, and a parallel SUBFIND algorithm to identify substructures within FoF halos.

The numerical model self-consistently follows the evolution of hydrogen, helium and 9 metal elements (C, Ca, O, N, Ne, Mg, S, Si and Fe) released from supernovae (SNIa and SNII) and low and intermediate mass stars. The chemical evolution scheme is based on the stochastic star formation model implemented in the simulations (Tornatore et al. 2007). It accounts for the age of stars of different mass; hence, the amount of metals released over time varies with the mass of the stars.

The lifetime function from Padovani & Matteucci (1993) for stars with mass m is adopted. The stellar yields quantify the amount of different metals which is released during the evolution of the stellar population, as follows: (i) SNIa: Thielemann et al. (2003); (ii) SNII (massive stars): Woosley & Weaver (1995); (iii) low and intermediate mass (AGB) stars: van den Hoek & Groenewegen (1997). As one of the main contributors to the reionization of the Universe is the POP III stars (a very massive and short-life population), they are best described by a Chabrier (2003) initial mass function (IMF).

Galactic scale winds were introduced in GADGET simulations by Springel & Hernquist (2003) to regulate the star formation, spread metals from the galaxies and high-density regions to the IGM and shock-heated gas, and prevent the overcooling of gas. The phenomenological model for energy-driven wind feedback is presented in Springel & Hernquist (2003). It assumes that the mass-loss rate associated with the winds, \dot{M}_w , is proportional to the star formation rate \dot{M}_* , such that $\dot{M}_w = \eta \dot{M}_*$, with η the wind mass loading factor that accounts for the efficiency of the wind. The kinetic energy of the wind is related to the energy input of the supernova. The velocity of the wind is given by the expression $v_w = 2\sqrt{\frac{GM_h}{R_{200}}} = 2 \times v_{\text{circ}}$. Due to the conservation of the wind energy, the velocity of the wind goes as the square of the inverse of the loading factor $\eta = 2 \left(\frac{600 \text{ km/s}}{v_w} \right)^2$.

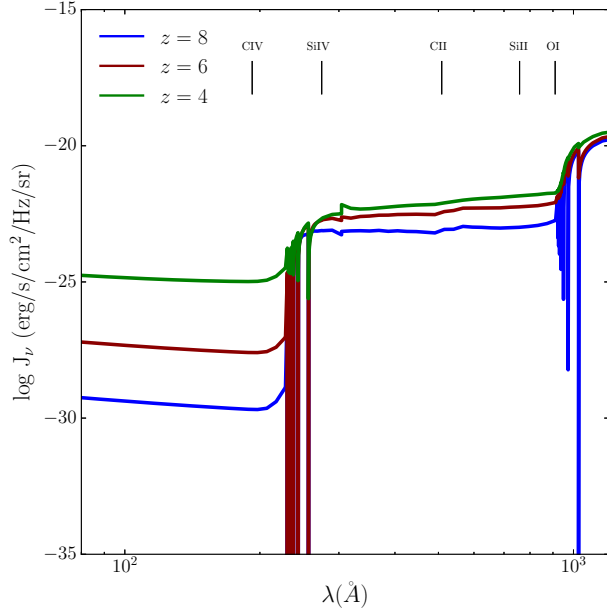


Fig. 1. UV emissivity for the uniform HM12 background at three different redshifts: $z = 8$, 6 and 4 (blue, dark red and green, respectively) compared with the wavelength of the radiation, in the wavelength range where the ion transitions occur. The color figure can be viewed online.

However, Puchwein et al. (2013) suggest that the the mass carried by the wind is not necessarily proportional to the SFR of the galaxy. In such case, it would be more natural to assume that there is a relation between the momentum flux (instead of the energy flux) of the wind and the SFR of the galaxy, thus η is proportional to the inverse of the wind velocity v_w , such that $\eta = 2 \times \frac{600 \text{ km/s}}{v_w}$.

Chemical pollution caused by star formation contributes to the cooling of gas. Some metal line cooling efficiencies peak at $T \approx 10^4$ K (mostly low ionization transitions, Gnat & Ferland 2012). These transitions are privileged in metal-poor high-density environments, as DLAs, where H is mostly neutral or in its molecular form. As discussed in Maio et al. (2007), molecular and low temperature metal cooling is particularly important when collapsed structures reach temperatures $T < 10^4$ K due to the formation of molecules. At this temperature, atomic cooling is not efficient and is highly suppressed, yet, molecular H continues to cool the gas.

The assumed cosmology is a flat Λ CDM model with cosmological parameters from Planck Collaboration (2015): $\Omega_{0m} = 0.307$, $\Omega_{0b} = 0.049$, $\Omega_{\Lambda} = 0.693$ and $H_0 = 67.74 \text{ km s}^{-1} \text{ Mpc}^{-1}$ (or $h = 0.6774$). The simulations considered in the paper are described in Table 1, with comoving box size and softening of

18 Mpc/h and 1.5 kpc/h, respectively. All the simulations have the same initial number of gas and DM particles (2×512^3), with masses of gas and dark matter particles of $M_{\text{gas}} = 5.86 \times 10^5 M_{\odot}/h$ and $M_{\text{DM}} = 3.12 \times 10^6 M_{\odot}/h$. Moreover, we include molecular and low-temperature metal cooling (Maio et al. 2007, 2015) in our simulations. The fiducial run is labelled Ch 18 512 MDW.

The numerical simulations are post-processed to recreate the observations of high redshift quasars and recover synthetic spectra for each ion along each sightline. The pipeline derived for this purpose relies on the physical conditions of the gas (reproduced with the hydrodynamical simulations), on top of a uniform field radiation that accounts for the cosmic microwave background (CMB) and the ultraviolet/X-ray background from quasars and galaxies HM12 (Haardt et al. 2012). The photoionization modeling for the metal transitions is computed with CLOUDY v8.1 (Ferland et al. 2013) for optically thin gas. In addition, a HI self-shielding prescription is imposed to the simulations to account for neutral hydrogen inside high-density regions where gas is optically thick. We choose a thousand random lines of sight along to the three perpendicular directions inside the box, and in each one of these sightlines we calculate a simulated spectrum, containing relevant physical information: HI flux/optical depth, density and temperature of the gas, and the number density of all the ions considered in the analysis, among other quantities. The box size Δv at a given redshift is translated to the equivalent redshift path through the relationship $\Delta z = (1+z) \frac{\Delta v}{c}$. Once the synthetic spectra are computed, they are convolved with Gaussian noise profiles with full width at half maximum FWHM = 7 km s⁻¹. Finally, the individual absorption line features are fitted with Voigt profiles with the code VPFIT v.10.2 (Carswell et al. 2014). We focus our attention on the ionic transitions shown in Table 2.

3. VARIATIONS OF THE UVB IN POST-PROCESS

Investigations carried out with a uniform UV background (Haardt et al. 2012) in García et al. (2017b) showed that the calculated column densities of the low ionization states (CII, SiII, OI) and their corresponding observables (comoving mass density, column density distribution function, etc.) leave room for improvement when compared with observations. There is general agreement that current simulations do not have enough resolution on the scale of the ab-

TABLE 1
SUMMARY OF THE SIMULATIONS USED IN THIS WORK

Simulation	Box size (cMpc/h)	Comoving softening (ckpc/h)	Model for SN-driven winds	low-T metal & molecular cooling
Ch 18 512 MDW	18	1.5	Momentum-driven	
Ch 18 512 MDW mol	18	1.5	Momentum-driven	✓
Ch 18 512 EDW	18	1.5	Energy-driven	

Column 1: Run name. Column 2: Box size. Column 3: Plummer-equivalent comoving gravitational softening length. Column 4: Feedback model. Column 5: Inclusion of low-temperature metal and molecular cooling (Maio et al. 2007, 2015). The first run, Ch 18 512 MDW, is the fiducial model. The second one, Ch 18 512 MDW mol, has exactly the same configuration as the reference run, but includes low-T metal and molecular cooling.

TABLE 2
LIST OF THE ION LINES INCLUDED IN THIS WORK

Ion i	λ (Å)	f	$E_{i \rightarrow i+1}$ (eV)	$\log Z$ (Z_{\odot})
HI	1215.67	0.4164	13.6	0
CII	1334.53	0.1278	24.38	-3.57
CIV	1548.21	0.1899	64.49	-3.57
SiII	1526.71	0.1330	16.35	-4.49
SiIV	1393.76	0.513	45.14	-4.49
OI	1302.17	0.0480	13.62	-3.31

The first column contains the ions, the second one the rest-frame wavelength λ of the transition with the highest oscillator strength. The third column, the oscillator strength f of each absorption line; the fourth shows the ionization energy E associated to each state, and the fifth column, the metal abundance $\log Z$ (in solar units), taken from Asplund et al. (2009).

Note: The energy E shown in the fourth column is the energy required to reach the next ionization state $i + 1$ from the state i .

sorbers with low ionization energies. However, uncertainties in the high- z UVB suggest that varying its normalization is a first step towards a better agreement with the observations at high redshift.

Here we explore the sensitivity of the results presented in García et al. (2017b) to the presence of different ultraviolet/X-ray ionizing backgrounds by modifying the normalization factor at 1 Ryd of the uniform HM12 UVB in post-process. Preliminary work allows us to conclude that decreasing the UVB intensity at $z = 6$ is equivalent to imposing an ionizing background at times earlier than redshift 6. Therefore, low ionization ions would prevail in the early stages of the epoch of reionization. Hence, reductions of more than one order of magnitude in the

UVB are very aggressive for high ionization species and, simultaneously, lead to an overproduction of the low ionization ones. Consequently, a variation of 1 dex below the fiducial emissivity in HM12 is conservative but offers a non-negligible imprint on the calculated ions.

Variations of the UVB spectrum (quasars+galaxies model) from the original HM12 (see Figure 1) require modified input files to run new CLOUDY tables.

The procedure followed here is explained in § 2 and it has been tuned and applied in García et al. (2017b,a), with some small adjustments: the normalization parameter at 1 Ryd is reduced by an order of magnitude below the fiducial value in HM12 at all redshifts. This leads to a softer UVB. Hereafter, the test is referred as $\log J_{\nu} - 1$ (see § 3.1).

3.1. Change in the Normalization of HM12

It is a reasonable expectation that the presence of a softer UVB input than the uniform HM12 in the photoionization model would favor low ionization states and more neutral states would show large incidence rates. In order to test this hypothesis, the UV emissivity J_{ν} at 1 Ryd is reduced by one dex compared with the value defined by the uniform HM12 at all redshifts. This leads to a softer UVB.

In order to avoid introducing more variables to this test, the box size has been fixed to 18 Mpc/h. The simulations used to recover the observables are Ch 18 512 MDW, Ch 18 512 MDW mol and Ch 18 512 EDW. The convergence and resolution tests are not included in this document, but they can be found in García et al. (2017b).

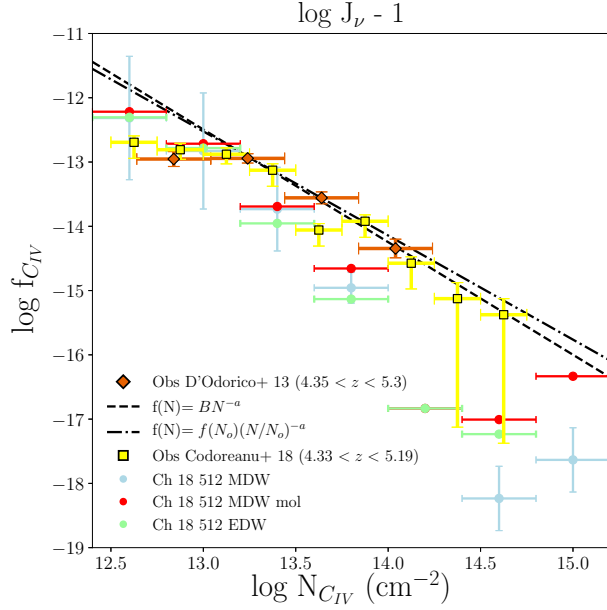


Fig. 2. CIV column density distribution function at $z = 4.8$ and comparison with observational data by D'Odorico et al. (2013), orange diamonds and Codoreanu et al. (2018), yellow squares. The black dashed line represents the fitting function $f(N) = BN^{-\alpha}$ with $B = 10.29 \pm 1.72$ and $\alpha = 1.75 \pm 0.13$ and the dotted-dashed line $f(N) = f(N_0)(N/N_0)^{-\alpha}$ with $f(N_0) = 13.56$ and $\alpha = 1.62 \pm 0.2$, from D'Odorico et al. (2013). The error bars are the Poissonian errors for the reference run and are a good representation of the errors in the other models. The plot illustrates results with the test $\log J_{\nu} - 1$, for the simulations Ch 18 512 MDW, Ch 18 512 MDW mol and Ch 18 512 EDW. In simulations without molecular cooling implemented, the number of CIV absorbers in the $\log J_{\nu} - 1$ case is under-represented in the range of column densities considered. The color figure can be viewed online.

The first comparison with observations explored here is the CIV column density distribution function (CDDF), defined in equation 1 as follows:

$$f(N, X) = \frac{n_{\text{sys}}(N, N + \Delta N)}{n_{\text{lov}} \Delta X}. \quad (1)$$

Here, n_{lov} is the number of lines of view considered. The absorption path $\Delta X = \frac{H_0}{H(z)}(1+z)^2 \Delta z$ relates the Hubble parameter at a given redshift z with the correspondent redshift path $\Delta z = (1+z) \frac{\Delta v}{c}$. The term Δv is the box size in km s^{-1} .

At $z = 4.8$ and 5.6 , the CCDFs are compared with observations from D'Odorico et al. (2013) and Codoreanu et al. (2018) in Figures 2 and 3, respectively. At $z = 6.4$, the simulated values of the CDDF

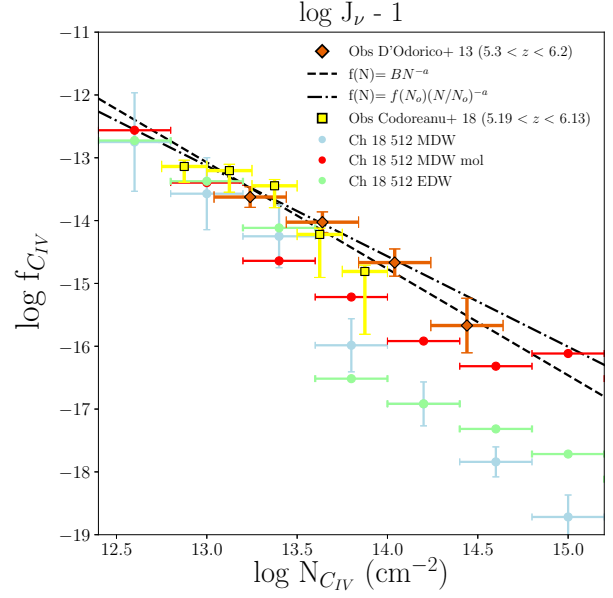


Fig. 3. CIV column density distribution function at $z = 5.6$ and comparison with observational data by D'Odorico et al. (2013), orange diamonds and Codoreanu et al. (2018), yellow squares. The black dashed line represents the fitting function $f(N) = BN^{-\alpha}$ with $B = 8.96 \pm 3.31$ and $\alpha = 1.69 \pm 0.24$ and the dotted-dashed line $f(N) = f(N_0)(N/N_0)^{-\alpha}$ with $f(N_0) = 14.02$ and $\alpha = 1.44 \pm 0.3$, from D'Odorico et al. (2013) work. The blue error bars are the Poissonian errors for the reference run and are a good representation of the errors in the other models. The diagram shows results with the test $\log J_{\nu} - 1$, for the simulations Ch 18 512 MDW, Ch 18 512 MDW mol and Ch 18 512 EDW. The color figure can be viewed online.

are compared with upper limits from Bosman et al. (2017) in Figure 4.

The key feature of Figures 2, 3, 4 is that all of them show a notable underproduction of the CIV absorbers at all redshifts when the emissivity is decreased. The calculated CDDFs are always below the observed values, and for high column densities, there is a clear departure from the fitting functions provided by D'Odorico et al. (2013). Nonetheless, the synthetic CDDFs show a closer match with the observational values from Codoreanu et al. (2018), in particular at high column densities. It is worth noting that Bosman et al. (2017) data are just upper limits for the CIV-CDDF at $6.2 < z < 7.0$. Nevertheless, the computed values in this test are significantly underrepresented.

There is a change in the number of CIV absorbers when the UVB emissivity is lower than the original HM12. This result gives a hint in regard to the num-

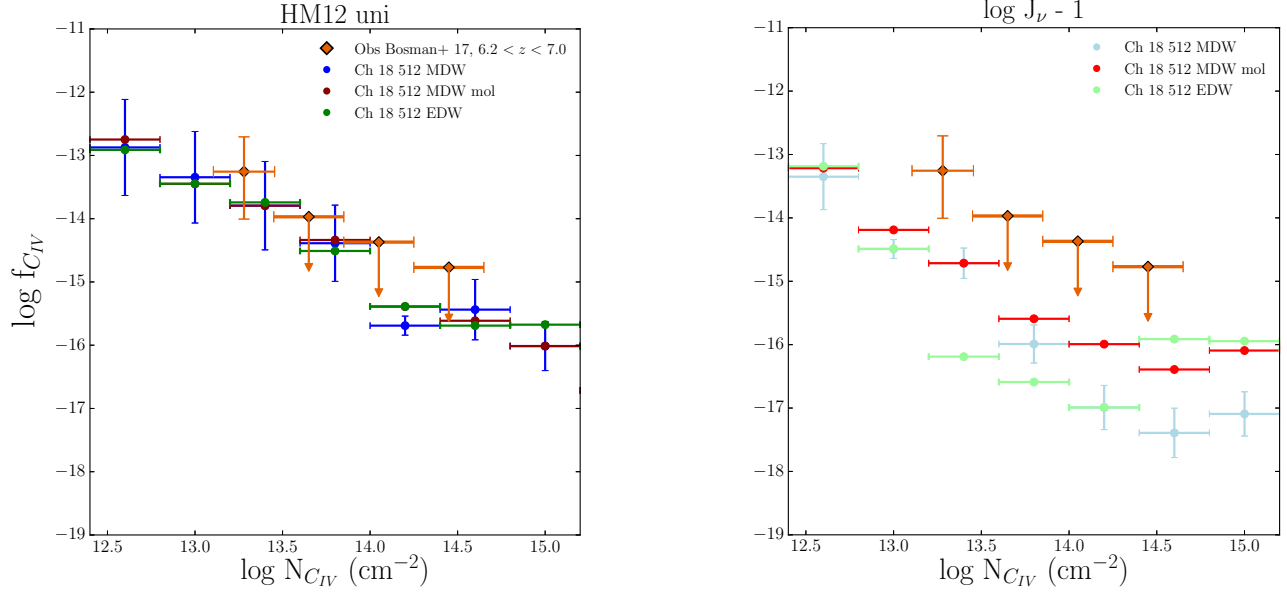


Fig. 4. CIV column density distribution function at $z = 6.4$ and comparison with observational data by Bosman et al. (2017), orange diamonds. The error bars are the Poissonian errors for the reference run and are a good representation of the errors in the other models. The left panel shows results with the uniform HM12 and the right panel the results with the test $\log J_\nu - 1$, both for the simulations Ch 18 512 MDW, Ch 18 512 MDW mol and Ch 18 512 EDW. The color figure can be viewed online.

ber of the CIV absorbers: the test $\log J_\nu - 1$ is too aggressive, with high ionization states of C lying in the IGM.

Next, we compute the cosmological mass density Ω_{CIV} . The cosmological mass density of an ion is defined as:

$$\Omega_{\text{ion}}(z) = \frac{H_0 m_{\text{ion}} \sum N(\text{ion}, z)}{c \rho_{\text{crit}} n_{\text{lov}} \Delta X}, \quad (2)$$

with m_{ion} the mass of the ionic species, n_{lov} the number of lines of view, ρ_{crit} the critical density today, and ΔX is expressed above.

Figure 5 shows a comparison of the calculated CIV cosmological mass density at $4 < z < 8$ for synthetic absorbers in the range $13.8 < (\log N_{\text{CIV}}/\text{cm}^{-2}) < 15.0$ and observations by Pettini et al. (2003) and Ryan-Weber et al. (2009) as orange circles, Codoreanu et al. (2018) as yellow circles, Songaila et al. (2001, 2005) as cyan triangles, Meyer et al. (2019) as magenta triangles, Simcoe et al. (2011) as dark green inverted triangles, D’Odorico et al. (2013) as pink squares, Boksenberg et al. (2015) as a grey diamond, upper limits from Bosman et al. (2017) as a purple star and Díaz et al. (2016) as black pentagons.

As a consequence of the discrepancy presented in Figures 2, 3 and 4, the CIV cosmological mass den-

sity in the right hand panel of Figure 5 is at least an order of magnitude below the reference case on the left panel, because the number of absorbers in the range $13.8 < \log N_{\text{CIV}}(\text{cm}^{-2}) < 15.0$ is underproduced by the simulations in the framework of the modified UVB. The most remarkable difference is visible in the reference run Ch 18 512 MDW, with an order of magnitude shift between the blue curve (on the left) and the light blue one (on the right).

Therefore, strong variations of the UVB around 1 Ryd (specifically, normalization changes in the wavelength range where the transition occurs) seem to have a large impact on the number of CIV absorbers at all redshifts. Figures 6 and 7 draw a comparison of the evolution of CII and CIV in the redshift range $4 < z < 8$, with the original HM12 (on the left panel) and the test $\log J_\nu - 1$ (on the right). As discussed above, the cosmological mass density of CIV is underrepresented. However, the resulting mass density of CII significantly improves with a softer UVB, indicating that the hypothesis made to perform this test is well-motivated. Effectively, the number of large column density CII absorbers increases and the right panels of Figures 6 and 7 are now compatible with the limits measured by Becker et al. (2006) and the most recent estimates made by Cooper et al. (2019).

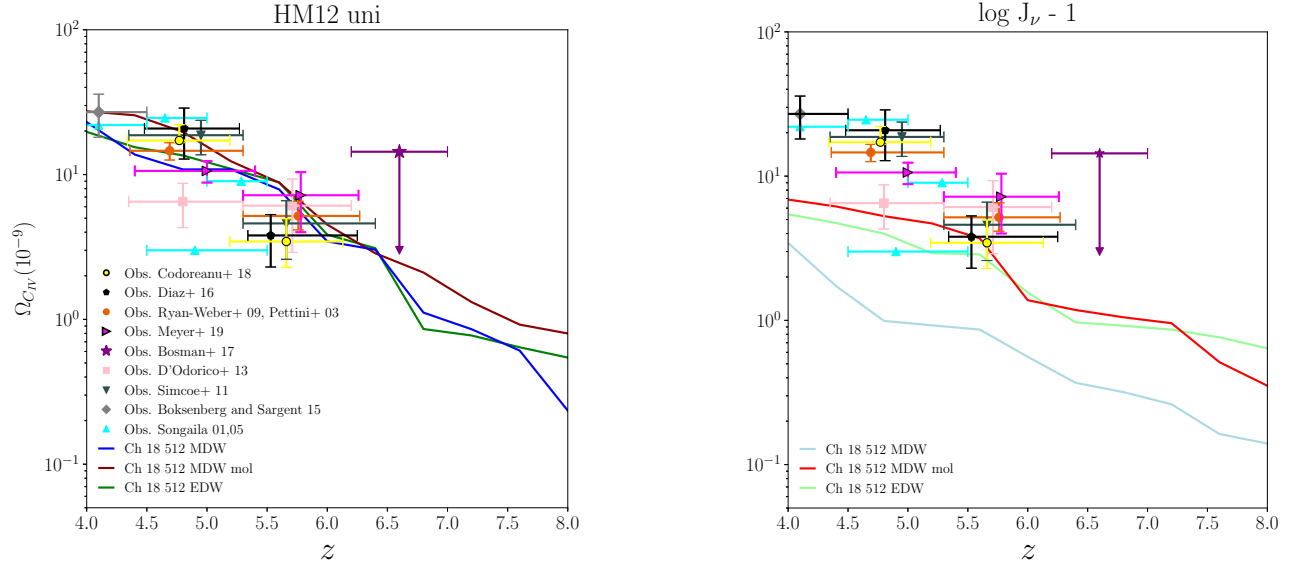


Fig. 5. CIV cosmological mass density at $4 < z < 8$ for $13.8 < \log N_{\text{CIV}}(\text{cm}^{-2}) < 15.0$. Comparison between the simulated data and observations by Pettini et al. (2003) and Ryan-Weber et al. (2009), orange circles; Codoreanu et al. (2018), yellow circles; Songaila et al. (2001, 2005), cyan triangles; Meyer et al. (2019), magenta triangles; Simcoe et al. (2011), dark green inverted triangles; D’Odorico et al. (2013), pink squares; Boksenberg et al. (2015), grey diamond; upper limits from Bosman et al. (2017), purple star and Díaz et al. (2016), black pentagons. Pettini, Ryan-Weber, Codoreanu and Díaz measurements are converted to the Planck cosmology, while for the others this recalibration was not possible due to missing details of the precise pathlength probed. On the left panel the results with the uniform HM12 are presented. The right panel shows Ω_{CIV} in the framework of the test $\log J_{\nu} - 1$. In both cases, the simulations used are Ch 18 512 MDW, Ch 18 512 MDW mol and Ch 18 512 EDW. As a consequence of the low number of absorbers in this column density range, when the UVB normalization is varied, Ω_{CIV} is at least an order of magnitude lower than the case with the original UVB. The color figure can be viewed online.

The feedback prescription does not play a major role in the evolution of CII in this redshift range, while the molecular cooling run Ch 18 512 MDW mol shows a relatively good agreement with the observational data.

Due to the different orders of magnitude between the calculated mass densities of CII and CIV, the right panels of Figures 6 and 7 show no crossover of the low and high ionization states of carbon. A natural conclusion from this could be that decreasing the intensity of the UV background leads to an improvement in the low ionization states at the expense of a poor calculation of CIV absorbers, which are traditionally well constrained by observations.

As pointed out before, CIV is not well represented by this variation of the UVB, but there is a good improvement in the column densities of CII. However, it is difficult to draw definitive conclusions from the column density relationships, because the number of absorbers depends strongly on the ion, with less CIV synthetic absorbers in the case of $\log J_{\nu} - 1$. We suggest variations in the UVB smaller

than the original HM12 emissivity, but not below an order of magnitude, so as to preserve the improvements in the low-ionization states while keeping positive results in CIV.

4. VARIATION OF THE ASSUMED HI SELF-SHIELDING PRESCRIPTION

A final test that can be done with our simulations is a variation of the HI self-shielding prescription. García et al. (2017b) briefly discuss the need for low ionization states self-shielding (SSh) treatment. However, here we try to quantify the impact of a HI self-shielding prescription different from the extensively used one by Rahmati et al. (2013a) with the HM12 model. For this purpose, we use the new HI SSh model described by Chardin et al. (2018). Their best fitting parameters as a function of redshift were obtained with radiative transfer simulations (calibrated with Ly α forest data after the EoR). One of the merits of these models is that they focused on redshifts corresponding to reionization. Instead, the Rahmati et al. (2013a) HI SSh prescription is valid up to $z = 5$,

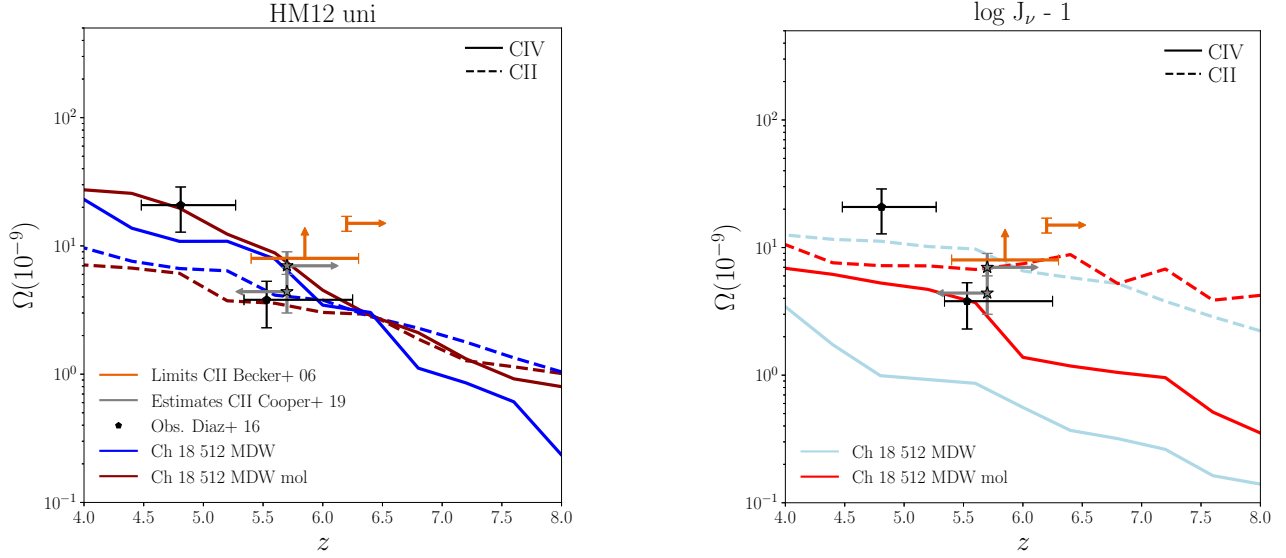


Fig. 6. Evolution of the CII and CIV cosmological mass density when the normalization of the UVB is varied at 1 Ryd (comparison of molecular cooling content). On the left panel the results with the uniform HM12 are presented. The right panel shows results of the test $\log J_\nu - 1$. In both cases, the runs used are Ch 18 512 MDW and Ch 18 512 MDW mol. The solid lines mark the evolution of Ω_{CIV} for $13.8 < \log N_{\text{CIV}}(\text{cm}^{-2}) < 15.0$, and the dashed lines Ω_{CII} in the range $13.0 < \log N_{\text{CII}}(\text{cm}^{-2}) < 15.0$. The orange points with errors represent the observational lower limits for Ω_{CII} from Becker et al. (2006) and the grey arrows the corresponding estimates made by Cooper et al. (2019). The latter estimates have been done for $z > 5.7$ and $z < 5.7$, shown as right and left arrows, respectively. Although in the case with softer UVB there is no crossover of CII and CIV (due to the low number of CIV absorbers), the mass density of CII matches the limits from Becker et al. (2006) and Cooper et al. (2019) in both simulations, and CIV matches the observational detection at $z = 5.7$ by Díaz et al. (2016) in the molecular cooling run. The color figure can be viewed online.

which constitutes a limitation when applying this formulation in our models, as commented in García et al. (2017b). Here we compare results for the metal ions with the HI SSh treatments by Rahmati et al. (2013a) and Chardin et al. (2018) -hereafter R13 and C17, respectively-

The evolution of the photoionization rate Γ_{phot} is calculated using RT codes, such that:

$$\frac{\Gamma_{\text{phot}}}{\Gamma_{\text{UVB}}} = (1-f) \left[1 + \left(\frac{n_{\text{H}}}{n_0} \right)^\beta \right]^{\alpha_1} + f \left[1 + \left(\frac{n_{\text{H}}}{n_0} \right) \right]^{\alpha_2}, \quad (3)$$

where Γ_{UVB} is the photoionization rate as a function of redshift and it is assumed from the UVB field. Here, f , α_1 , α_2 , β and n_0 are free parameters of the model, calculated with RT; the number density of hydrogen n_{H} and the temperature T are taken directly from the numerical simulation used.

The best fitting parameters of equation 3 as a function of redshift found by R13 and C17 are shown in Table 3.

In contrast to the outcome for the metal ions studied in the previous section, one would expect

that HI would be more sensitive to a variation of the self-shielding prescription adopted for this transition. In fact, works by Rahmati et al. (2013a) and Chardin et al. (2018) self-consistently calculate the distribution of neutral hydrogen with RT codes, based on the number density of hydrogen. We compute the following observables for HI: the column density distribution function (CDDF) f_{HI} , the HI cosmological mass density Ω_{HI} , and the mass density associated to DLA systems Ω_{DLA} .

In Figure 8 is shown the HI-CDDF at $z = 4$, comparing the two self-shielding prescriptions (R13 and C17) and simulations with different molecular cooling contents, Ch 18 512 MDW and Ch 18 512 MDW mol. In addition, we compare our theoretical predictions with observational detections of HI-CDDF at z around 4 in two regimes: the range of column densities $12 < \log N_{\text{HI}}(\text{cm}^{-2}) < 22$ in the left panel, and a zoom around the DLAs region, $20.3 < \log N_{\text{HI}}(\text{cm}^{-2}) < 22$, in the right panel. In the first case, observations by Prochaska et al. (2005) are plotted in grey, O'Meara et al. (2007) in

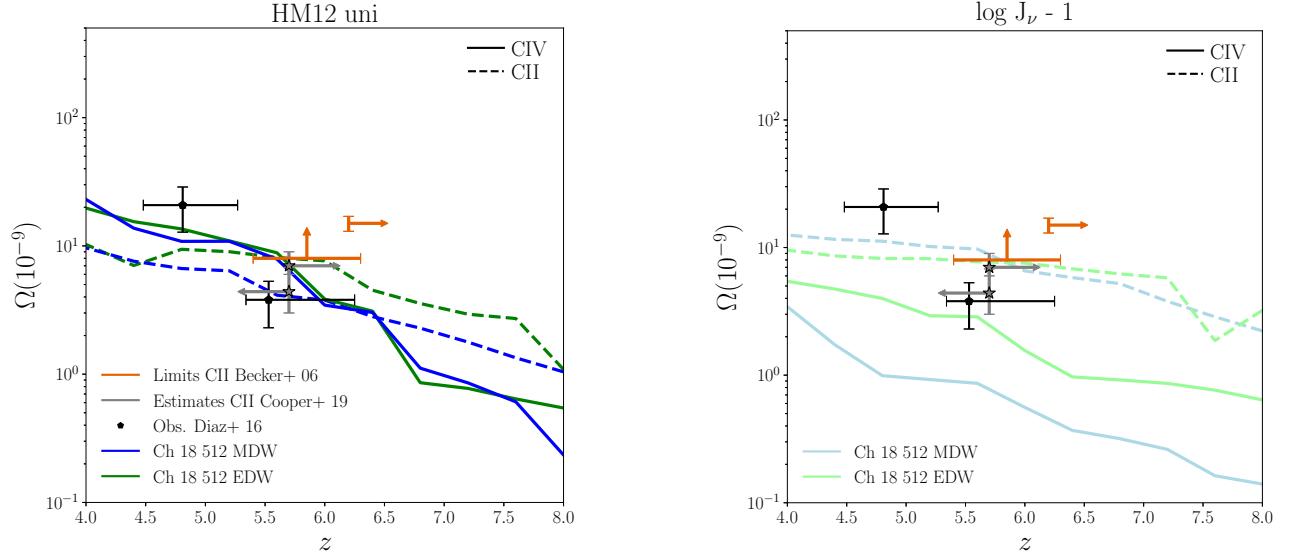


Fig. 7. Evolution of the CII and CIV cosmological mass density when the normalization of the UVB is varied at 1 Ryd (comparison of MDW and EDW feedback prescriptions). On the left panel the results with the uniform HM12 are presented. The right panel shows results of the test $\log J_\nu - 1$. In both cases, the runs used are Ch 18 512 MDW and Ch 18 512 EDW. The solid lines mark the evolution of Ω_{CIV} for $13.8 < \log N_{\text{CIV}}(\text{cm}^{-2}) < 15.0$, and the dashed lines Ω_{CII} in the range $13.0 < \log N_{\text{CII}}(\text{cm}^{-2}) < 15.0$. The orange points with errors represent the observational lower limits for Ω_{CII} from Becker et al. (2006), and the grey arrows, the estimates from Cooper et al. (2019). There is no crossover of CII and CIV at any redshift, because of the different orders of magnitude of the mass densities of these ions. In addition, different feedback prescriptions do not seem to give rise to a remarkable distinction in the evolution of CII. Yet, the plot reveals that a softer UVB effectively favours low ionization states as CII, and brings down the gap between the observations from Becker et al. (2006) and Cooper et al. (2019) and the simulated column densities. The color figure can be viewed online.

TABLE 3

BEST FITTING PARAMETERS FOR SSH MODELLING

Model	z	n_0 (cm^{-3})	α_1	α_2	β	f
R13	1 - 5	$1.003 \pm 0.005 n_{\text{H,SSH}}$	-2.28 ± 0.31	-0.84 ± 0.11	1.64 ± 0.19	0.02 ± 0.0089
	4.0	0.009346	-0.950010	-1.503310	5.873852	0.015308
	5.0	0.010379	-1.294665	-1.602099	5.056422	0.024356
C17	6.0	0.006955	-0.941372	-1.507124	6.109438	0.028830
	7.0	0.002658	-0.866887	-1.272957	7.077863	0.040894
	8.0	0.003974	-0.742237	-1.397100	7.119987	0.041213

The free parameters correspond to equation (3) from RT calculations derived by Rahmati et al. (2013a), R13, and Chardin et al. (2018), C17. The term $n_{\text{H,SSH}}$ corresponds to the self-shielding density threshold.

black, Crighton et al. (2015) in orange, and Bird et al. (2017) in purple. Instead, in the DLA zoom, a comparison is drawn with the fitting function proposed by Prochaska et al. (2009) for DLA systems at redshift 4.0–5.5.

One can see a difference between the two self-shielding prescription implemented at $z = 4$. The

Chardin et al. (2018) model predicts a larger amount of neutral hydrogen hosted in systems in the Lyman- α forest and fewer systems in the sub-DLA and DLA regimes, indicating that the HI mass density should be larger with the Rahmati et al. (2013a) SSH prescription. In García et al. (2017b), we find that the largest contribution to Ω_{HI} comes from systems with

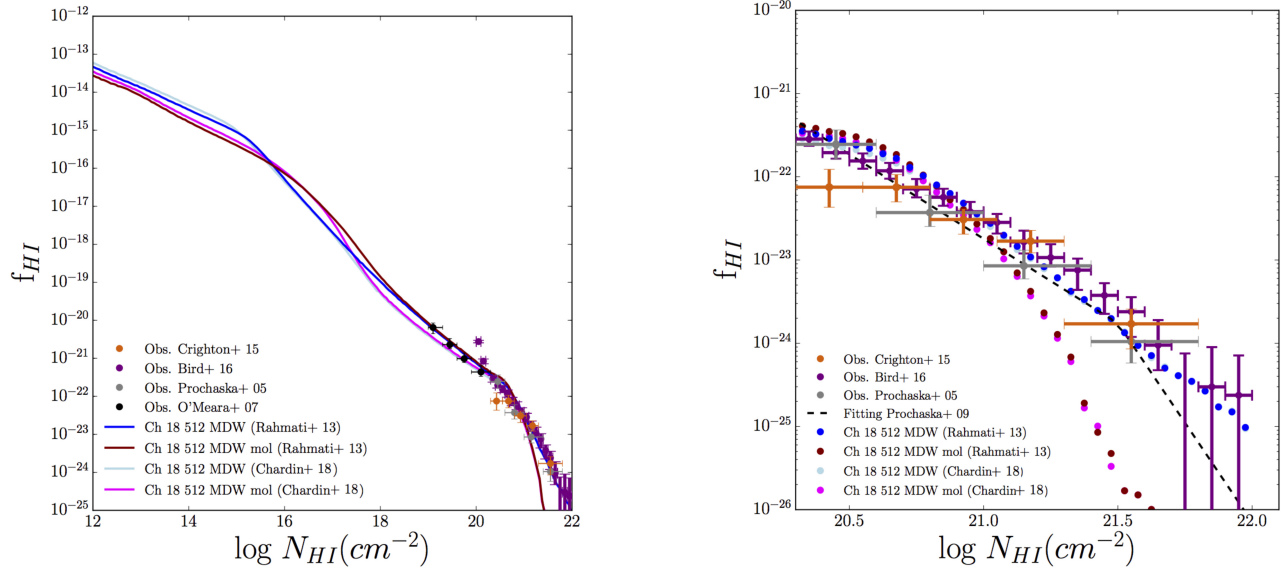


Fig. 8. HI column density distribution function at $z = 4$ comparing two self-shielding prescriptions (Rahmati et al. 2013a; Chardin et al. 2018) in simulations with different molecular cooling content (Ch 18 512 MDW and Ch 18 512 MDW mol) and the HM12 model. On the left side is shown the simulated HI-CDDF in the range $12 < \log N_{HI}(\text{cm}^{-2}) < 22$ and a comparison with observations by Prochaska et al. (2005) in grey, O'Meara et al. (2007) in black, Crighton et al. (2015) in orange and Bird et al. (2017) in purple. In the right panel, the CDDFs are limited to the DLA regime ($20.3 < \log N_{HI}(\text{cm}^{-2}) < 22$) and compared with the fitting function by Prochaska et al. (2009) for DLA systems at redshift 4.0–5.5 (black dashed line). The color figure can be viewed online.

large column densities, in particular, DLAs. We predict higher values of Ω_{HI} with the R13 HI SSh formulation than C17, regardless of the molecular cooling model considered. It is important to remember that at this redshift ($z = 4$), both formulations are valid, and their best fitting parameters are calibrated with observations. Thus, our conclusions are not limited by different constraints of the HI SSh modelling.

Interestingly, the number of systems in a column density bin at a given absorption path is barely affected by the SSh prescription, but it depends strongly on the chemistry of the molecules; the gap between the number of systems is approximately fixed when comparing two simulations with and without molecules in the Lyman α forest regime (blue and dark red, and light blue and magenta cases, respectively).

Figure 9 (left panel) displays the cosmic mass density of neutral hydrogen with the self-shielding prescriptions by Rahmati et al. 2013a (blue and dark red for the runs Ch 18 512 MDW and Ch 18 512 MDW mol, respectively) and Chardin et al. 2018 (light blue and magenta corresponding to Ch 18 512 MDW and Ch 18 512 MDW mol, respectively) and compares them with observations by Prochaska et al. (2005) and Prochaska et al. (2009),

grey inverted triangles; Zafar et al. (2013), pink square; and Crighton et al. (2015) red stars. As predicted above, the SSh prescription by Rahmati et al. (2013a) gives rise to a larger amount of neutral hydrogen when compared with the results for Ω_{HI} of the Chardin et al. (2018) model. Interestingly, the introduction of this new self-shielding treatment reduces the tension between our models without molecular cooling and the observations at $z = 4$, and accurately predicts the HI mass density when molecular cooling is taken into account.

This is by far the most important effect of the implementation of a different self-shielding prescription in our simulations: the amount of HI mass density at redshifts between 4–6 is in better agreement with observational detections.

Finally, we point out that models including molecular cooling give a better prediction of Ω_{HI} compared with observations, because they take into account the conversion of atomic to molecular hydrogen at very high densities, where the self-shielding of HI is occurring.

On the right hand side of Figure 9 we show a comparison of Ω_{HI} and Ω_{DLA} (solid and dashed lines, respectively) with observations for Ω_{DLA} by Bird et al. (2017). The amount of HI mass density hosted

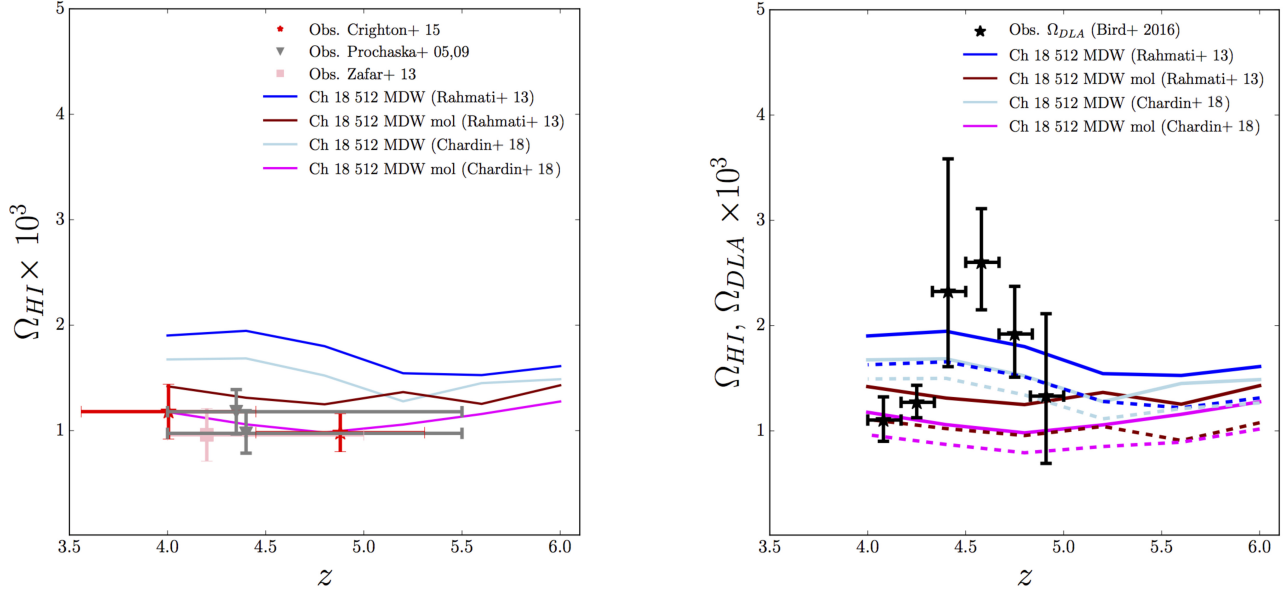


Fig. 9. Cosmological mass density of HI with different HI self-shielding treatments: Rahmati et al. (2013a) and Chardin et al. (2018). The left diagram shows the prediction of the HI mass density from simulations with specific molecular cooling content (Ch 18 512 MDW and Ch 18 512 MDW mol) and a comparison with Prochaska et al. (2005, 2009), grey inverted triangles; Zafar et al. (2013), pink square; and Crighton et al. (2015) red stars. The right panel displays the cosmological mass density associated to neutral hydrogen and DLAs, Ω_{HI} and Ω_{DLA} (solid and dashed lines, respectively) and the observational data for Ω_{DLA} by Bird et al. (2017), black stars. The color figure can be viewed online.

in DLAs (dashed lines) converges at high redshift ($z \approx 6$) for models with a different SSh prescription when the molecular cooling content is fixed. This is indeed quite an interesting result because the R13 SSh prescription has not been calibrated at this redshift, although it is extensively used in the literature at redshifts higher than 5. One can say that the use of the model is justified at $z = 6$.

Additionally, there is agreement between the predicted trends for Ω_{DLA} (with different self-shielding prescriptions and molecular cooling content models) and observations of this quantity by Bird et al. (2017).

It is worth noting that the column density distribution functions in Figure 8 show that molecular cooling is driven by the conversion of neutral hydrogen to H₂, that becomes important in high-density regions where new stars are being formed. The molecules cool the surrounding gas and atomic hydrogen is less abundant. This effect is particularly important in the regime of DLAs (García et al. 2017b). Interestingly, molecular chemistry plays a more relevant role in the amount of neutral hydrogen than the HI self-shielding model itself, although the evolution of the Chardin et al. (2018) model is

more dynamic at high redshift than the Rahmati et al. (2013a) one.

Figure 9 leads to the same conclusion in a different way: simulations without molecular cooling (Ch 18 512 MDW) boost the amount of HI compared with Ch 18 512 MDW mol, regardless of the SSh prescription considered. Then, the cosmological mass density increases by a factor of 2 compared with simulations containing molecular cooling. The effect is more pronounced contrasting HI and DLA cosmic mass density: there are two processes involved, the molecular cooling that converts HI into H₂ and reduces the amount of HI in the DLA column density range, but also the evolution of the HI-SSh modeling, that becomes more critical at high redshift Rahmati et al. (2013a). SSh stops being valid at $z = 6$, whilst the Chardin et al. (2018) model is valid up to $z = 10$.

5. DISCUSSION AND CONCLUSIONS

This work contains a compilation of variations to the uniform HM12 ionizing field assumed in the photoionization models to obtain the results presented in García et al. (2017a) and García et al. (2017b). We find that the large uncertainties in the UVB, espe-

cially at high redshift, require better constraints for several probes, and of course, improved UVB models.

In a similar vein, observational detections of metal ionic species could be used to constrain the UVB spectral normalization in the wavelength range where these states occur (100-1000 Å). A careful fine-tuning is required, but most of the steps are clear: a reduction in the normalization of the UV emissivity improves the number of absorbers with low ionization potential energy.

When the emissivity of the assumed UVB is reduced by one dex, we find that the total number of CIV absorbers significantly decreases compared with the original HM12, and that absorbers in the range of the detections by D’Odorico et al. (2013) are definitely not well represented (e.g. there is a discrepancy of the CIV comoving mass density and CIV CDDF with the observations). Instead, there is a moderate improvement in the calculated number of absorbers for SiIV with a softer UVB, in agreement with findings by Bolton et al. (2011).

It is particularly encouraging that the number of absorbers of CII, SIII and OI in the range of the observations also rises when the UVB implemented is softer, independently of the simulation used; therefore, the estimate of the column densities of these low ionization states improves, justifying the hypothesis that led us to do this test. Additional work can be done in this direction, with a more moderate reduction in the emissivity of the UVB that would give better predictions for the column density of low ionization states, and be more compatible with the CIV absorbers incidence rate inferred from the D’Odorico et al. (2013) observations and our mock spectra for that ion.

We also computed some hydrogen statistics up to $z = 6$. We limited our calculations to this redshift for two reasons: (1) at high redshift a uniform UVB does not provide a good representation of the rapid evolution of HI during reionization; (2) the self-shielding prescription from Rahmati et al. (2013a) is calibrated with the photoionization rates of HM12. To alleviate the absence of a self-consistent SSh at higher redshifts we compared our previous results with a recent SSh prescription by Chardin et al. (2018), whose best-fit parameters were calibrated up to $z = 10$.

We find that at $z = 4$, the HI CDDF predicted by the Chardin et al. (2018) model produces more neutral hydrogen in systems with low column densities (the Lyman- α forest) and fewer systems in the sub-DLAs and DLAs range. This result leads to

higher mass densities of HI, Ω_{HI} , with the Rahmati et al. (2013a) SSh prescription than with Chardin et al. (2018), independently of the molecular cooling model considered. At $z = 4$, both formulations (Rahmati et al. 2013a; Chardin et al. 2018) were calibrated with observations. Therefore, our results for the HI CDDF and the cosmological mass density of neutral hydrogen are valid, regardless of the assumptions of each HI self-shielding model.

Regardless of the intensity of the UVB field considered, we find a non-negligible number of ion absorbers with column densities above $\log N \geq 15 \text{ cm}^{-2}$. This prediction from our models can be tested with future observations that, in principle, will be able to detect rarer high column density systems. In addition, an appreciable difference in the number of high column density absorbers would be detected if we traced high gas overdensity, but our pipeline is currently not tracing gas in this region for statistical reasons, since we produce random lines of sight inside the box.

As discussed in García et al. (2017b), we confirm that different feedback prescriptions (EDW, MDW) do not make a significant difference in the calculation of the number of absorbers of the ionic transitions. The same conclusion is also true for different models with/without molecular cooling for observables associated to the metal ions. Instead, the low temperature and molecular cooling module has proven to be quite important to match the calculated HI CDDF, Ω_{HI} and Ω_{DLA} with observations available at $z = 4 - 6$.

The numerical runs and the pipeline of this paper were calibrated to resemble the physical conditions of the gas residing in the CGM and IGM at $z \approx 6$. Most of the observables at that time of the Universe are well represented by our theoretical models. Nonetheless, there are a few caveats in this work: first, more observations of metal absorption lines in the spectra of high redshift quasars are required. Although we have included the largest catalogue of HI and ionic detections at high redshift, more observational data are needed to better constrain the emissivity of the UVB. Second, the numerical resolution is still not enough to fully trace the environments where the low ionization states lie, and simultaneously describe the IGM. A new generation of numerical simulations will improve the description of these species, without sacrificing the physics occurring in the inter- and circumgalactic medium. Finally, we stress that radiative transfer effects are not included in our models and, therefore, we do not follow the progression of reionization, nor the evolution of the HII bubbles or

their topology. The implicit assumption is that our boxes (that are small compared to the size of the HII bubbles at the redshifts of interest) represent a region of the Universe already reionized at a level given by the HM12 UVB. At $6 < z < 8$, chemical enrichment occurs mostly inside and in close proximity of galaxies (interstellar medium, CGM and high density IGM) where, assuming an inside-out progression of reionization, the gas in which metals lie should be ionized. Although proper RT calculations would be more accurate, they are extremely expensive from the computational point of view, but could be done in the future.

A fundamental issue persists in the field from the numerical point of view: it is extremely challenging to model the low ionization states present in the gas and to provide a good description of the environment where they lie, mainly due to insufficient resolution and to the lack of a proper self-shielding treatment for the ions. We considered only the effect of HI self-shielding (Rahmati et al. 2013a; Chardin et al. 2018), but did not introduce any self-shielding of low ionization absorbers (which lie in clumpy structures). A first attempt was proposed for DLA systems at low redshift by Bird et al. (2017). However, current works miss this component at high redshift because it is still not well understood how high density regions self-shield the gas during the progression of reionization.

In summary, we have compared HI and ion observables available at high redshift and found that most of the results discussed are compatible in the redshift range $4 < z < 8$. When discrepancies between observations and synthetic calculations arised, we provided a physical explanation of their nature. It is worth noting that all results from mock spectra will be improved in the future with more observational detections of ion absorbers in the high redshift quasar spectra.

REFERENCES

- Abel, T., Bryan, G. L., & Norman, M. L. 2002, *Sci*, 295, 93
- Asplund, M., Grevesse, N., Sauval, A. J., & Scott, P. 2009, *ARA&A*, 47, 481
- Barnes, L. A. & Haehnelt, M. G. 2009, *MNRAS*, 397, 511
- Becker, G. D., Sargent, W. L. W., Rauch, M., & Simcoe, R. A. 2006, *ApJ*, 640, 69
- Becker, G. D., Sargent, W. L. W., Rauch, M., & Calverley, A. P. 2011, *ApJ*, 735, 93
- Becker, G. D., Pettini, M., Rafelski, M., et al. 2019, *ApJ*, 883, 163
- Bird, S., Vogelsberger, M., Haehnelt, M., et al. 2014, *MNRAS*, 445, 2313
- Bird, S., Haehnelt, M., Neeleman, M., et al. 2015, *MNRAS*, 447, 1834
- Bird, S., Garnett, R., & Ho, S. 2017 *MNRAS*, 466, 2111
- Boksenberg, A. & Sargent, W. L. W. 2015, *ApJS*, 218, 7
- Bolton, J. S., Haehnelt, M. G., Viel, M., & Springel, V. 2005, *MNRAS*, 357, 1178
- Bolton, J. S. & Viel, M. 2011, *MNRAS*, 414, 241
- Bosman, S. E. I., Becker, G. D., Haehnelt, M. G., et al. 2017, *MNRAS*, 470, 1919
- Bromm, V., Coppi, P. S., & Larson, R. B. 2002, *ApJ*, 564, 23
- Carswell, R. F. & Webb, J. K. 2014, *Astrophysics Source Code Library*, record ascl:1408.015
- Cen, R. & Chisari, N. E. 2011, *ApJ*, 731, 11
- Chabrier, G. 2003, *PASP*, 115, 763
- Chardin, J., Kulkarni, G., & Haehnelt, M. G. 2018, *MNRAS*, 478, 1065
- Ciardi, B. & Ferrara, A. 2005, *Space Sci. Rev.*, 116, 625
- Codoreanu, A., Ryan-Weber, E. V., García, L. Á., et al. 2018, *MNRAS*, 481, 4940
- Cooke, J., Ryan-Weber, E. V., Garel, T., & Díaz, C. G. 2014, *MNRAS*, 441, 837
- Cooper, T. J., Simcoe, R. A., Cooksey, K. L., et al. 2019, *ApJ*, 882, 77
- Crighton, N. H. M., Murphy, M. T., Prochaska, J. X., et al. 2015, *MNRAS*, 452, 217
- Díaz, C. G., Ryan-Weber, E. V., Cooke, J. D., Crighton, N. H., & Díaz, R. J. 2016, *BAAA*, 58, 51
- Dijkstra, M., Haiman, Z., & Loeb, A. 2004, *ApJ*, 613, 646
- D’Odorico, V., Cupani, G., Cristiani, S., et al. 2013, *MNRAS*, 435, 1198
- Doughty, C., Finlator, K., Oppenheimer, B. D., Davé, R., & Zackrisson, E. 2018, *MNRAS*, 475, 4717
- Doughty, C. & Finlator, K. 2019, *MNRAS*, 489, 2755
- Ferland, G. J., Porter, R. L., van Hoof, P. A. M., et al. 2013, *RMxAA*, 49, 137
- Finlator, K., Muñoz, J. A., Oppenheimer, B. D., et al. 2013, *MNRAS*, 436, 1818
- Finlator, K., Thompson, R., Huang, S., et al. 2015, *MNRAS*, 447, 2526
- Finlator, K., Oppenheimer, B. D., Davé, R., et al. 2016, *MNRAS*, 459, 2299
- Finlator, K., Keating, L., Oppenheimer, B. D., Davé, R., & Zackrisson, E. 2018, *MNRAS*, 480, 2628
- García, L. A., Tescari, E., Ryan-Weber, E. V., & Wyithe, J. S. B. 2017a, *MNRAS*, 469, 53
- . 2017b, *MNRAS*, 470, 2494
- Gnat, O. & Ferland, G. J. 2012, *ApJS*, 199, 20
- Haardt, F. 1999, *Mem. Soc. Astron. Italiana*, 70, 261
- Haardt, F. & Madau, P. 2001, *Clusters of galaxies and the high redshift universe observed in X-rays*, ed. by D. M. Neumann & J. T. T. Van, id.64
- Haardt, F. & Madau, P. 2012, *ApJ*, 746, 125

- Haiman, Z. 2016, *ASSL*, 423, 1
- Hassan, S., Davé, R., Mitra, S., et al. 2018, *MNRAS*, 473, 227
- Katsianis, A., Tescari, E., Wyithe, J. S. B. 2015, *MNRAS*, 448, 3001
- . 2016, *PASA*, 33, 29
- Katsianis, A., Tescari, E., Blanc, G., & Sargent, M. 2017, *MNRAS*, 464, 4977
- Keating, L. C., Haehnelt, M. G., Becker, G. D., & Bolton, J. S. 2014, *MNRAS*, 438, 1820
- Keating, L. C., Puchwein, E., Haehnelt, M. G., Bird, S., & Bolton, J. S. 2016, *MNRAS*, 461, 606
- Kennicutt, R. C., Jr. 1998, *ApJ*, 498, 541
- Lidz, A., Oh, S. P. & Furlanetto, S. R. 2006, *ApJ*, 639, L47
- Lidz, A. 2016, *ASSL*, 423, 23, arXiv: 1511.01188
- Maio, U., Dolag, K., Ciardi, B., & Tornatore, L. 2007, *MNRAS*, 379, 963
- Maio, U. & Tescari, E. 2015, *MNRAS*, 453, 3798
- Mellema, G., Iliiev, I. T., Pen, U.-L., & Shapiro, P. R. 2006, *MNRAS*, 372, 679
- Meyer, R. A., Bosman, S. E. I., Kakiichi, K., & Ellis, R. S. 2019, *MNRAS*, 483, 19
- Mortlock, D. J., Warren, S. J., Venemans, B. P., et al. 2011, *Natur*, 474, 616
- Nagamine, K., Springel, V., & Hernquist, L. 2004, *MNRAS*, 348, 421
- O’Meara, J. M., Prochaska, J. X., Burles, S., et al. 2007, *ApJ*, 656, 666
- Oppenheimer, B. D. & Davé, R. 2006, *MNRAS*, 373, 1265
- Oppenheimer, B. D., Davé, R., & Finlator, K. 2009, *MNRAS*, 396, 729
- Padovani, P. & Matteucci, F. 1993, *ApJ*, 416, 26
- Pallottini, A., Ferrara, A., Gallerani, S., Salvadori, S., & D’Odorico, V. 2014, *MNRAS*, 440, 2498
- Pettini, M., Madau, P., Bolte, M., et al. 2003, *ApJ*, 594, 695
- Planck Collaboration, Ade, P. A. R., Aghanim, N., et al. 2015, *A&A*, 580, 13
- Pontzen, A., Governato, F., Pettini, M., et al. 2008, *MNRAS*, 390, 1349
- Prochaska, J. X., Herbert-Fort, S., & Wolfe, A. M. 2005, *ApJ*, 635, 123
- Prochaska, J. X. & Wolfe, A. M. 2009, *ApJ*, 696, 1543
- Puchwein, E. & Springel, V. 2013, *MNRAS*, 428, 2966
- Rahmati, A., Pawlik, A. H., Raičević, M., & Schaye, J. 2013, *MNRAS*, 430, 2427
- Rahmati, A., Schaye, J., Pawlik, A. H., & Raičević, M. 2013, *MNRAS*, 431, 2261
- Rahmati, A., Schaye, J., Bower, R. G., et al. 2015, *MNRAS*, 452, 2034
- Rahmati, A., Schaye, J., Crain, R. A., et al. 2016, *MNRAS*, 459, 310
- Ryan-Weber, E. V., Pettini, M., Madau, P., & Zych, B. J. 2009, *MNRAS*, 395, 1476
- Simcoe, R. A. 2006, *ApJ*, 653, 977
- Simcoe, R. A., Cooksey, K. L., Matejek, M., et al. 2011, *ApJ*, 743, 21
- Smith, A., Bromm, V., & Loeb, A. 2017, *MNRAS*, 464, 2963
- Songaila, A. 2001, *ApJ*, 561, L153
- . 2005, *AJ*, 130, 1996
- Springel, V. 2005, *MNRAS*, 364, 1105
- Springel, V. & Hernquist, L. 2003, *MNRAS*, 339, 289
- Tescari, E., Viel, M., Tornatore, L., & Borgani, S. 2009, *MNRAS*, 397, 411
- Tescari, E., Viel, M., D’Odorico, V., et al. 2011, *MNRAS*, 411, 826
- Tescari, E., Katsianis, A., Wyithe, J. S. B., et al. 2014, *MNRAS*, 438, 3490
- Thielemann, F.-K., Argast, D., Brachwitz, F., et al. 2003, *Nucl. Phys. A*, 718, 139
- Tornatore, L., Borgani, S., Dolag, K., & Matteucci, F. 2007, *MNRAS*, 382, 1050
- van den Hoek, L. B. & Groenewegen M. A. T. 1997, *A&AS*, 123, 305
- Woosley, S. E. & Weaver, T. A. 1995, *ApJS*, 101, 181
- Yoshida, N., Sokasian, A., Hernquist, L., & Springel, V. 2003, *ApJ*, 598, 73
- Zafar, T., Péroux, C., Popping, A., et al. 2013, *A&A*, 556, 141

Luz Ángela García: Universidad ECCI, Cra. 19 No. 49-20, Bogotá, Colombia, Código Postal 111311 (lgarciap@ecc.edu.co).

Emma V. Ryan-Weber: Swinburne University of Technology, Hawthorn, VIC 3122, Australia (eryanweber@swin.edu.au).

SEARCH FOR STABLE ORBITS AROUND THE BINARY ASTEROID SYSTEMS 1999 KW4 AND DIDYMOS

Thais C. Oliveira and Antonio F. B. A. Prado

Space Mechanic and Tecnology, National Institute for Space Research/INPE, Sao Jose dos Camopo, SP, Brazil.

Received July 4 2019; accepted January 29 2020

ABSTRACT

This work includes analytical and numerical studies of spacecrafts orbiting two binary asteroid systems: 1999 KW4 and Didymos. The binary systems are modeled as full irregular bodies, such that the whole evolution of the results will show the impact of the irregular gravity field in the lifetime and dynamics of the spacecraft's orbit. The equations of motion of the binary system and the spacecraft are derived from Lagrange Equations. The solar radiation pressure is considered in the dynamics of the spacecraft. Two distinct methods are used to search for stable orbits around the binary systems. One is called the grid search method, which defines the main body as a point mass to estimate the initial state of the spacecraft based on a circular Keplerian orbit. The second method is the search for periodic orbits based on zero-velocity surfaces.

RESUMEN

Este trabajo presenta estudios analíticos y numéricos sobre naves espaciales en órbita en torno a dos asteroides binarios: 1999 KW4 y Didymos. Se modelan los sistemas binarios como cuerpos irregulares, de modo que la evolución muestre el impacto del campo de gravedad irregular sobre los tiempos de vida y la dinámica de la órbita de la nave. Se derivan las ecuaciones de movimiento del sistema binario y de la nave a partir de las ecuaciones de Lagrange. Se considera la presión de radiación solar. Se buscan órbitas estables en torno a los sistemas binarios mediante dos métodos. El primero se conoce como el método de búsqueda en la malla, y considera al cuerpo principal como punto masa para estimar el estado inicial de la nave a partir de una órbita Kepleriana circular. El segundo busca órbitas periódicas mediante las superficies de cero velocidad.

Key Words: methods: numerical — minor planets, asteroids: general — space vehicles

1. INTRODUCTION

There is a great scientific interest in asteroids due to their relatively unchanged status as remnant debris from the solar system formation process, around 4.6 billion years ago.

Asteroids are leftovers from the Solar System that can offer clues to the chemical mixture from which planets were formed. In addition, asteroids can pose a danger to Earth depending on the size and course of the object. Therefore, gaining a better understanding of the physical and chemical parameters of the asteroids can help humans to prevent impacts between these objects and the Earth, e.g. by using a gravity tractor, a nuclear explosion, a conventional rocket engine, or a solar energy engine. Moreover, some asteroids have the potential of being used for mining.

The Solar System has different groups of asteroids. The near-Earth asteroids (NEAs) group includes asteroids in the Earth's neighborhood and that have a perihelion distance less than 1.3 AU (NASA 2019). Over

20,000 NEAs have been discovered, of which more than 895 are large asteroids with an estimated diameter greater than 1 km while over 8,600 NEAs have an estimated diameter between 140 m to 1 km (JPL 2019).

The group with the largest population of asteroids is the main-belt group. The main-belt asteroids orbit the Sun and lie between Mars and Jupiter. The belt is estimated to contain between 1.1 and 1.9 million asteroids larger than 1 km in diameter, and millions of smaller ones (NASA 2019).

The last group of asteroids is the Trojan. The Trojans share an orbit with a larger planet. They are located at the Lagrangian points L_4 and L_5 . The Jupiter Trojans form the most significant population of Trojan asteroids. It is thought that they are as numerous as those of the main-asteroid belt (NASA 2019).

There are some asteroids that have natural satellites. The first one was discovered in 1993 around 243 Ida. Since then, many other binary systems have been discovered. It is estimated that there are more than 160 binary asteroid systems: around 15% are NEAs, 2 to 3% are in the main-belt and between 10 to 30% belong to other groups of trans-Neptunian objects (Johnston 2014; Margot et al. 2015). Therefore, it is not surprising that missions to binary asteroid systems will occur in the future.

The Asteroid Impact and Deflection Assessment (AIDA) mission is a proposed pair of space probes which would study and demonstrate the kinetic effects of crashing an impactor spacecraft into the secondary body of a binary asteroid system. Its target would be the moonlet of the binary near-Earth asteroid (65803) Didymos, which is one of the two binary asteroid systems studied in this paper.

The second binary asteroid system studied in this paper is 1999 KW4. This primary asteroid was discovered by LINEAR on May 20, 1999. Its companion was discovered 2001 May 21 using radar and light curve observations (Ostro et al. 2006). 1999 KW4 has the least accessible ΔV for a spacecraft mission of any known binary near-Earth asteroid due to its heliocentric inclination of 39 degrees, eccentricity of 0.7, and semi-major axis of 0.64 au (astronomical units). 1999 KW4 has been classified as a “Potentially Hazardous Asteroid” by the Minor Planet Center (JPL 2019).

The search for stable orbits around a binary system is performed by utilizing theoretical results and numerical methods that have been used in the circular restricted three-body problem (Scheeres et al. 1996; Woo 2014; Yu & Baoyin 2012a; Yu & Baoyin 2012b).

Among the many research topics in the circular restricted three-body problem, the periodic orbit is a fundamental and important part. Generally, there are five kinds of periodic orbits in the global spatial space: libration point orbits, orbits about the primary, orbits about the secondary, orbits about the whole binary system, and other orbits about neither asteroid (Shi et al. 2018a).

The study of periodic orbits provides a general understanding of the stability and formation of natural orbits; stable orbits can be directly adopted for close-proximity operations in space (Hu & Scheeres 2004). Particularly, in the study of asteroids, periodic orbits indicate the potential locations of mutual satellites, which is significant for assessing the spatial environment (Yu & Baoyin 2012b).

Periodic orbits around asteroids have been approximated using models with various degrees of sophistication. In general, one will make some assumptions, such as using a simple shape model and restricting the binary system to be synchronous. Then, the dynamical substitutes in a more precise model can be further determined based on the prior calculated results (Chappaz & Howell 2015; Hou & Xin 2018). To describe the non-spherical shape of an asteroid, an ellipsoid can be used to represent it, which generates the sphere-ellipsoid model and the ellipsoid-ellipsoid model for the binary asteroid systems. Bellerose & Scheeres (2008, 2008) studied the periodic orbits in the sphere-ellipsoid binary system, especially the libration point orbits. Both the sphere-ellipsoid binary system and the ellipsoid-ellipsoid binary system were investigated by Chappaz & Howell (2015), where the resonant orbits were calculated and analyzed in addition to the libration point orbits. Shang et al. (2015) searched the global periodic orbits in the ellipsoid-ellipsoid binary system based on the symmetry of the orbits and obtained different families of periodic orbits. Their results showed that the periodic orbits in an ellipsoid-ellipsoid binary system are analogous to those in the circular restricted three-body problem. The same results are obtained in this paper.

A crucial difference is that the ellipsoid model shows symmetry while the real asteroid does not. The high-fidelity models, such as the polyhedron model and the spherical harmonics model, can reflect the asymmetry of the real binary system. Particularly, the polyhedron model derived by Scheeres (1996) is suitable near the surface of the asteroid. Libration point orbits of Mars-Phobos binary system were investigated by Biggs (2015) using spherical harmonics. They indicated that the irregular shape has a significant influence and that the connections between families of periodic orbits are different from those in the circular restricted three-body

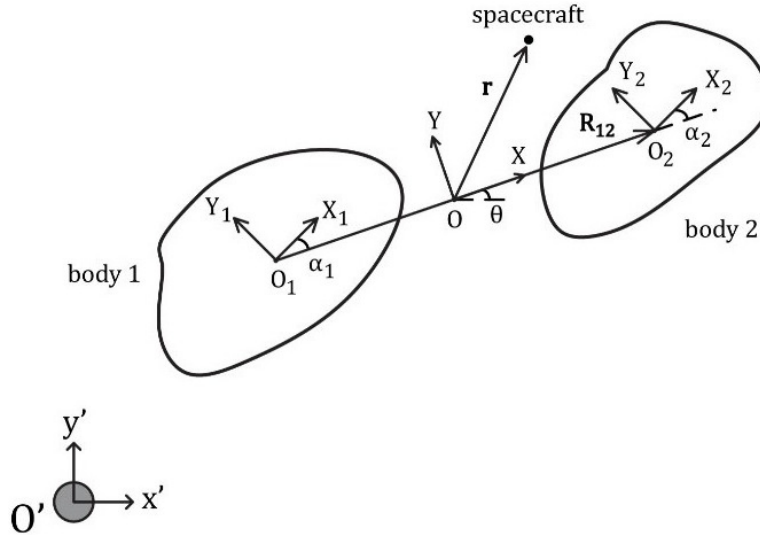


Fig. 1. Illustration of the binary system (Woo & Misra 2013).

problem. Based on the polyhedron model, Scheeres et al. (2017) also revealed differences of the libration point orbits and investigated the retrograde periodic orbits about the Phobos. Shi et al. (2018b) studied the libration point orbits near the binary asteroid system 1999 KW4 using a polyhedron-polyhedron model.

This paper considers the dynamics of the 1999 KW4 and Didymos binary systems as full irregular bodies, from ellipsoids to double-truncated cones. This paper focuses on the search for stable orbits for spacecrafts around these systems based on two distinct methods: the grid search method and zero velocity curves. The grid search method defines the main body as a point mass to estimate the initial state of the spacecraft based on a Keplerian orbit. The second method searches for periodic orbits based on zero-velocity surfaces. All the simulations consider the solar radiation pressure as a disturbing force on the dynamics of the spacecraft. The solar radiation force is a non-conservative force and it can play a key role in the spacecraft orbits around the Solar System. The solar radiation pressure originates from the interaction of the satellite’s surface with the photons emitted by the Sun. It is assumed that each photon that hits the satellite is either absorbed or reflected in a specular or diffuse way.

Periodic orbits are important keys to understand the motion of a massless particle in the vicinity of a binary asteroid system. Due to the complex gravity generated by the irregular-shaped asteroids, it is difficult to generate periodic orbits with an analytical method, except with linearized dynamics in a small region around the libration points. This paper presents a numerical method to search for planar periodic orbits in a global space. The search method can also be used to find periodic orbits in the vicinity of other binary systems.

2. MATHEMATICAL FORMULATION

This paper studies the planar motion of a binary asteroid system, where a full two body problem is considered to account for the mutual motion of the asteroids. The two arbitrarily shaped asteroids have masses m_1 and m_2 , as shown in Figure 1. The system $O'x'y'z'$ is an inertial reference frame with the unit vectors \mathbf{i}' , \mathbf{j}' and \mathbf{k}' .

The center of mass of the binary system is located at O , which is also the origin of the local system $OXYZ$. The unit vectors of the coordinate system $OXYZ$ are given by \mathbf{i} , \mathbf{j} and \mathbf{k} . Note that this reference frame is a synodic one.

The centers of mass of m_1 and m_2 are given by O_1 and O_2 , respectively. The vector \mathbf{R}_{12} connects the point O_1 to O_2 . The direction of \mathbf{R}_{12} is the positive X axis orientation of the right-handed coordinate system $OXYZ$. The orientation of $OXYZ$ relative to the inertial frame is given by the angle θ (Woo & Misra 2014).

Each asteroid has a body-fixed frame, given by $O_iX_iY_iZ_i$, for $i = 1, 2$. The orientation of the body i with respect to the local frame is given by the angle α_i . The unit vectors of the body-fixed frame i is given by \mathbf{i}_i , \mathbf{j}_i and \mathbf{k}_i .

The mass of the spacecraft is negligible for the system dynamics and the motion of the spacecraft is given by the vector $\mathbf{r} = x\mathbf{i} + y\mathbf{j} + z\mathbf{k}$ at the local reference frame OXYZ.

2.1. Dynamics of the System

2.1.1. Lagrange's Mathematical Formulation

The equations of motion of the asteroid binary system are derived from the Lagrange equations. The generalized coordinates are the distance R_{12} , the orientation angle θ and the orientation body angles α_1 and α_2 .

The kinetic energy for the planar binary system based on Figure 1 is given by (Woo & Misra 2013):

$$T = \frac{1}{2}(m_1 + m_2)V_0^2 + \frac{1}{2} \frac{m_1 m_2}{m_1 + m_2} (\dot{R}_{12}^2 + R_{12}^2 \dot{\theta}^2) + \frac{1}{2} I_{zz1} (\dot{\theta} + \dot{\alpha}_1)^2 + \frac{1}{2} I_{zz2} (\dot{\theta} + \dot{\alpha}_2)^2, \quad (1)$$

where $V_0 = (\dot{\mathbf{R}}_0 \cdot \dot{\mathbf{R}}_0)^{1/2}$ is the speed of the center of mass in the inertial frame and \mathbf{R}_0 is the position vector of O in the inertial system; finally, I_{xxi} , I_{yyi} and $I_{zz i}$ are the moments of inertia of the i^{th} body in the $OX_i Y_i Z_i$ coordinate system, for $i = 1, 2$.

The potential energy is given by (Woo & Misra 2013):

$$U = -\frac{Gm_0(m_1 + m_2)}{R_0} - \frac{Gm_1 m_2}{R_{12}} + \frac{3Gm_2}{2R_{12}^3} \left[I_{xx1} \cos^2 \alpha_1 + I_{yy1} \sin^2 \alpha_1 - \frac{1}{3} (I_{xx1} + I_{yy1} + I_{zz1}) \right] + \frac{3Gm_1}{2R_{12}^3} \left[I_{xx2} \cos^2 \alpha_2 + I_{yy2} \sin^2 \alpha_2 - \frac{1}{3} (I_{xx2} + I_{yy2} + I_{zz2}) \right], \quad (2)$$

where m_0 is the mass of the Sun.

Assuming no other external forces, the Lagrange equations are given by:

$$\frac{d}{dt} \frac{\partial T}{\partial \dot{q}_j} - \frac{\partial T}{\partial q_j} + \frac{\partial U}{\partial q_j} = 0, \quad (3)$$

where $q_j = R_{12}, \theta, \alpha_1$ and α_2 .

2.1.2. Non-Dimensionalization and other Variables Definitions

We will use dimensionless variables to study the system. To this end, we introduce the mass ratio $v = \frac{m_1}{m_1 + m_2}$, the characteristic length of the bodies r_0 and the characteristic length of the mutual bodies L .

The moments of inertia I_{xx} , I_{yy} and I_{zz} of each body are described by their non-dimensional radii of gyration p_{xx} , p_{yy} and p_{zz} . The radii of gyration are given by $p_{xxi} = \sqrt{\frac{I_{xxi}}{m_i r_0^2}}$, $p_{yyi} = \sqrt{\frac{I_{yyi}}{m_i r_0^2}}$ and $p_{zz i} = \sqrt{\frac{I_{zz i}}{m_i r_0^2}}$, for $i = 1, 2$ (Woo & Misra (2013, 2014)).

The non-dimensionalized position vector of the spacecraft is given by:

$$\bar{\mathbf{r}} = \frac{\mathbf{r}}{L} = \frac{x}{L} \mathbf{i} + \frac{y}{L} \mathbf{j} + \frac{z}{L} \mathbf{k}. \quad (4)$$

The non-dimensionalized time is defined by: $\tau = nt$, where n is the mean motion of a circular orbit with radius L . The mean motion is given as follows: (Bellerose & Scheeres 2008; Woo & Misra 2014)

$$n = \sqrt{G(m_1 + m_2)/L^3}. \quad (5)$$

The time derivatives can be written as:

$$\frac{d(\cdot)}{dt} = n \frac{d(\cdot)}{d\tau} = n(\cdot)'. \quad (6)$$

The distance R_{12} is replaced by the variable: $u = L/R_{12}$.

2.2. *The Circular Mutual Orbit Between the Binary Asteroid System*

The equations of motion derived in equation 3 in terms of the non-dimensional quantities are given by (Woo & Misra 2013):

$$u'' - \frac{2u'^2}{u} + u\theta'^2 - u^4 - \epsilon \frac{3}{4} u^6 (k_{12}^2 + 3k_1^2 \cos 2\alpha_1 + 3k_2^2 \cos 2\alpha_2) = 0, \tag{7}$$

$$\frac{d}{dt} \left(\theta' + \epsilon u^2 \left[\frac{p_{zz1}^2}{1-v} (\theta' + \alpha'_1) + \frac{p_{zz2}^2}{v} (\theta' + \alpha'_2) \right] \right) = 0, \tag{8}$$

$$\theta'' + \alpha_1'' + \frac{3}{2} (1-v) \frac{k_1^2}{p_{zz1}^2} u^3 \sin(2\alpha_1) = 0, \tag{9}$$

$$\theta'' + \alpha_2'' + \frac{3}{2} v \frac{k_2^2}{p_{zz2}^2} u^3 \sin(2\alpha_2) = 0, \tag{10}$$

where $\epsilon = \left[\frac{r_0}{L} \right]^2$; $k_{12}^2 = 2p_{zz1}^2 - p_{xx1}^2 - p_{yy1}^2 + 2p_{zz2}^2 - p_{xx2}^2 - p_{yy2}^2$; $k_1^2 = p_{yy1}^2 - p_{xx1}^2$; and $k_2^2 = p_{yy2}^2 - p_{xx2}^2$.

This paper considers binary systems in a mutual circular orbit. This means that the system is in a relative equilibrium, where u, θ', α_1 and α_2 are constant. In other words, $u''(\tau) = u'(\tau) = \theta''(\tau) = \alpha_1''(\tau) = \alpha_2''(\tau) = 0$.

It is assumed that $\alpha_1(\tau = 0) = \alpha_2(\tau = 0) = 0$ for all simulations and also that the body-fixed frames centered at O_1 and O_2 are chosen to be aligned with the principal axes. The initial condition for the planar binary system to move in a circular orbit taking $\alpha_1 = \alpha_2 = 0$ is given as follows (Woo 2014; Woo & Misra 2013):

$$\theta' = H \left[1 + \epsilon u^2 \left(\frac{p_{zz1}^2}{1-v} + \frac{p_{zz2}^2}{v} \right) \right]^{-1}, \tag{11}$$

where H is the constant of integration of equation 8.

2.3. *The Equation of Motion of the Spacecraft*

The orbital motion of the spacecraft is studied by considering the restricted full three-body problem. The term “restricted” indicates that the mass of the spacecraft does not affect the dynamics of the binary asteroid bodies. Assuming that the binary asteroid system orbits in a circular orbit, the equations of motion of the spacecraft in the OXYZ reference frame are given by (Woo & Misra 2015):

$$x'' - 2\theta'y' - \theta'^2 x = f_1(x, y, z), \tag{12}$$

$$y'' + 2\theta'x' - \theta'^2 y = f_2(x, y, z), \tag{13}$$

$$z'' = f_3(x, y, z), \tag{14}$$

where

$$f_1(x, y, z) = -v \left[\frac{1}{r_{13}^3} + \frac{3}{2r_{13}^5} \epsilon \left[3p_{xx1}^2 + p_{yy1}^2 + p_{zz1}^2 - \frac{5}{r_{13}^2} \left[\left(\frac{1-v}{u} + x \right)^2 p_{xx1}^2 + y^2 p_{yy1}^2 + z^2 p_{zz1}^2 \right] \right] \right] \left(\frac{1-v}{u} + x \right) - (1-v) \left[\frac{1}{r_{23}^3} + \frac{3}{2r_{23}^5} \epsilon \left[3p_{xx2}^2 + p_{yy2}^2 + p_{zz2}^2 - \frac{5}{r_{23}^2} \left[\left(-\frac{v}{u} + x \right)^2 p_{xx2}^2 + y^2 p_{yy2}^2 + z^2 p_{zz2}^2 \right] \right] \right] \left(-\frac{v}{u} + x \right), \tag{15}$$

$$f_2(x, y, z) = -v \left[\frac{1}{r_{13}^3} + \frac{3}{2r_{13}^5} \epsilon [p_{xx1}^2 + 3p_{yy1}^2 + p_{zz1}^2 - \frac{5}{r_{13}^2} \left[\left(\frac{1-v}{u} + x \right)^2 p_{xx1}^2 + y^2 p_{yy1}^2 + z^2 p_{zz1}^2 \right]] \right] y -$$

$$(1-v) \left[\frac{1}{r_{23}^3} + \frac{3}{2r_{23}^5} \epsilon [p_{xx2}^2 + 3p_{yy2}^2 + p_{zz2}^2 - \frac{5}{r_{23}^2} \left[\left(-\frac{v}{u} + x \right)^2 p_{xx2}^2 + y^2 p_{yy2}^2 + z^2 p_{zz2}^2 \right]] \right] y, \quad (16)$$

$$f_3(x, y, z) = -v \left[\frac{1}{r_{13}^3} + \frac{3}{2r_{13}^5} \epsilon [p_{xx1}^2 + p_{yy1}^2 + 3p_{zz1}^2 - \frac{5}{r_{13}^2} \left[\left(\frac{1-v}{u} + x \right)^2 p_{xx1}^2 + y^2 p_{yy1}^2 + z^2 p_{zz1}^2 \right]] \right] z -$$

$$(1-v) \left[\frac{1}{r_{23}^3} + \frac{3}{2r_{23}^5} \epsilon [p_{xx2}^2 + p_{yy2}^2 + 3p_{zz2}^2 - \frac{5}{r_{23}^2} \left[\left(-\frac{v}{u} + x \right)^2 p_{xx2}^2 + y^2 p_{yy2}^2 + z^2 p_{zz2}^2 \right]] \right] z, \quad (17)$$

and $r_{13}^2 = \left(\frac{1-v}{u} + x \right)^2 + y^2 + z^2$ and $r_{23}^2 = \left(-\frac{v}{u} + x \right)^2 + y^2 + z^2$.

Equations 12 to 14 are given in a rotating reference frame, under the assumption that binary asteroid moves in a circular orbit, where the primaries are located on the x axis.

2.4. Lagrangian Points and Zero-Velocity Curves

There are five Lagrangian points in the classical three-body problem with point masses. Three of them are collinear (L_1, L_2, L_3) and two non-collinear (L_4, L_5). The Lagrangian points L_4 and L_5 , in the classical formulations, are located at equal distances from the primary bodies (Thornton & Mariom 2004; Valtonen & Karttunen 2006). This paper uses the classical approach to locate the equilibrium points in a full three body problem. The Lagrangian points are found by assuming that all of the forces acting on the system are in relative equilibrium.

The Lagrange equations are found just like in the classical method to locate the equilibrium points in a full three-body problem by letting $z = 0, x' = y' = z' = 0, x'' = y'' = z'' = 0$ in equations 12 to 14. This paper presents only the Lagrangian points that are close to the classical ones; the other points are ignored. To be brief, this paper omits a deep discussion about equilibrium points, but related references can be found in Woo (2014) and Woo & Misra (2014).

The zero-velocity curves are found with the Jacobi constant. The equations of motion in equations 12 to 14 can be written as:

$$x'' - 2\theta'y' = \frac{\partial \check{U}}{\partial x}, \quad (18)$$

$$y'' + 2\theta'x' = \frac{\partial \check{U}}{\partial y}, \quad (19)$$

$$z'' = \frac{\partial \check{U}}{\partial z}, \quad (20)$$

where the gravitational potential \check{U} is given by (Woo, 2014):

$$\check{U}(x, y, z) = \frac{1}{2} \theta'^2 (x^2 + y^2) + v \left[\frac{1}{r_{13}} + \epsilon \frac{3}{2r_{13}^3} \left[\frac{P_1}{3} - \frac{\left(\frac{1-v}{u} + x \right)^2 p_{xx1}^2 + y^2 p_{yy1}^2 + z^2 p_{zz1}^2}{r_{13}^2} \right] \right] +$$

$$(1-v) \left[\frac{1}{r_{23}} + \epsilon \frac{3}{2r_{23}^3} \left[\frac{P_2}{3} - \frac{\left(-\frac{v}{u} + x \right)^2 p_{xx2}^2 + y^2 p_{yy2}^2 + z^2 p_{zz2}^2}{r_{23}^2} \right] \right], \quad (21)$$

where $P_i = p_{xxi}^2 + p_{yyi}^2 + p_{zz_i}^2$ for $i = 1, 2$.

The Jacobi constant can be re-written as:

$$C(x, y, z, x', y', z') = 2\check{U}(x, y, z) - (x'^2 + y'^2 + z'^2). \tag{22}$$

Equation 22 can be re-arranged as a zero-velocity surface equation as follows:

$$2\check{U}(x, y, z) - C(x, y, z, x', y', z') = (x'^2 + y'^2 + z'^2) > 0. \tag{23}$$

The Lagrangian points can be used to find critical values of the Jacobi constant C , e.g. $C_{L1} = C(x_{L1}, 0, 0, 0, 0, 0)$ where x_{L1} is the position of the L_1 Lagrangian point.

2.5. Search for Stable Orbits around the Binary System

2.5.1. Periodic Orbits

The numerical search for periodic orbits, in this work, uses the same mathematical formulation as Roy (2005). The search for periodic orbits is conducted on the $X - Y$ plane, which rotates with velocity θ' along with the OXYZ plane. It is considered that the third-body is on the X axis and its velocity is on the perpendicular Y axis, i.e., $x' = z' = y = z = 0$ and $y' \neq 0$.

Therefore, a periodic orbit in this case is the position x_{per} that the satellite has when it crosses the x -axis at times $\tau_1(x_{per}), \tau_2(x_{per}), \tau_3(x_{per}), \dots$, with the velocity x' assumed to be zero. The period of the orbit is given by $T = \tau_i(x_{per}) - \tau_j(x_{per})$, for $i = j + 1$ and $i \geq 2$ (Roy 2005).

The Jacobi constant is used for the search of periodic orbits. Substituting: $x' = z' = y = z = 0$; $x = x_{per}$ and $y' = y'_{per} \neq 0$ in equation 23, we have (Roy 2005; Woo 2014):

$$y'^2 = \theta'^2 x_{per}^2 + 2v \left(\frac{1}{r_{13p}} + \frac{\epsilon}{2r_{13p^3}} (P_1 - 3p_{xx1}^2) \right) + 2(1 - v) \left(\frac{1}{r_{23p}} + \frac{\epsilon}{2r_{23p^3}} (P_2 - 3p_{xx2}^2) \right) - C, \tag{24}$$

where $r_{13p} = \left| \frac{1}{\frac{1-v}{u} + x_{per}} \right|$ and $r_{23p} = \left| \frac{1}{\frac{-v}{u} + x_{per}} \right|$.

2.5.2. The Grid Search Method

The Grid Search Method (GSM) is used in this section to find stable orbits around the KW4 and Didymos binary systems.

The binary system will be modeled as irregular bodies, but for the grid search method it will be assumed that the primary asteroid is a point mass, to determine the initial state of the spacecraft.

The initial state of the spacecraft orbit is based on a circular Keplerian orbit around the primary body of the binary system; the second body is ignored in the computation. Therefore, the initial state of the spacecraft orbit is defined by the classical Keplerian elements: semi-major axis, eccentricity, inclination and true anomaly. The other two variables of the Keplerian elements are assumed to be zero. The center of the system used to compute the initial state of the spacecraft is the center of mass of the primary body. To compute the initial state of the spacecraft the mass of the system is considered to be the mass of the primary body. This estimation works well in this paper since the mass of the primary body is much larger than that of the secondary for both binary systems studied. Some adaptations should be done if the secondary body has a considerable mass compared to the primary body. The semi-major axis is normalized by dividing it by L . The inclination and true anomaly can be 0 or 180 degrees.

Numerical integrations map the orbits, and measure the lifetime of the orbits before a collision with one of the asteroids or an escape occurs. The GSM provides good data visualization of the regions where there are stable orbits. These maps were first shown in Oliveira & Prado (2017).

The maximum simulation time if there is no escape or collision with one of the asteroids was arbitrarily chosen to be $\tau = 42$. This period of time is assumed to be sufficient to estimate if the orbit is stable around the asteroids. The solar radiation pressure acts as a perturbation force that will always interferes with the trajectory of the satellite. Therefore, even if a closed periodic orbit is found around a binary system, the solar radiation pressure will eventually disturb the trajectory.

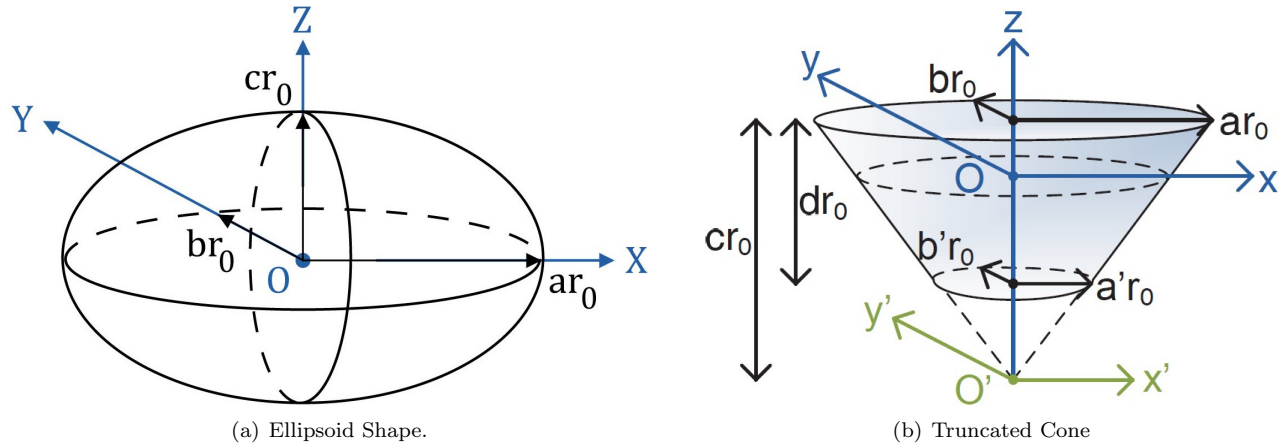


Fig. 2. The shape of irregular bodies. The color figure can be viewed online.

2.6. The Shape of the Asteroids

The irregular shapes are shown in Figure 2 and the mathematical formulations of the gyration radii are given in Woo (2014) and Woo & Misra (2013). The origin of the body-fixed $x_i y_i z_i$ frame is attached to the center of mass O_i , where $i = 1$ or 2 . The $x_i y_i z_i$ are oriented along the principal axes. The dimensions of the ellipsoid are ar_0 , br_0 , cr_0 in the x_i , y_i , z_i directions, respectively.

For the truncated cone, at its largest base, the dimensions are ar_0 and br_0 in the x_i and y_i directions, respectively. At the small base, the x and y dimensions are $a'r_0$ and $b'r_0$, respectively. The height of the full cone would be cr_0 . The height of the truncated cone is dr_0 . For ease of integration, a second $x' y' z'$ frame is attached to the vertex O' of the full cone. The distance between O and O' is obtained by computing the location of the center of mass O in the $x' y' z'$ frame.

2.7. The Solar Radiation Pressure

The solar radiation pressure is the pressure exerted upon any surface due to the exchange of momentum between the area of the surface and the momentum of light or electromagnetic radiation which is absorbed, reflected, or otherwise diffused.

The solar radiation force is non-conservative, and it can play a key role in spacecraft orbits in the Solar System. All spacecraft experience such a pressure, except when they are behind the shadow of a larger orbiting body.

In this work, the solar radiation flux is calculated based on the solar constant which is 1361 W/m^2 at 1 au (Kopp & Lean 2011). The solar radiation flux depends on the distance between the spacecraft and the Sun.

The solar radiation pressure is not considered in the Lagrangian points and zero-velocity curves computation. All of the simulations consider the solar radiation pressure as a disturbing force in the dynamics of the spacecraft. The simulations start at the perigee of the center of mass of the binary system, where the solar radiation pressure has the largest influence on the spacecraft's dynamics. It is assumed that the spacecraft is a cube with one of the faces always facing the center of mass of the primary body. Each face is 10 m^2 ; the mass of the spacecraft is considered to be 500 kg .

The surface area element dA is the elementary area of the spacecraft in m^2 . The constant c is the speed of light. The solar flux is given by Ψ (W/m^2).

The unit vector $\hat{\mathbf{s}}$ has the spacecraft-to-Sun direction. The unit vector $\hat{\mathbf{n}}$ is the surface area element unit normal vector. The angle ϕ is the angle between the surface normal and $\hat{\mathbf{s}}$. If $\cos(\phi)$ is negative, then the area element is not illuminated by the Sun and will not experience any radiation pressure.

For each surface area element dA of the spacecraft, the coefficients α , ρ , and δ represent the fraction of the incident radiation that is absorbed, reflected, or diffused, respectively. These coefficients are related as follows:

$$\alpha + \rho + \delta = 1. \tag{25}$$

The total differential force due to solar radiation pressure on a surface area element $d\mathbf{F}$ is the sum of the differential forces of the absorbed $d\mathbf{F}_\alpha$, the specularly reflected $d\mathbf{F}_\rho$ and the diffuse $d\mathbf{F}_\delta$ differential forces, given by the following equation (Lyon 2004):

$$d\mathbf{F} = d\mathbf{F}_\alpha + d\mathbf{F}_\rho + d\mathbf{F}_\delta, \tag{26}$$

where

$$d\mathbf{F}_\alpha = -\frac{\Psi dA \cos(\phi)}{c} \alpha \hat{\mathbf{s}}, \tag{27}$$

$$d\mathbf{F}_\rho = -\frac{\Psi dA \cos(\phi)}{c} 2 \cos(\theta) \rho \hat{\mathbf{n}}, \tag{28}$$

$$d\mathbf{F}_\delta = -\frac{\Psi dA \cos(\phi)}{c} \delta \left(\hat{\mathbf{s}} + \frac{2}{3} \hat{\mathbf{n}} \right). \tag{29}$$

The equation for the force due to radiation pressure acting on each flat plate is obtained by integrating equation 26 over the surface area, A , of each side of the spacecraft's faces:

$$\mathbf{F} = -\frac{\Psi A \cos \theta}{c} \left[(1 - \rho) \hat{\mathbf{s}} + 2 \left[\frac{\delta}{3} + \rho \cos \theta \right] \hat{\mathbf{n}} \right]. \tag{30}$$

After the non-dimensionalization of the variables given in § 2.1.2, the solar radiation pressure acceleration is added to the equations of motion of the spacecraft given in equations 12 to 14.

3. RESULTS

3.1. Physical Parameters for 1999 KW4 and Didymos

Tables 1 and 2 present the physical parameters of the 1999 KW4 binary system and Tables 3 and 4 those of the Didymos binary system.

3.2. Initial Parameters and Asteroid Shapes for 1999 KW4 and Didymos

Tables 5 to 8 present the gyration radii and the initial parameters used in the simulations. The initial parameters for both binary asteroid system u , θ , α_1 , α_2 , u' , θ' , α'_1 and α'_2 were carefully chosen to satisfy a mutual circular orbit. The choice of α_1 and α_2 , not being constants, must be included in equations (15) to (17). Due to lack of space, the equations were omitted here but can be found in Appendix A of Woo & Misra (2014).

The primary asteroid of 1999 KW4 was modeled as a double truncated cone, the secondary as an ellipsoid. The values of the parameters a , b , c and d for the asteroid shapes and also r_0 are based on the physical parameters given in Table 2.

Figures 3 and 4 present the distance between the asteroid bodies R_{12} in meters and the rotation period of the primary ($\theta + \alpha_1$) and secondary ($\theta + \alpha_2$) bodies for 10 orbital periods for 1999 KW4 and Didymos, respectively. The numerical simulations of Figures 3 and 4 are consistent with the numerical data for the binary system in Tables 1 to 4. The bodies move in a nearly circular orbit and the rotation period of the asteroids is constant and stable. There are small variations of the distance between the bodies, but for practical purposes when the zero velocity curves are computed it is considered that the mutual asteroid orbits are circular.

For Didymos, the asteroid shape, dimensions and some of the initial parameters are estimated based on the current knowledge of its physical properties. The binary system is tidally locked (Landis & Johnson 2019), therefore $\alpha'_2 = 0$.

Current theories of asteroid satellite formation predict that the satellites should have similar or smaller densities than the primaries. From the system mass 5.27×10^{11} kg and the diameter ratio Scheirich & Pravec (2009), the calculated mass of the secondary is 5×10^9 kg (Cheng et al. 2016).

The primary and secondary Didymos bodies are shaped as ellipsoids and their dimensions are based on Table 4, and the mass estimation on Scheirich & Pravec (2009); Cheng et al. (2016).

TABLE 1
ORBITAL DATA FOR THE 1999 KW4 BINARY SYSTEM

	Binary Asteroid System ¹	Center of Mass around the Sun ²
Semi-major Axis	2548 m	0.642291859 au
Eccentricity	0.0004	0.68846023
Orbital Period	17.4216 h	0.514762413 yr

¹(Ostro et al. 2006). ²(Benner 2014).

TABLE 2
PHYSICAL PARAMETERS FOR 1999 KW4*

	Primary Body	Secondary Body
Mass	2.253×10^{12} kg	2.488×10^{11} kg
Dimensions	$1532 \times 1495 \times 1347$ m	$571 \times 463 \times 349$ m
Rotation Period	2.7645 h	17.4223 h

*(Ostro et al. 2006; Shi et al. 2017; Fahnestock & Scheeres 2008).

TABLE 3
ORBITAL DATA FOR THE DIDYMOS SYSTEM*

	Binary Asteroid System	Center of Mass around the Sun
Semi-major Axis	1180 m	1.6445 au
Eccentricity	0.06	0.3836
Orbital Period	0.4958 d	2.1087 yr

*(Zhang et al. 2017; Dell'Elce et al. 2017).

TABLE 4
PHYSICAL PARAMETERS FOR THE DIDYMOS SYSTEM*

Primary diameter	780 m
Secondary Diameter	163 m
Total mass	5.278×10^{11} kg
Density (ρ)	2100 kg /m ³
Primary rotation period	2.26 h

*(Zhang et al. 2017; Dell'Elce et al. 2017).

TABLE 5
SHAPE AND GYRATION RADII FOR THE 1999 KW4 ASTEROID BODIES

	a	b	c	d	p_{xx}	p_{yy}	p_{zz}
Double Truncated Cone	1	0.9758	1.2	0.8792	0.4379	0.4462	0.5460
Ellipsoid	0.3727	0.3022	0.2278	-	0.1662	0.1953	0.2146

TABLE 6
INITIAL PARAMETERS FOR 1999 KW4

u_c	θ_c	α_1	α_2	u'_c	θ'_c	α'_1	α'_2	v	ε	L	r_0
1.0010	0	0	0	0	1.0112	5.3014	0.0012	0.9457	0.0904	2548 m	766 m

TABLE 7
SHAPE AND GYRATION RADII FOR THE DIDYMOS ASTEROID BODIES

	mass	a	b	c	p_{xx}	p_{yy}	p_{zz}
Primary Ellipsoid	5.288×10^{11}	1	0.9500	0.8697	0.5760	0.5927	0.6168
Secondary Ellipsoid	5×10^9	0.2090	0.1990	0.1900	0.1230	0.1263	0.1291

TABLE 8
INITIAL PARAMETERS FOR THE DIDYMOS ASTEROIDS

u_c	θ_c	α_1	α_2	u'_c	θ'_c	α'_1	α'_2	v	ε	L	r_0
0.998	0	0	0	0	1.0028	6.2559	0	0.9905	0.1092	1180 m	390 m

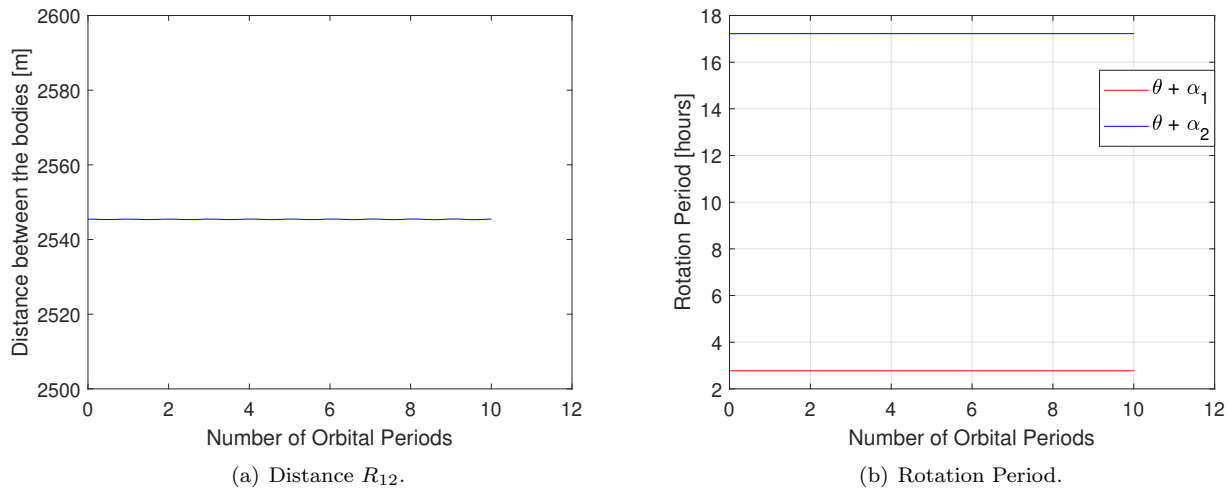


Fig. 3. 1999 KW4 binary system simulation. The color figure can be viewed online.

3.2.1. GSM application in the Binary Asteroid System

This section presents the results of the GSM for the 1999 KW4 and Didymos binary systems. The GSM maps for 1999 KW4 and Didymos are very similar, therefore only the best GSM maps are shown for Didymos when the orbits are retrograde (Morais & Giuppone 2012; Scheeres et al. 2017).

Figures 5a and 5b present the maps, based on the GSM, for the 1999 KW4 binary system when the inclination is zero and the true anomaly is 0 and π , respectively. The zero inclination results in prograde orbits.

Figures 6a and 6b present the maps, based on the GSM, for the 1999 KW4 binary system for retrograde orbits when the inclination is π and the true anomaly is 0 and π , respectively. Figures 7a and 7b show maps for the Didymos binary system when the inclination is π and the true anomaly is 0 and π , respectively.

As expected, there are many more stable retrograde orbits than prograde orbits around the binary asteroid systems (Morais & Giuppone 2012; Scheeres et al. 2017). The GSM is a good method to find stable orbits

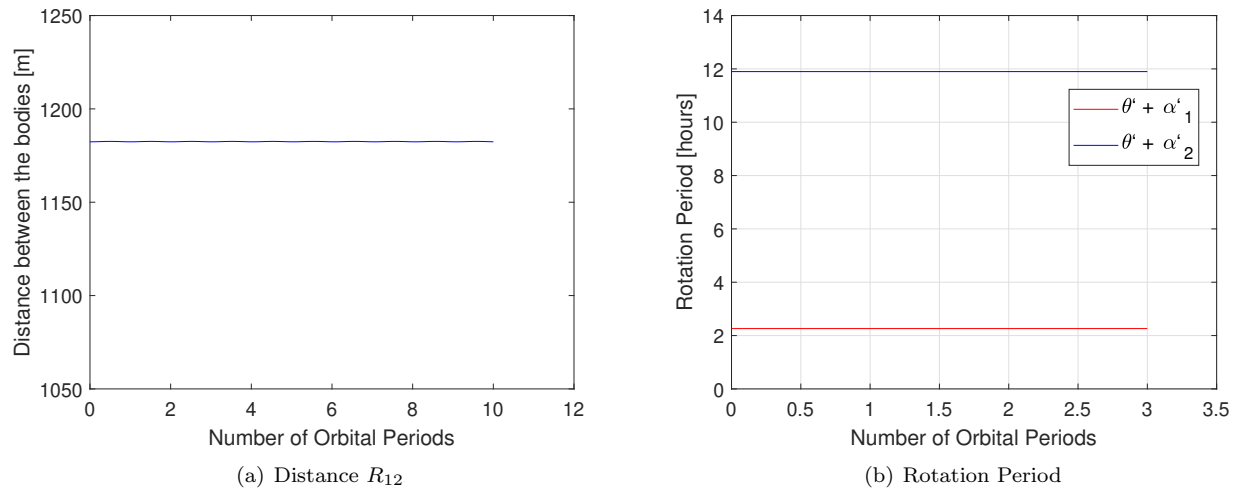


Fig. 4. Dydymos Binary System Simulation. The color figure can be viewed online.

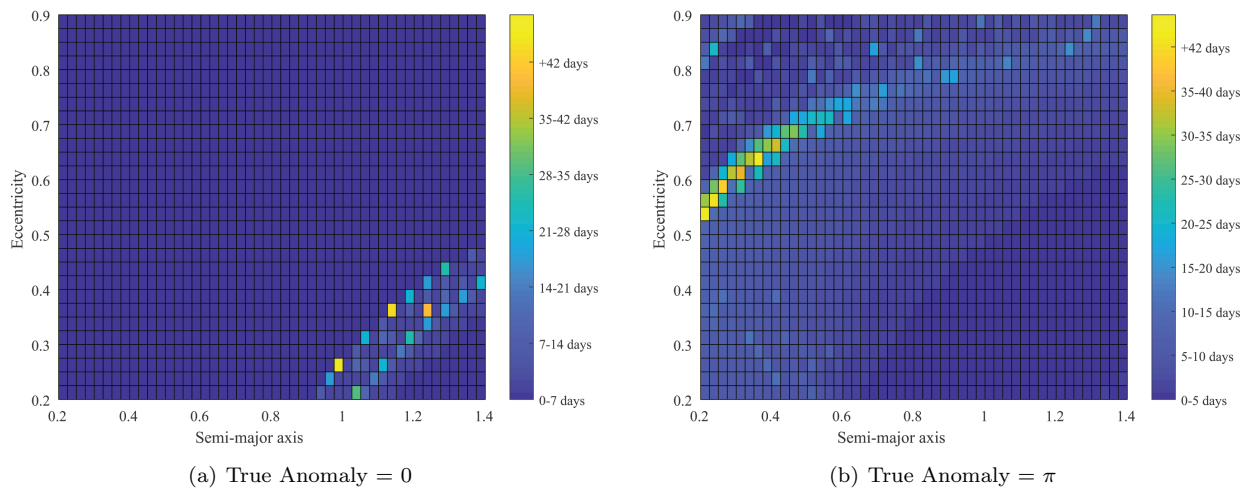


Fig. 5. Prograde orbits around 1999 KW4. The color figure can be viewed online.

around binary asteroid systems when the mass of the primary body is much bigger than that of the secondary. The secondary body acts as a perturbation on the Keplerian orbit, along with the non-spherical shape of the asteroid bodies and the solar radiation pressure. The inner orbits in the stable orbit band of Figure 6 are the best candidate orbits in which to place the spacecraft. These orbits are surrounded by stable orbits as well, therefore slight external disturbing forces such as the solar radiation pressure will not significantly change the stability.

Figure 8 shows examples of stable orbits around 1999 KW4 based on the orbits found by the GSM shown in Figure 6.

3.3. Zero-Velocity Curves

Zero-velocity curves can be used to find stable orbits confined to certain regions, e.g., an orbit confined around the primary body.

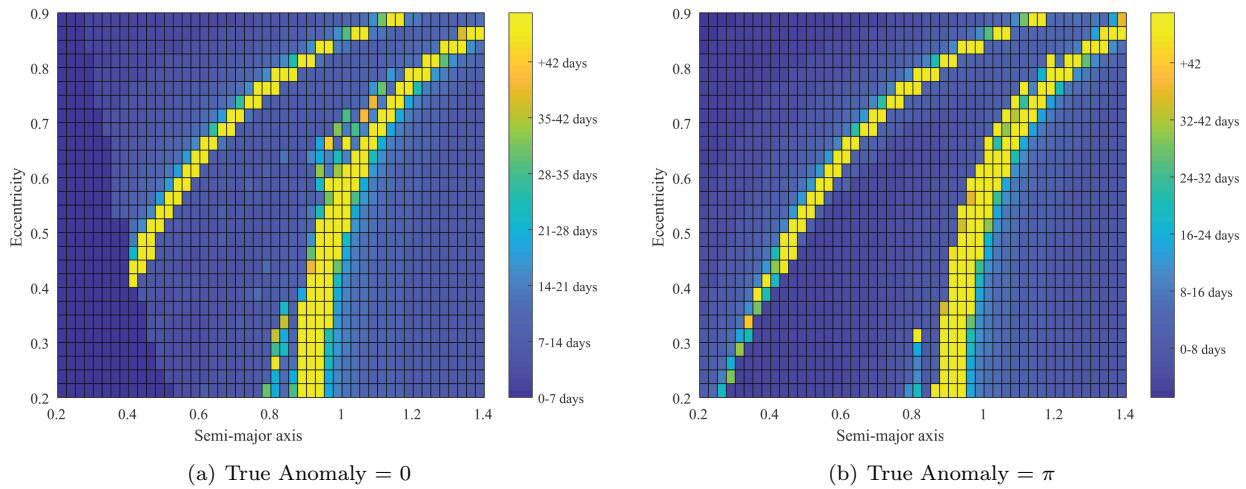


Fig. 6. Retrograde orbits around 1999 KW4. The color figure can be viewed online.

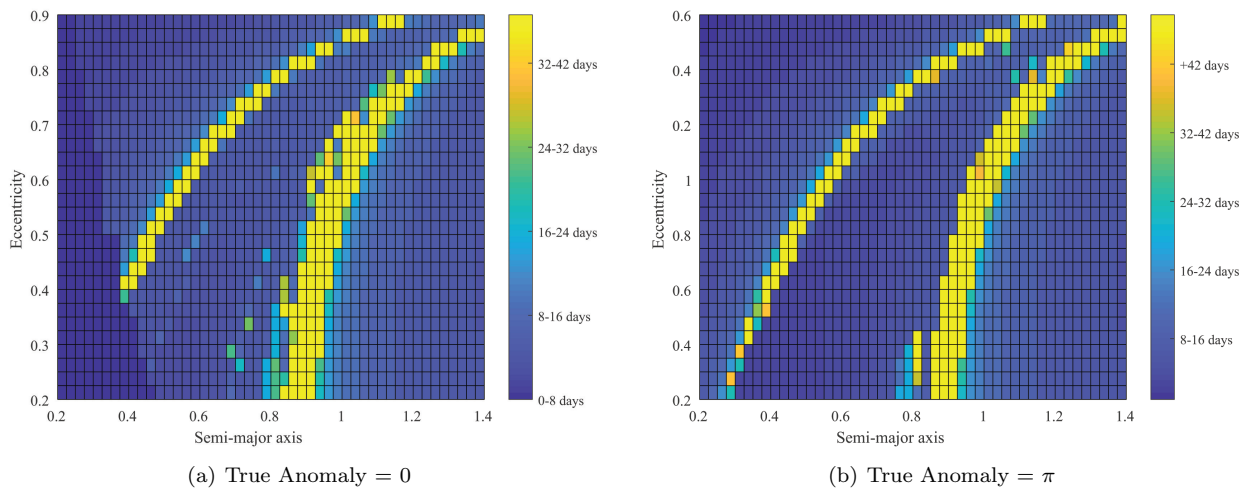


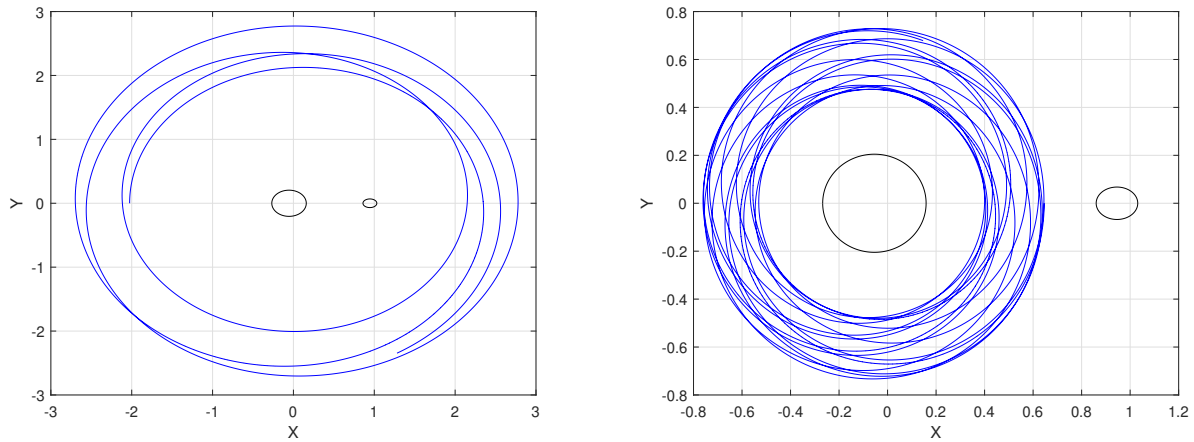
Fig. 7. Retrograde orbits around Didymos. The color figure can be viewed online.

Table 9 presents the Lagrangian points and also the Jacobi constant C based on these Lagrangian points computed for 1999 KW4 and Didymos, respectively. Figures 9 show the Jacobi constant C of KW4 and Didymos based on the Lagrangian points L_1, L_2 and L_3 , labelled C_{L1}, C_{L2} and C_{L3} , respectively.

As shown in Figure 9, for a spacecraft with a specific value of $C_0 > C_{L1}$, the zero-velocity surface consists of small ellipsoid-like geometries around the primary and secondary, and a large cylindrical-like surface surrounding the two-body system. The grey ellipsoidal shapes denote the asteroid bodies; the purple stars indicate the locations of the Lagrangian points. For $C_{L1} > C_0 > C_{L2}$, the allowable region for the spacecraft is the two ellipsoidals connected around the asteroid bodies. And for $C_{L2} > C_0 > C_{L3}$, the inner and outer allowable regions connect behind the secondary body.

Figure 10 presents orbits around the primary asteroid for planar motion, where $C_0 = 3.55$.

From a numerical search for the 1999 KW4 system, it was found that $x(0) = -0.5$ produces a retrograde orbit around the primary body with $y(0) = z(0) = x'(0) = z'(0) = 0$. From equation 24, $y'(0) = -1.0672$ (see Figure 10a).

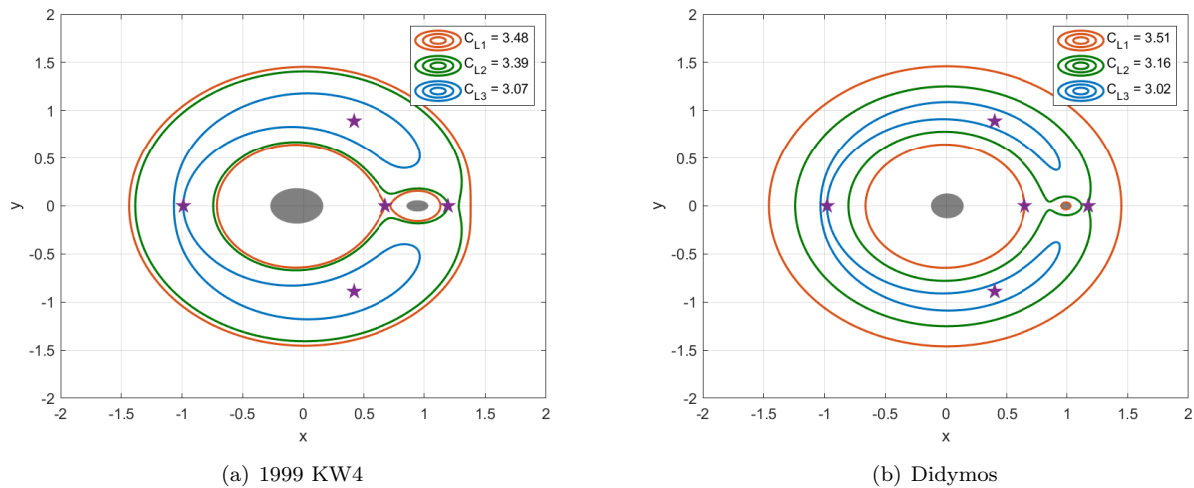


(a) Semi-major axis = 2.05, eccentricity = 0, true anomaly = 0. (b) Semi-major axis = 0.35, eccentricity = 0.75, true anomaly = π .

Fig. 8. Stable orbits around 1999 KW4. The color figure can be viewed online.

TABLE 9
LAGRANGIAN POINTS

		L_1	L_2	L_3	L_4	L_5
KW4	(x,y)	(0.6792, 0)	(1.1953, 0)	(-0.9887, 0)	(0.4192, 0.8897)	(0.4192, -0.8897)
	C	3.4812	3.3931	3.0701	2.9873	2.9873
Didymos	(x,y)	(0.6907, 0)	(1.2098, 0)	(-1.0235, 0)	(0.4032, 0.8972)	(0.4032, -0.8972)
	C	3.3725	3.1853	3.0229	2.9985	2.9985



(a) 1999 KW4

(b) Didymos

Fig. 9. Zero-velocity curves for C_1 , C_2 and C_3 . The color figure can be viewed online.

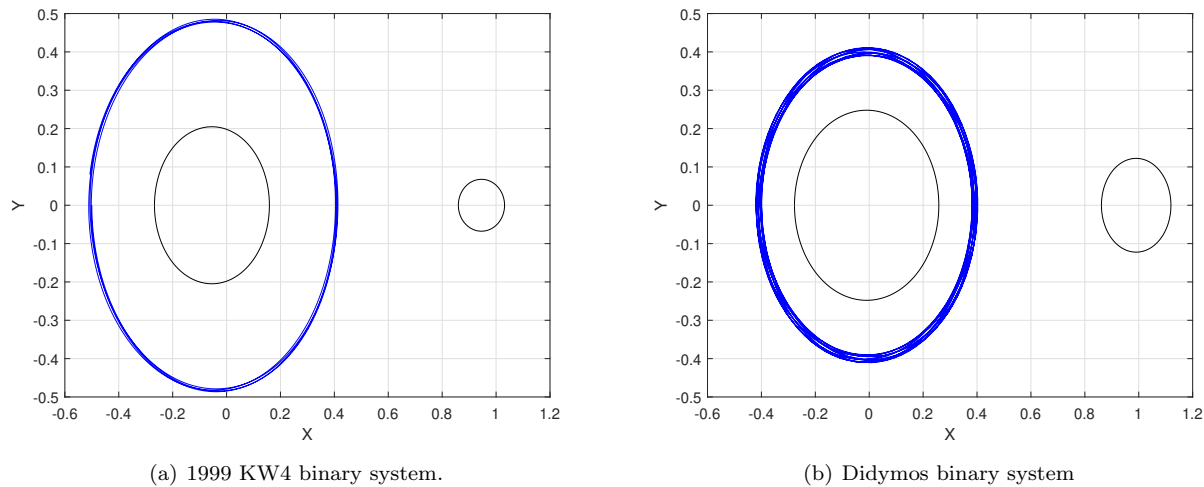


Fig. 10. Trajectory of the spacecraft in the XY -plane around the primary asteroid. The color figure can be viewed online.

For Didymos, a numerical search found a periodic retrograde orbit when $x(0) = -0.4$ and $y'(0) = -1.2759$ (see Figure 10b).

Due to the high sensitivity on the initial conditions and to the solar radiation pressure perturbation, the resulting trajectories in Figure 10 are not perfectly periodic, but they may be sufficient for practical purposes.

4. CONCLUSION

The binary asteroid systems are modeled as full irregular bodies in a restricted three-body problem. The physical and orbital parameters of binary asteroid systems 1999 KW4 and Didymos are considered in the mathematical formulation of the shape and dynamics of the system. Both binary asteroid systems have nearly circular mutual orbits; therefore, zero-velocity curves can also be used to find stable orbits around the system.

The paper proposes two distinct methods to search for stable orbits around the binary asteroids. The first method, named the grid search method, results in easy and practical visualization of stable orbits around the binary system. The maps are based on the initial state of the spacecraft and the time period of the spacecraft orbit before a collision or an escape occurs.

The second method to look for stable orbits is based on zero-velocity curves. The method has proved to be efficient to find stable orbits around different allowable regions based on the Jacobi constant.

The greatest advantage of the methods studied in this paper is to easily find stable orbits around binary asteroid systems in a fast and practical way using the grid search method and/or zero-velocity curves based on the full restricted circular three-body problem.

The authors gratefully acknowledge the financial support of FAPESP (2016/01430-7).

REFERENCES

- | | |
|--|---|
| <p>Bellerose, J. & Scheeres, D. J. 2008, <i>AcAau</i>, 62, 563, https://doi.org/10.1016/j.actaastro.2008.01.018</p> <p>Bellerose, J. & Scheeres, D. J. 2008, <i>JGCD</i>, 31, 1, https://doi.org/10.2514/1.30937</p> <p>Benner, L. A. M. 2014, Binary and ternary near-Earth asteroids detected by radar, JPL, website: http://echo.jpl.nasa.gov/~lance/binary.neas.html, accessed March 26, 2019</p> | <p>Chappaz, L. & Howell, K. C. 2015, <i>CeMDA</i>, 123, 123, https://doi.org/10.1007/s10569-015-9632-5</p> <p>Cheng, A. F., et al. 2016, <i>AcAau</i>, 115, 262, doi: 10.1016/j.pss.2015.12.004</p> <p>Dell'Elce, L., Baresi, N., Naidu, S. P., Benner, L. A. M., & Scheeres, D. J. 2017 <i>AdSpR</i>, 59, 1304, https://doi.org/10.1016/j.asr.2016.12.018</p> <p>Fahnestock, E. G. & Scheeres, D. J. 2008, <i>Icar</i>, 194, 410</p> |
|--|---|

- Hou, X. & Xin, X. 2018, *AsDyn*, 2, 39, <https://doi.org/10.1007/s42064-017-0010-9>
- Hu, W. & Scheeres, D. J. 2004, *P&SS*, 52, 685, doi: 10.1016/j.pss.2004.01.003
- Johnston, W. R. 2014, *PDSS*, 219
- JPL, 2019, Center for Near Earth Object Studies, <https://cneos.jpl.nasa.gov/stats/totals.html> (2019), Accessed 01 May 2019
- JPL, 2019, Goldstone Radar Observations Planning: Asteroid 1999 KW4 in 2019, https://echo.jpl.nasa.gov/asteroids/1999KW4/1999KW4_planning.2019.html (2019), Accessed 15 May 2019
- Kopp, G. & Lean, J. L. 2011, *GeoRL*, 38, 1706, doi: 10.1029/2010GL045777
- Landis, R. & Johnson, L. 2019, *AcAau*, 156, 394, <https://doi.org/10.1016/j.actaastro.2018.06.020>
- Lyon, R. H. 2004, *Geosynchronous Orbit Determination Using Space Surveillance Network Observations and Improved Radiative Force Modeling*, Mater of Science, Department of Aeronautics and Astronautics, 2004
- Margot, J.-L., Pravec, P., Taylor, P., Carry, B., Jacobson, S. 2015, in *Asteroids IV*, ed. P. M. F. DeMeo and W. F. Bottke (Tucson, AZ: University of Arizona Press), 355
- Morais M. H. M., Giuppone C. A. 2012, *MNRAS*, 424, 52, <https://doi.org/10.1111/j.1365-2966.2012.21151.x>
- NASA, 2019, Science: Solar System Exploration, <https://solarsystem.nasa.gov/asteroids-comets-and-meteors/asteroids/in-depth> (2019), Accessed 25 April 2019
- Oliveira, T. C. & Prado, A. F. B. 2017, *AdAns*, 160, 17
- Ostro, S. J., et al. 2006, *Sci*, 314, 1276
- Roy, A. E. 2005, *Orbital Motion* (4th ed.; Bristol UK: Institute of Physics Publishing)
- Scheirich, P. & Pravec, P. 2009, *Icar*, 200, 531
- Scheeres, D. J., Ostro, S. J., Hudson, R. S., & Werner, R. A. 1996, *Icar*, 121, 67, <https://doi.org/10.1006/icar.1996.0072>
- Scheeres, D. J., Williams B. G., & Miller, J. K. 2000, *JGCD*, 23, 466, <https://doi.org/10.2514/2.4552>
- Scheeres, D. J., Van Wal, S., Olikara, Z., & Baresi, N. 2017, in: *International Symposium on Space Technology and Science*, Ehime, Japan, 3-9
- Shang, H., Wu, X., & Cui, P. 2015, *Ap&SS*, 355, 69, <https://doi.org/10.1007/s10509-014-2154-x>
- Shi, Y., Wang, Y., & Xu, S. 2017, *CeMDA*, 129, 307, doi: 10.1007/s10569-017-9776-6.
- _____. 2018a, *AcAau*, 163, 11, <https://doi.org/10.1016/j.actaastro.2018.10.014>
- _____. 2018b, *CeMDA*, 130, 32, <https://doi.org/10.1007/s10569-018-9827-7>
- Thornton, S. T. & Marion, J. B. 2004, *Classical Dynamics of Particles and Systems*, (5th ed.; Thomson Brooks/Cole)
- Valtonen, M. & Karttunen, H. 2006, *The Three-Body Problem*, (Cambridge, MA: CUP)
- Woo, P. 2014, *Dynamics of a Spacecraft in the Vicinity of a Binary Asteroid System*, Thesis, McGill University
- Woo, P., Misra, A. K., & Keshmiri, M. 2013, *CeMDA*, 117, 263, <https://doi.org/10.1007/s10569-013-9512-9>
- Woo, P. & Misra, A. K. 2014, *AcAau*, 99, 158, <https://doi.org/10.1016/j.actaastro.2014.02.019>
- _____. *AcAau*, 110, 313, <https://doi.org/10.1016/j.actaastro.2014.11.001>
- Werner, R. A. & Scheeres, D. J. 1996, *CeMDA*, 65, 313, <https://doi.org/10.1007/BF00053511>
- Yu, Y. & Baoyin, H. 2012a, *AJ*, 143, 62, doi: 10.1088/0004-6256/143/3/62
- _____. 2012b, *MNRAS*, 427, 872, doi: 10.1111/j.1365-2966.2012.21963.x
- Zamaro, M. & Biggs, J. 2015, *CeMDA*, 122, 263, <https://doi.org/10.1007/s10569-015-9619-2>
- Zhang, Y., et al. 2017, *Icar*, 294, 98, <https://doi.org/10.1016/j.icarus.2017.04.027>

CCD PHOTOMETRY AND EVOLUTIONARY STATUS OF THE PULSATING VARIABLE CSS J051053.0+071722

K. B. Alton

Desert Blooms Observatory, USA.

Received November 28 2019; accepted January 29 2020

ABSTRACT

Multi-color (BVI_c) CCD-derived photometric data were acquired for CSS J051053.0+071722, a pulsating variable classified as a high amplitude δ Scuti-type system. Analysis of precise time-series lightcurve data was accomplished using discrete Fourier transformation which revealed a mean fundamental mode (f_0) of oscillation at $14.5097 \pm 0.0001 \text{ d}^{-1}$ along with two other partial harmonics ($2f_0$ and $4f_0$). No other statistically significant frequency shared by all bandpasses was resolved following successive pre-whitening of each residual signal. Except for 36 new times-of-maximum light produced from the present study, no other values were found in the literature; therefore, potential secular period changes could not be evaluated. The evolutionary status, age and physical nature of CSS J051053.0+071722 were investigated using the PAdova & TRieste Stellar Evolution Code for generating stellar tracks and isochrones.

RESUMEN

Se obtuvieron datos fotométricos CCD multicolor (BVI_c) para CSS J051053.0+071722, una variable pulsante clasificada como un sistema tipo δ Scuti de gran amplitud. El análisis de la curva de luz de alta precisión se realizó mediante la transformada de Fourier discreta, la cual reveló un modo fundamental medio de oscilación (f_0) en $14.5097 \pm 0.0001 \text{ d}^{-1}$, junto con otros dos armónicos parciales ($2f_0$ y $4f_0$). No se encontró ninguna otra frecuencia apreciable compartida por todos los anchos de banda después del pre-blanqueo sucesivo de cada señal residual. No se encontraron en la literatura datos para los tiempos de máxima luz que complementen los 36 presentados aquí. Por ello, no fue posible estudiar posibles cambios seculares del período. El estado evolutivo, la edad y la naturaleza física de CSS J051053.0+071722 se investigaron usando el código de evolución estelar PAdova&TRieste para generar trayectorias evolutivas e isocronas.

Key Words: Hertzsprung-Russell and colour-magnitude diagrams — stars: evolution — stars: oscillations — stars: variables: Scuti

1. INTRODUCTION

High amplitude δ Scuti stars, hereafter HADS, constitute a very small percentage (<1%) of all δ Sct variables (Lee et al. 2008). They commonly oscillate ($\Delta V > 0.1 \text{ mag}$) via low-order single or double radial pulsation modes (Poretti 2003a,b; Niu et al. 2013, 2017) driven by the κ -mechanism resulting from partial ionization of He II (Pamyatnykh 1999). Many ($\approx 40\%$) are double pulsators showing simultaneous pulsations in the fundamental and the first overtone mode, with amplitudes generally higher in the fundamental mode (McNa-

mara 2000). Non-radial pulsations have also been detected in the HADS variable V974 Oph (Poretti 2003a,b). HADS variables have historically been divided according to metallicity relative to the Sun ($[Fe/H]=0$). The metal-poor ($[Fe/H]<0$) group is classified as SX Phe-like stars based on the prototype SX Phoenicis. Purportedly they have shorter periods ($0.02 < P < 0.125 \text{ d}$) and lower masses ($\approx 1.0\text{--}1.3 M_\odot$) than their related HADS variables possessing near solar metal abundance (McNamara 2011). SX Phe stars frequently reside in globular clusters (GC) which are ancient collections of Pop-

ulation II stars. Therein, the majority of these pulsators are classified as blue straggler stars, paradoxically appearing much younger than their GC cohorts. Balona & Nemec (2012) proposed that it is not possible to differentiate between δ Sct and field SX Phe variables based on pulsation amplitude, the number of pulsation modes, period or even metallicity (Garg et al. 2010). Highly sensitive space telescopes like Kepler (Gilliland et al. 2010), CoRoT (Baglin 2003) and MOST (Walker et al. 2003) have discovered many examples that contradict these traditionally accepted definitions. Balona & Nemec (2012) further contend that the evolutionary status of each star is the only way to distinguish between these two classes.

An additional classification scheme for δ Scuti stars was recently examined by Qian et al. (2017). Therein two distinct groups of δ Scuti stars were uncovered from the LAMOST survey (Zhou et al. 2009) that fundamentally differed in effective temperature. One group was identified as normal δ Scuti stars (NDSTs) when T_{eff} ranged between 6700-8500 K while the other was considered as unusual and cool variable stars (UCVs) with T_{eff} values less than 6700 K. A more restrictive fundamental pulsation range (0.09-0.22 d) coupled with being slightly metal poor ($[Fe/H] = -0.25 - 0.0$) further differentiates the UCVs from the NDST group. Furthermore, once the UCV stars were excluded from consideration, empirically based temperature-period, $\log g$ -period, and metallicity-period relationships were developed for NDSTs.

The variability of CSS J051053.0+071722 (J2000-05:10:53.0976 +07h 17m 21.984s; $l=194.1681$ $b=-18.49118$) was first recorded in unfiltered photometric data (also known as NSVS 9510981 and NSVS 12312737) collected during the ROTSE-I Survey (Akerlof et al. 2000). These sparsely sampled lightcurve (LC) data collected between 1999-2000 can be retrieved from the Northern Sky Variable Survey¹ (Woźniak et al. 2004). More robust supporting evidence used to establish the primary oscillation period of this intrinsic variable (CSS J051053.0+071722) was gathered between 2001-2009 during the Catalina Sky Survey² (Drake et al. 2009). Its variability was also identified from an evaluation of photometric data (also known as ASAS J051053+0717.4) collected (2005-2013) during the All Sky Automated Survey³ (Pojmanski 2000). This report marks the first multi-color

photometric study of CSS J051053.0+071722 which also describes the physical nature of this radial pulsator and critically assesses its classification as a HADS variable.

2. OBSERVATIONS AND DATA REDUCTION

Time-series images were acquired at Desert Blooms Observatory (DBO, USA - 110.257 W, 31.941 N) with an STT-1603ME CCD camera (Diffraction Limited) mounted at the Cassegrain focus of a 0.4-m ACF-Cassegrain telescope. This telecompressed (0.62 \times) f/6.8 instrument produced an image scale of 1.36 arcsec/pixel (bin=2 \times 2) and a field-of-view (FOV) of 11.6' \times 17.3'. Image acquisition (75-s) was performed using *TheSkyX Pro* Version 10.5.0 (Software Bisque). The CCD-camera is equipped with B , V and I_c filters manufactured to match the Johnson-Cousins Bessell prescription. Dark subtraction, flat correction and registration of all images collected at DBO were performed with *AIP4Win* v2.4.0 (Berry & Burnell 2005). Instrumental readings were reduced to catalog-based magnitudes using the AAVSO Photometric All-Sky Survey (APASS) star fields (Henden et al. 2009, 2010, 2011; Smith et al. 2011) built into *MPO Canopus* v10.7.1.3 (Minor Planet Observer). LCs for CSS J051053.0+071722 were generated using an ensemble of five non-varying comparison stars. The identity (HST Guide Star Catalog, Version GSC-ACT), J2000 coordinates and APASS color indices ($B - V$) for these stars are provided in Table 1. Data from images taken below 30 $^\circ$ altitude (airmass >2.0) were excluded. Given that all program stars share the same FOV, differential atmospheric extinction was ignored. During each imaging session comparison stars typically stayed within ± 0.009 mag for the V and I_c filters and ± 0.018 mag for the B passband. All relevant lightcurve data (HJD, APASS magnitude, err, filter) acquired during this study at DBO can be retrieved from the AAVSO archives (<https://www.aavso.org/data-download>).

3. RESULTS

Photometric values in B (n=249), V (n=262), and I_c (n=263) passbands were each processed to produce LCs that spanned 30 d between 25 Dec 2018 and 25 Jan 2019 (Figure 2). Time-of-maximum (ToMax) estimates (Table 2) were derived using the polynomial extremum fit utility featured in *Peranso v2.6* (Paunzen & Vanmunster 2016). In this case a mean period solution for all passbands (0.068921 \pm 0.000007 d) was obtained using the Fourier curve fitting utility (Harris et al. 1989, FALC) featured in

¹<https://skydot.lanl.gov/nsvs/nsvs.php>

²<http://nessi.cacr.caltech.edu/DataRelease/>

³<http://www.astrouw.edu.pl/asas/?page=acvs>

TABLE 1
ASTROMETRIC COORDINATES (J2000), V -mag AND COLOR INDICES ($B - V$)*

FOV ID	GSC ID	R.A. h m s	Dec. deg m s	APASS ^a V -mag	APASS ^a ($B - V$)
T	0111-02001	05 10 53.0976	+07 17 21.984	12.78	0.24
1	0111-02132	05 10 59.3688	+07 21 42.876	12.02	0.62
2	0111-01355	05 11 21.6096	+07 14 17.520	13.28	0.48
3	0111-00631	05 10 56.5632	+07 14 54.780	12.81	0.66
4	0111-00973	05 10 47.2464	+07 13 40.764	14.28	0.56
5	0111-01041	05 10 22.4184	+07 15 31.572	13.06	0.64

*For CSS J051053.0+071722 (GSC 0111-02001) and five comparison stars (1-5) used during this photometric study.

^a V -mag and ($B - V$) derived from APASS DR9 database.

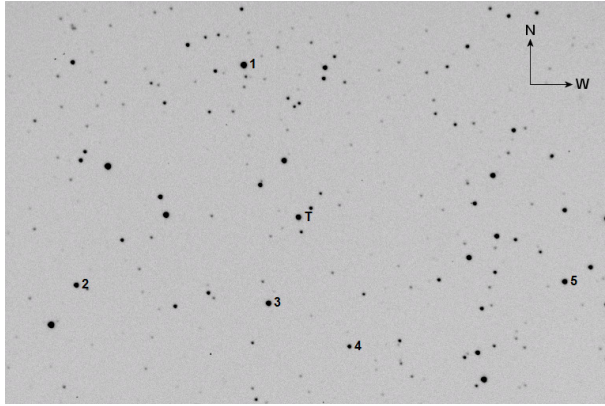


Fig. 1. FOV (17.3×11.6 arcmin) containing CSS J051053.0+071722 (T) along with the five comparison stars (1-5) used to reduce time-series images to APASS-catalog based magnitudes.

MPO Canopus v10.7.1.3. Thereafter, period determinations of survey data (NSVS, ASAS and CSS) were performed using *Peranso v2.6* by applying periodic orthogonal (Schwarzenberg-Czerny 1996) to fit observations, and analysis of variance to assess fit quality. Folding together the sparsely sampled NSVS survey data revealed a period at 0.068919 ± 0.000024 d (Figure 3). The ASAS (Pojmanski 2000) photometric data acquired in 2003-2009 were period-folded and reached superimposition when $P=0.068920 \pm 0.000024$ d (Figure 4). Finally, unfiltered CCD data mined from the Catalina Sky Survey (CSS) were similarly evaluated (Figure 5) to produce a fundamental period of $P=0.068919 \pm 0.000036$ d. Since no ToMax data for this variable star were found in the literature only new maxima ($n=36$) from DBO which appear in Table 2 were used to ana-

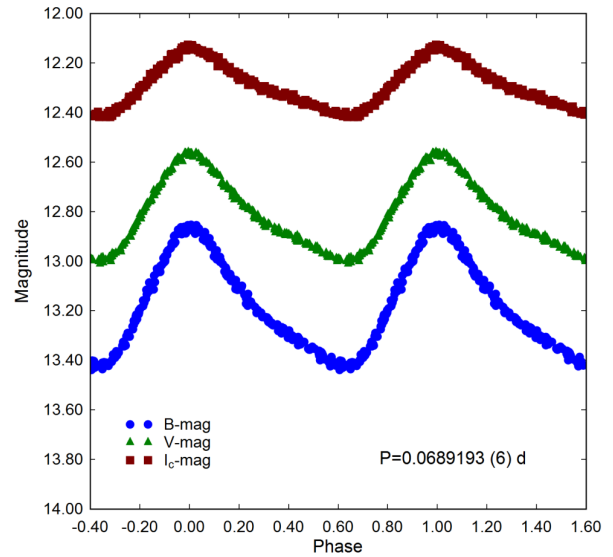


Fig. 2. Period folded (0.0689193 ± 0.0000006 d) LCs for CSS J051053.0+071722 produced from photometric data obtained between 25 Dec 2018 and 25 Jan 2019 at DBO. LCs shown at the top (I_c), middle (V) and bottom (B) represent catalog-based (APASS) magnitudes determined using *MPO Canopus*. The color figure can be viewed online.

lyze fundamental pulse period timings (PPT). PPT differences *vs.* cycle number (Table 2) can be described by a straight line relationship from which a new linear ephemeris was calculated (equation 1):

$$\text{Max}(HJD) = 2\,458\,508.7047(1) + 0.0689193(6) E. \quad (1)$$

These results along with the LCs from DBO (Figure 2), NSVS (Figure 3), ASAS (Figure 4) and CCS (Figure 5) also reveal that the fundamental pulsa-

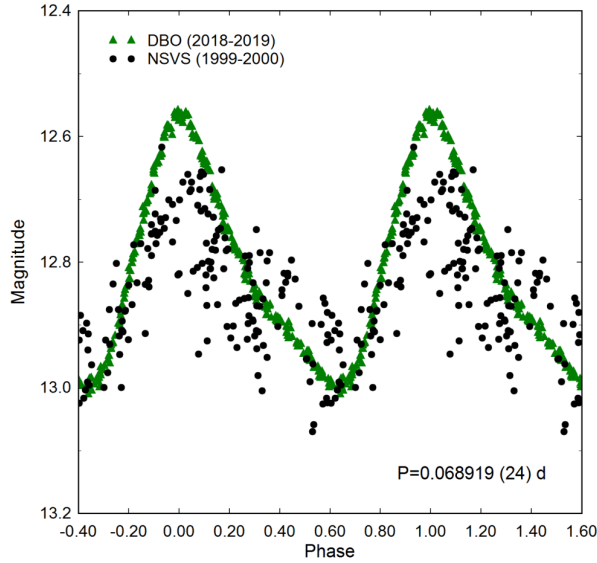


Fig. 3. Period folded (0.068919 ± 0.000024 d) LCs for CSS J051053.0+071722 produced with sparsely sampled data (NSVS 9510981 and NSVS 12312737) from the NSVS (1999-2000) Survey. Precise time-series V -mag data acquired at DBO (2018-2019) are superimposed for direct comparison with ROTSE- I magnitudes which have been offset to conform to the DBO-derived values. The color figure can be viewed online.

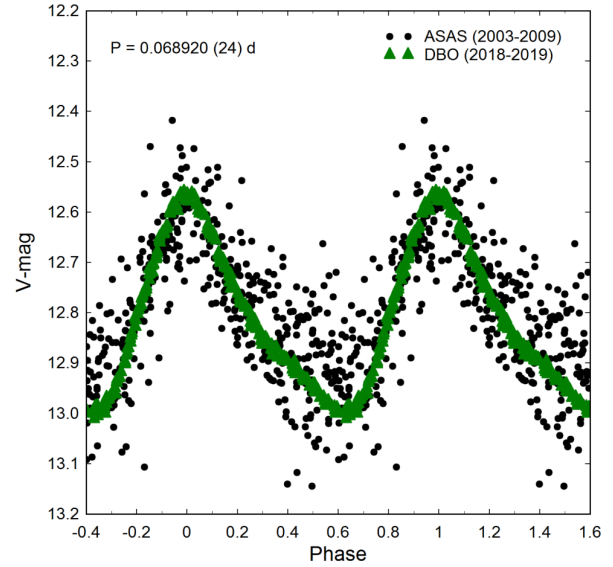


Fig. 4. Period-folded (0.068920 ± 0.000024 d) LCs for CSS J051053.0+071722 produced with photometric data (ASAS J051053+0717.4) from the ASAS survey (2003-2009). Precise time-series V -mag data acquired at DBO (2018-2019) are superimposed for direct comparison with ASAS magnitudes (I -band: Schott RG-9) which have been offset to conform to the DBO-derived values. The color figure can be viewed online.

tion period has been consistent since 1999. Due to the short duration (30 d) of available ToMax timings no attempt was made to evaluate any underlying secular changes in period.

3.1. Light Curve Behavior

Morphologically, LCs of HADS variables are asymmetrical with rapid brightening to produce a sharply defined maximum peak. Thereafter a slower decline in magnitude results in a broad minimum. The largest difference between maximum and minimum light is observed in the blue passband ($\Delta B = 0.56$ mag), followed by V ($\Delta V = 0.43$ mag) and finally the smallest difference detected in infrared ($\Delta I_c = 0.28$ mag). Plotting $(B - V)$ against phase (Figure 6) shows significant color amplitude (0.125 mag) going from maximum [$(B - V) \simeq 0.3$] to minimum light [$(B - V) \simeq 0.425$]. This behavior, commonly observed with pulsating F- to A-type stars, is more closely associated with a decrease in the effective surface temperature during minimum light.

Interstellar extinction was obtained according to Amôres & Lépine (2005)⁴ which re-

quires galactic coordinates (l , b) and distance (kpc). Accordingly, the Model A reddening value ($E(B - V) = 0.065 \pm 0.003$ mag), corresponds to an intrinsic color index $(B - V)_0$ for CSS J051053.0+071722 that varies between 0.239 ± 0.013 mag at maximum light and 0.358 ± 0.013 mag at minimum brightness. Easy access to accurate distances from the Gaia mission (Brown et al. 2018) offers an advantage over the dust maps generated by Schlegel et al. (1998) and later adjusted by Schlafly and Finkbeiner (2011) wherein extinction is based on total dust in a given direction without regard to the target distance. This often leads to an overestimation of the reddening within the Milky Way galaxy, most commonly determined as $E(B - V) = A_V/3.1$. The average effective temperature (T_{eff}) was estimated to be 7222 ± 94 K according to the polynomial transformation equations derived by Flower (1996). These results based strictly on $(B - V)$ photometry at DBO are somewhat higher but within the uncertainty included ($T_{\text{eff}} = 7173^{+302}_{-142}$ K) in the Gaia DR2 release of stellar parameters (Andrae et al. 2018). The final T_{eff} (7178 ± 119 K) adopted for this study represents a mean value from 2MASS (7141 ± 264 K) using J , K and H transforms (Warner 2007) to

⁴<http://www.galexin.org/v1p0/>

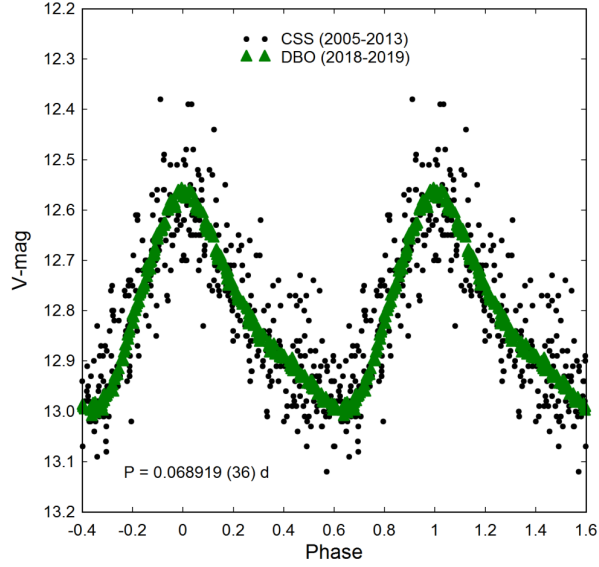


Fig. 5. Period folded (0.068919 ± 0.000036 d) LCs for CSS J051053.0+071722 produced with unfiltered CCD-derived photometric data (2005-2013) from the CSS archives. Precise time-series V -mag data acquired at DBO (2018) are superimposed for direct comparison with the CSS data which have been offset to conform to the DBO-derived values. The color figure can be viewed online.

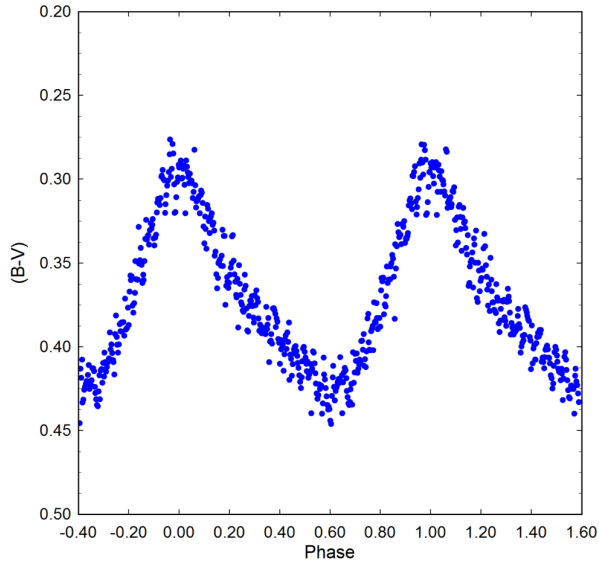


Fig. 6. CSS J051053.0+071722 LC illustrating significant color change as maximum light slowly descends to minimum light ($B - V \simeq 0.425$ mag). This effect is most closely associated with a decrease in the effective surface temperature during minimum light. The color figure can be viewed online.

TABLE 2
TIMES OF MAXIMUM FOR
CSS J051053.0+071722*

ToMax ^a (HJD-2400000)	Uncertainty	Filter	Cycle No.	PTD
58477.6910	0.0006	<i>V</i>	0	0.0000
58477.6911	0.0006	<i>B</i>	0	0.0001
58477.6916	0.0013	<i>I_c</i>	0	0.0006
58477.7597	0.0007	<i>V</i>	1	-0.0002
58477.7598	0.0005	<i>B</i>	1	-0.0001
58477.7603	0.0011	<i>I_c</i>	1	0.0004
58477.8279	0.0014	<i>V</i>	2	-0.0010
58477.8293	0.0007	<i>B</i>	2	0.0004
58477.8307	0.0008	<i>I_c</i>	2	0.0019
58483.6180	0.0006	<i>B</i>	86	-0.0001
58483.6181	0.0007	<i>V</i>	86	0.0001
58483.6182	0.0012	<i>I_c</i>	86	0.0002
58483.6866	0.0007	<i>V</i>	87	-0.0004
58483.6869	0.0005	<i>B</i>	87	-0.0001
58483.6874	0.0012	<i>I_c</i>	87	0.0004
58483.7558	0.0009	<i>V</i>	88	-0.0001
58483.7560	0.0005	<i>B</i>	88	0.0002
58483.7566	0.0010	<i>I_c</i>	88	0.0007
58483.8235	0.0008	<i>I_c</i>	89	-0.0013
58483.8243	0.0006	<i>B</i>	89	-0.0005
58483.8244	0.0009	<i>V</i>	89	-0.0004
58486.6506	0.0009	<i>V</i>	130	0.0001
58486.6508	0.0006	<i>B</i>	130	0.0003
58486.6516	0.0011	<i>I_c</i>	130	0.0011
58487.6152	0.0008	<i>V</i>	144	-0.0001
58487.6155	0.0005	<i>B</i>	144	0.0001
58487.6157	0.0008	<i>I_c</i>	144	0.0004
58487.6837	0.0013	<i>I_c</i>	145	-0.0006
58487.6839	0.0006	<i>B</i>	145	-0.0004
58487.6843	0.0008	<i>V</i>	145	0.0000
58508.6359	0.0005	<i>B</i>	449	0.0002
58508.6359	0.0008	<i>V</i>	449	0.0002
58508.6362	0.0011	<i>I_c</i>	449	0.0005
58508.7044	0.0005	<i>V</i>	450	-0.0003
58508.7046	0.0003	<i>B</i>	450	-0.0001
58508.7049	0.0006	<i>I_c</i>	450	0.0003

*Uncertainty, filter, epoch and fundamental pulsation timing differences (PTD) used to calculate a new linear ephemeris.

^aAll values acquired at DBO (2018-2019).

Johnson-Cousins, Gaia DR2 ($T_{\text{eff}} = 7173^{+302}_{-142}$ K) and DBO (7222 ± 94 K); the spectral type of this variable would likely range between A9 and F2. According to Qian et al. (2017), CSS J051053.0+071722 would be considered a NDST rather than a UCV since T_{eff} is between 6700 and 8500 K while the fundamental pulsation period is less than 0.09 d.

3.2. Lightcurve Analysis by Discrete Fourier Transformation

Discrete Fourier transformation (DFT) was used to extract the fundamental pulsating frequency (spectral window = 100 d^{-1}) using *Period04* (Lenz &

TABLE 3

FUNDAMENTAL FREQUENCY (d^{-1}) AND CORRESPONDING PARTIAL HARMONICS*

	Freq. (d^{-1})	Freq. Err	Amp. (mag)	Amp. Err	Phase	Phase Err	Amp. S/N
f_0 -B	14.5097	0.0001	0.2500	0.0009	0.3563	0.0006	331
f_0 -V	14.5097	0.0001	0.1919	0.0020	0.1604	0.0009	774
f_0 -I _c	14.5096	0.0001	0.1172	0.0006	0.3968	0.0007	194
$2f_0$ -B	29.0193	0.0002	0.0690	0.0007	0.8116	0.0017	95
$2f_0$ -V	29.0194	0.0001	0.0543	0.0024	0.6045	0.0013	122
$2f_0$ -I _c	29.0193	0.0006	0.0339	0.0024	0.3810	0.0048	120
$4f_0$ -B	58.0386	0.0025	0.0065	0.0008	0.3097	0.0200	10
$4f_0$ -V	58.0379	0.3259	0.0039	0.0008	0.7072	0.1473	11
$4f_0$ -I _c	58.3238	1.2568	0.0038	0.0010	0.1418	0.1428	7

*Detected following DFT analysis of time-series photometric data (BVI_c) from CSS J051053.0+071722.

Breger 2004). Pre-whitening steps which successively remove the previous most intense signals were employed to tease out other potential oscillations from the residuals. Only those frequencies with a $S/N \geq 6$ (Baran et al. 2015) in each passband are presented in Table 3. In all cases, uncertainties in frequency, amplitude, and phase were estimated by the Monte Carlo simulation ($n = 400$) routine featured in *Period04*. Representative amplitude spectra (f_0 , $2f_0$ and $4f_0$) from B -mag data acquired at DBO are shown in Figure 7. Since the oscillation frequencies obtained from the V - and I_c -bandpasses are essentially redundant, they are not shown herein.

3.3. Global Parameters

Well over 100 years ago Henrietta Leavitt discovered a period-luminosity relationship (PLR) from Cepheid variables in the Small Magellanic Cloud (Leavitt & Pickering 1912) and ever since pulsating stars have endured as standard candles for estimating cosmic distances. This PLR was refined afterwards to reconcile differences between metal rich (Population I) and metal-poor (Population II) Cepheids (Baade 1956). Like Cepheids, other variable stars that pulsate via the κ -mechanism were found to obey distinct PLRs. The earliest PLRs for δ Sct variables were published by Frolov (1969) and Dworak & Zieba (1975). An improvement of the PLR for δ Sct variables was reported by McNamara (2011) albeit with Hipparcos parallaxes. A new PLR using, for the most part, more accurate values determined by the Gaia Mission (Lindegren et al. 2016; Brown et al. 2018) was recently published (Ziaali et al. 2019). Accordingly this empirically-derived expression (equation 2):

$$M_V = (-2.94 \pm 0.06) \log(P) - (1.34 \pm 0.06), \quad (2)$$

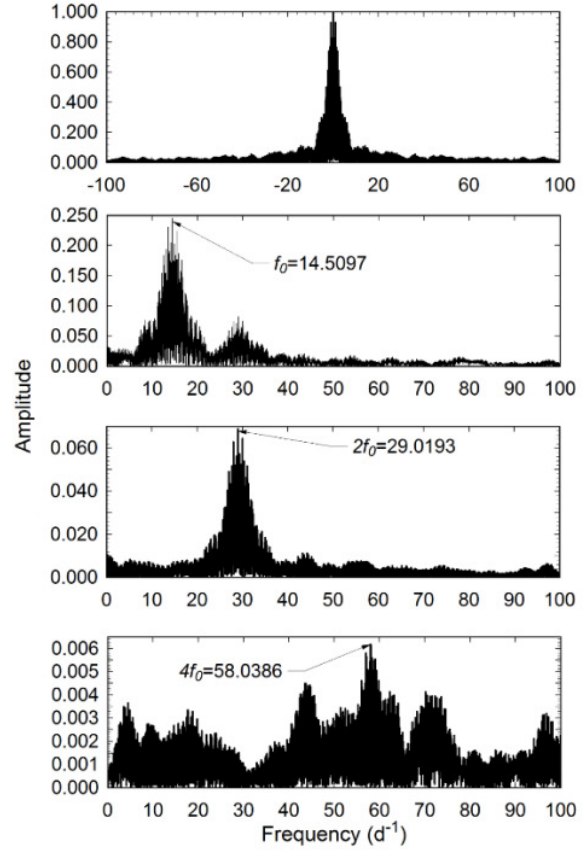


Fig. 7. Spectral window (top panel) and amplitude spectra (f_0 , $2f_0$ and $4f_0$) showing all significant pulsation frequencies following DFT analysis of B -mag photometric data from CSS J051053.0+071722 acquired at DBO between 25 Dec 2018 and 25 Jan 2019. This includes the fundamental f_0 frequency through its highest partial harmonic $4f_0$ which was detected ($S/N \geq 6$) following prewhitening.

is similar to the equation published by McNamara (2011) but with improved precision.

Absolute V_{mag} (M_V) was estimated (2.08 ± 0.09) after substituting the fundamental pulsation period (0.0689193 d) into equation 2. The reddening corrected distance modulus (equation 3):

$$d(\text{pc}) = 10^{(m - M_V - A_V + 5)/5} \quad (3)$$

produced an estimated distance (1263 ± 54 pc) to CSS J051053.0+071722 using observed values for m ($V_{\text{avg}} = 12.78 \pm 0.01$) and A_V (0.200 ± 0.008). By comparison, the Gaia DR2 parallax-derived distance (Bailer-Jones 2015) reported for this variable (1504^{+123}_-106) is 16% farther. CSS J051053.0+071722 is positioned ≈ 400 pc below the Galactic plane sug-

gesting residence in the thick disc (Li & Zhao 2017) rather than in the halo where many metal poor ($[Fe/H] < -1.6$) stars like SX Phe-type variables reside (Carollo et al. 2010).

The pulsation period and temperature/color were measured by direct observation. Similarly, the luminosity (11.28 ± 1.72) can be determined according to equation 4:

$$L_*/L_\odot = 10^{((M_{bol\odot} - M_{bol*})/2.5)}, \quad (4)$$

when $M_{bol\odot} = 4.74$, and $M_{bol*} = 2.11 \pm 0.09$, where $M_V = 2.08 \pm 0.09$ and $BC = 0.034$. However, the mass of an isolated field star like CSS J051053.0+071722 is very difficult to determine directly. Instead it is possible under certain conditions ($1.05 < M_\odot \leq 2.40$) to estimate the mass of a lone star according to a mass-luminosity relationship derived from main sequence (MS) stars in detached binary systems (Eker et al. 2018). This expression (equation 5):

$$\log(L) = 4.329(\pm 0.087) \cdot \log(M) - 0.010(\pm 0.019), \quad (5)$$

leads to a mass ($1.76 \pm 0.06 M_\odot$). Fairly typical for a HADS variable, this result and all others derived from DBO data are summarized in Table 4. Finally, the radius in solar units ($R_* = 2.17 \pm 0.21$) was estimated using the well-known relationship (equation 6) where:

$$L_*/L_\odot = (R_*/R_\odot)^2 (T_*/T_\odot)^4. \quad (6)$$

Derived values for the density (ρ_\odot), surface gravity ($\log g$), and pulsation constant (Q) are also included in Table 4. The stellar density (ρ_*) in solar units (g/cm^3) was calculated according to equation 7:

$$\rho_* = 3 \cdot G \cdot M_* \cdot m_\odot / (4\pi(R_* \cdot r_\odot)^3), \quad (7)$$

where G is the *cgs* gravitational constant, m_\odot =solar mass (g), r_\odot =solar radius (cm), M_* is the mass and R_* the radius of CSS J051053.0+071722 in solar units. Using the same algebraic assignments, surface gravity ($\log g$) was determined by the following expression (equation 8):

$$\log g = \log(M_* \cdot m_\odot / (R_* \cdot r_\odot)^2). \quad (8)$$

The dynamical time that it takes for a p-mode acoustic wave to internally traverse a star is strongly correlated to the stellar mean density. The pulsation constant (Q) is defined by the period-density relationship (equation 9):

$$Q = P \sqrt{\bar{\rho}_* / \bar{\rho}_\odot}, \quad (9)$$

TABLE 4

GLOBAL STELLAR PARAMETERS FOR
CSS J051053.0+071722*

Parameter	DBO
Mean T_{eff} [K]	7178 ± 119
Mass [M_\odot]	1.76 ± 0.06
Radius [R_\odot]	2.17 ± 0.21
Luminosity [L_\odot]	11.28 ± 1.72
ρ [g/cm^3]	0.24 ± 0.07
$\log g$ [cgs]	4.01 ± 0.07
Q [d]	0.029 ± 0.002

*Using values determined directly from observations at DBO.

where P is the pulsation period (d) and $\bar{\rho}_*$ and $\bar{\rho}_\odot$ are the mean densities of the target star and Sun, respectively. The mean density can be expressed (equation 10) in terms of other measurable stellar parameters where:

$$\log(Q) = -6.545 + \log(P) + 0.5 \log(g) + 0.1 M_{bol} + \log(T_{\text{eff}}). \quad (10)$$

The full derivation of this expression can be found in Breger (1990). The resulting Q value (0.029 ± 0.002) provided in Table 4 is slightly smaller than what would be expected ($Q = 0.03 - 0.04$ d) from fundamental radial pulsations observed with other δ Sct variables (Breger & Bregman 1975; Breger 1979; Joshi & Joshi et al. 2015; Antonello & Pastori 2005). It is conceivable that a more extensive dataset collected at multiple sites over a much longer period of time could reveal other oscillation modes that were not detected in this study.

4. EVOLUTIONARY STATUS OF CSS J051053.0+071722

The evolutionary status of CSS J051053.0+071722 was evaluated (Figure 8) using the PADova & TRieste Stellar Evolution Code (PARSEC) for stellar tracks and isochrones (Bressan et al. 2012) and then plotted ($\log T_{\text{eff}}$ vs. $\log(L/L_\odot)$) in a theoretical Hertzsprung-Russell diagram (HRD). The thick solid green-colored line defines the zero-age main sequence (*ZAMS*) position for stars with metallicity $Z = 0.014$. The two broken lines nearly perpendicular to the *ZAMS* delimit the blue (left) and red (right) edges of the theoretical instability strip for radial low- p modes (Xiong et al. 2016). Also included are

the positions of several known HADS and SX Phe-type variables (Balona 2018). The solid black circle indicates the position of CSS J051053.0+071722 using the DBO derived parameters (T_{eff} and L_{\odot}) provided in Table 4.

Interestingly a single undisputed value for the solar metallicity remains elusive. Over the last few decades, the reference metallicity values used by several authors for computing stellar models have ranged between $Z=0.012$ and 0.020 (Amard et al. 2019). Investigations still focused on finding a definitive value for Z_{\odot} have been recently reported (von Steiger & Zurbuchen 2016; Serenelli et al. 2016; Vagnozzi 2017). Despite the uncertainty in defining an absolute value for Z_{\odot} , an estimate for metal abundance is required in order to determine the mass, radius and age of CSS J051053.0+071722 from theoretical evolutionary tracks. A Z -value can be estimated indirectly from its Galactic coordinates in that its distance from the galactic plane (-400 pc) favors a thick disc membership rather than residence in the halo where metal poor stars ($[Fe/H] < -1.6$) are found. Furthermore, Qian et al. (2017) report an empirical relationship between metallicity ($[Fe/H]$) and the fundamental pulsation period P for an NDST star according to the following (equation 11)

$$[Fe/H] = -0.121(\pm 0.026) + 0.92(\pm 0.25) \times P. \quad (11)$$

As expected for a thick disk resident, the predicted value ($[Fe/H] = -0.058 \pm 0.031$) suggests that CSS J051053.0+071722 approaches solar metallicity, or is at most a few times lower.

Two separate PARSEC evolutionary models (Bressan et al. 2012) ranging in age between 1×10^8 and 2.63×10^9 y are illustrated in Figure 8. The red solid lines show the model tracks ($M_{\odot}=1.70$, 1.725 and 1.75) over time when $Z=0.020$ while the blue, dash-dotted lines define the models ($M_{\odot}=1.35$, 1.40 and 1.45) where $Z=0.004$. The latter simulations correspond to a decrease in metallicity by a factor of 3 to 5 depending on the reference solar metallicity. Assuming $Z=0.020$, it can be shown that CSS J051053.0+071722 would have a mass of $1.71 \pm 0.03 M_{\odot}$ and a radius of $2.15 \pm 0.06 R_{\odot}$. The position of this intrinsic variable near the $M_{\odot}=1.70$ evolutionary track extrapolates to an age of 1.24 ± 0.05 Gyr suggesting it is a moderately evolved MS object lying amongst other HADS closer to the blue edge of the instability strip.

By comparison, if CSS J051053.0+071722 is a metal poor ($Z=0.004$) star, then it would have a somewhat greater radius ($2.44 \pm 0.02 R_{\odot}$), but

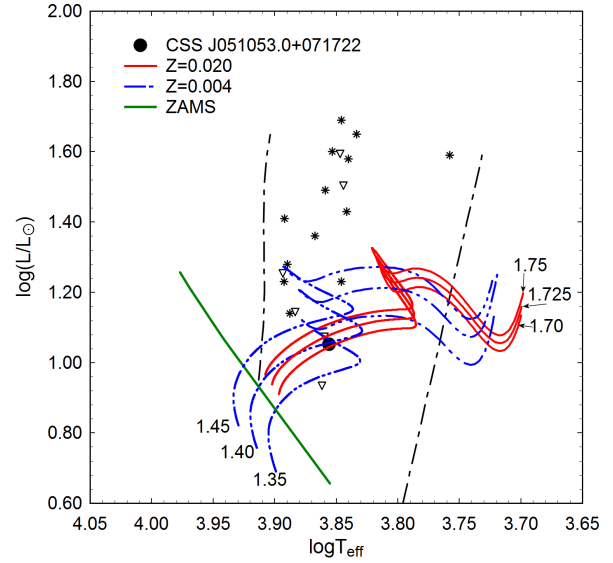


Fig. 8. Evolutionary tracks (red solid lines; $Z=0.020$ and blue dashed lines; $Z=0.004$) derived from PARSEC models (Bressan et al. 2012) showing position of CSS J051053.0+071722 (black filled circle) relative to ZAMS (thick green line) and within the theoretical instability strip (black dashed lines) for low-order radial mode δ Scuti pulsators. The position of other HADS (*) and SX Phe (open triangle) variables reported by Balona (2018) are included for comparison. The color figure can be viewed online.

would be less massive ($1.40 \pm 0.02 M_{\odot}$). Its position very close to the $1.4 M_{\odot}$ track lies prior to the HRD region where evolutionary tracks of low metallicity stars begin stellar contraction near the end of hydrogen burning in the core. This star would still be a MS object but with an age approaching 2.44 ± 01 Gyr. Alternatively, an even less massive and smaller ($R_* < 2.21 R_{\odot}$) star positioned slightly higher than the $1.35 M_{\odot}$ trajectory would be found inside the HRD region where the evolutionary tracks of low metallicity stars begin to zigzag due to stellar contraction. Based on this scenario the age of CSS J051053.0+071722 would approach 2.55 Gyr.

In summary, the theoretical mass ($1.71 \pm 0.03 M_{\odot}$) where $Z=0.020$ favors the higher metallicity of CSS J051053.0+071722 which is also in good agreement with results ($1.76 \pm 0.06 M_{\odot}$) independently determined using an empirical mass-luminosity relationship. If or when high resolution spectroscopic data become available in the future, uncertainty about the mass and metallicity of CSS J051053.0+071722 will likely decrease.

5. CONCLUSIONS

This first multi-color (BVI_c) CCD study of CSS J051053.0+071722 has produced 36 new times-of-maximum. Due to the short duration and lack of other published ToMax values, no attempt was made to evaluate secular changes in the fundamental mode of oscillation. Deconvolution of time-series photometric data by discrete Fourier transformation shows that this star is a monoperoiodic radial pulsator ($f_0=14.5097 \text{ d}^{-1}$) which also oscillates in at least 2 other partial harmonics ($2f_0$ and $4f_0$). A mean effective temperature for CSS J051053.0+071722 ($7178 \pm 119 \text{ K}$) was estimated from a composite of Gaia DR2, 2MASS and DBO results which likely corresponds to spectral type A9-F2. The pulsation period ($\approx 0.068919 \text{ d}$), radial oscillation mode, V_{mag} amplitude (0.43 mag), spectral type and LC morphology are all consistent with the defining characteristics of a HADS variable. It should be noted that these attributes do not necessarily exclude the possibility that CSS J051053.0+071722 is a field SX Phe-type variable. However, the generally accepted threshold for SX Phe stars is $<1.3 M_{\odot}$ (McNamara 2011) which in this case is far less than the mass predicted from a $M - L$ relationship ($\approx 1.76 M_{\odot}$) and evolutionary modeling ($\approx 1.71 M_{\odot}$). Given these results, the weight of evidence confirms the classification of CSS J051053.0+071722 as a HADS variable.

This research has made use of the SIMBAD database operated at Centre de Données astronomiques de Strasbourg, France. In addition, the Northern Sky Variability Survey hosted by the Los Alamos National Laboratory, the All Sky Automated Survey Catalogue of Variable Stars and the Catalina Surveys Data Release 2 archives were mined for essential information. This work also presents results from the European Space Agency (ESA) space mission Gaia. Gaia data are being processed by the Gaia Data Processing and Analysis Consortium (DPAC). Funding for the DPAC is provided by national institutions, in particular the institutions participating in the Gaia MultiLateral Agreement (MLA). The Gaia mission website is <https://www.cosmos.esa.int/gaia> while the Gaia archive website is <https://archives.esac.esa.int/gaia>. The careful review and helpful commentary provided by an anonymous referee is gratefully acknowledged.

REFERENCES

Akerlof, C., Amrose, S., Balsano, R., et al. 2000, *PASP*, 122, 131

- Amard, L., Palacios, A., Charbonnel, C., et al. 2019, *A&A*, 631, A77
- Amôres, E. B. & Lépine, J. R. D. 2005, *AJ*, 130, 659
- Andrae, R., Fouesneau, M., Creevey, O., et al. 2018, *A&A*, 616, A8
- Antonello, E. & Pastori, L. 1981, *PASP*, 93, 237
- Baade, W. 1956, *PASP*, 68, 5
- Baglin, A. 2003, *AdSpR*, 31, 345
- Bailer-Jones, C. A. L. 2015, *PASP*, 127, 994
- Balona, L. A. & Nemec, J. M. 2012, *MNRAS*, 426, 2413
- Balona, L. A. 2018, *MNRAS*, 479, 183
- Baran, A. S., Koen, C., & Porkrzywka, B. 2015, *MNRAS*, 448, L16
- Berry, R. & Burnell, J. 2005, *The Handbook of Astronomical Image Processing*, Wilmann-Bell, Inc., Richmond, VA
- Breger, M. 1979, *PASP*, 91, 5
- _____. 1990, *DSSN*, 1, 13
- Breger, M. & Bregman, J. N. 1975, *ApJ*, 200, 343
- Bressan, A., Marigo, P., Girardi, L., G., et al. 2012, *MNRAS*, 427, 127
- Brown, A. G. A., Vallenari, A., Prusti, T., et al. 2018, *A&A*, 616, A1
- Carollo, D., Beers, T. C., Chiba, M., et al. 2010 *ApJ*, 712, 692
- Drake, A. J., Djorgovski, S. G. Mahabal, A., et al. 2009, *ApJ*, 696, 870
- Dworak, T. Z. & Zieba, S. 1975, *IBVS*, 1005, 1
- Eker, Z., Bakış, V., Bilir, S., et al. 2018, *MNRAS*, 479, 5491
- Flower, P. J. 1996, *ApJ*, 469, 355
- Frolov, M. S. 1969, *ATsir*, 505, 1
- Garg, A., Cook, K. H., Nikolaev, S., et al. 2010, *AJ*, 140, 328
- Gilliland, R. L., Brown, T. M., Christensen-Dalsgaard, J., et al. 2010, *PASP*, 122, 131
- Harris, A. W., Young, J. W., Bowell, E., et al. 1989, *Icar*, 77, 171
- Henden, A. A., Welch, D. L., Terrell, D., & Levine, S. E. 2009, *AAS*, 41, 669
- Henden, A. A., Terrell, D., Welch, D. L., & Smith, T. C. 2010, *American Astronomical Society Meeting Abstracts*, 42, 515
- Henden, A. A., Levine, S. E., Terrell, D., et al. 2011, *American Astronomical Society Meeting Abstracts*, 43, 2011
- Joshi, S. & Joshi, Y. C. 2015, *JApA*, 36, 33
- Leavitt, H. S. & Pickering, E. C. 1912, *Harvard College Observatory Circular*
- Lee, Y.-H., Kim, S. S., Shin, J., et al. 2008, *PASJ*, 60, 3
- Lenz, P. & Breger, M. 2004, *IAUS*, 224, 786
- Li, C. & Zhao, G. 2017, *ApJ*, 850, 25
- Lindgren, L., Lammers, U., Bastian, U., et al. 2016, *A&A*, 595, A4
- McNamara, D. H. 2000, *ASPC*, 210, 373
- McNamara, D. H. 2011, *AJ*, 142, 110
- Niu, J. S., Fu, J.-N., & Zong, W.-K. 2013, *RAA*, 13, 1181

- Niu, J. S., Fu, J.-N., Li, Y., et al. 2017, *MNRAS*, 467, 3122
- Pamyatnykh, A. A. 1999, *AcA*, 49, 119
- Paunzen, E. & Vanmunster, T. 2016, *AN*, 337, 239
- Pojmanski, G. 2000, *AcA*, 50, 177
- Poretti, E. 2003a, *A&A*, 409, 1031
- _____. 2003b, *ASPC*, 292, 145
- Qian, S.-B., Li, L.-J., He, J.-J., et al. 2017, *MNRAS*, 475, 478
- Schwarzenberg-Czerny, A. 1996, *ApJ*, 460, L107
- Schlafly, E. F. & Finkbeiner, D. P. 2011, *ApJ*, 737, 103
- Serenelli, A., Scott, P., Villante, F. L., et al. 2016, *MNRAS*, 463, 2
- Smith, T. C., Henden, A. A., & Starkey, D. R. 2011, *SASAS*, 30, 121
- Vagnozzi, S., Freese, K. & Zurbuchen, T. H. 2017, *ApJ*, 839, 55
- von Steiger, R. & Zurbuchen, T. H. 2016, *ApJ*, 816, 13
- Walker, G., Matthews, J., Kuschnig, R., et al. 2003, *PASJ*, 115, 1023
- Warner, B. D. 2007, *Minor Planet Bulletin*, 34, 113
- Woźniak, P. R., Vestrand, W. T., Akerlof, C. W., et al. 2004, *AJ*, 127, 2436
- Xiong, D. R., Deng, L., Zhang, C., & Wang, K. 2016, *MNRAS*, 457, 3163
- Zhou, A.-Y., Jiang, X.-J., Zhang, Y. P., & Wei, J.-Y. 2009, *RAA*, 9, 349
- Ziaali, E., Bedding, T. R., Murphy, S. J., et al. 2019, *MNRAS*, 486, 4348

ON THE EVOLUTION OF ANGULAR MOMENTUM, MAGNETIC ACTIVITY AND MASS LOSS RATE OF LATE TYPE MAIN SEQUENCE STARS

J. Bohigas

Instituto de Astronomía, Universidad Nacional Autónoma de México, México.

Received July 21 2019; accepted February 13 2020

ABSTRACT

With the best data, I find that nearly all 0.5 to 1.2 M_{\odot} main sequence stars converge to a single rotational mass-dependent sequence after 750 Myr; when $M > 0.8 M_{\odot}$, most of them converge in ≈ 120 Myr. If stars rotate as rigid bodies, most have angular momenta within clear bounds. The lower bound defines a terminal main sequence rotational isochrone, the upper one coincides with slow rotators from the Pleiades; stars from Praesepe delineate a third one. Mass dependent exponential relationships between angular momentum and age are determined. Age estimates based on the angular momentum are acceptable for stars older than 750 Myr and with $M > 0.6 - 0.7 M_{\odot}$. The Rossby number indicates that the Parker dynamo may cease early on in stars with $M/M_{\odot} \geq 1.1$. An empirical formula and a model for the torque, and a relation between rotational period and magnetic field, lead to a formula for the evolution of the mass loss rate; the present solar rate is near a minimum and was about five times larger when life on Earth started.

RESUMEN

Con los mejores datos, encuentro que después de 750 Ma, casi todas las estrellas de 0.5 a 1.2 M_{\odot} de la secuencia principal convergen a una secuencia rotacional dependiente de la masa. Si $M > 0.8 M_{\odot}$, la mayoría converge en ≈ 120 Ma. Si rotan como cuerpo rígido, casi todas tienen momentos angulares entre límites bien definidos. El inferior define la isocrona rotacional terminal, el superior coincide con rotores lentos de las Pléyades; las estrellas del Pesebre delinean un tercer límite. Se obtienen relaciones exponenciales entre momento angular y edad. Las edades basadas en el momento angular son aceptables para estrellas de edad mayor que 750 Ma y masa mayor que 0.6–0.7 M_{\odot} . El número de Rossby indica que el dínamo de Parker se interrumpe tempranamente si $M/M_{\odot} \geq 1.1$. Una fórmula empírica y un modelo para la torca, y una relación entre periodo rotacional y campo magnético conducen a una ecuación para la tasa de pérdida de masa; la tasa solar actual está cerca del mínimo y era cinco veces mayor cuando empezó la vida en la Tierra.

Key Words: stars: evolution — stars: late-type — stars: magnetic fields — stars: mass loss — stars: rotation

1. INTRODUCTION

There is a transition from rapidly to slowly rotating main sequence stars when the mass is less than ≈ 1.2 to 1.3 M_{\odot} (Struve & Elvey, 1931; Herbig & Spalding, 1955; Slettebak, 1955; Tremain, 1960). Concurrently, chromospheric and coronal activity step up in the lower mass range (Wilson 1966; Pallavicini et al. 1981). In the Sun, chromospheric active regions and magnetic fields evolve in parallel (Bumba

& Howard 1965) and X-ray images show that there is a relationship between magnetic fields and the hot corona (Vaiana et al. 1981). These connections lead to the notion that magnetic energy is the main source of chromospheric and coronal heating (*e.g.*, Parker 1988; Cranmer & Saar 2011; van Ballegoijen, Asgari-Targhi & Berger, 2014). In turn, the highly pressurized hot corona expands to produce a stellar wind (Parker 1958; Cranmer et al. 2007;

Suzuki et al. 2013; van der Holst et al. 2014; Usmanov et al. 2018).

Noting that low mass stars have convective envelopes, Schatzman (1962) reasoned that the magnetic fields generated by dynamo processes in a spinning star with a convective envelope (the $\alpha-\Omega$ mechanism, Parker 1955), compel the stellar wind to rotate with the star even at very large distances, where it carries away their angular momentum. Schatzman predicted a secular decrease in the angular momentum of these stars, and this was confirmed when Kraft (1967) compared the average surface values of the rotational velocity of $1.2 M_{\odot}$ stars from the Pleiades and Hyades open clusters. All these associations were explicitly identified by Skumanich (1972), who argued that Ca II emission, angular velocity and magnetic field strength are proportional to each other in this kind of stars, and predicted that these quantities decay as the inverse square root of time, inspiring the idea of using rotation and stellar activity as timekeeping devices for low mass stars.

Thus, there is a feedback loop between rotation and magnetic field, leading to angular frequency, field strength, activity and wind power decreasing with age if no other factors are involved. This feedback is also observed in fully convective stars (McQuillan, Agrain & Mazeh 2013; Newton et al. 2018), where the magnetic field can not be produced by the $\alpha-\Omega$ mechanism. It has been submitted that a large density of small scale magnetic fields induced by a turbulent velocity field (Durney, De Young & Roxburgh 1993), is even capable of, for instance, maintaining a hot coronal plasma (and a stellar wind) in M9 V type stars (Robrade & Schmitt, 2009). An important point is that the X-ray and chromospheric to bolometric luminosity ratios reach a maximum constant value when the rotational period is less than ≈ 2 days (Soderblom et al. 1993; Pizzolato et al. 2003). In non-fully convective stars this is connected to a saturation value close to 4 kG for the magnetic field strength (Reiners et al. 2014), but significantly larger field strengths have been measured in fully convective M dwarfs (Shulyak et al. 2017 and 2019). This has been associated to the dominance of axisymmetric poloidal and nearly dipolar magnetic fields in this type of stars, as opposed to the prevalence of multipolar fields in dwarf stars with a convective envelope and a radiative interior (Morin et al. 2010).

Using the equations of magnetohydrodynamics, Schatzman's (1962) idea has been linked to different versions of stellar wind theories and various possibilities for the structure of the coronal magnetic field

in a rotating star (*e.g.*, Weber & Davis, 1967; Mestel 1968, 1984; Mestel & Spruit, 1987; Réville et al. 2015). But due to the complex nature of angular momentum evolution of low mass main sequence stars, most theoretical work has been based on heuristic arguments, in order to find manageable equations for a mass and time dependent torque. These semi-empirical prescriptions make assumptions on the properties of the stellar wind and magnetic field, and their relation with the angular velocity and other observable stellar parameters, such as the Rossby number or the filling factor of the magnetized surface. Assumptions have changed in step with our understanding of the theoretical and observational properties of these stars, but the final equations for the torque still involve one or more calibration constants, as well as loose power law relations with the mass, radius, mass loss rate and angular velocity (*e.g.*, Bohigas et al. 1986; Kawaler, 1988; Reiners & Mohanty, 2012; Matt et al. 2015; Gallett & Bouvier, 2015; Johnstone et al. 2015a).

Since the stellar angular momentum is removed from the atmosphere, it was initially believed that the radiative core would be spinning much faster than the convective envelope. Brown et al. (1989) established that this is not the case in the Sun, and we now know that the radial average of its rotational velocity is roughly constant at least down to $0.15 R_{\odot}$ (Kozennik & Eff-Darwich, 2012; Eff-Darwich & Korzennik, 2013). Evidence of flat differential rotation in solar type stars has been produced using asteroseismological techniques (Benomar et al. 2015; Nielsen et al. 2017). All these implies that there are efficient transport mechanisms of angular momentum from the radiative core to the convective envelope (see recent review in Aerts, Mathis & Rogers 2019). Currently, models for angular momentum transport include an heuristic approximation where the transferred amount is just enough to maintain equilibrium at the core-envelope interface (MacGregor & Brenner 1991; Gallet & Bouvier 2015), braking the inner core by a pre-existing poloidal magnetic field (Mestel & Weiss 1987; Charbonneau & MacGregor 1993; Dennisenkov 2010), internal gravity waves generated at the convective envelope (Charbonnel & Talon 2005; Charbonnel et al. 2013) and – without being able to simultaneously reproduce the surface period, rotational profile and lithium abundance of the Sun – internal transport of angular momentum by meridional circulation (Denisenkov 2010; Charbonnel et al. 2013; Amard et al. 2016).

Obviously, the angular momentum transfer rate depends on the torque running at the convective en-

velope and combinations of rotational braking and angular momentum transport models have been designed by Denisenkov et al. (2010), Gallet & Bouvier (2013 and 2015) and Amard et al. (2016). When dealing with close binary systems, a tidal synchronization torque must be included (Johnstone et al. 2019). And during the pre-main sequence phase, angular momentum transfer between the central star and the accretion disk can have a central role.

Setting “initial” conditions has not been easy. The existence of a wide spectrum of rotational periods in nearly equal mass stars from young clusters – such as η and α Persei, NGC 2547 and Pleiades (Stauffer et al. 1984 and 1985; Irwin et al. 2008; Moraux et al. 2013) – implies that initial conditions are not unique. Even when they end up having the same mass, members of the same cluster are not born at the same time, and with identical rotation rates and physical structures (*e.g.*, Henderson & Stassun 2012). Furthermore, Bouvier et al. (1993) found that the mean rotational period is significantly longer in classical T Tauri stars (CTTS) than in weak line T Tauri stars (WTTS). Noting that accretion disks and powerful winds are detected in CTTS, but not in WTTS, they explained this difference arguing that WTTS spin up as they contract without losing angular momentum, whereas CTTS do not spin up as much (if at all) since angular momentum is still being removed by a powerful wind that is thought to be created by magnetic coupling between the central star and the accretion disk (Koenigl 1991; Collier Cameron & Campbell 1993; Collier Cameron, Campbell & Quaintrell 1995). Observations indicate that the rotational period is roughly constant during the disk locking phase (Rebull et al. 2004; Gallet & Bouvier 2013). Longer periods and disk locking times are associated to slow rotators: for a solar mass star, around 8 days and 9 Myr *vs.* 1.4 days and 2 Myr for fast rotators (Gallet & Bouvier 2015).

Angular momentum losses are greatly reduced after star-disk decoupling. The star spins up as it contracts and the rotational velocity reaches its largest value when the star arrives at the ZAMS – after 40 and 200 Myr for a 1.2 and 0.6 M_{\odot} star – and its internal structure is stabilized. Thereon, the rotational history is essentially – but not exclusively – determined by the magnetic braking mechanism first described by Schatzman (1962).

Over the last two decades, this field of research has been greatly favored by vast improvements in observational procedures and methods of analysis focused on measuring the rotational period, parallax

and magnitudes of stars. These were developed by research groups engaged in one particular field of stars or connected to long term and/or wide field campaigns, such as the Two Micron All Sky Survey (2MASS), the European Space Mission satellite *Gaia* and NASA’s *Kepler* satellite Mission. At least equally important has been the unfolding of exciting ideas and techniques – asteroseismology, Zeeman splitting and Doppler imaging, and astrospheric absorption – with which we are beginning to know the internal rotational structure, the superficial magnetic field intensity and geometry, and the mass loss rate of late type main sequence stars. Lastly, the connection with basic stellar parameters – such as mass, radius, temperature, convective turnover time and moment of inertia – has been made possible thanks to evolutionary models that are regularly being updated (*i.e.*, VandenBerg et al. 2006; Feiden et al. 2011; Baraffe et al. 2015; Choi et al. 2016; Marigo et al. 2017; Spada et al. 2017).

This paper collects a vast amount of rotational, photometric and parallax data, to re-analyze the angular momentum history of $\approx 0.5 - 1.2 M_{\odot}$ main sequence stars, with an emphasis on those that are at least as old as the Pleiades cluster. All rotational periods, apparent magnitudes and any other observed parameter used to analyze some of these questions, are taken from the literature. In order to have a data set as uniform as possible, all infrared *JHK* magnitudes were collected from the 2MASS project, and visual magnitudes were derived from the *Gaia* DR2 *G*, *BP* and *RP* band magnitudes. Likewise, only *Gaia* DR2 parallaxes have been used. To minimize uncertainties and improve data set quality, stars with additional causes of variability, poorly determined period and photometry, and uncertain parallax, were excluded from the analysis. Rotational periods are taken from several sources, but not all of them report error estimates. It is worth noting that discrepancies found in some rotational periods measured by more than one research group can be much larger than the reported errors. Therefore, rotational periods are the least reliable element in this compilation, which contains one of the largest and better selected data required to analyze the evolution of angular momentum of ≈ 0.5 to $1.2 M_{\odot}$ main sequence stars. A general discussion of data sources is presented in §2.1, and the criteria that were used to select the best possible information are discussed in §2.2. Procedures used to obtain absolute magnitudes and stellar parameters are described in subsections §2.3 and §2.4.

The distribution of rotational periods as a function of mass and time is presented and discussed in §3.1. Assuming rigid body rotation, the behavior of angular momentum as a function of mass and age is discussed in subsection §3.2. This is not the usual approach used to study the rotational history of low mass main sequence stars but, as noticed by other authors (Johnstone et al. 2015a), the observational evidence we now have on their inner rotational structure, as well as models for angular momentum redistribution within them, indicate that this is not an unlikely hypothesis for stars older than a few hundred million years, or maybe less. Formulae relating mass and angular momentum in three rotational isochrones are included in this subsection. These are used to introduce two possible approximations for the evolution of angular momentum in main sequence stars having a mass between 0.5 and $1.2 M_{\odot}$, using a $0.1 M_{\odot}$ bin to downsize variations due to mass differences. The special circumstances and time periods under which it is possible to obtain an age estimate directly from the rotational period are discussed in §3.3. Magnetic activity as a function of mass and time is analyzed in §3.4. Another important bonus of the rigid body rotation hypothesis is that it leads directly to simple empirical formulae for the torque as a function of mass and time, without having to use shortcuts to put together relationships between, among other things, mass, magnetic field, mass loss rate and angular velocity (subsection §3.5). To some extent, it turns the problem around. For instance, in combination with known connections between age and the magnetic intensity at the stellar surface, and a simple model for the magnetic field source, these formulae lead to a clear-cut procedure to assess the mass loss rate (subsection §3.6), the least known important trait of low mass main sequence stars. The most significant results of this paper are summed up in the final section.

2. DATA

Star spots and plages transiting the stellar surface can produce a quasi-periodic modulation of light intensity that is correlated with a stellar rotation rate, Ω . Supported by long term photometric observations, readily available rotational data from a vast number of field and cluster late type main sequence stars have been produced by several research groups over the last two decades. These groups carried out meticulous time series analyses of light curves in order to determine rotational periods, in most cases using different formulations of the Lomb-Scargle method (Lomb 1976; Scargle 1982, 1989).

But notice that there is an inherent uncertainty in the physical connotation of the computed value of the rotational period at the stellar surface, since the correlation between light intensity and period is not straight forward or unambiguous. The position, lifetime and extension of star spots, plages and other superficial features, are conditioned by the latitudinal rotational shear, which is caused by rotating stellar convection transporting angular momentum from the pole to the equator, and thermal energy in the opposite direction (Busse 1970; Durney 1970; Kitchatinov & Rüdiger 2005; Küker & Rüdiger 2008). Differential rotation tends to be more pronounced in stars with lower rotational periods (Henry et al. 1995), higher effective temperatures (Barnes et al. 2005) and shallower convective regions (Küker & Rüdiger 2008). Thus, the relation between these inconstant superficial features and rotational period depends on stellar mass, metallicity and age, increasingly so in spectral types where differential rotation is more pronounced and variable, and when stars are close to the beginning or the end of main sequence. As a matter of fact, Epstein & Pinsonneault (2014) noticed that latitudinal surface differential rotation introduces significant ambiguities into rotation period measurements, leading to a ≈ 2000 Myr uncertainty in rotation-based age estimates. All these should not be forgotten when the mass and time dependence of the rotational evolution of late type main sequence stars is considered.

2.1. Data Sources

The rotational periods of field and open cluster stars contained in 28 publications were collected in order to investigate the evolution of angular momentum during the main sequence. Twenty three of these papers are dedicated to 17 open star clusters in the Milky Way. The open cluster sample was put together with the intention of covering the largest possible range of ages after the termination of the disk locking phase. With an estimated age of 13 and 3500 Myr, η Persei and M 67 are the youngest and oldest open clusters inspected in this work. The central positions (epoch 2000.0), angular radii (Θ), parallaxes, ages, color excesses ($E(B - V)$) and metallicities ($[Fe/H]$) of these clusters are laid out in Table 1 (references in Appendix A). Some of these numbers were used in data selection and extinction correction, §2.2 and §2.3. The cluster age, metallicity and assumed initial helium abundance (Y_0) are the input parameters for the evolutionary tracks used to derive the physical properties of cluster stars from their visual and infrared colors, §2.4.

TABLE 1
CLUSTER PARAMETERS*

Cluster	RA deg	DEC deg	Θ deg	Parallax mas	Age Myr	$E(B-V)$ –	$[Fe/H]$ –	Y_0
h Persei	34.770	57.150	1.75	0.547±0.122	13±1	0.515±0.035	0.00	0.28
IC 4665	266.498	5.565	1.00	2.892±0.003	40±10	0.177±0.003	-0.06±0.10	0.27±0.01
NGC 2547	122.565	-49.050	0.30	2.544±0.002	40±10	0.050±0.010	-0.14±0.10	0.27±0.01
Blanco 1	1.029	29.833	2.90	4.194±0.041	100±30	0.010±0.000	0.03±0.07	0.28±0.01
Pleiades	56.300	24.120	6.40	7.364±0.005	120±20	0.037±0.007	0.00±0.05	0.28±0.01
M 35	92.268	24.296	0.95	1.119±0.002	155±30	0.228±0.028	-0.21±0.10	0.27±0.01
NGC 2301	102.940	0.460	0.25	1.026±0.084	180±40	0.029±0.001	0.05±0.05	0.28±0.01
M 34	40.584	42.703	0.37	1.954±0.003	210±40	0.070±0.000	0.02±0.06	0.28±0.01
M 37	88.070	32.550	0.32	0.704±0.072	450±100	0.291±0.050	0.02±0.05	0.28±0.01
M 48	123.383	-5.736	0.73	1.290±0.002	500±150	0.030±0.010	0.08±0.03	0.28±0.01
Coma Berenices	185.620	25.850	7.50	11.640±0.034	600±50	0.010±0.010	0.00±0.08	0.28±0.01
Hyades	66.725	15.867	13.35	21.052±0.065	750±50	0.005±0.005	0.14±0.02	0.28±0.01
Praesepe	130.090	19.690	3.00	5.371±0.003	750±50	0.018±0.009	0.16±0.08	0.29±0.01
NGC 6811	294.310	46.390	0.30	0.873±0.014	1000±200	0.062±0.012	0.03±0.03	0.28±0.01
NGC 752	29.520	37.810	1.45	2.330±0.143	1350±50	0.040±0.000	-0.06±0.03	0.27±0.01
NGC 6819	295.320	40.190	0.22	0.335±0.023	2100±400	0.133±0.033	0.09±0.02	0.28±0.01
M 67	132.848	11.837	0.31	1.133±0.001	3500±500	0.039±0.011	0.03±0.05	0.28±0.01

*RA and DEC are the right ascension and declination of the cluster center in degrees, epoch 2000.0; Θ is the cluster angular radius (degrees); the mean parallax is given in miliarcseconds; ages are given in million year units (Myr); $E(B-V)$ is the color excesses; $[Fe/H]$ is the metallicity with respect to the solar value; Y_0 is the initial helium mass abundance assumed for the evolutionary tracks used to compute physical properties of cluster stars.

Rotational periods of field stars were computed by several research groups using observations from the *CoRoT* satellite (Affer et al. 2012), the *HATNet* survey for transiting extrasolar planets (Hartman et al. 2011), and the *Kepler* satellite project (Nielsen et al. 2013; Reinhold et al. 2013; McQuillan, Mazeh & Aigrain 2014).

To homogenize the data set, the VizieR¹ facility was used to collect the spectral type, visual magnitude and classification of each star as reported by SIMBAD², their G , BP and RP band magnitudes and parallax from *Gaia* DR2³, and their J , H and K magnitudes from the Two Micron All Sky Survey⁴ (herein *2MASS*).

¹This research has made use of the VizieR catalogue access tool, CDS, Strasbourg, France (Ochsenbein, Bauer & Marcout 2000) and the cross-match service provided by CDS.

²This research has made use of the SIMBAD database, operated at CDS, Strasbourg, France (Wenger et al. 2000).

³This work has made use of data from the European Space Agency (ESA) mission *Gaia*, processed by the *Gaia* Data Processing and Analysis Consortium. Funding for the DPAC has been provided by national institutions, in particular the institutions participating in the *Gaia* Multilateral Agreement.

⁴This publication makes use of data products from the Two Micron All Sky Survey, which is a joint project of the

This information is collected in a number of tables containing stellar coordinates (degrees, epoch 2000; precise within 1 arcsec), spectral types (“*?” when unknown), visual magnitude as reported in SIMBAD (as a reference), Johnson-Cousins visual magnitudes calculated from the *Gaia* DR2 G , BP and RP band magnitudes and the transformation laws found by Evans et al. (2018), J , H and K *2MASS* magnitudes, rotational periods (days) and *Gaia* DR2 parallaxes (miliarcsec). When there is no information for any of these quantities, the corresponding field value is 999.9.

These tables include all the stars reported in each rotational data source. Rotational periods in the *Kepler* field and the Pleiades, M 34, Hyades and Praesepe open clusters were searched for by more than one research group. Additional tables excluding duplicate stars were produced for these clusters and the field. Mean periods are reported for stars with multiple measurements, with the period error being

University of Massachusetts and the Infrared Processing and Analysis Center/California Institute of Technology, funded by the National Aeronautics and Space Administration and the National Science Foundation.

equal to half the difference between the shortest and longest period.

Several filters were applied to select stars with good photometric and astrometric data quality and no possible caveats regarding contamination from other motives of variability besides single star rotation. As explained in the following subsection, distinctive flags are added when these filters are activated.

2.2. Data Filters

A flag following the visual magnitude derived from the *Gaia* data is set to ‘XX’ under column *GP*, when it could not be calculated because at least one of the *Gaia* DR2 *G*, *BP* and *RP* magnitudes and their errors is missing, or the photometric flux over error in any of these bands is smaller than 5. Otherwise, the *Gaia* flag *GP* is set to ‘-’.

A flag following *2MASS* magnitudes is set to ‘XX’ under column *2P* if either one of the *J*, *H* and *K* magnitudes and their errors is absent, the photometric flux over error in any band is smaller than 5, the *2MASS* quality flag is not set to ‘AAA’ and the star may be contaminated by an extended source (their *Xflg* is larger than zero). Otherwise, the *2MASS* flag *2P* attached to the *J*, *H* and *K* magnitudes is set to ‘-’.

Databases were used to identify possible non main sequence stars, object types that may indicate that the angular momentum evolution of a single star may have been affected by an external agent (such as stellar companions and planetary systems) or light curve modulations produced by other sources of variability besides single star rotation. Namely, the following types (in parenthesis, condensed name for object classification recommended by SIMBAD):

- stars with known exoplanets (P1*) as of 02-07-2019, according to the NASA Exoplanet Science Institute⁵,
- double or multiple stars (**, *i*) and spectroscopic binaries (SB*), according to the *Ninth Catalogue of Spectroscopic Binary Orbits* (Pourbaix et al. 2004), SIMBAD, *Washington Double Star Catalog*⁶ and other sources,

⁵This research has made use of the NASA Exoplanet Archive, which is operated by the California Institute of Technology, under contract with the National Aeronautics and Space Administration under the Exoplanet Exploration Program

⁶This research has made use of the *Washington Double Star Catalog* maintained at the U.S. Naval Observatory.

- Algol, β -Lyrae, W-Uma, RS CVn and X-ray and eclipsing binaries (Al*, bL*, WU*, RS*, XB*, EB*, EB*WUma, EB*betLyr.), according to SIMBAD and other sources,
- ellipsoidal, symbiotic, cataclysmic, pulsating, δ -Scuti, γ -Doradus, RR-Lyrae, classical Cepheid, Cepheid, SX Phe and Mira and long period variables (El*, Sy*, CV*, Pu*, dS*, gD*, RR*, cC*, Ce*, SX*, LPV*), according to SIMBAD, Holl et al. (2018) and other sources,
- brown dwarfs (BD*) and T-Tauri stars (TT*), according to SIMBAD and
- not in main sequence, according to SIMBAD and other sources (No-MS*; this abbreviation is not used by SIMBAD).

When present, these name tags are reported under column label Comment. This Comment may also include the following name tags

- XPlx if there is no *Gaia* DR2 parallax measurement, the parallax error is larger than 20%, the astrometric excess noise (*epsi*) is larger than 2, the used visibility periods (*Nper*) are less than 8 and duplicate sources (*Dup*) may be present,
- XPer when no rotational period is measured or the rotational period is reported as questionable or the period-to-period-error ratio is smaller than 5. When there is more than one data source – as in the Hyades, M 34, Pleiades and Praesepe clusters, as well as in the *Kepler* field stars – the period is assumed to be equal to the mean value and the period error is taken as half the difference between the shortest and longest period. Period uncertainty was significant in stars from the *Kepler* field and the M 34 and Pleiades open clusters (4925, 18 and 36 rejections), implying that formal errors in the mathematical analysis may underestimate other basic sources of uncertainty in the determination of rotational periods. Some sources of uncertainty may be associated to the wavering nature of stellar activity. Unfortunately, errors in the reported rotational period are not given in a large number of papers, so that an indefinite number of stars with less than adequate period measurements could not be identified.

The final comment is set to ‘-’ when the star has not been associated to any of the preceding types and the stellar parallax and period have been adequately measured. There are electronic versions of tables

TABLE 2
COMA BERENICES. DATA

AR(2000) deg	DEC(2000) deg	SpType	V Simbad	V Gaia	GP	J 2MASS	H 2MASS	K 2MASS	2P	Period days	Parallax mas	Comment
177.157089	28.275139	G7	10.380	10.414± 0.001	–	9.015± 0.026	8.629± 0.029	8.585± 0.020	–	9.430±999.900	11.199± 0.037	–
178.888962	29.728251	K0V	11.420	11.611± 0.001	–	9.692± 0.022	9.188± 0.022	9.057± 0.017	–	11.550±999.900	11.056± 0.051	–
180.217667	27.323305	G9	11.510	11.482± 0.001	–	9.674± 0.022	9.115± 0.021	8.996± 0.018	–	10.630±999.900	0.892± 0.052	–
180.595245	22.916306	K4	12.220	12.602± 0.001	–	999.900±999.900	999.900±999.900	999.900±999.900	XX	14.110± 0.080	5.381± 0.040	–
181.990494	25.586472	K3.1	11.060	11.318± 0.001	–	9.534± 0.022	9.028± 0.019	8.906± 0.017	–	10.280±999.900	10.784± 0.113	–
182.150421	31.102751	K7	11.030	999.900±999.900	XX	10.167± 0.022	9.545± 0.021	9.402± 0.017	–	11.920±999.900	11.238± 0.041	–
182.896454	29.379028	K2.8	11.210	11.252± 0.001	–	9.575± 0.022	9.053± 0.027	8.979± 0.024	–	10.255± 0.115	11.194± 0.043	–
183.221786	26.250360	K2.2	11.400	11.390± 0.001	–	9.577± 0.018	9.106± 0.016	8.990± 0.018	–	10.880±999.900	11.589± 0.041	–
185.315079	26.153889	K3.5	11.500	11.446± 0.001	–	9.614± 0.019	9.087± 0.024	8.972± 0.020	–	10.880±999.900	11.776± 0.044	–
185.946747	23.245640	K4	11.210	11.563± 0.001	–	9.677± 0.021	9.129± 0.022	9.018± 0.018	–	11.183± 0.055	11.751± 0.038	–
186.505463	34.352333	G8	11.980	11.624± 0.002	–	9.845± 0.022	9.276± 0.016	9.143± 0.017	–	11.900±999.900	0.662± 0.033	–cC*
186.712631	26.267166	K4.8	11.730	999.900±999.900	XX	9.855± 0.022	9.275± 0.026	9.156± 0.020	–	11.527± 0.245	11.632± 0.058	–
186.735336	22.681862	?	11.030	15.064± 0.000	–	12.300± 0.020	11.655± 0.023	11.454± 0.018	–	11.540±999.900	5.416± 0.032	–
186.836166	23.329834	G7.9	10.320	10.293± 0.000	–	8.912± 0.021	8.537± 0.021	8.451± 0.017	–	9.050±999.900	11.898± 0.041	–
186.951202	28.194389	G5.4	9.600	999.900±999.900	XX	8.436± 0.023	8.050± 0.046	8.050± 0.023	–	8.602± 0.040	12.228± 0.044	–
187.235123	26.549278	G9IV	10.800	10.752± 0.001	–	9.208± 0.026	8.768± 0.031	8.661± 0.023	–	9.420± 0.160	11.856± 0.048	–NoMS*
187.425629	28.620722	K2.5	11.320	11.278± 0.001	–	9.791± 0.027	9.304± 0.031	9.198± 0.020	–	16.050±999.900	0.790± 0.060	–
188.129456	35.331165	G0	9.700	9.580± 0.000	–	8.407± 0.019	8.132± 0.023	8.086± 0.018	–	7.690±999.900	11.960± 0.044	–XPix
188.333374	22.406473	G7.8	10.320	10.268± 0.001	–	8.855± 0.019	8.470± 0.023	8.402± 0.020	–	8.330±999.900	11.915± 0.060	–XPix
188.424500	29.233805	K4	11.580	11.437± 0.001	–	9.545± 0.028	8.981± 0.067	8.863± 0.020	–	16.880±999.900	8.370± 0.038	–
188.425507	25.942778	G6III:	10.590	10.504± 0.000	–	9.031± 0.029	8.601± 0.036	8.584± 0.020	–	8.400± 0.020	11.092± 0.055	–XPix-NoMS*
188.475922	27.134640	K3.3	11.800	11.717± 0.001	–	10.014± 0.022	9.487± 0.021	9.384± 0.020	–	16.540±999.900	0.646± 0.050	–
188.726212	27.455610	G4.8	9.000	9.016± 0.000	–	7.897± 0.029	7.583± 0.040	7.510± 0.020	–	10.980±999.900	8.336± 0.357	–XPix
189.547791	23.556168	M0	11.030	13.645± 0.000	–	10.776± 0.022	10.163± 0.023	9.963± 0.020	–	14.460±999.900	11.453± 0.041	–
189.924957	21.582777	K5	11.890	11.564± 0.001	–	9.488± 0.020	8.934± 0.022	8.799± 0.018	–	9.570±999.900	0.086± 0.037	–XPix
190.646423	41.091026	K0III	11.700	11.787± 0.001	–	9.956± 0.027	9.398± 0.030	9.273± 0.022	–	11.760±999.900	0.634± 0.028	–NoMS*
190.789703	24.784779	?	11.030	13.832± 0.001	–	10.712± 0.020	10.076± 0.021	9.896± 0.020	–	2.770±999.900	10.551± 0.098	–
191.347290	42.851223	?	11.030	14.565± 0.001	–	10.788± 0.027	10.239± 0.032	9.987± 0.024	–	12.050±999.900	11.562± 0.079	–
192.251755	25.359888	K5V	12.000	11.958± 0.001	–	9.750± 0.020	9.190± 0.021	9.069± 0.015	–	12.270±999.900	12.294± 0.064	–
192.376785	25.536417	K0III	11.440	11.554± 0.002	–	9.613± 0.021	9.053± 0.015	8.931± 0.019	–	19.165± 0.345	1.021± 0.054	–NoMS*
192.507080	21.053362	K3	11.160	11.226± 0.001	–	9.558± 0.021	9.075± 0.019	8.976± 0.015	–	13.340±999.900	4.419± 0.459	–XPix
193.048370	25.373472	F8V	8.830	8.840± 0.000	–	7.881± 0.021	7.652± 0.021	7.609± 0.015	–	6.920±999.900	11.747± 0.043	–XPix
193.311127	24.053778	K5	11.030	12.216± 0.003	–	10.202± 0.023	9.573± 0.031	9.452± 0.024	–	19.020±999.900	0.615± 0.035	–
193.579498	32.826416	?	11.030	13.186± 0.000	–	10.305± 0.020	9.666± 0.016	9.496± 0.016	–	15.690±999.900	14.939± 0.041	–XPix
194.403580	28.979084	G4V	10.360	10.211± 0.001	–	8.897± 0.026	8.539± 0.046	8.473± 0.020	–	7.940±999.900	10.901± 0.066	–
194.865631	19.687529	K5	12.110	11.830± 0.002	–	9.726± 0.022	9.196± 0.023	9.034± 0.019	–	11.240±999.900	0.812± 0.045	–
196.433289	20.055944	K2	11.030	11.318± 0.001	–	9.527± 0.020	9.011± 0.017	8.922± 0.022	–	11.040±999.900	0.961± 0.035	–**

for primary data from field and open cluster stars (<http://vizier.u-strasbg.fr/viz-bin/VizieR?-source=J/other/RMxAA/56.1>, <ftp://cdsarc.u-strasbg.fr/pub/cats/J/other/RMxAA/56.1>). As an example, see Table 2.

The number of stars with measured rotational periods in each cluster and field is given under Column *Per* in Table 3. The number of stars that were selected after passing all data filters is under Column *OK* in the same table. Notice that there is a large fraction of rejected stars in most open clusters. There are many reasons for this to be so, but the most frequent is insufficiently accurate parallax (94, 60 and 47% in h Persei, M 37 and NGC 6819), generally in clusters that are farther away. Stellar parallax is also poor in a large fraction of stars associated to the two open clusters that are closer to us, Hyades and Coma Berenices (43 and 21%). The next two main reasons for rejection are poor or non-existent *2MASS* photometry and association to a multiple system, with very high levels of incidence in h Persei, IC 4665 and NGC 6819. Parallax was too inaccurate in 59% of the *HATNet* field stars, and 42% of the

CoRoT field stars are not in the main sequence. Fortunately, all these problems affected a much smaller fraction of *Kepler* field stars.

In total, the rotational period has been measured for 3769 members of the 17 clusters listed in Table 1, and for 45235 field stars observed by the *CoRoT*, *HATNet* and *Kepler* projects. Out of these, the data filters approved 1876 cluster and 32641 field stars.

2.3. Extinction Correction

Gaia DR2 provides an estimate of line-of-sight extinction, A_G , and reddening, $E(BP - RP)$ for each star. After a careful analysis of the *Gaia* DR2 database, Andrae et al. (2018) concluded that these line-of-sight extinction estimates are not accurate at the single star level and, concurrently, that there are no clearly defined transformations between A_G and A_V , and $E(BP - RP)$ and $E(B - V)$. Consequently, absolute magnitudes of open cluster stars were determined assuming that the color excess is the same for all stars and is as given in Table 1. This is a particularly weak assumption in young clusters, where dust distribution can be very inhomogeneous at the

TABLE 3
STARS IN EACH CLUSTER AND FIELD*

Cluster	<i>Per</i>	<i>OK</i>	<i>VIR</i>	<i>IR</i>	Cluster	<i>Per</i>	<i>OK</i>	<i>VIR</i>	<i>IR</i>
h Persei ^a	586	20	19	19	IC 4665 ^b	19	6	0	5
NGC 2547 ^c	176	152	6	110	Blanco 1 ^d	33	23	19	20
Pleiades-C ^e	132	70	–	–	Pleiades-H ^f	516	368	–	–
Pleiades-R ^g	759	611	–	–	Pleiades-All	997	741	64	320
M 35 ^h	441	297	82	282	NGC 2301 ⁱ	133	83	83	82
M 34-I ^j	83	60	–	–	M 34-J ^k	55	34	–	–
M 34-M ^l	120	22	–	–	M 34-All	243	102	89	102
M 37 ^m	657	125	31	119	M 48 ⁿ	54	51	51	51
Coma Ber ^o	37	20	6	8	Hyades-De ^p	62	30	–	–
Hyades-Do ^q	48	14	–	–	Hyades-R ^r	22	6	–	–
Hyades-All	123	58	7	19	Praesepe-A ^s	40	20	–	–
Praesepe-D ^t	52	0	–	–	Praesepe-S ^u	54	36	–	–
Praesepe-All	137	114	28	90	NGC 6811 ^v	71	53	52	52
NGC 752 ^w	12	8	8	8	NGC 6819 ^x	30	7	6	7
M 67 ^y	20	16	16	16					
Field	<i>Per</i>	<i>OK</i>	<i>VIR</i>	<i>IR</i>	Field	<i>Per</i>	<i>OK</i>	<i>VIR</i>	<i>IR</i>
CoRoT ^a	1978	781	694	761	HATNet ^b	2018	704	176	322
Kepler-M ^c	34186	28507	–	–	Kepler-N ^d	12151	9841	–	–
Kepler-R ^e	24124	20027	–	–	Kepler-All	41239	31156	27494	29032

*Per: stars with measured rotational periods. OK: stars that passed all data filters. VIR: stars where the visual and infrared magnitudes were matched by a stellar model. IR: stars where only the infrared magnitudes were reproduced by a stellar model. Cluster period data: (a) Moraux et al. 2013; (b) Scholz, Eisloffel & Mundt 2009; (c) Irwin et al. 2008; (d) Cargile et al. 2014; (e) Covey et al. 2016; (f) Hartman et al. 2010; (g) Rebull et al. 2016; (h) Meibom, Mathieu & Stassun 2009; (i) Sukhbold & Howell 2009; (j) Irwin et al. 2006; (k) James et al. 2010; (l) Meibom et al. 2011; (m) Messina et al. 2008, Hartman et al. 2009 & Nuñez et al. 2015; (n) Barnes et al. 2016; (o) Collier Cameron et al. 2009; (p) Delorme et al. 2011; (q) Douglas et al. 2016; (r) Radick et al. 1987 & 1995; (s) Agüeros et al. 2011; (t) Delorme et al. 2011; (u) Scholz et al. (2011); (v) Meibom et al. 2011; (w) Agüeros et al. 2018; (x) Meibom et al. 2015; (y) Barnes et al. (2016). Field period data: (a) Affer et al. 2012; (b) Hartman et al. 2011; (c) McQuillan, Mazeh & Aigrain 2014; (d) Nielsen et al. 2013; (e) Reinhold et al. 2013.

intra-cluster and individual level. For field stars, the extinction model is a smooth vertically-exponential dust disk, and the extinction coefficient at galactic latitude b and distance d is

$$C(b) = C(0)[1 - H \exp(-d \sin b/h)/\sin b], \quad (1)$$

where $C(0)$ is the mid-plane extinction coefficient and h is the model scale-height, which is taken as equal to 0.14 kpc (Koppen & Vergely 1998; Marshal et al. 2006; Brown et al. 2011). The assumed mid-plane extinction coefficients are $C_V = 1.0$, $C_J = 0.35$, $C_H = 0.25$ and $C_K = 0.15$ magnitudes per kiloparsec (Indebetouw et al. 2005). Implicitly, line of sight variations are supposed to be a minor correction.

2.4. Stellar Parameters

Stellar parameters were inferred matching (within error bars) the observed absolute magnitudes in the Johnson-Cousins V band, and the Bessel & Brett J , H and K bands, with those deduced from the latest Yale-Potsdam stellar isochrones (Spada et al. 2013; Spada et al. 2017, herein YaPSI) and the semi-empirical color-temperature calibration of Worthey & Lee (2011). The $2MASS$ magnitudes were converted to the Bessel & Brett system using formulae derived by Carpenter (2001). The parameter space of YAPSI models is dense enough to carry out detailed interpolations over a broad spectrum of possibilities: from the birth line to the onset of helium

ignition in the core, 0.15 to $5.0 M_{\odot}$, $[Fe/H] = -1.5$ to 0.3 and $Y_0 = 0.25$ to 0.37 . Notice that these are iron and helium abundances at the birth line, not the larger values they have at a posterior time. Besides the usual parameters (mass, gravity, luminosity, temperature, etc.), the YaPSI archives also include the depth of the convective envelope, the convective overtime timescale and the moments of inertia of the entire star and its convective envelope. These quantities are essential in the understanding of the evolution of angular momentum, magnetic activity and mass loss.

The physical parameters of open cluster stars are assumed to be equal to the mean values of models having 27 different age, $[Fe/H]$ and Y_0 combinations, with each of these parameters being equal to the minimum, mean and maximum values given in Table 1. For instance, the YaPSI models used for the Pleiades are 27 combinations of three age estimates (100, 120 and 140 Myr), three initial iron abundances (-0.05 , 0.00 and 0.05) and three initial helium abundances (0.27 , 0.28 and 0.29). No attempt is made to estimate and use the initial abundances of iron and helium, but these are probably close to the minimum values. In Table 3, the number of stars with a model accounting for their visual and infrared magnitudes is under Column VIR, and in Column IR when only the infrared magnitudes were matched. To exclude multiple observations of individual stars, data files from the Pleiades, M 34, Hyades and Praesepe clusters were merged into one (name-All).

The visual and infrared magnitudes of a substantial fraction of stars in the Hyades (65%), Pleiades (57%) and NGC 2547 (29%) open clusters could not be reproduced with any of the corresponding YaPSI models, suggesting that there may be larger than explored differences in the chemical makeup of stars that are thought to be part of these open clusters and/or that extinction corrections were inadequate in a large number of them. In this respect, model matching including visual magnitudes was substantially more ineffective in IC 4665, NGC 2547, Pleiades, M 37, M 35, Praesepe and Hyades, which may imply that uniform extinction is an inadequate assumption for these relatively young associations. Notice that this does not hold in every young cluster (for instance, h Persei, M 48, NGC 2301 and Blanco 1) and certainly not in those that are older than 1000 Myr. Fluctuations in the predicted values of all physical parameters were less than 10% in nearly all open cluster stars. The most notable exception is NGC 2301, where all predicted stellar parameters fluctuate more than 30% in every star.

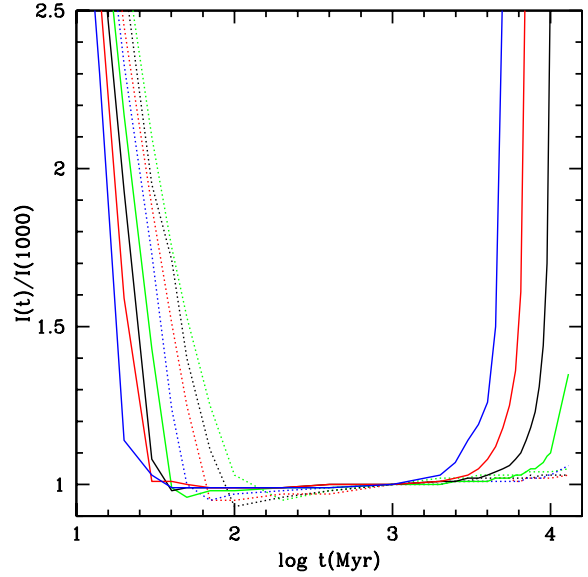


Fig. 1. Ratio of the moment of inertia at time t , $I(t)$, with respect to the moment of inertia at $t = 1000$ Myr. Dotted lines are for $M/M_{\odot} = 0.5$ (green), 0.6 (black), 0.7 (red) and 0.8 (blue). Continuous lines are for $M/M_{\odot} = 0.9$ (green), 1.0 (black), 1.1 (red) and 1.2 (blue). The color figure can be viewed online.

Model results were equally discouraging in 1 out of 4 stars from the Hyades and 3 out of 7 in NGC 6819. Unfortunately, being more massive than $1.35 M_{\odot}$, the few remaining stars from the relatively and conveniently old NGC 6819 open cluster are probably not subject to rotational braking. To use a sufficiently large amount of data, the impending analysis will include cluster stars where the visual magnitude could not be matched.

The physical parameters of field stars were extracted after inspecting a set of models with an initial close to solar-like metallicity and helium abundance ($[Fe/H] = 0.0$ and $Y_0 = 0.28$) and 37 possible ages, from 1 to 13000 Myr. The observed period was used as a roughly confined mass dependent age restriction. This is imperative, since there are important changes in the moment of inertia at the beginning (first ≈ 100 Myr) and during the second half of the main sequence, as can be appreciated in Figure 1.

The visual and infrared magnitudes of a very small fraction of *HATNet* field stars with high quality data and no other possible sources of variability could be reproduced with a YaPSI model, and nearly half of these models were theoretically inaccurate at the 30% level or more. A stellar model matching visual and infrared magnitudes could be found for the majority of *CoRoT* field stars that survived the

TABLE 4
COMA BERENICES. PARAMETERS*

AR(2000)	DEC(2000)	MM_{\odot}	T	L/L_{\odot}	R/R_{\odot}	$\log g$	I_e/I_t	Period	J_{47}	NM
178.888962	29.728251	0.79±0.01	4780± 47	0.240± 0.006	0.71±0.00	4.62±0.00	0.26±0.01	11.55±999.90	28.821± 0.992	7
183.221786	26.250360	0.77±0.00	4842± 11	0.244± 0.001	0.70±0.00	4.63±0.00	0.24±0.00	10.88±999.90	28.544± 0.538	2
185.315079	26.153889	0.78±0.01	4734± 60	0.226± 0.007	0.71±0.00	4.63±0.00	0.26±0.01	10.88±999.90	29.915± 1.404	6
186.735336	22.681862	0.61±0.01	4047± 47	0.079± 0.002	0.57±0.01	4.70±0.00	0.36±0.01	11.54±999.90	17.351± 0.943	19
186.836166	23.329834	0.90±0.00	5445± 25	0.514± 0.007	0.81±0.00	4.58±0.00	0.17±0.01	9.05±999.90	44.585± 0.406	2
189.547791	23.556168	0.58±0.01	3963± 41	0.065± 0.001	0.54±0.01	4.73±0.00	0.39±0.01	14.46±999.90	12.206± 0.621	3
190.789703	24.784779	0.63±0.00	4095± 14	0.089± 0.001	0.59±0.00	4.69±0.00	0.35±0.00	2.77±999.90	78.544± 1.405	4
194.403580	28.979084	0.95±0.01	5641± 84	0.660± 0.029	0.85±0.00	4.55±0.00	0.14±0.01	7.94±999.90	55.409± 2.500	6

* I_e/I_t is the envelope-to-total moment of inertia ratio. J_{47} is the solid body angular momentum in units of 10^{47} gr cm²/s. NM is the number of models that matched the infrared and visual magnitudes.

data filters, but more than half of them were also inexact to a very high level. To exclude multiple observations, *Kepler* field data files were merged into Kepler-All. At least one stellar model was able to account for the visual and/or infrared magnitudes of $\approx 90\%$ of main sequence *Kepler* field stars. The predicted mass, temperature, radius and gravity (its logarithm) of the vast majority of these stars (at least 8 out of 10) is theoretically accurate at the 90% level or better, and less than 66% certain in roughly 1 out of 40 stars. The moment of inertia is precise at the 90% level in 8 out of 10 stars, but very uncertain in 1 out of 10. Results are slightly worse for the stellar luminosity. Since many more *Kepler* field stars were observed with a higher quality and success rate, *CoRoT* and *HATNet* field stars will no longer be considered. Being more reliable, the ensuing analysis will only deal with *Kepler* field stars for which the visual and infrared magnitudes are reproduced.

At least one model matched the infrared magnitudes of 1311 and 30115 open cluster and field stars, and the visual and infrared magnitudes of 566 and 28364 of these stars. Electronic versions of tables with physical parameters of stars in each cluster and field are available upon request (<http://vizier.u-strasbg.fr/viz-bin/VizieR?-source=J/other/RMxAA/56.1>, <ftp://cdsarc.u-strasbg.fr/pub/cats/J/other/RMxAA/56.1>). As an example, see Table 4.

3. ANALYSIS AND DISCUSSION

3.1. Rotational Period as a Function of Mass and Time. First Round.

With their data, McQuillan, Mazeh & Aigrain (2014) produced a figure for the logarithm of the rotational period as a function of mass for *Kepler* field stars (their Figure 1). Almost all periods are within rather well defined lower and upper mass dependent limits. Referring to empirical gyrochronology models, they mention that the upper envelope period distribution

is broadly consistent with an age of 4500 Myr. The rotational period lower boundary was not discussed and, consequently, no age estimate was provided for this border.

McQuillan, Mazeh & Aigrain (2014) also point out that their figure exhibits a bimodal period distribution for stellar masses less than $\approx 0.6 M_{\odot}$. The existence of large dispersions and bimodality in the rotation rates of young open cluster G and K main sequence stars has been noticed for some time (Soderblom, Jones & Walker, 1983). Tracing fast and moderate-to-slow rotation sequences in several young clusters, Meibom et al. (2011a) found that this distribution tends to vanish in older clusters, with more massive stars being more likely to converge on a single rotational sequence. The bimodal period distribution of late K and M dwarf field stars is in line with this observation.

The rotational period as a function of mass for the *Kepler* field stars that passed all data filters and had their visual and infrared colors reproduced by a YaPSI model (as described above), is shown in the upper panel of Figure 2. The Sun, α Cen A and B (4850 ± 500 Myr; Bazot et al. 2007; Dewart, Datin & Guinan 2010) and 16 Cygnus A and B (6800 ± 400 Myr; Davies et al. 2015) are included in this figure. McQuillan, Mazeh & Aigrain (2014) introduced a limit of $T_{\text{eff}} < 6500K$ in their analysis, since they were only interested in stars with convective envelopes. When this limit is not introduced, an unanticipated result is a large number of slow rotators that are more massive than $\approx 1.3 M_{\odot}$. A smaller number of such stars are also found in the Reinhold et al. (2013) analysis of the *Kepler* database. If on the main sequence, these stars are predicted to be rotating more rapidly, since they have a very shallow convective envelope (if at all) and therefore no enhanced magnetic field to lessen their angular momentum. On the other hand, longer periods and lower temperatures are expected if they are turning

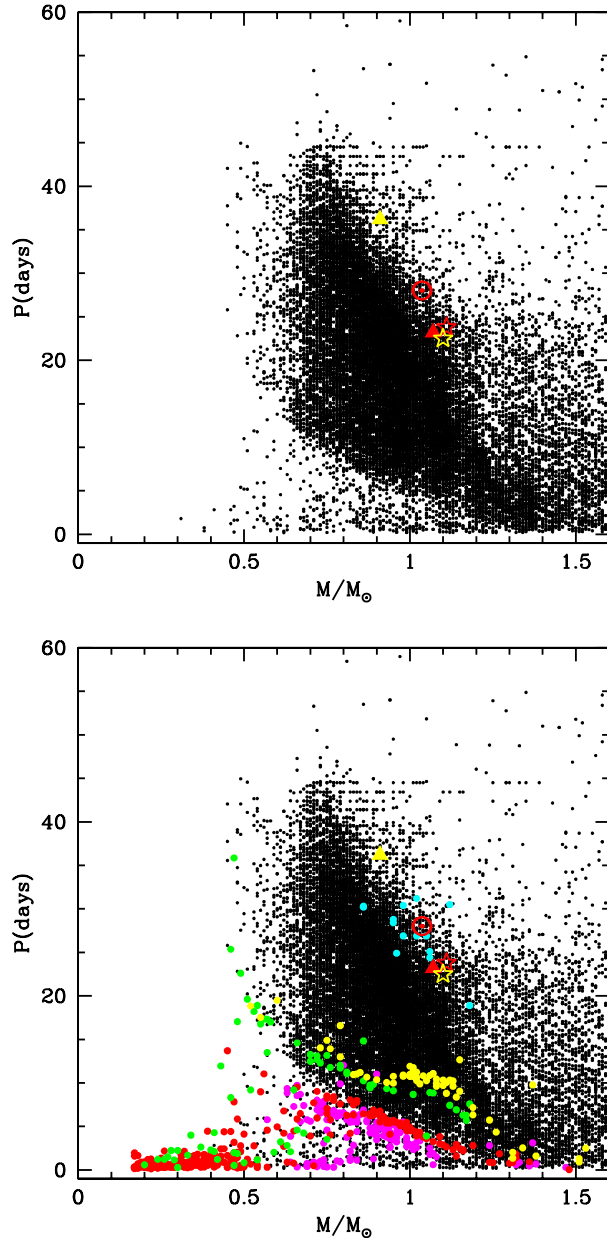


Fig. 2. Rotational period (P , days) as a function of mass (solar units). Upper and lower panel: Kepler field stars (black). Lower panel: stars from the Pleiades (red, 120 Myr), M 35 (magenta, 155 Myr), Praesepe (green, 750 Myr), NGC 6811 (yellow, 1000 Myr), NGC 752 (yellow, 1350 Myr) and M 67 (cyan, 3500 Myr) open clusters. Only open cluster stars with errors less than 10% in their observational parameters are shown in this figure. Open stars and filled triangles are for α Cen A and B (yellow) and 16 Cygnus A and B (red). The data for these stars are in Table 6. The color figure can be viewed online.

away from main sequence. This combination is found in a number of cases. As can be seen in Figure 2, very few stars less massive than $\approx 0.5 M_{\odot}$ were left after the data filters were applied and this may be the reason why the bimodal period distribution of low mass field stars is no longer apparent. Besides these two questions, there are no other overall differences between this figure and Figure 1 in McQuillan, Mazeh & Aigrain (2014).

Most of the lower boundary of the cone defined by the *Kepler* field stars draws the rotational period of stars once they have stabilized in the main sequence, sometime after reaching a steady rotational shear and moment of inertia. An age estimate of the lower boundary for the period distribution can be established plotting the period as a function of mass in stars from young open clusters with known age. The lower panel of Figure 2 also contains the rotational periods of stars from several open clusters. To avoid cluttering, only open cluster stars with errors less than 10% in their observational parameters are shown in this figure. The same conclusions are obtained when all the stars used in the numerical analysis (errors less than 20%) are included in this plot. It is quite remarkable that most of the lower boundary coincides with the position occupied by slowly rotating Pleiades stars, setting the location of a zero age rotational main sequence for late type stars at approximately 120 Myr after birth. The location of slow rotators in the M 35 cluster runs in parallel but with slightly shorter periods, suggesting that this cluster is not 155 Myr old, but younger than the Pleiades.

There is a single, well defined, mass dependent period distribution in the Pleiades, M 35 and Praesepe open clusters, as long as the stellar mass is larger than $\approx 0.8 M_{\odot}$. Early convergence to a single period distribution in the high mass range is supported by the fact that no fast $0.7 - 1.2 M_{\odot}$ rotators were found in M 37 (450 Myr) and M 48 (500 Myr). On the other hand, M 34 is a 210 Myr old open cluster supporting the notion that convergence to a single distribution in this mass range may take more than 120 Myr; the rotational periods of most Pleiades and M 34 stars more massive than $0.8 M_{\odot}$ are comparable, but quite a few stars in M 34 are fast rotators with significantly lower periods than Pleiades and M 35 stars with a similar mass. Unfortunately, in NGC 2301 (180 Myr) there are no rotational periods for stars more massive than $\approx 0.8 M_{\odot}$. In conclusion, high quality data indicate that after ≈ 120 Myr, most $\approx 0.8 - 1.2$ main sequence stars converge to the rotational sequence defined by

the Pleiades. This is earlier than previously thought (around 600 Myr). One of the possible reasons for this discrepancy is that past estimates used a larger mass bin (at least $0.2 M_{\odot}$ in Gallet & Bouvier 2013 and 2015) and combined data from clusters with different ages (Johnstone et al. 2015a). Notice that the dispersion – and the impression that there is no convergence – will increase when these operations are carried out. Finally, there are signs of a bimodal period distribution in Pleiades, M 35 and Praesepe (750 Myr) stars less massive than $\approx 0.8 M_{\odot}$, but no indication of such a thing in older clusters. Notice that there are relatively few fast rotators in Praesepe and, at least down to $\approx 0.5 M_{\odot}$, apparently none in clusters older than 750 Myr, such as NGC 6811 (1000 Myr) and NGC 752 (1350 Myr). Thus, nearly all $0.5 - 0.8 M_{\odot}$ stars seem to merge into a single mass dependent rotational evolutionary sequence sometime after 750 Myr.

The relative position of the rotational period distributions of stars from the Pleiades, M 35, Praesepe, NGC 6811 (1000 Myr), NGC 752 (1350 Myr) and M 67 (3500 Myr) open clusters leaves no doubt that there is an evolutionary sequence. Stars from the oldest open cluster depicted in this figure, M 67, do not draw a similarly clear continuous line as the Pleiades stars, and the upper boundary (long periods) drawn by *Kepler* field stars is not as well defined. An interesting point is that α Cen A and B, which are ≈ 1000 older than M 67, are close to the site occupied by stars from this open cluster. This indicates that once they merge into a single rotational sequence, angular momentum evolution of single solar type stars (mass between 0.9 and $1.1 M_{\odot}$) is weakly dependent on binarity when the orbital period is sufficiently long (79 years in α Cen AB). Additionally, it implies that rotational braking of solar type stars is increasingly inefficient as they grow old. The second conclusion is strongly supported by the fact that there is hardly any difference between the rotational period of these stars and 16 Cygnus A and B, which are ≈ 3000 Myr older than the M 67 cluster. It is worth noting that the long-term rotational evolution of the Sun as a single star does not seem to have been affected in a major way by our planetary system. It remains to be seen which conditions are necessary for this to happen.

3.2. Rigid Body Angular Momentum as a Function of Mass and Time

Since angular momentum and rotational energy are the physical quantities that change during stellar evolution, we can not expect a clearly defined signa-

ture for the mass and time dependence of the mean rotational period at the stellar surface. A comprehensive and definite knowledge of these quantities – angular momentum and energy – is still beyond reach, since little is known on the radial dependence of the angular velocity as a function of stellar mass and age. Assumptions have to be made, and these are greatly influenced by what we know about the Sun, which is well advanced into its rotational history (as evinced in Figure 2).

Helioseismology has shown that the radiative core of the Sun rotates rigidly at a rate of 431 nHz (period close to 27 days) at least down to $\approx 0.15 R_{\odot}$ (Kozennik & Eff-Darwich, 2012; Eff-Darwich & Kozennik, 2013). Taking a radial average, the convective envelope rotates at a similar rate (or slightly higher according to Tomczyk, Schou & Thompson 1995). Since the outer layers are slowed down by magnetic braking, this signifies that angular momentum transport from the radiative core to the convective envelope has been equally efficient for some time.

But not much is known on the internal rotation of other stars, and Lund, Miesch & Christensen-Dalsgaard (2014) argued that asteroseismological measurements of Sun-like stars cannot result in clean-cut inferences on the radial profile of the rotational period. Even so, Nielsen et al. (2017) concluded that the interior and envelope rotation rates cannot differ by more than $\approx 30\%$ in 5 solar-like stars (insofar as mass and age are concerned), and Collier Cameron et al. (2009) claim that F, G and K main sequence stars rotate as rigid bodies after ≈ 600 Myr. Fully convective main and pre-main sequence stars are expected to rotate as rigid bodies, and Charbonnel et al. (2013) showed that the rotational frequency of a solar mass ZAMS star peaks at $\approx 0.25 R_{\odot}$ and is approximately constant beyond $\approx 0.5 R_{\odot}$, if angular momentum is redistributed by internal gravity waves.

Modeling the rate at which angular momentum is lost at the stellar surface, and examining the constraints on internal angular momentum transport which can be inferred from the $0.2 M_{\odot}$ mass bin period distributions of several clusters, Denissenkov et al. (2010) concluded that $0.4 \leq M/M_{\odot} \leq 1.2$ stars with an initial rotation period of less than ≈ 2 days, will rotate as rigid bodies during most of their main sequence evolutionary stage. But if the initial period is between 2 and 4 days, the core-envelope coupling timescale will be 50 ± 25 Myr when $M = 1.0 \pm 0.1 M_{\odot}$, or 175 ± 25 Myr when $M = 0.8 \pm 0.1 M_{\odot}$. More extended periods lead to longer coupling times. Notice

that by the time they reach the zero age rotational main sequence, ≈ 120 Myr after birth, the rotational period is close to 10 days when $M/M_{\odot} \simeq 0.7$ and less than 5 days if $M/M_{\odot} > 1$ (see Figure 2). Obviously, the initial rotational periods had to be smaller.

From the preceding paragraphs, it seems that a rigid rotation model may be not too far-off from reality. It may even be an almost precise description of stars that are older than a few hundred Myr, but not too close to the end of their main sequence lifetime. Needless to say, rigid body rotation is also the simplest way to carry out an inspection of angular momentum evolution. The rest of this paper will discuss this subject, under the hypothesis that late-type main sequence stars rotate as rigid bodies. Arguing that there seems to be moderate differential rotation between core and envelope in stars older than ≈ 100 Myr, Johnstone et al. (2015a) introduced the rigid body assumption into the magnetic braking torque formula derived by Watt et al. (2012), to estimate the evolution of rotation and winds. In this work, the solid body assumption is used to determine the mass and time dependence of the angular momentum and, thereon, develop very simple equations for the evolution of the Rossby number (a surrogate for magnetic activity), the torque, and the mass loss rate.

The product $J = I\Omega = 2\pi I/P$ – where J is the angular momentum if the star is indeed rotating as a rigid body, I is the moment of inertia of the whole star as given by the YaPSI model, Ω is the observed angular frequency and P is the rotational period – is plotted as a function of stellar mass in Figure 3. For the same reason as in Figure 2, only open cluster stars with errors less than 10% in their observational parameters are shown in this figure. Take notice on the following:

- (i) The apparent or rigid body angular momentum of the vast majority of *Kepler* field stars lies in an area contained within well defined upper and lower limits, as long as $M/M_{\odot} \leq 1.2$.
- (ii) There is a wide range of rigid body angular momenta among the least massive Pleiades and Praesepe stars, with no indication of a bimodal distribution. Rather than this, this dispersal conveys the impression that it is partly due to random initial conditions and times of birth. On the other hand, the possibility of a separate population of rapidly spinning low mass stars ($M/M_{\odot} \leq 0.7$) is favored by the substantial number of fast rotators in the Praesepe cluster, where the imprint of initial conditions

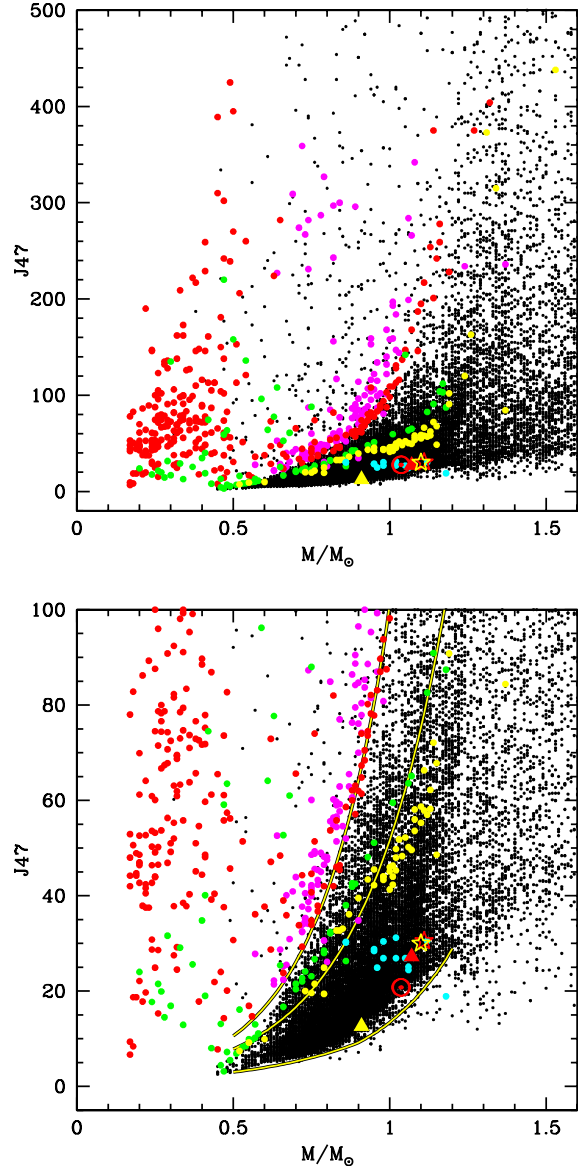


Fig. 3. Rigid body angular momentum (J_{47} , 10^{47} $\text{gr cm}^{-2} \text{s}^{-1}$) as a function of mass (solar units) in *Kepler* field (black), Pleiades (red, 120 Myr), M 35 (magenta, 155 Myr), Praesepe (green, 750 Myr), NGC 6811 (yellow, 1000 Myr), NGC 752 (yellow, 1350 Myr) and M 67 (cyan, 3500 Myr) stars. Only stars with errors of less than 10% in their observational parameters are shown in this figure. Stars and triangles are for α Cen A and B (yellow) and 16 Cygnus A and B (red). Yellow lines in the lower panel are rough approximations to a zero age rotational main sequence isochrone as defined by the Pleiades cluster (Equation 2), the 750 Myr Praesepe isochrone (Equation 3) and the terminal main sequence rotational isochrone. (Equations 4 and 5). The color figure can be viewed online.

is anticipated to be nearly gone. In any case, this dispersal is a major obstacle to an unambiguous age determination of stars less massive than $\approx 0.7 M_{\odot}$ and younger than ≈ 750 Myr.

- (iii) The angular momentum tends to pile up in a decreasing range of values in the low mass range. This implies that age estimates based on rotational periods or angular momenta should be increasingly unreliable when the stellar mass is less than $\approx 0.6 M_{\odot}$. In addition, Epstein & Pinsonneault (2014) observed that the inherent uncertainty of the initial conditions remains large for old stars below $0.6 M_{\odot}$.
- (iv) For any given mass, the upper boundary (large angular momentum) of *Kepler* field stars coincides with the position defined by the Pleiades stars with the smallest angular momentum. Once again, it sets a well defined zero age rotational main sequence at ≈ 120 Myr. It is depicted by the upper yellow line shown in the lower panel of Figure 3, and can be roughly traced with the following equation if $0.5 \leq M/M_{\odot} \leq 1.2$,

$$J_{ple} = 1.19 \times 10^{47} 10^{1.953 M/M_{\odot}} \text{ gr cm}^2/\text{s}. \quad (2)$$

Notice that there is a factor of ≈ 100 between the angular momentum of low and high mass stars, once they reach the zero age rotational main sequence.

- (v) Quite evidently, notwithstanding the possibility of a rapidly spinning population, lower mass stars lose a larger fraction of their angular momentum before settling on the zero age rotational main sequence and take a longer time to do so.
 - (vi) An angular momentum sequence for slowly rotating stars from the Praesepe open cluster is also evident. It corresponds to the middle yellow line, and in the same mass range it is approximately given by,
- $$J_{pre} = 1.18 \times 10^{47} 10^{1.640 M/M_{\odot}} \text{ gr cm}^2/\text{s}. \quad (3)$$
- (vii) In contrast with the period distribution, a lower boundary for the angular momentum is very well defined by *Kepler* field stars. The terminal (as of today) main sequence rotational isochrone (bottom yellow line in the lower panel of Figure 3) is charted by the following equations,

$$J_{ter} = 2.94 \times 10^{46} 10^{1.661 M/M_{\odot}} \text{ gr cm}^2/\text{s}, \quad (4)$$

if $0.9 \leq M/M_{\odot} \leq 1.2$, and

$$J_{ter} = 7.41 \times 10^{46} 10^{1.214 M/M_{\odot}} \text{ gr cm}^2/\text{s}, \quad (5)$$

if $0.5 \leq M/M_{\odot} \leq 0.9$.

The fact that less massive stars have not yet completed their main sequence rotational history is the likely reason why the slope changes at $M/M_{\odot} \simeq 0.9$.

- (viii) As mentioned above, McQuillan, Mazeh & Aigrain (2014) use gyrochronology models (Barnes, 2007; Mamajek & Hillenbrand, 2008; Meibom et al. 2009) to set an age of 4500 Myr for stars occupying the lower boundary of the angular momentum (upper boundary for the period), but they conclude that these models under-predict stellar ages. A simpler and more intuitive estimate, is to set the timeline for this boundary considering that it must be defined by stars having nearly the same age as their main sequence lifetime ($\tau_{ms} \simeq 10^4 (M/M_{\odot})^{-2.5}$ Myr) if $M/M_{\odot} \geq 0.9$, and somewhat less than the age of the Milky Way, say $\tau_0 = 13\,000$ Myr, when $M/M_{\odot} \leq 0.9$ ($\tau_0 \leq \tau_{ms}$ in these low mass stars).
- (ix) For stellar masses between ≈ 0.9 and $1.2 M_{\odot}$, the rigid body angular momentum of quite a few stars is less than the terminal value. If this is real, these stars may be leaving the main sequence. If so, they are expanding rapidly, their rotational shear and moment of inertia are escalating equally fast and, apparently, the most prominent star spots are spinning down by an even larger amount. Less massive stars are not doing so, since they are far from completing their main sequence lifetime.

Empirical relations between rigid body angular momentum and age for a specific mass can be found using either one or a combination of the Pleiades, Praesepe and terminal main sequence isochrones.

The simplest and more often used relation is an inverse square root law (a Skumanich-like relation). Choosing the Praesepe isochrone as the anchor line,

$$J_{sqr} = J_{pre} (t/750)^{-1/2}, \quad (6)$$

with J_{pre} as given in Equation 3 and t in Myr. Notice that this solution assumes a time invariant shape for the angular momentum distribution as a function of mass, in this case defined by the Praesepe open cluster stars. Comparing Equations 2 and 3, we can see that this assumption is not verified in the

Pleiades star cluster, and we can expect poor results when Equation 6 is applied to stars that are somewhat younger than the Praesepe cluster. On the contrary, the similar shape of the Praesepe and terminal (for $M/M_{\odot} \geq 0.9$) angular momentum distributions, implies that satisfactory results can be anticipated when Equation 6 is applied to older solar type stars.

Obviously, better adjustments valid for slowly rotating stars older than 120 Myr, can be obtained from three parameter solutions involving the three isochrones, such as the following exponential law,

$$J_{exp} = A \exp(-B t^C), \quad (7)$$

where t is in Myr, and A, B and C are mass dependent constants. These are given in Table 5 for a few selected masses. The table includes two e-folding times for the angular momentum, \mathcal{T}_0 and \mathcal{T}_{120} (in Myr), *i.e.*, the time it takes to reduce it by a factor equal to $1/e$ after the birth line, $t = 0$, and after the age of the Pleiades, $t = 120$. The e-folding time after the birth line may be deceptive, since there is no reason why we should expect that the power law approximation can be extrapolated to stellar ages that are less than 120 Myr. The e-folding time after the Pleiades rotational isochrone shows that the torque is increasingly vigorous in more massive stars. An interesting result is that after spending ≈ 13 to 19% of their main sequence lifetime ($\approx 15\%$ after discounting the Pleiades age), all 0.5 to 1.2 M_{\odot} main sequence stars lose $\approx 85\%$ of the angular momentum they had when they were 120 Myr old.

Since a simpler exponential relation, $J = A \exp(Bt)$, can be summoned for fast rotators with a saturated magnetic field (Chaboyer et al. 1995) and a fixed moment of inertia (Dennisenkov 2010; Amard et al. 2016), it is worth noticing that such a relation is completely at odds with the data when it is calibrated with the Pleiades and Praesepe isochrones. Thus, the stars defining these isochrones are not in the saturated regime and, obviously, are not fast rotators.

The mean and minimum stellar angular momenta found in the open clusters listed in Table 1 are displayed in Figures 4 and 5. By reason of insufficient data, stars less massive than 0.65 M_{\odot} are not considered. Since there is a limited amount of information for clusters older than ≈ 1000 Myr, main sequence stars with ages derived from asteroseismological data modeling are included. Listed in Table 6, some of these stars are binaries or host planetary systems (as the Sun, which is also included). The inverse square root and exponential relations between angular mo-

TABLE 5
EXPONENTIAL FITS*

M/M_{\odot}	A	B	C	\mathcal{T}_0	\mathcal{T}_{120}
0.50	1.62e+48	0.105	0.293603	2157	7261
0.60	3.19e+48	0.200	0.247530	666	5091
0.70	6.97e+48	0.365	0.206752	131	3583
0.80	1.50e+49	0.540	0.183679	29	2675
0.90	3.67e+49	0.812	0.159828	3.7	2042
1.00	7.56e+49	0.949	0.157111	1.4	1563
1.10	1.33e+50	0.976	0.162967	1.2	1274
1.20	2.08e+50	0.919	0.175548	1.6	1075

*Constants in exponential fits to the angular momentum, as given in Equation 7. The e-folding times, \mathcal{T}_0 and \mathcal{T}_{120} (both in Myr), are such that $B\mathcal{T}_0^C = -1$ and $B(\mathcal{T}_{120}^C - 120^C) = -1$.

mentum and age have been added to these figures (continuous line, equation 6; dotted line, equation 7).

These figures show that most of the angular momentum of all late type main sequence slow rotators, is lost during their first ≈ 500 Myr. This implies that the torque is exceptionally strong during this period. Thereon, the torque must be much more moderate, since angular momentum is lost in a very sedate fashion. As expected, the inverse square root relation defined by the Praesepe isochrone is inconsistent with the mean and minimum values of the angular momentum in clusters that are younger than 450 Myr. For these clusters, the exponential fit is more often than not compatible with the minimum value of the angular momentum. When $M/M_{\odot} \geq 0.9$ and the cluster age is larger than ≈ 450 Myr, both relations are consistent with the mean value of the angular momentum, and their difference is usually smaller than the observational uncertainties. This statement is also valid when stars are older than 750 Myr, and their mass is somewhat larger than 0.8 M_{\odot} . With a couple of exceptions, these observations can be applied to stars with asteroseismological data.

According to equations 6 and 7, the rigid body angular momentum of a 4500 Myr solar mass star should be 2.1 and 2.2×10^{48} gr cm⁻² s⁻¹, only $\approx 10\%$ larger than the rigid body angular momentum of the Sun, 1.9×10^{48} gr cm⁻² s⁻¹. Since scaling is implicitly included, the similarity with the power law fit is not surprising. On the other hand, the semblance with the inverse square root relation is suggestive, since no scaling is built into it. These equations can also be used to produce an age estimate using the rigid body angular momentum; in the solar case the result is 5500 and 5600 Myr.

TABLE 6
STARS WITH ASTEROSEISMOLOGICAL DATA *

Name	Mass	Age	Period	I53	J47
α Cen A	1.10 \pm 0.01	4850 \pm 500	22.50 \pm 5.90	9.29 \pm 0.20	30.0 $^{+53.1}_{-6.75}$
α Cen B	0.91 \pm 0.01	4850 \pm 500	36.20 \pm 1.40	6.25 \pm 0.02	12.6 $^{+0.55}_{-0.51}$
16 Cyg A	1.11 \pm 0.02	6800 \pm 400	23.8 $^{+1.5}_{-1.8}$	9.98 \pm 0.72	30.5 $^{+2.73}_{-3.87}$
16 Cyg B	1.07 \pm 0.02	6800 \pm 400	23.2 $^{+11.5}_{-3.2}$	8.68 \pm 0.44	27.2 $^{+5.94}_{-9.93}$
KIC 4914923	1.10 \pm 0.01	6180 \pm 180	20.49 \pm 0.00	17.93 $^{+35.0}_{-7.72}$	63.6 $^{+124}_{-27.4}$
KIC 6521045 ^p	1.04 \pm 0.02	6240 \pm 640	25.34 \pm 2.78	8.63 $^{+2.30}_{-1.07}$	24.8 $^{+10.4}_{-5.20}$
KIC 7871531	0.84 \pm 0.02	9150 \pm 470	33.72 \pm 2.60	5.58 $^{+0.20}_{-0.20}$	12.0 $^{+1.50}_{-1.20}$
KIC 8006161	1.04 \pm 0.02	4690 \pm 530	29.79 \pm 3.09	6.32 $^{+0.32}_{-0.28}$	15.4 $^{+2.70}_{-2.00}$
KIC 9955598 ^p	0.93 \pm 0.04	6479 \pm 450	34.75 \pm 6.31	6.25 $^{+0.72}_{-0.61}$	13.1 $^{+4.70}_{-3.10}$
KIC 10644253	1.13 \pm 0.05	1070 \pm 250	10.91 \pm 0.87	7.94 $^{+0.24}_{-0.24}$	52.9 $^{+6.40}_{-5.30}$
KIC 10963065 ^p	1.07 \pm 0.03	4260 \pm 400	12.38 \pm 1.22	35.1 $^{+74.2}_{-22.9}$	206 $^{+506}_{-141}$

*Mass given in solar units, age in million years, period in days, I53 moment of inertia in 10^{53} gr cm² and J47 angular momentum in 10^{47} gr cm² s⁻¹. Periods for α Cen A and B are from Bazot et al. (2007) and Dewarf, Datin & Guinan (2010), and their mass and age are from Thévenin et al. (2002). Data for 16 Cygnus A and B, Davis et al. (2015). For the rest, the data is from Mathur et al. (2012), Metcalfe et al. (2014) and Ceillier et al. (2016). Superscript “p” is for stars with planets. Moment of inertia from YaPSI models, assuming $[Fe/H] = 0.0$ and $Y_0 = 0.28$.

Thus, the rigid body angular momentum (as well as the rotational period) gives an indication of the evolutionary stage of any main sequence star, but the observational database shows that it can not be used to determine with any degree of precision the age of F and G main sequence stars younger than ≈ 450 Myr or K type stars younger than ≈ 750 Myr. This limit is likely to be substantially higher for later spectral types. On the other hand, the exponential relation supported by the Pleiades, Praesepe and terminal isochrones for the rigid body angular momentum, or the simple inverse square root relation based on the Praesepe isochrone, may provide acceptable but not too precise estimates for the ages of older stars.

3.3. Rotational Period as a Function of Mass and Time. Second Round

The rigid body angular momentum depends on the detected rotational period and the unobserved moment of inertia ($J = 2\pi I/P$). Since the moment of inertia is mass, metallicity and time dependent, the relation between rotational period and age should be more complicated.

The metallicity dependence of the moment of inertia is weak, but not insignificant. For otherwise identical conditions, higher metallicities produce larger moments of inertia, with an up to $\approx 10\%$ difference between the highest ($[Fe/H] = 0.3$, $Y_0 = 0.31$) and lowest ($[Fe/H] = -0.5$, $Y_0 = 0.25$) values

considered by YaPSI, the gap being smaller for lower mass stars.

As mentioned before, the time dependence of the moment of inertia can be substantially more important. The evolution of the moment of inertia of $0.5 - 1.2 M_{\odot}$ stars with a solar composition was depicted in Figure 1. It shows that it declines very rapidly at the beginning of the main sequence. After 100 Myr or so it settles at a relatively stable value that lasts until roughly half the main sequence lifetime. During this stage, the moment of inertia of ≈ 0.4 to $1.2 M_{\odot}$ stars is approximately equal to its 1000 Myr old value. YaPSI models for 1000 Myr old stars with $[Fe/H] = 0.0$ and $Y_0 = 0.28$, lead to the following fit to the moment of inertia for a stellar mass range between 0.5 and $1.2 M_{\odot}$,

$$I \simeq 6.99 \times 10^{52} 10^{0.965 M/M_{\odot}} \text{ gr cm}^2. \quad (8)$$

The regression coefficient and the square root of the mean square error are equal to 0.98 and 0.09. The metallicity effect may add an additional uncertainty of $\approx 5\%$ in the high mass limit, less than this in lower mass stars. For a one solar mass star, the moment of inertia predicted by this Equation is 6.45×10^{53} gr cm², somewhat less than the precise value, 6.71×10^{53} gr cm², and appreciably smaller than the moment of inertia of a 4500 Myr old one solar mass star, 6.95×10^{53} gr cm².

Equation 8 and the inverse square root relation between angular momentum and age lead to the fol-

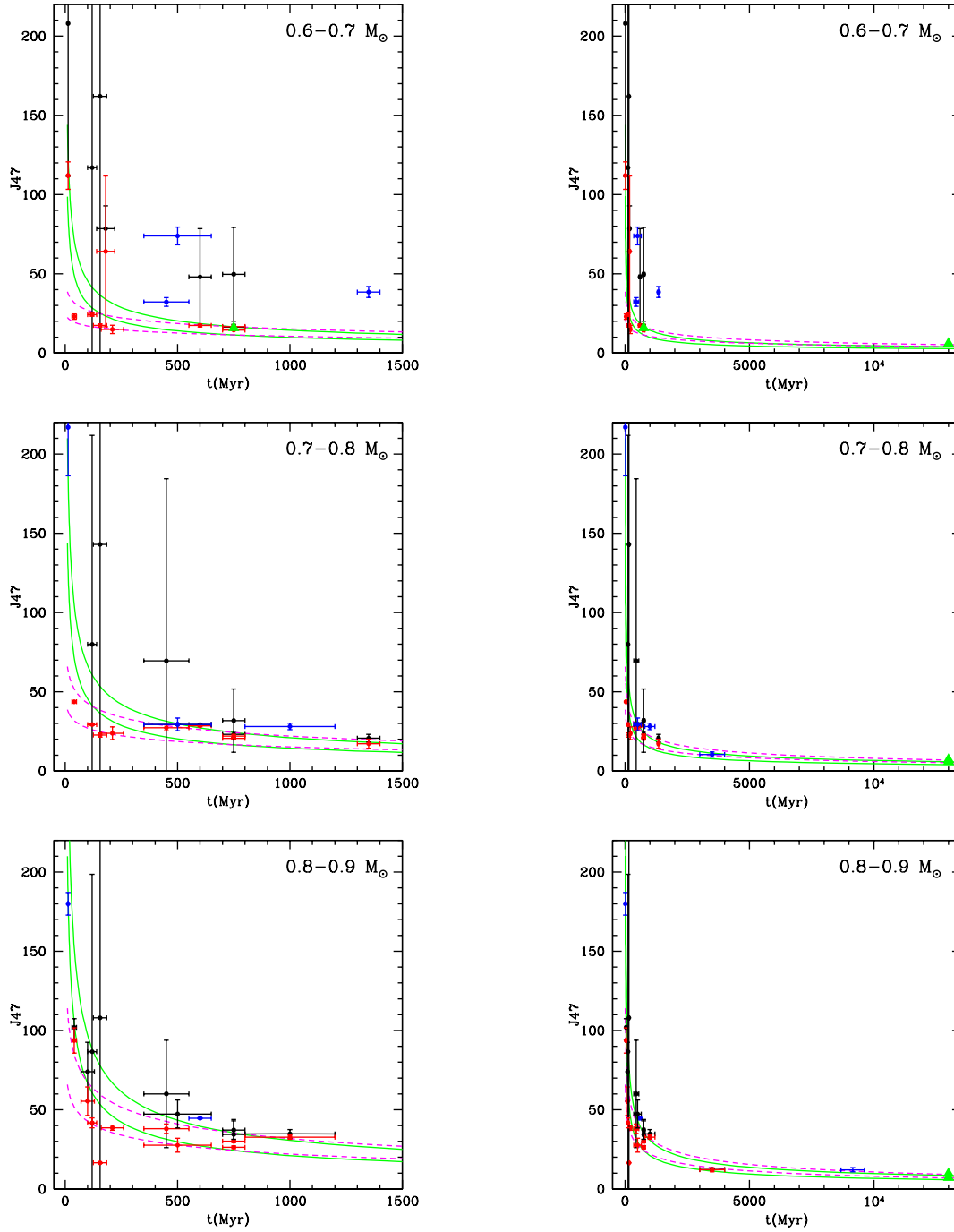


Fig. 4. Rigid body angular momentum (J_{47} , 10^{47} gr $\text{cm}^2 \text{s}^{-1}$) as a function of time for stellar masses between 0.6 and $1.2 M_{\odot}$ in $0.1 M_{\odot}$ intervals. Mean and minimum angular momentum values for the open cluster stars listed in Table 1 are shown in black and red. Single stars from a cluster or from the group of stars listed in Table 6 are shown in blue. The Sun is represented with a red circle and the green triangles in the right hand side figures stand for the angular momentum of the terminal rotational main sequence. The continuous and dotted lines are the inverse square root (green) and exponential fits (magenta) to the angular momentum of the lower and upper mass limits written at the top right hand side of these figures. The color figure can be viewed online.

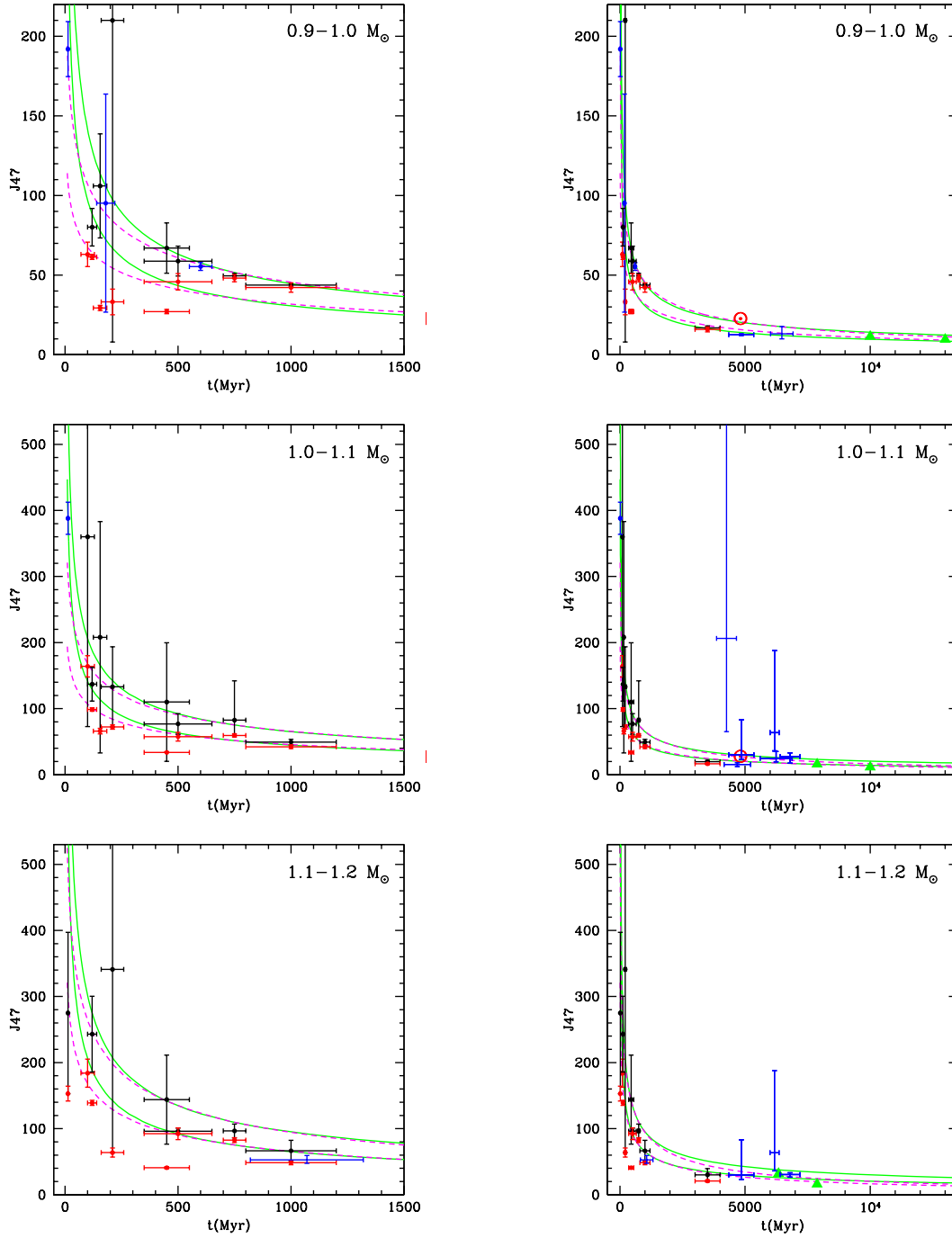


Fig. 5. Same caption as in Figure 4. The color figure can be viewed online.

lowing direct connection between age and rotational period during the time span where the moment of inertia is approximately constant,

$$t \simeq 0.404 \cdot 10^{1.35 M/M_{\odot}} P_d^2 \text{ Myr.} \quad (9)$$

This equation returns a disappointing age of 6600 Myr for the Sun. The exponential fit leads to

a more intricate relationship, but gives the same age for our star, *i.e.*, ≈ 1000 Myr more than the age estimate based on the rigid body angular momentum.

In the second half of their main sequence lifetime, stars build an increasingly larger moment of inertia and the mean rotational period will increase even

in the absence of rotational braking. Notice that the consequence on surface rotation may be more pronounced, since differential rotation may result as the core contracts and spins up and the envelope expands and slows down. These effects are still insignificant in lighter stars, but gain in importance in 1.2, 1.1, 1.0 and 0.9 M_{\odot} stars as soon as they are $\approx 1400, 3600, 4500$ and 7900 Myr old. For instance, without rotational braking, the solar period will be around 32, 38 and 68 days when our star is 8000, 9000 and 10000 Myr old. The rotational period would be equal to 38, 47 and 90 days if the evolution of angular momentum resembles the inverse square root relation (Equation 6) or 39, 49 and 95 days if it is described by the exponential law (Equation 7). Since the longest rotational period of the one solar mass stars included in this paper is 63 days, these numbers suggest that other drivers of rotational braking (mass loss, magnetic field intensity, wind acceleration) are secondary agents in the evolution of stellar periods during the second half of the main sequence. Actually, there may be some evidence for inefficient magnetic braking in the Sun, where the high latitude wind was found to be super-Alfvénic close to the solar surface (McComas et al. 2000).

3.4. Magnetic Activity as a Function of Mass and Time

Stellar dynamos sustain poloidal-toroidal magnetic fields (the $\alpha-\Omega$ mechanism) as long as Coriolis forces dominate inertial forces within the convective region (Durney & Latour 1978). The relation between these forces is quantified with the Rossby number, which can be defined as

$$R_o = P/\tau_c = 2\pi I/\tau_c J, \quad (10)$$

where τ_c is the convective turnover time.

A strong argument for the conjecture that the magnetic field of main sequence stars with a convective envelope is produced by the $\alpha-\Omega$ dynamo mechanism is based on the observation that the X-ray and chromospheric to bolometric luminosity ratios are proportional to R_o^{-2} in the non-saturated regime (Noyes et al. 1984; Pizzolato et al. 2003). This thesis has been disputed by Reiner, Schüssler & Passegger (2014), arguing that these relations hold if the convective overturn time scales as $L_{bol}^{-1/2}$. Since both quantities are roughly constant during most of main sequence, this proportionality should be true for any star during this relatively stable time period. On the other hand, the proportionality constant may depend on the stellar mass. Interestingly, during this

stable phase $L_{bol}^{1/2} \times \tau_c \approx 30$ (L_{bol} in solar units, τ_c in days) if $0.4 \leq M/M_{\odot} \leq 1$, close to 20 if $M/M_{\odot} = 1.1$ and around 7 when $M/M_{\odot} = 1.2$. Admittedly, the convective turnover time provided by YAPSI is associated to the tachocline, not to the position where the dynamo is more effective. Even so, these numbers suggest that the Parker dynamo mechanism has an effect on magnetic braking, at least in non-fully convective stars less than, or as massive as, the Sun. Whichever the case, Reiner et al. (2014) rightly emphasize the need to explore and consider a wider range of mechanisms for the generation of magnetic fields in low mass main sequence stars.

Thus, assuming that the $\alpha-\Omega$ mechanism is operative, magnetic activity and rotational braking will tend to be suppressed when the Rossby number is large. It has been argued that this explains the existence of anomalously rapid rotation in some old field stars (van Saders et al. 2016), and it may be the reason why KIC 4914923, KIC 5184732 and KIC 10963065 have such an atypically large angular momentum (see Table 6).

The value of the convective turnover time depends on the convection parameter (usually taken as equal to the solar value, $\alpha = 1.875$) and the assumed depth of the region where the dynamo is being generated. Under the same circumstances, lengthier convection times and smaller Rossby numbers are obviously associated to dynamos running closer to the tachocline but, except for the scale difference, the mass and time dependence of the convective turnover time does not seem to be affected by this supposition (Landin, Mendes & Vaz 2010).

According to YaPSI models with solar-like composition ($[Fe/H] = 0.0$ and $Y_0 = 0.28$), the convective turnover time of all late type main sequence stars is equal to a few hundred days during the first 10 to 100 Myr. Later on, it remains roughly constant, almost up to the end of main sequence. Consequently, as stars spin down during their main sequence evolution, the Rossby number will increase, the $\alpha-\Omega$ mechanism will weaken and magnetic braking will become increasingly inefficient. Since the convective turnover time during this stage is ≥ 100 days when $M \leq 0.6 M_{\odot}$, and $\approx 70, 55, 40, 30, 15$ and 5 days when $M = 0.7, 0.8, 0.9, 1.0, 1.1$ and $1.2 M_{\odot}$, the demise of the dynamo effect may begin significantly earlier in stars with shallow convective regions.

The history of the Rossby number for 0.5 to 1.2 M_{\odot} stars was determined using the exponential and inverse square root approximations for the evolution of the angular momentum (similar results are

obtained). In these calculations the Rossby number of a 4500 Myr old one solar mass star is equal to 0.87. This is significantly less than an often quoted value (2.16 in van Saders et al. 2016) but, as discussed above, part of this difference is probably related to the assumed depth of the dynamo producing region. Thus, depending on the precise definition of the convective turnover time, either one of these numbers (both close to one) can be taken as the Rossby number where magnetic activity and rotational braking may begin to decline.

The evolution of the Rossby number is shown in Figure 6. Notice that $R_o \geq 1$ for 1.2, 1.1, 1.0 and $0.9 M_\odot$ stars once they are older than ≈ 500 , 2500, 5500, and 9500 Myr. In 1.2 and $1.1 M_\odot$ stars, the cessation of the dynamo mechanism may occur before there is a significant change in their moment of inertia. With the un-anticipated exception of $1.2 M_\odot$ stars, the possible disruption of the magnetic dynamo occurs much later than the \mathcal{T}_{120} e-folding times for the angular momentum.

Kitchainov & Nepomnyashchikh (2017) had noticed that the interruption of large scale dynamos may be the reason why gyrochronology fails to predict the age of older stars. If this is correct, their surviving magnetic fossil field may be the main rotational braking source during the time interval between the fading $\alpha - \Omega$ mechanism and the swelling moment of inertia. Later on, the transformation of the moment of inertia will eventually determine the evolution of the rotational period. In less massive stars, dynamo activity will decline at the same time as the moment of inertia escalates, and their continuously changing relative importance will impress the history of the rotational period during the second half of the main sequence stage.

3.5. Torque as a Function of Mass and Time

Differences in angular momentum between pairs of isochrones with respect to the youngest of the two, are displayed on the left hand side of Figure 7 (associated formulas are shown in this figure). The corresponding mean loss rates per Gyr are shown on the right hand side.

Close to 60% and 25% of the initial rigid body angular momentum of 1.2 and $0.5 M_\odot$ slowly rotating stars is lost during the few hundred million years separating the Pleiades and Praesepe isochrones. At this stage, the mean loss rate is around 90% and a bit more than 40% per Gyr for 1.2 and $0.5 M_\odot$ stars. Loss rates are much smaller after ≈ 750 Myr. Near the end of their main sequence lifetime, 88% and 86% of the initial angular momentum of 1.2 and

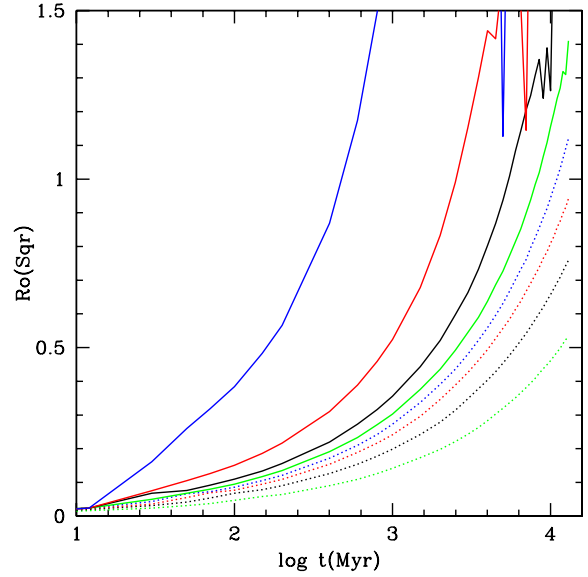


Fig. 6. Evolution of the Rossby number during the main sequence stage, assuming that the angular momentum is as given in equation 6. Dotted lines stand for $M/M_\odot = 0.5$ (green), 0.6 (black), 0.7 (red) and 0.8 (blue). Continuous lines stand for $M/M_\odot = 0.9$ (green), 1.0 (black), 1.1 (red) and 1.2 (blue). The color figure can be viewed online.

$0.9 M_\odot$ stars has been lost. At this point in time, the oldest 0.7 and $0.5 M_\odot$ stars have lost 80% and 73% of the angular momentum they had when landing on the Pleiades isochrone. From these two figures, it is once again clear that the relative and absolute rigid body angular momentum loss rates are always appreciably larger in shorter-lived, more massive, stars.

The inverse square root and exponential fits to angular momentum evolution (Equations 6 and 7), lead to the following expressions for the angular momentum loss rates (*i.e.*, the torque $\tau = dJ/dt$) acting on slowly rotating late type main sequence stars older than approximately 120 Myr,

$$\begin{aligned} \tau_{sqr} &= -J_{pre} 750^{1/2} t^{-3/2}/2, \\ \tau_{sqr} &= -1.62 \times 10^{48} 10^{1.640 M/M_\odot} t^{-3/2} \\ &\quad \text{gr cm}^2 \text{s}^{-1} \text{Myr}^{-1}, \end{aligned} \quad (11)$$

$$\tau_{exp} = A B C \exp(B t^C) t^{C-1} \text{ gr cm}^2 \text{s}^{-1} \text{Myr}^{-1}, \quad (12)$$

with t in Myr, and constants A , B and C as given in Table 5. Notice that in both cases the torque can be re-written in the following way

$$\tau = K J t^\gamma = K I \Omega t^\gamma, \quad (13)$$

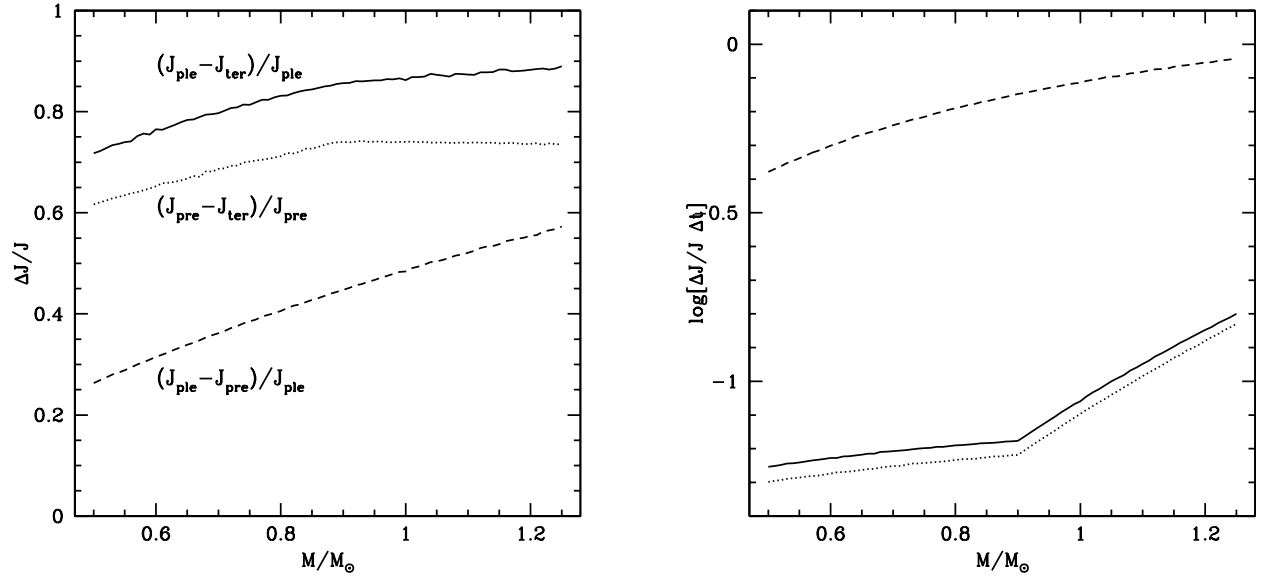


Fig. 7. On the left, differences in the angular momentum between the Pleiades, Praesepe and terminal isochrones, relative to the angular momentum of the younger one ($\Delta J/J$). On the right, logarithm of the mean relative angular momentum loss rate per Gyr, $\log[\Delta J/J \Delta t]$, for the time interval between the Pleiades and terminal isochrone (continuous line), the Praesepe and terminal isochrones (dotted line) and the Praesepe and Pleiades isochrones (short-dashed line).

with $K = -1/2$ and $\gamma = -1$ in the inverse square root relation, and $K = -BC$ and $\gamma = C - 1$ in the exponential approximation.

These torques are usually smaller than those where the radiative core is spinning faster than the envelope, since there is less angular momentum when the entire star rotates at the surface rate. This can be visualized in Figure 8. Beyond 100 Myr, both of them are up to a factor of 5 smaller than the torques produced by a couple of models for the slowly rotating branch of one solar mass stars, where solid body rotation is not assumed and angular momentum is transferred from the radiative core to the convective envelope in two different ways (Amard et al. 2016).

The temporal evolution of the absolute value of the torque under the inverse square root and exponential approximations is plotted in Figure 9. As can be seen, there is a conspicuous difference between the inverse square root and exponential approximations when stars are younger than a few hundred million years. This disparity extends for a longer time and is more pronounced in low mass stars. Since an inverse square root law is at odds with the observed evolution of angular momentum in young stars, particularly young low mass stars (see § 3.2), it follows that equation 11 cannot be a close description of the torques applied to these objects. On the other hand, the exponential fit is a reasonably close approxima-

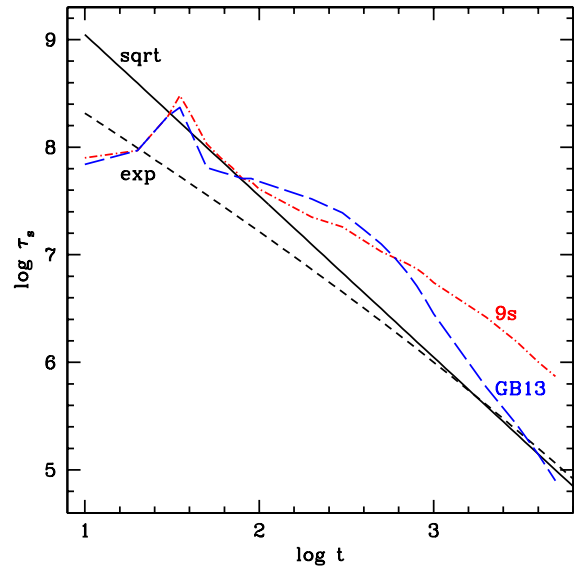


Fig. 8. Absolute value of the specific torque per year, τ_s , as a function of time (Myr), for a stellar mass equal to $1.0 M_{\odot}$. The continuous (sqrt) and dotted (exp) lines are the inverse square root and exponential fits as given by equations 11 and 12. The blue (GB13) and red (9s) tracks are from Amard et al. (2016). The color figure can be viewed online.

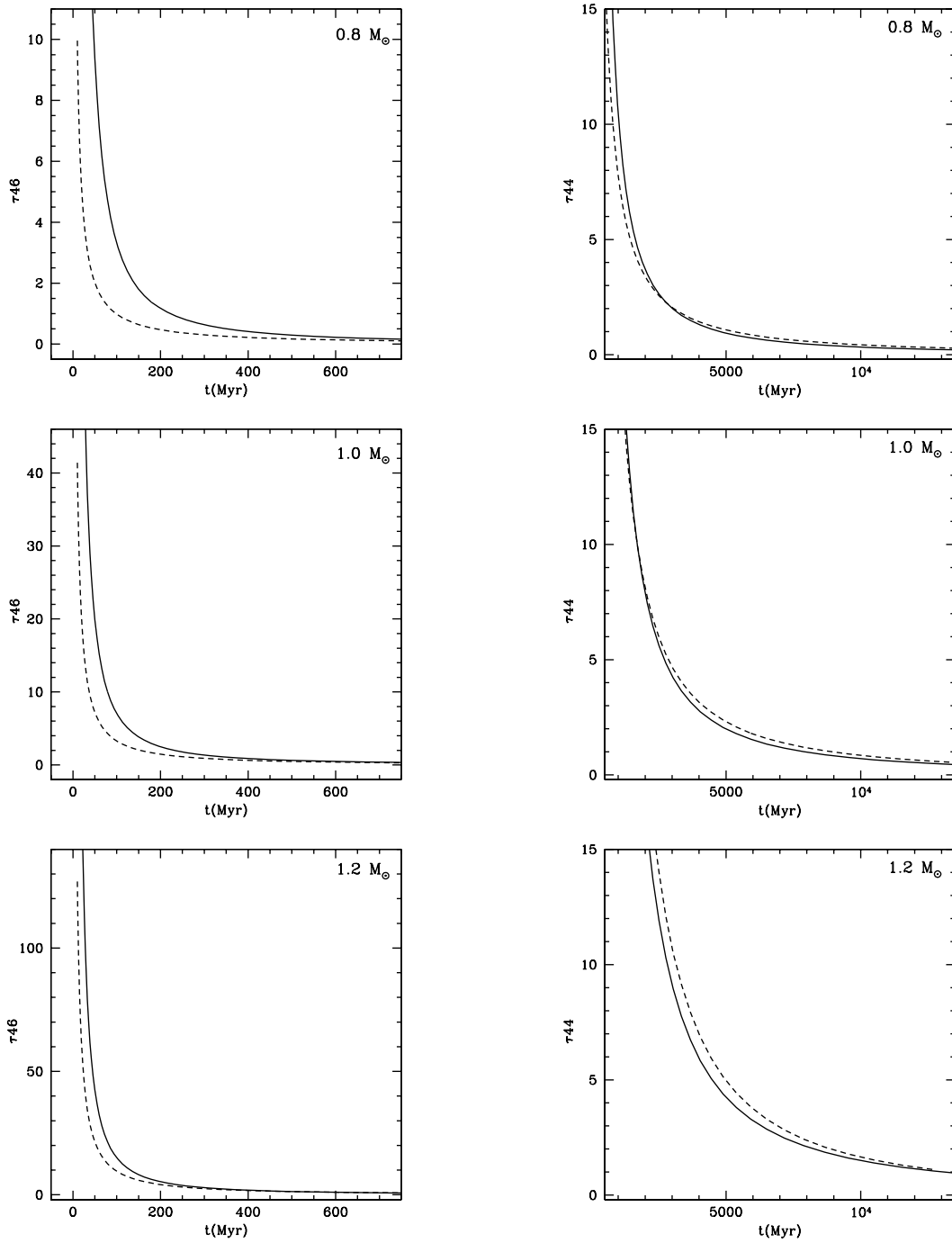


Fig. 9. Absolute value of the torque in units of 10^{46} and $10^{44} \text{ gr cm}^2 \text{ s}^{-1} \text{ Myr}^{-1}$ (τ_{46} and τ_{44}) as a function of time, for stellar masses equal to 0.8 , 1.0 and $1.2 M_{\odot}$. The upper age limit on the left hand side figures is 750 Myr , and the lower age limit on the right hand side figures is 500 Myr . The continuous and dotted lines are torques produced by the inverse square root and exponential fits to the evolution of the angular momentum (equations 11 and 12).

tion to the angular momentum evolution of young stars, so it should lead to a more accurate depiction of the real torque for slowly rotating stars that are

at least as old as the Pleiades cluster, as long as radial differential rotation is nearly absent. Notice that the magnitude of the torque at any given age is

much smaller when the exponential fit is used, and that the demands imposed by a smaller torque are more easily met.

Figure 9 also confirms that the torque is very powerful and variable at least during the first ≈ 500 Myr. After dropping by a couple of orders of magnitude, it is increasingly weaker and stable. Thus, it seems that at least one of the agents driving angular momentum losses, be it the magnetic field strength and/or the mass loss rate, is extremely robust and mutable during the early stages of main sequence evolution. Later on, when the torque is less effective and variable, at least one of these agents must be considerably more stable and moderate. Notice that after ≈ 500 Myr, the torques inferred from inverse square root and exponential relations for the angular momentum are almost indistinguishable.

3.6. A Simple Model for the Torque and Mass Loss Rate as a Function of Time

These empirical approximations and an idealized model of the torque, can be used to explore the mass loss rate as stars evolve during the main sequence. At any given point and time, the torque is given by

$$\tau = \dot{M}\Omega R_c^2, \quad (14)$$

where \dot{M} is the mass loss rate, Ω is the rotational frequency and the lever arm R_c – known as the co-rotation or Alfvén radius – is the distance between the stellar surface and the point where angular momentum is being lost. The co-rotation radius is determined from the proposition that angular momentum is lost when the stellar wind is detached from the magnetic field. This happens when fluid pressure equals magnetic pressure,

$$\rho V^2 = \rho V R_c \Omega = \dot{M}\Omega/4\pi R_c = B_c^2/4\pi, \quad (15)$$

where B_c is the magnetic flux density at R_c . Since the mass loss rate and the magnetic field strength are latitude, longitude and time dependent, and the angular velocity is latitude and time dependent, it follows that the co-rotation radius cannot be uniform and stable. Thus, a continuously changing crumpled ball of paper – definitely not a smooth and steady regular figure – is a plausible visual representation of the co-rotation surface,

The detailed configuration of the magnetic field above the stellar surface has long been recognized as a very difficult problem (Mestel 1968), since it is an extremely complex mixture of small, medium and large scale dynamic structures rising throughout the convective envelope (*e.g.*, Lang et al. 2014).

But it is worth remembering that the dipole is the constituent with the slowest radial decay and therefore presides over the strength of the magnetic field at the co-rotation radius, as was shown by Finley & Matt (2018) after analyzing the combined effect that dipolar, quadrupolar and octupolar geometries had on the magnetic braking mechanism.

In the present day Sun, magnetic fields are produced close to the tachocline, the thin layer between the radiative core and the convective envelope (Charbonneau 2010). But different processes are involved in other stars. In fully convective stars, magnetic fields cannot be generated by the classical $\alpha - \Omega$ process, and it is possible that small scale magnetic fields are produced at various depths by turbulent velocity fields (Durney, De Young & Roxburgh 1993). Additionally, strong toroidal azimuthal fields can show up directly at the stellar surface of stars with a mass between 0.1 and 1.5 M_\odot , and it has been suggested that these are produced by dynamos distributed throughout the convection zone (Donati et al. 1992; Donati & Collier Cameron 1997; See et al. 2015), an idea supported by Brown et al. (2010). Thus, different magnetic energy sources can be located relatively close to the stellar surface but not beyond the tachocline (if there is one).

An extreme, manageable and sensible simplification is to assume that the magnetic field is produced by a collection of dipoles placed at various distances h under the stellar surface. If h is much larger than the physical size of each dipole,

$$B_c = B_s h^3 / (h + R_c)^3, \quad (16)$$

where B_s is the dipole's magnetic field density emerging at the stellar surface. Magnetic braking is effective if the co-rotation radius is at least a few stellar radii from the surface, so that it is quite likely that $h/R_c < 0.01$. If this is so, and the stellar surface is covered by any number of magnetic active regions produced by identical dipolar fields, the total torque is

$$\tau \simeq (f_s B_s)^{4/5} h^{12/5} \dot{M}^{3/5} \Omega^{3/5}, \quad (17)$$

where the filling factor, f_s , is the area covered by the regions that contribute to rotational braking, over the stellar surface area. Notice that the surface field, the mass loss rate and the angular velocity (B_s , \dot{M} and Ω) are averages of these quantities over a time period where all longitudinal and latitudinal fluctuations have been smoothed out, *i.e.*, the twisted short-time dependent co-rotation surface has been idealized as a smooth long-time dependent spherical figure. This implies that the long-time period must comprise several stellar cycles and, even

so, it is almost certain that the distance between the stellar and co-rotation surfaces depends on latitude. Consequently, these averages cannot be expected to be equal or similar to values obtained from observations, since these are completed in shorter time spans.

Mean values of the total field strength can be obtained by measuring Zeeman splitting of unpolarized spectral lines, a procedure known as the ZB technique. This method provides no information on the magnetic field geometry, but it includes the contribution of magnetic field structures of all magnitudes and sizes. Notice that some of these structures may not participate in the magnetic braking process. With a data base of close to a couple of dozen late type main sequence stars, Saar (1996, 2001) found that, except for the most active, their magnetic field density was close to the photospheric equipartition value (same magnetic and thermal pressures), $f_s B_s$ is between ≈ 20 and 4000 G and $f_s B_s$ is nearly proportional to $\Omega^{5/3}$ if the rotational period is more than 3 days (the reported exponent is 1.7). The data show that there is an almost linear relation between the X-ray flux and $f_s B_s$, but there is no mention of possible correlations between magnetic field and age or spectral type.

The ZDI technique has been applied to Stokes V profiles, but in this case the magnetic field flux density, $\langle |B_V| \rangle$, does not include the longitudinal component and small scale fields. Using this technique, Vidotto et al. (2014) calculated the large scale surface magnetic field densities of some 60 main sequence stars, and found that $\langle |B_V| \rangle$ is no larger than ≈ 100 G when the spectral type is between F7 and M3, but larger than this and up to 1580 G in later spectral types. From a sample of close to 60 stars, they worked out that $\langle |B_V| \rangle$ is nearly proportional to $\Omega^{4/3}$ (their exponent is 1.32), though there is a very large scatter and the correlation coefficient is not particularly good. Using age estimates based on different methods, they conclude that $\langle |B_V| \rangle \propto t^{-0.655}$. They also suggest that small and large scale fields could share the same dynamo generation process, but no mention is made of a detailed connection between spectral type and magnetic field in main sequence stars.

Taking these relations between magnetic field and angular velocity into account,

$$\tau \propto h^{12/5} \Omega^{(4\beta+3)/5} \dot{M}^{3/5}, \quad (18)$$

with $\beta \simeq 4/3$ for the global field (ZDI technique) or $5/3$ when all magnetic structures are included (ZB technique). Combining this with equation 13 for the

torque, the evolution of the mass loss rate is given by

$$\dot{M}(M, t) = A(M) I^{(1-4\beta)/3} t^{5\gamma/3} J^{(2-4\beta)/3} h^{-4}, \quad (19)$$

where $A(M)$ is a mass dependent function.

Two solutions for the ratio of the mass loss rate at any time, with respect to the mass loss rate at $t = 100$ Myr, $\dot{M}(100)$, are displayed in Figure 10. These figures are for $\beta = 5/3$ (very similar figures are obtained when $\beta = 4/3$). Being a much better approximation to the evolution of angular momentum during the entire main sequence, the exponential fit (equation 7, $\gamma = C - 1$ and C as given in Table 5) was used to compute the mass loss rate. The moment of inertia is taken from YaPSI models with $[Fe/H] = 0.0$ and $Y_0 = 0.28$. On the left hand side, the average depth of the magnetic field source (h) is assumed to be constant in time, and is therefore included in the empirical mass dependent function $A(M)$. On the right hand side, h does change in time but not the ratio h/h_t , where h_t is depth of the convective envelope. In this case, h/h_t is included in $A(M)$ and the depth of the convective envelope is an additional mass and time dependent parameter. As the moment of inertia, h_t is taken from YaPSI models with $[Fe/H] = 0.0$ and $Y_0 = 0.28$.

If this simple model for the torque is basically correct and the magnetic field behaves as has been discussed, these figures call upon these outcomes:

- (i) After ≈ 100 Myr, the mass loss rate functions of all $0.5 - 1.2 M_\odot$ slowly rotating main sequence stars converge to a time dependence that is approximately proportional to t^{-1} . After ≈ 750 Myr, the inverse square root approximation for the angular momentum can be used to describe the torque and it is easy to see that \dot{M} is proportional to $t^{-8/9}$ if $\beta = 5/3$, and to $t^{-10/9}$ if $\beta = 4/3$. This time dependence lasts up to the first half of the main sequence lifetime of these stars, *i.e.*, as long as there are no major alterations in the moment of inertia and the depth of the magnetic field source. Other authors obtained very similar time dependencies for the mass loss rate of inactive $1 M_\odot$ stars: $t^{-1.1}$ for ages between 200 and 7000 Myr (Cramer & Saar 2011), $t^{-1.23}$ (Suzuki et al. 2013) and $t^{-0.75}$ (Johnstone et al. 2015a) for stars older than 700 Myr.
- (ii) If the mean physical depth of magnetic field sources is constant in time, mass loss rates of all spectral types increase during the first

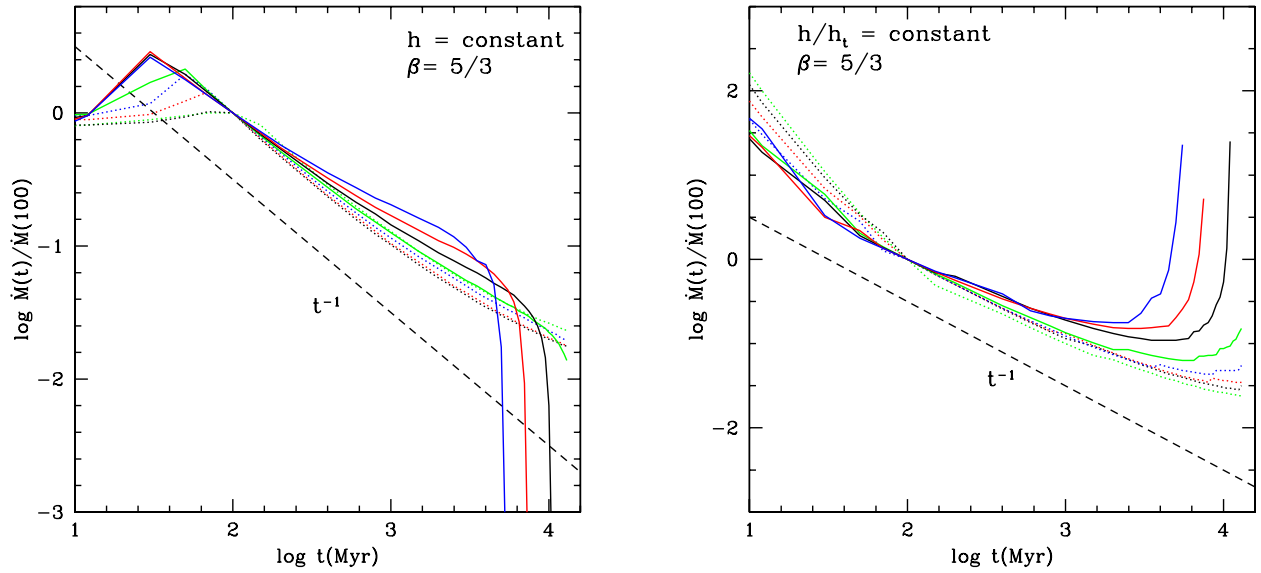


Fig. 10. Ratio of the mass loss rate at time t , $\dot{M}(t)$, with respect to the mass loss rate at $t = 100$ Myr, $\dot{M}(100)$. Dotted lines are for $M/M_{\odot} = 0.5$ (green), 0.6 (black), 0.7 (red) and 0.8 (blue). Continuous lines are for $M/M_{\odot} = 0.9$ (green), 1.0 (black), 1.1 (red) and 1.2 (blue). As indicated, the black dashed line shows the $1/t$ function, which is a good approximation to the mass loss rate when the moment of inertia is constant and the evolution of the angular momentum is described by an inverse square root law. The color figure can be viewed online.

100 Myr and decrease very rapidly as the star approaches the end of main sequence. Obviously, this is mainly driven by changes in the moment of inertia. Intuitively, this does not make sense. The mass loss rate is expected to decrease as the star enters the main sequence since, among other things, the surface area will shrink and the escape velocity will increase as the star contracts. On the contrary, towards the end of main sequence the mass loss rate should tend to increase since the area will be larger and the escape velocity smaller as the star expands. Thus, a constant physical depth for the magnetic sources leads to an unlikely scenario.

- (iii) If the physical depth of magnetic field sources relative to the physical depth of the convective envelope, h/h_t , is constant in time, mass loss rates of all spectral types decrease during the first 100 Myr and increase during the second half of their main sequence. This is mainly driven by changes in the moment of inertia and depth of the convective envelope. Since this is a more likely scenario, it follows that this is a better case for this magnetic torque model, as long

as the empirical formula for the torque holds its ground for stars younger than the Pleiades cluster.

In either one of these scenarios (h or h/h_t constant in time) the mass dependent function, $A(M)$, can be calibrated using a star with known mass, age and mass loss rate. At present, these quantities are known with any certainty for only one star, the Sun. Assuming that it did not have a unique rotational history, the magnetic torque model where h/h_t is constant implies that the present solar mass loss rate is very close to its lowest value ($2 - 3 \times 10^{-14} M_{\odot} \text{ yr}^{-1}$, Wang 1998) and, if magnetic braking is still dominant, leads to a mass loss rate that may be $5 - 8 \times 10^{-14} M_{\odot} \text{ yr}^{-1}$ when our star is 9000 Myr old. Under this scenario, the mass loss rate may have been 2 to $3 \times 10^{-13} M_{\odot} \text{ yr}^{-1}$ when the Sun was around 100 Myr old, if its rotational period was similar to the rotational period of solar type stars in the Pleiades cluster (as discussed in § 3.1, this is not unlikely).

Mass loss rates of a handful of late type main and post-main sequence stars have been calculated from astrospheric absorption in the stellar Lyman- α emission line (Wood et al. 2005; Linsky & Wood 2014),

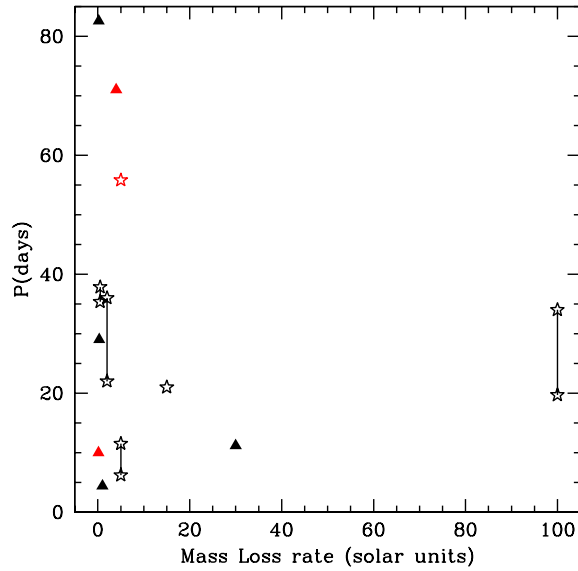


Fig. 11. Rotational periods as a function of mass loss rates. Main sequence stars in black, post-main sequence stars in red. Triangles stand for single star measurements and starred symbols (linked by a line when more than one period has been measured) for measurements including both stars. All mass loss rates are taken from Wood et al. (2005). Rotational periods stem from a variety of sources: Proxima Cen (Collins, Jones & Barnes 2017), α Cen A (Bazot et al. 2007), α Cen B (Dewarf, Datin & Guinan 2010), ϵ Eri (Frölich 2007), 61 Cyg A, 36 Oph A and B, 70 Oph A and B, 61 Vir and δ Eri (Baliunas, Sokoloff & Soon 1996), λ And (Kukarkin et al. 1971), EV Lac (Contadakis 1995), ξ Boo A and B (Noyes et al. 1984) and DK UMa (Gondoin 2005). The color figure can be viewed online.

the only available technique to measure this quantity. There is a good looking correlation between mass loss rate and X-ray flux, as long as the latter is smaller than $\approx 10^6$ erg cm $^{-2}$ s $^{-1}$. Combining this correlation with an X-ray flux *vs.* age relationship (Ayes 1997), Wood et al. (2005) affirm that $\dot{M} \propto t^{-2.33 \pm 0.55}$ in stars where the X-ray flux is smaller than the aforementioned limit. Except for stars younger than ≈ 100 Myr, this relationship is at odds with all the estimates that have just been mentioned.

Different explanations can be tried to account for these discrepancies. But the problem may be directly associated to the mass loss rate *vs.* time relationship put forward by Wood et al. (2005), since there is no connection between the mass loss rate and the rotational period of these stars, as can be seen in Figure 11. Under this circumstance, it is

unlikely that a relation between mass loss rate and age is hidden in their data set. This result should not be unexpected, since the mass loss rate data set stems from a very diverse group of single and binary stars: giant, sub-giant and G2 to M5.5 dwarf stars. Furthermore, there is no way to know the individual mass loss rates in the binary systems α Cen, 36 Oph, λ And, 70 Oph and ξ Boo, since the size of the modeled astrosphere includes both stars. More measurements of the mass loss rate of late type main sequence stars are required to have a better understanding of this quantity as a function of mass and age. An important addition to this discussion is the effect that coronal mass ejections may have on the mass loss rate and rotational braking (*e.g.*, Cranmer 2017).

4. CONCLUSIONS

A database comprising the rotational period, 2MASS photometry and *Gaia* parallax and photometry of thousands of late type main sequence stars was put together. These stars were collected from the *CoRoT* satellite, the *HATNet* survey, the *Kepler* satellite field and 17 open clusters comprising a 13 to 3500 Myr age range. Special care was taken to exclude stars with a precision worse than 20% in their *Gaia* parallax and photometry and 2MASS photometry, that are or may be part of a multiple system, and that have light curve modulations produced by other sources of variability besides rotation. Stellar parameters were deduced matching their absolute magnitudes with those predicted by different sets of YAPSI stellar isochrones, in order to analyze the behavior of angular momentum and other physical quantities as a function of mass and age.

In a figure displaying rotational periods as a function of mass (Figure 2), the vast majority of *Kepler* field main sequence low mass stars lie within a region with clearly defined lower and upper limits (short and long periods). The lower boundary traces the rotational period of stars once they have stabilized in the main sequence. It is also traced by slowly rotating Pleiades stars. The M 35 cluster is supposed to be ≈ 35 Myr older than the Pleiades. The location of its slow rotators runs in parallel but with slightly shorter periods, suggesting that M 35 is younger than the Pleiades.

Very few fast rotating 0.5 - 0.8 M_{\odot} main sequence stars are present in Praesepe (750 Myr), and none are found in NGC 6811 (1000 Myr) and NGC 752 (1350 Myr). Thus, nearly all 0.5 - 0.8 M_{\odot} stars merge into a single slowly rotating mass dependent

sequence after ≈ 750 Myr. No fast $0.8 - 1.2 M_{\odot}$ rotators were found in M 48 (500 Myr), M 37 (450 Myr) and the Pleiades (120 Myr), a few in M 35 (155 Myr, probably less) and some more in M 34 (210 Myr). Thus, most $0.8 - 1.2 M_{\odot}$ main sequence stars seem to merge into a single slowly rotating sequence after ≈ 120 Myr. This implies that rotational convergence in the high mass range happens earlier than previously thought (around 600 Myr).

If stars rotate as rigid bodies – more precisely, if there is no gradient in the radial average of the angular velocity – the angular momentum of the vast majority of 0.5 to $1.2 M_{\odot}$ stars is confined within clearly outlined upper and lower bounds. The lower boundary is defined by a couple of equations. One is valid for $0.9 \leq M/M_{\odot} \leq 1.2$, and the age of this stars is taken as nearly equal to their main sequence lifetime. The second equation applies to less massive stars, with an assumed age that is close to the Milky Way's. It can be said that these equations define a terminal rotational main sequence isochrone. The upper boundary coincides with the position occupied by the slowest rotators of the Pleiades cluster, thus defining a zero age rotational main sequence at ≈ 120 Myr. Stars from the Praesepe cluster delineate a third rotational isochrone at ≈ 750 Myr. The difference between these isochrones is increasingly smaller for less massive stars, showing that the angular momentum loss rate during main sequence is less efficient in low mass stars.

Three types of relationships between angular momentum and age were compared with the average and minimum values of angular momenta of stars within open clusters with known age, as well as the angular momentum of the Sun and stars with ages derived from asteroseismological data modeling. A simple exponential relation, calibrated with the Pleiades and Praesepe isochrones, is at odds with the data. A “classical” inverse square root relation implies that the shape of the angular momentum *vs.* mass distribution is time invariant, but this is not observed. Calibrated with the Praesepe isochrone, this relationship does not hold for stars younger than ≈ 500 Myr, but is consistent with older stars that are more massive than $0.7 M_{\odot}$. A better fit throughout the entire age range is an exponential solution involving the three isochrones and three mass dependent parameters.

During the six hundred million years separating the Pleiades and Praesepe isochrones, the mean angular momentum loss rate is around 90 and a bit more than 40% per Gyr for 1.2 and $0.5 M_{\odot}$ stars. Afterwards, loss rates are much smaller and near

the end of main sequence $\approx 87\%$ of the initial angular momentum of 0.9 to $1.2 M_{\odot}$ stars has been lost. At this point in time, the oldest 0.7 and $0.5 M_{\odot}$ stars have lost 80% and 73% of the angular momentum they had when they set foot on the Pleiades isochrone.

Age estimates based on the angular momentum are likely to be reasonable for middle aged stars if $M \geq 0.7$. These estimates are unreliable at early times, since there is a wide range of periods in contemporary F and G stars younger than 450 Myr and 750 Myr when $0.6 \leq M/M_{\odot} \leq 0.7$. This is also true in aging stars, since rotational periods and angular momenta tend to accumulate in a decreasing range of values, particularly for lower mass stars.

An inverse square root relation between rotational period and age was found to be valid only after $\approx 500 - 750$ Myr and as long as there is no significant change in the moment of inertia, *i.e.*, roughly up to to the end of the first half of the main sequence (1400, 3600, 4500 and 7900 Myr if $M/M_{\odot} = 1.2, 1.1, 1.0,$ and 0.9). The data indicate that during the second half of the main sequence the evolution of the rotational period is increasingly being determined by changes in the moment of inertia, less so by other agents of rotational braking.

The evolution of the Rossby number was computed using the exponential and inverse square root approximations to the evolution of the angular momentum, in combination with YaPSI convective turnover times from isochrones with $[Fe/H] = 0.0$ and $Y_0 = 0.28$. It turns out that it is larger than one for $1.2, 1.1, 1.0$ and $0.9 M_{\odot}$ stars, once they are older than $\approx 500, 2500, 5500$ and 9500 Myr. This implies that the Parker dynamo mechanism may cease before there is a significant change in the moment of inertia of 1.2 and $1.1 M_{\odot}$ stars. If so, their surviving magnetic fossil field, other kind of dynamos – such as the Babcock-Leighton cycle – or local magnetic fields produced by turbulent plasmas, may be the main rotational braking source during the time interval between the interruption of the Parker dynamo and the onset of the phase where the moment of inertia grows in a significant way. Later on, the transformation of the moment of inertia determines the evolution of the rotational period. In less massive stars, dynamo activity will decrease at the same time as the moment of inertia escalates.

The exponential and inverse square root approximations to the evolution of the angular momentum were also used to obtain an empirical formula for the torque, which is very powerful and variable at least during the first ≈ 500 Myr. Thus, the magnetic

field strength and/or the mass loss rate is extremely robust and mutable during the early stages. Later on, after dropping by a couple of orders of magnitude, the torque and at least one of these agents must be increasingly weaker and stable. When this is so, the torques derived from the exponential and inverse square root approximations are nearly identical.

An idealized model of the torque based on these empirical approximations, on observed relationships between the rotational period and the superficial magnetic field (Saar 1996; Vidotto et al. 2014), and on the assumption that the magnetic field is produced by identical dipoles located at a physical depth that is constant in time with respect to the width of the convective envelope, leads to an uncalibrated mass and time dependent equation for the mass loss rate of late type stars. According to this model, after 100 Myr the mass loss rate functions of all 0.5 - 1.2 M_{\odot} stars converge to a time dependence that is roughly proportional to t^{-1} . Towards the end of the main sequence, the mass loss rate is swiftly taken back to its initial value. If the rotational period of the Sun was near the Pleiades isochrone when it was ≈ 100 Myr old, its mass loss rate may have been close to $3 \times 10^{-13} M_{\odot} \text{ yr}^{-1}$. If the magnetic torque is still dominant, it will have a mass loss rate between 5 and $8 \times 10^{-14} M_{\odot} \text{ yr}^{-1}$ when it hits the 9000 Myr mark. If this model is reasonably close to reality, the mass loss rate was about five times more vigorous when life on Earth started 4280 Myr ago (Dodd et al. 2017).

The author acknowledges an unknown referee for a rigorous and productive revision.

APPENDIX

A. DATA SOURCES FOR CLUSTER PARAMETERS

h Persei (Melotte 13; NGC 869). Cluster coordinates and angular radius, Kharchenko et al. (2005, henceforth Ka05); parallax, here; age, Mayne (2008) and Currie et al. (2010); color excess, Ka05 and Currie et al. (2010); $[Fe/H]$ (unknown). The cluster parallax is the mean *Gaia* DR2 parallax of 203 stars from Moraux et al. (2013); stellar parallaxes where the difference with the mean is greater than 0.227 mas were rejected. The mean parallax implies a distance of 1830 ± 400 pc, which is 20% smaller than other estimates (Slesnick, Hillenbrand & Masey 2002; Mayne & Naylor 2008; Currie et al. 2010).

IC 4665 (Collinder 349; Melotte179). Coordinates and parallax, Babusiaux et al. (2018, hence-

forth Ba18); angular radius, Ka05; age, Ka05, Manzi et al. (2008), Cargile & James (2010) and Nepotil et al. (2016, henceforth Ne16); color excess, Mermilliod (1981) and Dias et al. (2002, henceforth Di02); $[Fe/H]$, Ne16. There is a very small difference between the distance implied by the *Gaia* DR2 parallax, 346 pc, and previous determinations (Ka05; Cargile & James 2010).

NGC 2547. Coordinates and parallax, Ba18; angular radius, Ka05; age, Ka05 and Ne16; color excess, Clariá (1982), Naylor & Jeffries (2006), Paunzen et al. (2014) and Ba18; $[Fe/H]$, Ne16. There is a $\approx \pm 10\%$ difference between the inferred distance from the *Gaia* DR2 parallax, 393 pc, and other estimates (Ka05; Naylor & Jeffries 2006).

Blanco 1. Coordinates, Platais et al. (2011); angular radius, Ka05; parallax, here; age, Ne16, Cargile & James (2010) and Juárez et al. (2014); color excess, Di02 and Ba18; $[Fe/H]$, Ne16 and Ford, Jeffries & Smalley (2005). The cluster parallax is the mean *Gaia* DR2 parallax of 22 stars from Cargile et al. (2014); stellar parallaxes where the difference with the mean is greater than 0.080 mas were not considered. The mean parallax implies a distance of 238 ± 2 pc to Blanco 1, almost identical to other estimates (Ka05; van Leeuwen 2009, henceforth vL09; Ba18).

Pleiades (M 45; Melotte 22). Coordinates and angular radius, Ka05; parallax, Ba18; age, Basri & Marcy (1996), Barrado y Navascués et al. (2004), Ka05, vL09, Dahm (2015) and Ba18; color excess, O'Dell, Hendry & Collier Cameron (1994), Di02 and Ba18; $[Fe/H]$, Ne16. With the exception of vL09, there is a very small difference between previous distance estimates and the one inferred from the *Gaia* DR2 parallax, 136 pc.

M 35 (NGC 2168). Coordinates and parallax, Ba18; angular radius, Ka05; age, Barrado y Navascués, Deliyannis & Stauffer (2001), von Hippel et al. (2002), Kalirai et al. (2003), Ka05 and Ne16; color excess, Sung & Bessell (1999) and Di02; $[Fe/H]$, Ne16. The distance found from the *Gaia* DR2 parallax is 894 pc; previous reports from Sung & Bessell (1999), Kalirai et al. (2003) and McNamara et al. (2011) give a distance of 832, 830, 912 and 732 pc to the cluster.

NGC 2301. Coordinates and angular radius, Ka05; parallax, here; age, Ka05, Ne16 and univie.ac.at/webda/; color excess, univie.ac.at/webda/ and Di02; $[Fe/H]$, Ne16. The parallax is the mean *Gaia* DR2 parallax of 44 stars from the list of Sukhbold & Howell (2009); stellar parallaxes where the difference with the mean is smaller or greater

than 0.144 mas were rejected. The mean parallax implies a distance of 975 ± 80 pc to NGC 752 or $\approx 10\%$ larger than other reported values (Ka05; univie.ac.at/webda/).

M 34 (NGC 1039). Coordinates and parallax, Ba18; angular radius, Ka05; age, Ianna & Schlemmer (1993), Meynet, Mermilliod & Maeder (1993), Ka05 and Ne16; color excess, Canterna, Crawford & Perry (1970) and Di02; $[Fe/H]$, Ne16. The distance found from the *Gaia* DR2 parallax, 512 pc, is $\approx 5\%$ larger than previous calculations (Jones & Prosser 1996; Ka05).

M 37 (NGC 2099). Coordinates and angular radius, Ka05; parallax, here; age, Nilakshi & Sagar (2002), Ka05, Hartman et al. (2008) and Pancino et al. (2010); color excess, Di02; Nilakshi & Sagar (2002) and Pancino et al. (2010); $[Fe/H]$, Hartman et al. (2008), Pancino et al. (2010) and Ne16. The cluster parallax is the mean *Gaia* DR2 parallax of 309 stars from the list of Nuñez et al. (2015); stellar parallaxes where the difference with the mean is smaller or greater than 0.149 mas were rejected. The mean parallax implies a distance of 1420 ± 145 pc to M 37, nearly equal to other estimates (Kalirai et al. 2001a; Nilakshi & Sagar 2002; Ka05; Hartman et al. 2008).

M 48 (NGC 2548). Coordinates, Ka05 and Ba18; angular radius, Ka05; parallax, Ba18; age, Balaguer-Núñez et al. (2005), Ka05, Ne16 and Ba18; color excess, Di02, Balaguer-Núñez et al. (2005), Ka05 and Ba18; $[Fe/H]$, Di02, Balaguer-Núñez et al. (2005) and Ne16.

Coma Berenices (Melotte 111; Collinder 256). Coordinates and angular radius, Ka05 and vL09; parallax, Ba18; age, Ka05, Silag & Landstreet (2014), vL09, Ne16 and Ba18; color excess, Nicolet (1981), Di02, Taylor (2006) and Ba18; $[Fe/H]$, Ne16. The *Gaia* DR2 parallax implies a distance of 86 pc, a nearly perfect agreement with other estimates (Ka05; vL09; Majaess et al. 2011).

Hyades (Melotte 25; Collinder 50). Coordinates, univie.ac.at/webda/; angular radius, Perryman et al. (1998) with an assumed distance of 47 pc; parallax, Ba18; age, Brand & Huang 2015, Ne16 and Ba18; color excess, Di02, Taylor (2006) and Ba18; $[Fe/H]$, Cummings et al. (2017). The *Gaia* DR2 parallax implies a distance of 47.6 pc to the cluster, nearly identical to previous estimates (Perryman et al. 1998; vL09; Majaess et al 2011; McArthur et al. 2011).

Praesepe (M 44; NGC 2632). Coordinates and angular radius, Ka05; parallax, Ba18; age, Ka05, Ne16 and Ba18; color excess, Di02 and Taylor (2006);

$[Fe/H]$, Ne16 and Cummings et al. (2017). The distance found from the *Gaia* DR2 parallax is equal to 186 pc, almost identical to distances reported by Ka05 and vL09.

NGC 6811 (Melotte 222). Coordinates and angular radius, Ka05; parallax, here; age, Janes et al. (2013) and Molenda-Zakowicz et al. (2014); color excess, Janes et al. (2013) and Molenda-Zakowicz et al. (2014); $[Fe/H]$, Ne16. The cluster parallax given in Table 1 is the mean *Gaia* DR2 parallax of 34 stars from the list of Meibom et al. (2001b); stellar parallaxes where the difference with the mean is smaller or greater than 0.026 mas were rejected. The mean parallax implies a distance of 1145 ± 20 pc, 7% less than other distance reports (Ka05; univie.ac.at/webda/).

NGC 752 (Melotte 12). Coordinates, Ka05 and Agüeros et al. (2018); angular radius, Ka05; parallax, here; age, Ka05 and Agüeros et al. (2018); color excess, Ka05; $[Fe/H]$, Ne16. The cluster parallax is the mean *Gaia* DR2 parallax of 9 stars from the list of Agüeros et al. (2018); stellar parallaxes where the difference with the mean is smaller or greater than 0.333 mas were rejected. The mean parallax implies a distance of 440 ± 10 pc to NGC 752, nearly equal to other estimates distance (Ka05; Agüeros et al. 2018).

NGC 6819 (Melotte 223; Foxhead). Coordinates, Xin & Deng (2005); angular radius, Platais et al. (2013) and Yang et al. (2013); parallax, here; age, Ne16; color excess, Kalirai et al. (2001b), Di02 and Yang et al. (2013); $[Fe/H]$, Ne16. The cluster parallax is the mean *Gaia* DR2 parallax of 13 stars from the list of Meibom et al. (2015); stellar parallaxes where the difference with the mean is smaller or greater than 0.043 mas were rejected. The mean parallax implies a distance of 2985 ± 220 pc, substantially more (≈ 12 to 40%) than other estimates (Lindoff 1972; Auner 1974; Rosvick & VandenBerg 1998; Kalirai et al. 2001b).

M 67 (NGC 2682). Coordinates and parallax, Ba18; angular radius, Ka05; age, Ka05 and Ne16; color excess, Montgomery, Marschall & Janes (1993), Di02 and Ba18; $[Fe/H]$, Ne16. There is a small difference between the distance found from the *Gaia* DR2 parallax and previous estimates (Twarog, Ashman & Anthony-Twarog 1997; Ka05; Jacobson, Pilachowski & Friel 2011);

REFERENCES

- Aerts, C., Mathis, S., & Rogers, T. M. 2019, A&AR, 57, 35A
 Affer, L., Micela, G., Favata, F., & Flaccomio, E. 2012, MNRAS, 424, 11
 Agüeros, M. A., Bowsher, E. C., Bochanski, J. J., et al. 2018, ApJ, 862, 33

- Agüeros, M. A., Covey, K. R., Lemonias, J. J., et al. 2011, *ApJ*, 740, 110
- Amard, L., Palacios, A., Charbonnel, C., Gallet, F., & Bouvier, J. 2016, *A&A*, 587, A105
- Andrae, R., Foesneau, M., Creevey, O., et al. 2018, *A&A*, 616, 8A
- Auner, G. 1974, *A&AS*, 13, 143
- Ayres, T. R. 1997, *JGR*, 102, 1641
- Babusiaux, C., et al. 2018, *A&A*, 616, 10G (Ba18)
- Balaguer-Núñez, L., Jordi, C., & Galadí-Enríquez, D. 2005, *A&A*, 437, 457
- Baliunas, S., Sokoloff, D., & Soon, W. 1996, *ApJ*, 457, L99
- Baraffe, I., Homeier, D., Allard, F., & Chabrier, G. 2015, *A&A*, 577, A42
- Barnes, J. R., Collier Cameron, A., Donati, J.-F., et al. 2005, *MNRAS*, 357, L1
- Barnes, S. A. 2007, *ApJ*, 669, 1167
- Barnes, S. A., Weingrill, J., Fritzewski, D., Strassmeier, K. G., & Platais, I. 2016, *ApJ*, 823, 16
- Barrado y Navascués, D., Deliyannis, C. P., & Stauffer, J. R. 2001, *ApJ*, 549, 452
- Barrado y Navascués, D., Stauffer, J. R., & Jayawardhana, R. 2004, *ApJ*, 614, 386
- Basri, G., Marcy, G. W., & Graham, J. R. 1996, *ApJ*, 458, 600
- Bazot, M., Bouchy, F., Kjeldsen, H., et al. 2007, *A&A*, 470, 295
- Benomar, O., Takata, M., Shibahashi, H., Ceillier, T., & García, R. A. 2015, *MNRAS*, 452, 2654
- Bohigas, J., Carrasco, L., Torres, C. A. O., & Quast, G. R. 1986, *A&A*, 157, 278
- Bouvier, J., Cabrit, S., Fernández, M., Martin, E. L., & Mathews, J. M. 1993, *A&A*, 272, 176
- Brandt, T. D. & Huang, C. X. 2015, *ApJ*, 807, 58
- Brown, B. P., Browning, M. K., Brun, A. S., Miesch, M. S., & Toomre, J. 2010, *ApJ*, 711, 424
- Brown, T. M., Christensen-Dalsgaard, J., Dziembowski, W. A., et al. 1989, *ApJ*, 343, 526
- Brown, T. M., Latham, D. W., Everett, M. E., & Esquerdo, G. A. 2011, *AJ*, 142, 112
- Bumba, V. & Howard, R. 1965, *ApJ*, 141, 1492
- Busse, F. H. 1970, *ApJ*, 159, 629
- Canterna, R., Crawford, D. L., & Perry, C. L. 1970, *PASP*, 91, 541
- Cargile, P. A. & James, D. J. 2010, *AJ*, 140, 677
- Cargile, P. A., James, D. J., Pepper, J., et al. 2014, *ApJ*, 782, 29
- Carpenter, J. M. 2001, *AJ*, 121, 2851
- Ceillier, T., van Saders, J., García, R. A., et al. 2016, *MNRAS*, 456, 119
- Chaboyer, B., Demarque, P., & Pinsonneault, M. H. 1995, *ApJ*, 441, 865
- Charbonneau, P. & MacGregor, K. B. 1993, *ApJ*, 417, 762
- Charbonneau, P. 2010, *LRSP*, 7, 3
- Charbonnel, C. & Talon, S. 2005, *Science*, 309, 2189
- Charbonnel, C., Decressin, T., Amard, L., Palacios, A., & Talon, S. 2013, *A&A*, 554, A40
- Choi, J., Dotter, A., Conroy, C., et al. 2016, *ApJ*, 823, 102
- Clariá, J. J. 1982, *A&AS*, 47, 323
- Collier Cameron, A. & Campbell, C. G. 1993, *A&A*, 274, 309
- Collier Cameron, A., Campbell, C. G., & Quaintrell, H. 1995, *A&A*, 298, 133
- Collier Cameron, A., Davidson, V. A., Hebb, L., et al. 2009, *MNRAS*, 400, 451
- Collins, J. M., Jones, H. R. A., & Barnes, J. R. 2017, *A&A*, 602, A48
- Covey, K. R., Agüeros, M. A., Law, N. M., et al. 2016, *ApJ*, 822, 81
- Contadakis, M. E. 1995, *A&A*, 300, 819
- Cranmer, S. R., van Ballegoijen, A. A., & Edgar, R. J. 2007, *ApJS*171 520
- Cranmer, S. R. & Saar, S. H. 2011, *ApJ*, 741, 54
- Cranmer, S. R. 2017, *ApJ*, 840, 114
- Cummings, J. D., Deliyannis, C. P., Maderak, R. M., & Steinhauer, A. 2017, *AJ*, 153, 128
- Currie, T., Hernández, J., Irwin, J., et al. 2010, *ApJS*, 186, 191
- Dahm, S. E. 2015, *ApJ*, 813, 108
- Dartmouth, F. G., Chaboyer, B., & Dotter, A. 2011, *ApJ*, 740, L25
- Davies, G. R. et al. 2015, *MNRAS*, 446, 2259
- Delorme, P., Collier Cameron, A., Hebb, L., et al. 2011, *MNRAS*, 413, 2218
- Denissenkov, P. A., Pinsonneault, M., Terndrup, D. M., & Newsham, G. 2010, *ApJ*, 716, 1269
- Denissenkov, P. A. 2010, *ApJ*, 719, 28
- DeWarf, L., Datin, K., & Guinan, E. 2010, *ApJ*, 722, 343
- Dias, W. S., Alessi, B. S., Moitinho, A. & Lépine, J. R. D. 2002, *A&A*, 389, 871 (Di02)
- Dodd, M. S., Papineau, D., Grenne, T., et al. 2017, *Natur*, 543, 60
- Douglas, S. T., Agüeros, M. A., Covey, K. R., et al. 2016, *ApJ*, 822, 47
- Donati, J.-F. et al. 1992, *A&A*, 265, 682
- Donati, J.-F. & Collier Cameron, A. 1997, *MNRAS*, 291, 1
- Durney, B. 1970, *ApJ*, 161, 1115
- Durney, B. R. & Latour, J. 1978, *GApFD*, 9, 241
- Durney, B. R., De Young, D. S., & Roxburgh, I. W. 1993, *SoPh*, 145, 207
- Eff-Darwich, A. & Korzennik, S. G. 2013, *SoPh*, 287, 43
- Epstein, C. R. & Pinsonneault, M. H. 2014, *ApJ*, 780, 159
- Evans, D. W., Riello, M., DeAngeli, F., et al. 2018, *A&A*, 616, A4
- Finley, A. J. & Matt, S. P. 2018, *ApJ*, 854, 78
- Ford, A., Jeffries, E. D., & Smalley, B. 2005, *MNRAS*, 364, 272
- Fröhlich, H.-E. 2007, *AN*, 328, 1037

- Gebran, M., Monier, R., & Richard, O. 2008, *A&A*, 479, 189
- Gallet, F. & Bouvier, J. 2013, *A&A*, 556, A36
 ————. 2015, *A&A*, 577, A98
- Gondoin, P. 2005, *A&A*, 444, 531
- Han, E., Wang, S. X., Wright, J. T., et al. 2014, *PASP*, 126, 827
- Hartman, J. D., Gaudi, B. S., Holman, M. J., et al. 2008, *ApJ*, 675, 1233
- Hartman, J. D., Gaudi, B. S., Pinsonneault, M. H., et al. 2009, *ApJ*, 691, 342
- Hartman, J. D., Bakos, G. A., Kovács, G., & Noyes, R. W. 2010, *MNRAS*, 408, 475
- Hartman, J. D., Bakos, G. A., Noyes, R. W., et al. 2011, *ApJ*, 141, 166
- Henderson, C. B. & Stassun, K. G. 2012, *ApJ*, 747, 51
- Henry, G. W., Eaton, J. A., Hamer, J., & Hall, D. S. 1995, *ApJS*, 97, 513
- Herbig, G. & Spalding, J. F. 1955, *ApJ*, 121, 118
- Herbst, W., Bailer-Jones, C. A. L., Mundt, R., Meisenheimer, K., & Wackermann, R. 2002, *A&A*, 396, 513
- Holl, et al. 2018, *A&A*, 618, A30
- Ianna, P. A. & Schlemmer, D. M. 1993, *AJ*, 105, 209
- Irwin, J., Aigrain, S., Hodgkin, S., et al. 2006, *MNRAS*, 370, 954
- Irwin, J., Hodgkin, S., Aigrain, S., et al. 2008, *MNRAS*, 383, 1588
- Indebetouw, R., et al. 2005, *ApJ*, 619, 931
- Jacobson, H. R., Pilachowski, C. A., & Friel, E. D. 2011, *AJ*, 142, 59
- James, D. J., Barnes, S. A., Meibom, S., et al. 2010, *A&A*, 515, A100
- Janes, K., Barnes, S. A., Meibom, S., & Hoq, S. 2013, *AJ*, 145, 7
- Johnstone, C. P., Güdel, M., Brott, I., & Lüfänger, T. 2015a, *A&A*, 577, A28
- Johnstone, C. P., Güdel, M., Lüfänger, T., Toth, G., & Brott, I. 2015b, *A&A*, 577, A27
- Johnstone, C. P., Pilat-Lohinger, E., Lüfänger, T., Güdel, M., & Stöcl, A. 2019, *A&A*, 626, A22
- Jones, B. F. & Prosser, C. F. 1996, *AJ*, 111, 1193
- Juárez, A. J., Cargile, P. A., James, D. J., & Stassun, K. G. 2014, *ApJ*, 795, 143
- Kalirai, J. S., Ventura, P., Richer, H. B., et al. 2001a, *AJ*, 122, 3239
- Kalirai, J. S., Richer, H. B., Fahlman, G. G., et al. 2001b, *AJ*, 122, 266
- Kalirai, J. S., Fahlman, G. G., Richer, H. B., & Ventura, P. 2003 *AJ*, 126, 1402
- Kawaler, S. D. 1988, *ApJ*, 333, 236
- Kharchenko, N. V., Piskunov, A. E., Roeser, S., Schilbach, E., & Scholz, R.-D. 2005, *A&A*, 438, 1163 (Ka05)
- Kitchatinov, L. L. & Rüdiger, G. 2005, *AN*, 326, 379
- Kitchatinov, L. L. & Nepomnyashchikh, A. 2017, *MNRAS*, 470, 3124
- Koenigl, A. 1991, *ApJ*, 370, L39
- Koppen, J. & Vergely, J.-L. 1998, *MNRAS*, 299, 567
- Korzennik, S. G. & Eff-Darwich, A. 2012, *PASPC*, 462, 267
- Kraft, R. P. 1967, *ApJ*, 150, 551
- Küker, M. & Rüdiger, G. 2008, *JPhCS*, 118, 2029
- Kukarkin, B. V., Kholopov, P. N., Pskovskiy, Y. P., et al. 1971, *General catalog of Variable Stars*, 3rd ed.
- Landin, N. R., Mendes, L. T. S., & Vaz, L. P. R. 2010, *A&A*, 510, A46
- Lang, P., Jardine, M., Morin, J., et al. 2014, *MNRAS*, 439, 2122
- Lindoff, U. 1972, *A&AS*, 7, 497
- Linsky, J. L. & Wood, B. E. 2014, *ASTRP*, 1, 43
- Lomb, N. R. 1976, *Ap&SS*, 39, 447
- Lund, M. N., Miesch, M. S., & Christensen-Dalsgaard, J. 2014, *ApJ*, 790, 121
- MacGregor, K. B. & Brenner, M. 1991, *ApJ*, 376, 204
- Mädler, T., Jofre, P., Gilmore, G., et al. 2016, *A&A*, 595, A59
- Majaess, D. J., Turner, D. G., Lane, D. J., & Krajci, T. 2011, *JAVSO*, 39, 219
- Mamajek, E. E. & Hillenbrand, L. A. 2008, *ApJ*, 687, 1264
- Manzi, S., Randich, S., de Wit, W. J., & Palla, F. 2008, *A&A*, 479, 141
- Marigo, P. et al. 2017, *ApJ*, 835, 77
- Marshall, D. J., Robin, A. C., Reylé, C., Schulteis, M., & Picaud, S. 2006, *A&A*, 453, 635
- Mathur, S., Metcalfe, T. S., Woitaszek, M., et al. 2012, *ApJ*, 749, 152
- Matt, S. P., Brun, A. S., Baraffe, I., Bouvier, J., & Chabrier, G. 2015, *ApJ*, 799, L23
- Mayne, N. J. & Naylor, T. 2008, *MNRAS*, 386, 261
- McArthur, B. E., Benedict, G. F., Harrison, T. E., & van Altena, W. 2011, *AJ*, 141, 172
- McComas, D. J., Barraclough, B. L., Funsten, H. O., et al. 2000, *JGR*, 105, 10419
- McNamara, B. J., Harrison, T. E., McArthur, B. E., & Benedict, G. F. 2011, *AJ*, 142, 53
- McQuillan, A., Aigrain, S., & Mazeh, T. 2103, *MNRAS*, 432, 1203
- McQuillan, A., Mazeh, T., & Aigrain, S. 2014, *ApJS*, 211, 24
- Meibom, S., Mathieu, R. D., & Stassun, K. G. 2009, *ApJ*, 695, 679
- Meibom, S., Mathieu, R. D., Stassun, K. G., Liebesny, P., & Saar, S. H. 2011a, *ApJ*, 733, 115
- Meibom, S., et al. 2011b, *ApJ*, 733, L9
- Meibom, S., Barnes, S. A., Platias, I., et al. 2015, *Natur*, 517, 589
- Melis, C., Reid, M. J., Mioduszewski, A. J., Stauffer, J. R., & Bower, G. C. 2014, *Science*, 345, 1029
- Mermilliod, J. C. 1981, *A&A*, 97, 235
- Mestel, L. 1968, *MNRAS*, 138, 359
- Mestel, L. & Spruit, H. C. 1987, *MNRAS*, 226, 57
- Mestel, L. & Weiss, N. O. 1987, *MNRAS*, 226, 123
- Metcalfe, et al. 2014, *ApJS*, 214, 27
- Meynet, G., Mermilliod, J., & Maeder, A. 1993, *A&AS*, 98, 477

- Molenda-Zakowicz, J., Brogaard, K., Niemczura, E., et al. 2014, *MNRAS*, 445, 2446
- Montgomery, K. A., Marschall, L. A., & Janes, K. A. 1993, *AJ*, 106, 181
- Moraux, E., Artemenko, S., Bouvier, J., et al. 2013, *A&A*, 560, A134
- Morin, J., Donati, J.-F., Petit, P., et al. 2010, *MNRAS*, 407, 2269
- Naylor, T. & Jeffries, R. 2006, *MNRAS*, 373, 1251
- Nepotil, M., Paunzen, E., Heiter, U., & Soubiran, C. 2016, *A&A*, 585, A150 (Ne16)
- Newton, E. R., Mondrik, N., Irwin, J., Winters, J. G., & Charbonneau D. 2018, *AJ*, 156, 217
- Nicolet, B. 1981, *A&A*, 104, 185
- Nielsen, M. B., Gizon, L., Schunker, H., & Karoff, C. 2013, *A&A*, 557, L10
- Nielsen, M. B., Schunker, H., Schou, J., & Ball, W. H. 2017, *A&A*, 603, A6
- Nilakshi & Sagar, R. 2002, *A&A*, 381, 65
- Noyes, R. W., Hartmann, L. W., Baliunas, S. L., Duncan, D. K., & Vaughan, A. H. 1984, *ApJ*, 279, 763
- Núñez, A., Agüeros, M. A., Covey, K. R., et al. 2015, *ApJ*, , 809, 161
- Ochsenbein, F., Bauer, P., & Marcout, J. 2000, *A&AS*, 143, 23
- O'dell, M. A., Hendry, M. A., & Collier Cameron, A. 1994, *MNRAS*, 268, 181
- Pallavicini, R., Golub, L., Rosner, R., et al. 1981, *ApJ*, 248, 279
- Pancino, E., Carrera, R., Rossetti, E., & Gallart, C. 2010, *A&A*, 511, A56
- Parker, E. N. 1955, *ApJ*, 122, 293
- _____. 1958, *ApJ*, 128, 664
- _____. 1988, *ApJ*, 330, 474
- Paunzen, E., Netopil, M., Maitzen, H. M., et al. 2014, *A&A*, 564, A42
- Perryman, M. A. C., Brown, A. G. A., Lebreton, Y., et al. 1998, *A&A*, 331, 81
- Pizzolato, N., Maggio, A., Micela, G., Sciortino, S., & Ventura, P. 2003, *A&A*, 397, 147
- Platais, I., Girard, T. M., Vieira, K., et al. 2011, *MNRAS*, 413, 1024
- Platais, I., Gosnell, N. M., Meibom, S., et al. 2013, *AJ*, 146, 43
- Pourbaix, D., Tokovinin, A. A., Batten, A. H., et al. 2004, *A&A*, 424, 727
- Press, W. H. & Rybicki G. B. 1989, *ApJ*, 338, 277
- Radick, R. R., Thompson, D. T., Lockwood, G. W., Duncan, D. K., & Baggett, W. E. 1987, *ApJ*, 321, 459
- Radick, R. R., Lockwood, G. W., Skiff, B. A., & Thompson, D. T. 1995, *ApJ*, 452, 332
- Rebull, L. M., Wolff, S. C., & Strom, S. E. 2004, *AJ*, 127, 1029
- Rebull, L. M., et al. 2016, *AJ*, 152, 113
- Reiners, A. & Mohanty, S. 2012, *ApJ*, 746, 43
- Reiners, A., Schüssler, M., & Passetger, V. M. 2014, *ApJ*, 794, 144
- Reinhold, T., Reiners, A., & Basri, G. 2013, *A&A*, 560, A4
- Réville, V., Brun, A. S., Matt, S. P., Strugarek, A., & Brun, A. S. 2015, *ApJ*, 798, 116
- Robrade, J. & Schmitt, J. H. M. M. 2009, *A&A*, 496, 229
- Rosvick, J. M. & VandenBerg, D. 1998, *AJ*, 115, 1516
- Saar, S. H. 1996, *IAUS* 176, *Stellar Surface Structure*, ed. K. G. Strassmeier and J. F. Linsky, (Dordrecht), 237
- _____. 2001, *ASPC* 223, *11th Cambridge Workshop on Cool Stars, Stellar Systems and the Sun*, ed. R. J. García López, R. Rebolo, M. R. Zapatero Osorio, (San Francisco, CA: ASP), 292
- Scargle, J. D. 1982, *ApJ*, 263, 835
- _____. 1989, *ApJ*, 343, 874
- Schatzman, E. 1962, *AnAp*, 25, 18
- Scholz, A., Eislöffel, J., & Mundt, R. 2009, *MNRAS*, 400, 1548
- Scholz, A., Irwin, J., Bouvier, J., et al. 2011, *MNRAS*, 413, 2595
- Serenelli, A. & Basu, S. 2010, *ApJ*, 719, 865
- See et al. 2015, *MNRAS*, 453, 4301
- Shulyak, D., Reiners, A., Engeln, A., et al. 2017, *NatAs*, 1, A184
- Shulyak, D. et al. 2019, *A&A*, 626, A86
- Silag, J. & Landstreet J.D. 2014, *A&A*, 566, A132
- Skumanich, A. 1972, *ApJ*, 171, 565
- Slesnick, C. L., Hillenbrand, L. A., & Masey, P. 2002, *ApJ*, 576, 880
- Slettebak, A. 1955, *ApJ*, 121, 653
- Soderblom, D. R., Jones, B. F., & Walker, M. F. 1983, *ApJ*, 274, L37
- Soderblom, D. R., Stauffer, J. R., Hudon, J. D., & Jones, B. F. 1993, *ApJS*, 85, 315
- Spada, F., Demarque, P., Kim, Y.-C., Boyajian, T. S., & Brewer, J. M. 2017, *ApJ*, 838, 161 (YaPSI)
- Spada, F., Demarque, P., Kim, Y.-C., & Sills, A. 2013, *ApJ*, 776, 87
- Stauffer, J. R., Hartmann, L. W., Soderblom, D. R., & Burnham, N. 1984, *ApJ*, 280, 202
- Stauffer, J. R., Hartmann, L. W., Burnham, N., & Burton, F. F. 1985, *ApJ*, 289, 247
- Struve, O. & Elvey, C. T. 1931, *MNRAS*, 91, 663
- Sukhbold, T. & Howell, S. B. 2009, *PASP*, 121, 1188
- Suzuki, T. K., Imada, S., Kataoka, R., et al. 2013, *PASJ*, 65, 98
- Taylor, B. J. 2006, *AJ*, 132, 2453
- Thévenin, F., Provost, J., Morel, P., et al. 2002, *A&A*, 392, L9
- Tomczyk, S., Schou, J., & Thompson, M. J. 1995, *ApJ*, 448, 57
- Tonry, J. L., Stubbs, C. W., Lykke, K. R., et al. 2012, *ApJ*, , 750, 99
- Treanor, P. J. 1960, *MNRAS*, 121, 503
- Twarog, B. A., Ashman, K. M., & Anthony-Twarog, B. J. 1997, *AJ*, 114, 2556

- Usmanov, A. V., Matthaeus, W. H., Goldstein, M. L., & Chhiber, R. 2018, *ApJ*, 865, 25
- Vaiana, G. S. et al. 1981, *ApJ*, 244, 163
- VandenBerg, D. A., Bergbusch, P. A., & Dowler, P. D. 2006, *ApJS*, 162, 375
- van Ballegooijen, A. A., Asgari-Targhi, M., & Berger, M. A. 2014, *ApJ*, 787, 87
- van der Holst, B., Sokolov, I. V., Meng, X., et al. 2014, *ApJ*, 782, 81
- van Leeuwen, F. 2009, *A&A*, 497, 209 (vL09)
- van Saders, J. L., Ceillier, T., Metcalfe, T. S., et al. 2016, *Natur*, 529, 181
- Vidotto, A. A., Gregory, S. G., Jardine, M., et al. 2014, *MNRAS*, 441, 2361
- von Hippel, T., Steinhauer, A., Sarajedini, A., & Deliyannis, C. P. 2002, *AJ*, 124, 1555
- Wang, Y.-M. 1998, ASPC 154, *The Tenth Cambridge Workshop on Cool Stars, Stellar Systems and the Sun*, ed. R. A. Donahue & J. A. Bookbinder (San Francisco, CA: ASP), 131
- Weber, E. J. & Davis, L. 1967, *ApJ*, 148, 217
- Wenger, M. et al. 2000, *A&AS*, 143, 9
- Wilson, O. C. 1966, *ApJ*, 144, 695
- Wood, B. E., Redfield, S., Linsky, J. L., Müller, H.-R., & Zank, G. P. 2005, *ApJS*, 159, 118
- Worthey, G. & Lee, H.-c. 2011, *ApJS*, 193, 1
- Xin, Y. & Deng, L. 2005, *ApJ*, 619, 824
- Yang, S.-C., Sarajedini, A., Deliyannis, C. P., et al. 2013, *ApJ*, 762, 3

ERRATUM: ASYMMETRIC SHAPES OF RADIO RECOMBINATION LINES FROM IONIZED STELLAR WINDS. (RMxAA, 2019, 55, 31)

R. Ignace

Department of Physics & Astronomy, East Tennessee State University.

Received January 14 2020; accepted January 17 2020

A mistake was discovered in part of the derivation for analytic line shapes of radio recombination lines. The mistake does not change the functional form of the solution, but does alter an amplitude factor.

Ignace (2019) considered the analytic derivation for radio recombination lines (RRLs) under simplifying conditions of spherically symmetric, isothermal, and terminal speed flow in which both continuum (free-free) and line (recombination) opacities scale as the square of density. A mistake has been identified in equation (13). A second “formal” error was subsequently identified, but turns out to have no bearing on the derivation, as will be explained.

For context, the solution allowed for a power-law distribution in the clumping parameter:

$$D_{\text{cl}} \propto r^{-m}, \quad (1)$$

with m being the power-law exponent. In Ignace (2019), the solution for the emergent flux from the wind comes from an analytic integral. As published, equation (13) is

$$\int_0^\infty (1 - e^{-ax^\beta}) x dx = \frac{1}{\beta} \Gamma\left(\frac{2}{\beta}\right) a^{2/\beta}, \quad (2)$$

where Γ is the Gamma-function. However, the correct expression should be

$$\int_0^\infty (1 - e^{-ax^{-\beta}}) x dx = \frac{-1}{\beta} \Gamma\left(\frac{-2}{\beta}\right) a^{2/\beta}, \quad (3)$$

where minus signs had been dropped by mistake.

While correcting the above mistake, another error was identified. From Ignace (2019), equation (23) correctly provides the following analytic integral:

$$\int_0^\infty x^{-\beta} e^{-ax} dx = \Gamma(1 - \beta) a^{\beta-1}. \quad (4)$$

However, the domain of application requires that $\beta > -1$, but such is not the case, with $\beta = -(5+m)/(3+m)$. Application of this lookup integral was intended for the second and third terms of equation (22), for which the combined integral would be of the form

$$\int_0^\infty (1 - e^{-\tau_L}) e^{-\tau_W} p dp. \quad (5)$$

This integral does converge. What the paper does is to split up the integrand terms and apply equation (23) to each. Separately, these integrals formally diverge. However, it has been verified numerically for the examples of $m = 0$ and $m = 1$ that the correct answer still results. The solution for the flux needs corrected only for the mistake in equation (13).

Ultimately, that mistake propagates into equations (18), (20), (24), and implicitly (27), only in multiplicative coefficients. Equation (27) is corrected by setting $\gamma_m = 1$, to give

$$\frac{f(w_z)}{f_C} = \left[1 + \frac{t_{LC}(\lambda)}{G_m(\pi)} (\sin \theta)^{1+m} \right]^{2/(3+m)} + \delta_{LC} \left\{ \left[\frac{G_m(\theta)}{G_m(\pi)} + \frac{t_{LC}(\lambda)}{G_m(\pi)} (\sin \theta)^{1+m} \right]^{2/(3+m)} - \left[\frac{G_m(\theta)}{G_m(\pi)} \right]^{2/(3+m)} \right\}, \quad (6)$$

now with

$$f_C = \pi S_C \left(\frac{R_*^2}{d^2} \right) \Gamma \left(\frac{1+m}{3+m} \right) [G_m(\pi) \mathcal{T}_C(\lambda)]^{2/(3+m)}. \quad (7)$$

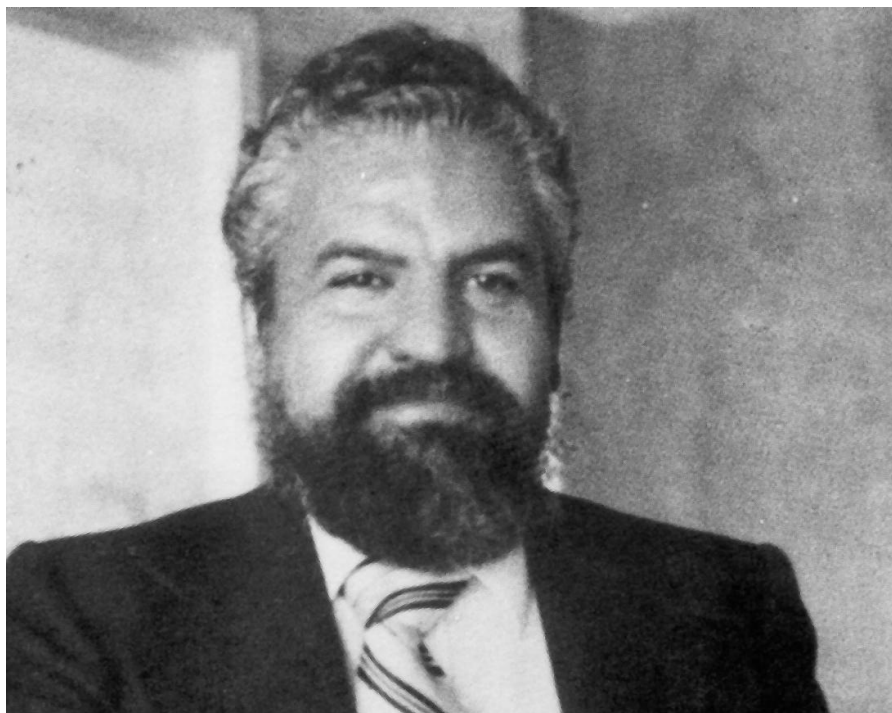
For Figures (2)–(5), the profiles are all correct, but not for the parameters as labeled. For a given profile in Ignace (2019), the mapping from the incorrect parameters (original, or “orig”) to the correct parameters (“new”) is:

$$\delta_{LC}^{\text{new}} = \delta_{LC}^{\text{orig}} \gamma_m^{\text{orig}}. \quad (8)$$

For $m = -0.5, 0$, and 1 , $\gamma_m^{\text{orig}} = 12.3, 8.9$, and 8.0 .

Appreciation is expressed to Ian Stevens for alerting me to the error in the published manuscript.

OBITUARY



Eugenio E. Mendoza Villareal 1927–2019

On October 21, 2019, the Mexican astronomical community mourned the loss of Dr. Eugenio Emilio Mendoza Villareal, a pioneering astronomer. He was 92 years old.

Eugenio was born in Mexico City on August 19, 1927. As a young student at the Escuela Nacional Preparatoria No. 1, Eugenio eagerly learned mathematics and astronomy. In 1949 he entered the Science Faculty of the Universidad Nacional Autónoma de México (UNAM) where he obtained his Bachelor's degree in 1952. Soon thereafter, he was recruited by Guillermo Haro and Paris Pismis, of the National Astronomical Observatory, as a promising candidate to be supported and sent to the USA to pursue a doctorate program in astronomy at a top university. In Tonantzintla he had already met W. W. Morgan, of the University of Chicago, and there he went to obtain his theoretical, spectroscopic and photometric training under W. W. Morgan himself, and also under S. Chandrasekhar and B. Strömberg. He completed his Ph.D. in 1957. After spending a year in Cambridge, England, working with Fred Hoyle, he returned to Mexico in 1958, as the second Mexican astronomer to hold a Ph.D.

At the Astronomy Institute, UNAM, he developed his training and became an acute observer. In the early sixties he undertook the task of searching for a proper site to install the new telescopes of the National Observatory. He is remembered as trekking and camping in the Sierra de San Pedro Mártir, in Northern Baja California, on mule-back, carrying scientific equipment. He found the place where the San Pedro Mártir Observatory stands today. Eugenio acted as the chief of the Observatory from 1970-1972.

Eugenio's astronomical fields of interest were broad, and his contributions were outstanding. Worth mentioning are his discovery of infrared excesses in T Tauri and FU Orionis stars (ApJ 143, 1010, 1966; ApJ 151, 977, 1968), and his infrared observations of V1057 Cyg (BOTT 6, No. 37, 1971; ApJ 169, L117, 1971), which anticipated the discovery of circumstellar disks in pre-main sequence stars.

His design and fabrication of narrow band filters centered on the luminosity-sensitive triplet OI 7774 provided a spectrophotometric measure of the stellar luminosity, and hence of the distance of individual luminous stars, as well as a calibration tool to be used for cosmic distance measurements.

As a well deserved recognition of his work, in 1967 he received the National Prize of Science of the Academia Mexicana de la Investigación Científica. In 1987 he was awarded the UNAM Prize in Exact Sciences.

From 1973 to 1977 he acted as one of the founding editors of the *Revista Mexicana de Astronomía y Astrofísica*, RMxAA.

He retired in 1993. During that year, the Institute of Astronomy held an international Symposium to honor him (RMxAC, Vol. 29, 1993). In 2016 the International School of Observational Astronomy for Latin American Students, at the Tonantzintla Observatory, was held in his honor.

Over nearly four decades he guided and counselled many students, thus establishing a foundation for future generations of astronomers. Those who had the fortune to interact with him were enriched by his expertise and wise guidance; they discovered, behind a rather austere personality, a warm, joyful and friendly person, interested in the problems of his colleagues and always willing to help. I benefitted from Eugenio's good advice and example to decide and find my own professional destiny. I am proud to be a co-author of his last two astronomical papers.

Dr. Eugenio Mendoza is survived by his daughter, Xochiquetzal, and his son, Tonatiuh. Several generations of Mexican astronomers shall remember him thankfully as one of the founders of modern Mexican astronomy.

Armando Arellano Ferro

La *Revista Mexicana de Astronomía y Astrofísica*, fundada en 1974, publica trabajos originales de investigación en todas las ramas de la astronomía, astrofísica y temas vinculados a éstas. Se editan dos números por año y su distribución es gratuita a todas las instituciones relacionadas con los campos cubiertos por esta revista.

La política editorial de la *RMxAA* consiste en enviar a arbitrar los artículos recibidos a especialistas en el campo. Los interesados en publicar en nuestra revista deberán enviar por correo electrónico, a la dirección rmaa@astro.unam.mx, la versión completa de su artículo en formato PostScript o PDF y el archivo LaTeX. Estos archivos deberán ir acompañados de una carta de presentación. Todos los trabajos deben ser preparados en inglés usando la versión más reciente del macro en LaTeX de la *RMxAA* “*rmaa.cls*” (disponible en <https://www.itya.unam.mx/rmaa/>). Se requiere un “Abstract” no mayor que 12 líneas, y un “Resumen” en español (este último podrá ser provisto por los editores de ser necesario); también se incluirán de 1 a 6 palabras clave (“Keywords”) de la lista de las revistas astronómicas internacionales. Se requiere que cada tabla incluida en el texto esté numerada y con título; las figuras deberán estar en formato PostScript (.ps) o PostScript encapsulado (.eps), estar numeradas y con leyenda explicativa. Se requiere que cada tabla y figura estén mencionadas en el texto. El estilo de las referencias sigue las normas astronómicas internacionales recientes. Para mayor información sobre el estilo de la *RMxAA* se puede consultar el archivo de ejemplo que viene incluido en los macros. La publicación es gratuita para los autores.

En 1995 se inició la Serie de Conferencias de la *Revista Mexicana de Astronomía y Astrofísica*, dedicada a la publicación de las memorias de reuniones astronómicas efectuadas en México y en otros países del continente. Hasta 1994 las memorias de reuniones astronómicas de la región se publicaron como volúmenes especiales de la *RMxAA*.

Las condiciones de publicación de cada volumen de las memorias de conferencias serán el resultado de un convenio establecido entre la *RMxAC* y los organizadores de cada evento. Los detalles de la publicación, que incluyen fechas y extensión de los textos, serán anunciados por los editores de cada conferencia. Las contribuciones extensas estarán en inglés con un resumen en español (o portugués en caso de las Reuniones regionales). Los resúmenes de las reuniones que no son temáticas tendrán una extensión máxima de 300 palabras incluyendo título, autores y afiliación; serán exclusivamente en inglés. Los macros LaTeX para las memorias se encuentran en <http://www.astroscu.unam.mx/~rmaa>. Todas las contribuciones y resúmenes deberán estar en estos formatos.

Se concede permiso a los autores de artículos y libros científicos para citar trabajos publicados en la *RMxAA* y en la *RMxAC* siempre y cuando se dé la referencia completa. También se permite la reproducción de figuras y tablas bajo las mismas condiciones.

La *RMxAA* aparece indexada en Current Contents, Science Citation Index, Astronomy and Astrophysics Abstracts, Physics Briefs, Publicaciones Científicas en América Latina, Astronomy and Astrophysics Monthly Index, PERIODICA, RedALyC, Latindex y SciELO.

The *Revista Mexicana de Astronomía y Astrofísica*, founded in 1974, publishes original research papers in all branches of astronomy, astrophysics and closely related fields. Two numbers per year are issued and are distributed free of charge to all institutions engaged in the fields covered by the *RMxAA*.

All papers received by the *RMxAA* are sent to a specialist in the field for refereeing. Authors interested in publishing in the *RMxAA* should send their papers to the e-mail address rmaa@astro.unam.mx, in PostScript or PDF format, along with the LaTeX file. A submission letter should also be sent. Papers should be prepared in English, using the most recent version of the *RMxAA* LaTeX document class “*rmaa.cls*” (available from <https://www.itya.unam.mx/rmaa/>). An “Abstract” of at most 12 lines is required, as well as a “Resumen” in Spanish. The latter can be provided by the Editors, if necessary. A total of six or fewer “Keywords”, taken from the lists of international astronomical journals should be included. Tables should be numbered and include a title. Figures should be submitted in PostScript (.ps) or Encapsulated PostScript (.eps) format, should be numbered, and should include a caption. Both tables and figures should be mentioned in the text. The style of the references follows recent international astronomical usage. For more information about the style norms of *RMxAA* please consult the example included in the LaTeX package. Publication in *RMxAA* is free of charge to authors.

The Conference Series of *Revista Mexicana de Astronomía y Astrofísica* was founded in 1995 to publish the proceedings of astronomical meetings held in Mexico and other countries throughout the continent. Until 1994 such proceedings had been published as special issues of *Revista Mexicana de Astronomía y Astrofísica*.

Conditions of publication of proceedings of each conference will be the result of a mutual agreement between the *RMxAC* and the organizing committee. Details of publication, including length of papers, will be announced by the editors of each event. The extensive contributions should be in English, and should include an abstract in Spanish (or Portuguese for regional meetings). The abstracts of non-thematic meetings should not exceed 300 words including title, authors, and affiliation; they should be exclusively in English. The LaTeX templates specially prepared for proceedings can be obtained at <http://www.astroscu.unam.mx/~rmaa>; all papers should be submitted in this format.

Authors of scientific papers and books may quote articles published both in *RMxAA* and *RMxAC* provided that a complete reference to the source is given. Reproduction of figures and tables is also permitted on the same basis.

The *RMxAA* is indexed in Current Contents, Science Citation Index, Astronomy and Astrophysics Abstracts, Physics Briefs, Publicaciones Científicas en América Latina, Astronomy and Astrophysics Monthly Index, PERIODICA, RedALyC, Latindex, and SciELO.